

**Ageing of bituminous materials  
Experimental and numerical characterization**

Jing, Ruxin

**DOI**

[10.4233/uuid:19e7a9ff-5336-419f-b49a-82bc7c644b02](https://doi.org/10.4233/uuid:19e7a9ff-5336-419f-b49a-82bc7c644b02)

**Publication date**

2019

**Document Version**

Final published version

**Citation (APA)**

Jing, R. (2019). *Ageing of bituminous materials: Experimental and numerical characterization*. [Dissertation (TU Delft), Delft University of Technology]. <https://doi.org/10.4233/uuid:19e7a9ff-5336-419f-b49a-82bc7c644b02>

**Important note**

To cite this publication, please use the final published version (if applicable).  
Please check the document version above.

**Copyright**

Other than for strictly personal use, it is not permitted to download, forward or distribute the text or part of it, without the consent of the author(s) and/or copyright holder(s), unless the work is under an open content license such as Creative Commons.

**Takedown policy**

Please contact us and provide details if you believe this document breaches copyrights.  
We will remove access to the work immediately and investigate your claim.

**Ageing of bituminous materials  
-Experimental and numerical characterization-**

**Proefschrift**

ter verkrijging van de graad van doctor  
aan de Technische Universiteit Delft,  
op gezag van de Rector Magnificus Prof. dr. ir. T.H.J.J. van der Hagen,  
voorzitter van het College voor Promoties,  
in het openbaar te verdedigen  
op maandag 25 februari 2019 om 10:00 uur

door

**Ruxin JING**

Master of Science in Highway and Railway Engineering  
Harbin Institute of Technology, China  
geboren te Inner Mongolia, China

This dissertation has been approved by the  
promotor: Prof. dr. A. Scarpas  
copromotors: Dr. X. Liu and Dr. ir. A. Varveri

Composition of the doctoral committee:

Rector Magnificus	Delft University of Technology, chairperson
Prof. dr. A. Scarpas	Delft University of Technology, promotor
Dr. X. Liu	Delft University of Technology, copromotor
Dr. ir. A. Varveri	Delft University of Technology, copromotor

Independent members:

Prof. dr. ir. S.M.J.G. Erkens	Delft University of Technology
Prof. dr. D.N. Little	Texas A&M University
Dr. A. Bhasin	University of Texas at Austin
Dr. M.L. Greenfield	University of Rhode Island

Reserve member:

Prof. dr. ir. H.E.J.G. Schlangen	Delft University of Technology
----------------------------------	--------------------------------



Rijkswaterstaat  
*Ministry of Infrastructure and the  
Environment*



This research was financially supported by the Ministry of Infrastructure and Environment, Rijkswaterstaat and China Scholarship Council.

Printed by: Ipskamp Printing

ISBN: 978-94-028-1377-7

An electronic version of this dissertation is available at <http://repository.tudelt.nl/>.

Copyright©2019 by Ruxin Jing

All rights reserved. No part of this publication may be reproduced, stored in a retrieval system or transmitted in any form or by any means, electronic or mechanical, including photocopying, recording or otherwise, without the prior written permission of the author.

To my family  
谨以此书献给我的父母



## **Acknowledgements/致谢**

This research was carried out in the Section of Pavement Engineering, Delft University of Technology (TUD). The AAP project was funded by the Dutch Ministry of Transport, Public works and Water Management (Rijkswaterstaat, RWS), and cooperated with Netherlands Organisation for Applied Scientific Research (TNO). I wish to extend my sincere gratitude to these organizations for their sponsorship and support. I would also like to thank the financial support on my living expense in the Netherlands from the Chinese Scholarship Council (CSC) for the past four years.

The story started in the winter of 2013, when I was doing my Master study in Harbin Institute of Technology (HIT), my good friend Chao Xing suggested me to apply the PhD position of TUD. I realised that it was a very good chance to go for further study, so I started to prepare intensely. Looking back to that exciting and worrying period, I would like to thank Prof. Decheng Feng who is my Master's Promotor. His greatly encouraged me to study abroad to broaden my academic horizon and even promised me a PhD position in his group as an alternative to make sure that I could get a position anyhow.

Firstly, I would like to express my gratitude to my promotor Prof. Athanasios Scarpas. I am so happy and honoured that I spent my most important four years studying under his supervision. His clear scientific mind can always point out the right way of my research. His rigorous attitude towards scientific research always helps to find some minor mistakes I made in my study. His humour in life makes me feel relaxed when I talk to him. Both of his directions on my research and his influences on my life are deeply appreciated. I would also like to thank Prof. Sandra Erkens. As one of the managers of the AAP project, her efforts on the coordinate among RWS, TNO and TUD greatly help the project be carried out smoothly. And I really appreciate her valuable

comments, fruitful discussions and finding financial support for the last half year of my research.

My sincere gratitude to my daily supervisors Dr. Xueyan Liu and Dr. Aikaterini Varveri. Dr. Xueyan Liu was the first person of TUD I contacted when I was in Harbin. His broad knowledge on modelling, and ideas and suggestions in research were always excellent and inspiring. In life, he is just like a parent to all the Chinese students in our group. He invited us to his family to celebrate New Year every year. There is an old Chinese saying: “All alone in a foreign land, I am twice as homesick on this day (独在异乡为异客，每逢佳节倍思亲)”. However, with the warm hospitality of his family, we do feel at home. I also wish to extend my appreciation to his wife and daughter, Mrs. Li and Liu Liu. Dr. Aikaterini Varveri is like a sister to me. We helped each other and learnt to grow up together in the PhD study. After she graduated in 2016, I became her first priority in supervision. I feel so appreciated that she was always there whenever I needed her. Her patience and kind guidance allowed me to explore freely in the study. Her detailed modifications and suggestions on my writing greatly helped to improve my thesis. I would like to specially thank Cor Kasbergen. He is a genius in the mathematic and programming. Without his help, it is definitely impossible for me to clearly understand the equations in this book in a short time and implemented them in program.

I would also grateful to my committee members Prof. Dallas Little, Prof. Amit Bhasin and Prof. Michael Greenfield for their time and effort.

I would like to thank all the other staff in the section of Pavement Engineering. I am very grateful for the help from Associate Professor Lamber Houben, Dr. Anupam Kumar and Dr. Alkhateed Loady. Discussion with them can always open my mind in research. I would like thank our technicians Marco Poot, Jan Willem and Michele Aggelen. With the great help of them, I could drill asphalt core, cut asphalt sample and familiar with the most of test equipment. I would also like to thank

our secretary Jacqueline and Claudia. They are always happy to practice Dutch with me, even though my Dutch level is still limited to “Alles goed?”. Special thanks also go to my PhD colleagues Leegwater Greet, Pavalatos Nikiforos, Hong Zhang (张红), Tianchi Tang (唐天驰), Haopeng Wang (王昊鹏), Zhaojie Sun (孙朝杰), Ilhan Cetin and Panos Apostolidis, and visiting scholars Dr. Sang-Soo Kim, Dr. Changhong Zhou (周长红), Dr. Mingxing Li (李明欣), Dr. Naipeng Tang (唐乃鹏), Dr. Chao Xing (邢超), Meng Zhang (张勳), Peng Lin (林鹏) and Yi Zhang (张义). Sharing and exchanging ideas with them can always collide the sparks of wisdom.

I would like to thank my dear friends Dr. Gang Liu (刘刚), Dr. Weigang Wang (王卫刚), Dr. Xuedong Zhang (张学东), Dr. Ran Shang (商冉), Dr. Cuijie Feng (冯翠杰), Dr. Jingyi Hu (胡静怡), Dr. Feifei Wang (王菲菲), Peng Wei (魏鹏), Ying Bai (白莹), Hongxiao Guo (郭鸿潇), Liangfu Wei (魏良福), Dongbin Cai (蔡东斌), Quanxin Xu (徐泉心), Amou Zegard, Farhad Helmand and Simone Leanne. They made my life in Netherlands more interesting and colourful. Special thanks also extend to my dear friends Dr. Qingpeng Li (李清鹏), Yuan Zhao (赵元), Zhijie Li (李智杰), Zhiwei Zhai (翟志伟), Nan Jiang (姜楠), Dr. Haiyan Lu (陆海燕) and Yifu Tian (田一夫). We came to Delft together from HIT in 2014. Starting a life is not easy at a new place, but their friendship and support certainly made things easier.

In case I forgot to mention other colleagues and friends, sorry for that, but I am definitely very grateful for your help in one way or another.

I would like to thank my parents for raising me to become the person I am today, and for their selfless love and endless support during all these years. 深深的感谢我的父亲和母亲，你们用辛勤汗水，哺育我成人；你们用深切教诲，教会我做人；你们无条件的爱和永无止尽的付出陪我一路走过，支持着我一步步完成学业。Special thanks to my



girlfriend, Jiafang (佳芳). All the love, understanding, encouragement and happiness that she gave me are greatly appreciated.

At the end, I would like to thank my grandfathers both on my father's and mother's side. They passed away in the spring of 2016. They knew the beginning of the story, unfortunately they did not make it to the end. I can feel they are living happily in another world, and praying for me and the whole families. Miss you! 最后，愿已此文告慰我的爷爷和姥爷。2016年春季他们相继离世，孙不孝未能在最后的日子陪伴。愿你们在天国一切安好，保佑家人幸福健康。

Ruxin Jing (荆儒鑫)

May 2018

Delft

# Contents

<b>1</b>	<b>INTRODUCTION.....</b>	<b>1</b>
1.1	BACKGROUND.....	2
1.2	BITUMINOUS MATERIALS AGEING MECHANISM .....	5
1.3	RESEARCH OBJECTIVE .....	7
1.4	THESIS OUTLINE.....	8
1.5	REFERENCES .....	10
<b>2</b>	<b>GAS DIFFUSION IN BITUMINOUS MATERIALS .....</b>	<b>13</b>
2.1	INTRODUCTION .....	14
2.1.1	Factors affecting gas diffusion.....	14
2.1.2	Gas diffusion coefficients of bituminous materials.....	16
2.2	GAS DIFFUSION MODEL.....	18
2.2.1	Description of gas diffusion equation .....	18
2.2.2	Boundary conditions .....	19
2.2.3	Solution procedure.....	20
2.2.4	Comparison between different methods .....	34
2.3	APPLICATION.....	37
2.3.1	Development of 3-D microscale FE meshes .....	37
2.3.2	Microscale finite element gas diffusion simulations.....	38
2.4	SUMMARY .....	40
2.5	REFERENCES .....	40
<b>3</b>	<b>OXYGEN DIFFUSION AND REACTION .....</b>	<b>43</b>
3.1	INTRODUCTION .....	44
3.2	FACTORS AFFECTING BITUMEN OXIDATION .....	44
3.3	OXIDATION MODEL.....	48
3.3.1	Chemical equation.....	48
3.3.2	Reaction rate .....	48
3.4	OXYGEN DIFFUSION AND REACTION MODEL .....	49
3.4.1	Basic diffusion and reaction equation .....	50
3.4.2	Boundary condition .....	50
3.4.3	Solution of the diffusion and reaction equation.....	50
3.4.4	Comparison between different methods .....	66
3.4.5	Comparison between diffusion and diffusion-reaction.....	69
3.4.6	Parametric analysis of diffusion-reaction system.....	71
3.5	APPLICATION.....	74
3.6	SUMMARY .....	76
3.7	REFERENCES .....	77

<b>4</b>	<b>PARAMETER DETERMINATION AND VERIFICATION OF OXYGEN DIFFUSION-REACTION MODEL.....</b>	<b>79</b>
4.1	INTRODUCTION .....	80
4.2	REVIEW ON THE EXPERIMENTAL DETERMINATION OF DIFFUSION COEFFICIENT AND REACTION RATE OF BITUMINOUS MATERIALS .....	80
4.3	METHODOLOGY TO DETERMINE THE DIFFUSION COEFFICIENT AND REACTION CONSTANT OF BITUMINOUS MATERIALS .....	86
4.4	OVERVIEW OF EXPERIMENTAL PROGRAM.....	90
4.4.1	Materials .....	91
4.4.2	Ageing method .....	91
4.4.3	Experimental method.....	91
4.5	RESULTS AND DISCUSSION .....	94
4.6	MODEL PARAMETERS DETERMINATION .....	96
4.6.1	Stoichiometry and reaction order .....	97
4.6.2	Initial concentration of reactive components .....	98
4.6.3	Diffusion coefficient .....	102
4.6.4	Reaction constant .....	109
4.7	MODEL VERIFICATION.....	111
4.8	SUMMARY .....	111
4.9	REFERENCES .....	112
<b>5</b>	<b>EFFECT OF AGEING ON BITUMEN CHEMISTRY AND RHEOLOGY. .....</b>	<b>115</b>
5.1	INTRODUCTION .....	116
5.2	OVERVIEW OF EXPERIMENTAL PROGRAM.....	117
5.2.1	Materials .....	117
5.2.2	Ageing method and testing matrix.....	117
5.2.3	Sample preparation .....	119
5.2.4	Experimental method.....	120
5.3	RESULTS AND DISCUSSION: CHEMICAL PROPERTIES.....	121
5.3.1	Effect of ageing time.....	121
5.3.2	Effect of ageing pressure .....	123
5.3.3	Effect of ageing temperature .....	125
5.3.4	Comparison and discussion.....	127
5.4	RESULTS AND DISCUSSION: MECHANICAL PROPERTIES .....	130
5.4.1	Amplitude sweep test.....	130
5.4.2	Frequency sweep test.....	135
5.4.3	Relaxation test .....	142
5.4.4	Fatigue test.....	147
5.5	SUMMARY.....	150
5.6	REFERENCES .....	152

<b>6</b>	<b>AGEING IN THE FIELD.....</b>	<b>155</b>
6.1	INTRODUCTION .....	156
6.2	OVERVIEW OF THE TEST SECTIONS .....	157
6.2.1	Asphalt mixture design .....	157
6.2.2	Construction .....	157
6.2.3	Instrumentation .....	159
6.2.4	UV reflective glass-plate.....	161
6.2.5	Drill core samples.....	161
6.3	TESTS ON ASPHALT MIXTURES .....	163
6.3.1	X-Ray CT scans.....	163
6.3.2	Indirect tensile test.....	164
6.4	TESTS ON RECOVERED BITUMEN .....	170
6.4.1	Bitumen extraction procedure.....	170
6.4.2	FTIR results .....	172
6.4.3	DSR results .....	174
6.4.4	Comparison between laboratory and field ageing .....	177
6.5	SUMMARY .....	180
6.6	REFERENCES .....	181
<b>7</b>	<b>CHEMO-MECHANICS OF AGEING.....</b>	<b>183</b>
7.1	INTRODUCTION .....	184
7.2	CHEMO-MECHANICS OF AGEING MODEL: EMPIRICAL MODEL .....	185
7.2.1	Complex modulus at 20 °C and 10 Hz.....	185
7.2.2	Crossover model and crossover modulus .....	188
7.3	AGEING EFFECT ON CONSTITUTIVE MODELS .....	191
7.3.1	Maxwell model.....	191
7.3.2	Kelvin model.....	193
7.3.3	Burgers model.....	195
7.3.4	Generalized Maxwell model.....	198
7.3.5	Huet model.....	201
7.3.6	Comparison and discussion .....	207
7.4	CHEMO-MECHANICS OF AGEING: CONSTITUTIVE MODELLING.....	208
7.4.1	Model development.....	208
7.4.2	Model implementation .....	211
7.4.3	Model validation.....	214
7.5	SUMMARY .....	217
7.6	REFERENCES .....	218

<b>8</b>	<b>CONCLUSIONS AND RECOMMENDATIONS.....</b>	<b>221</b>
8.1	CONCLUSIONS.....	222
8.1.1	Oxygen diffusion and reaction .....	222
8.1.2	Ageing effect on bitumen chemistry and rheology.....	223
8.1.3	Chemo-mechanics of ageing .....	224
8.2	RECOMMENDATIONS.....	225
	<b>SUMMARY.....</b>	<b>227</b>
	<b>SAMENVATTING .....</b>	<b>229</b>
	<b>CURRICULUM VITAE.....</b>	<b>231</b>
	<b>LIST OF PUBLICATIONS.....</b>	<b>232</b>

# 1

## INTRODUCTION

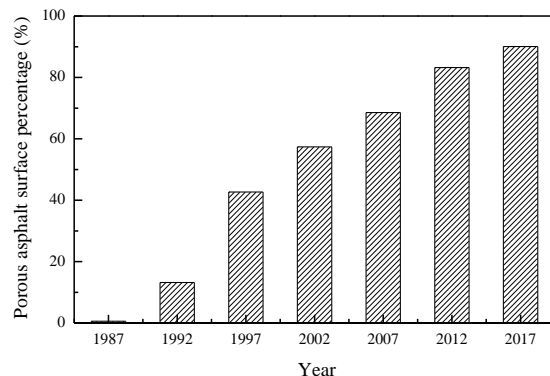
---

## 1.1 Background

With 139,000 km of public roads over an area of 42,000 km<sup>2</sup>, the Netherlands has one of the most dense road networks in the world, Figure 1.1(a). Among them, more than 90% of Dutch highway network is covered with porous asphalt concrete [1], which has been used as surface wearing courses since 1987 [2, 3], Figure 1.1(b). This type of mixtures forms a permeable composition that consists of a relatively high voids content. As a result, porous asphalt provides a significant reduction of noise [4-6], reduction of splash and spray in the wet weather conditions [7, 8], and improvement in skid resistance, drainage and rutting resistance [9, 10].



(a) Road map of the Netherlands



(b) Porous asphalt in the Netherlands

**Figure 1.1 Road map of the Netherlands and growth of porous asphalt in the Netherlands.**

However, the durability of a porous asphalt is different from a traditional dense asphalt concrete. Specifically, the service life of porous asphalt concrete is 20-30 % lower than that of dense asphalt concrete [11, 12]. The reason is that the high permeable voids in porous asphalt not only allow water to drain, but also allow air to flow into the pavement structure more easily. Over time, oxygen continues to diffuse into the pavement and react with asphalt binder. As a result, it accelerates ageing and makes the asphalt binder more brittle, which leads to increased pavement distress level [13-15].

Ravelling is the most common distress identified in porous asphalt concrete [16-18]. It is defined as the loss of stones from the road surface. It occurs either at the interface between the asphalt binder and the aggregates (adhesive damage) or within the asphalt binder (cohesive damage), Figure 1.2. Due to the loss of the stones, the roughness of the pavement increases, thus leading to unsafe driving conditions and high levels of noise pollution. The development of ravelling at the road surface shortens the service life of a pavement [19, 20].



**Figure 1.2 Ravelling failure modes.**

Ageing of bituminous materials is believed to be a major contributor to ravelling of asphalt pavements [21]. Although the amount of bitumen in asphalt mixtures is only 5-7% out of all components, it plays an important role in ensuring the performance and durability of the pavement. The mechanical and chemical properties of bitumen evolve with time, since bitumen is an organic substance. Studies have demonstrated that ductility and penetration of bitumen reduce, while its softening point increase as a result of ageing [22, 23]. Ultimately, the viscosity of the bitumen is increased and it becomes a stiffer material. This may cause the mixture to become excessively hard and brittle, and consequently more susceptible to cracking at low temperature [24]. In addition, ageing may also cause the mixture to become less durable in terms of wear resistance, moisture susceptibility and fatigue life [25, 26].

A deeper understanding of the ageing mechanisms in the Netherlands is crucial to deal with ageing infrastructure and the growing pressure on and lack of natural resources. The use of porous asphalt incurs the



additional costs because of the shorter service life and the more expensive maintenance required. According to the results in many countries, the maintenance costs for porous asphalt (from cleaning the clogged pores to replacement of those layers) are considered higher than for the conventional asphalt [27-29]. On the other hand, the Dutch road engineering community has made significant efforts in recycling of pavements after the end of their service life. Currently, 90% of the asphalt is demolished and used in new asphalt pavement. The very success of recycling in this sector also poses questions towards the future because we are rapidly approaching a situation where recycled materials will be recycled a second or third time. Ideally, it would be nice to keep recycling asphalt concrete indefinitely, but this should be done without loss of functionality or environmental risks.

The Ministry of Transport, Public Works and Water Management (RWS) in the Netherlands is facing a growing challenge in maintaining public roads. Therefore, a project named *Ageing: the road towards perpetual recycling* was carried out from the summer of 2014, in cooperation with Netherlands Organisation for Applied Scientific Research (TNO) and Delft University of Technology (TUD). This project aims to identify the ageing processes on a fundamental level and apply that knowledge to develop perpetual recycling approaches. The route of this project towards the understanding of the ageing phenomena is organized in different hierarchical levels, which focus on different length scales of porous asphalt, Figure 1.3.

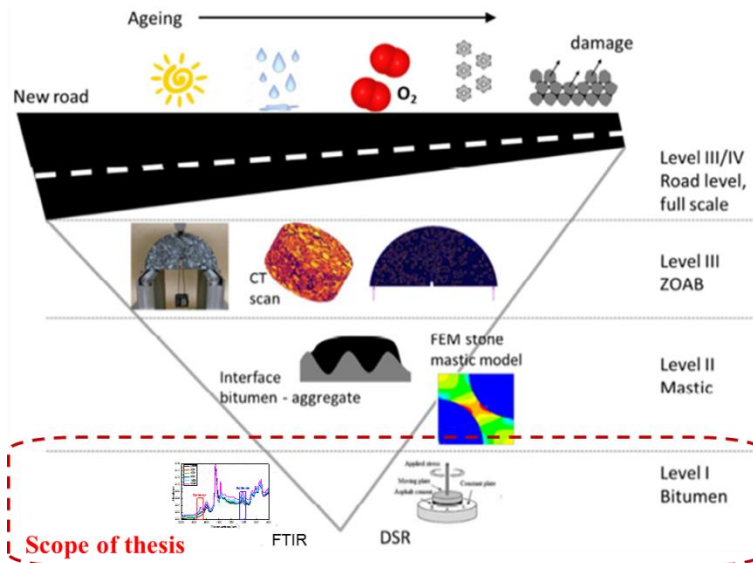


**Figure 1.3 Schematic of the hierarchical approach in project.**

This thesis mainly focuses on bitumen scale, referred to as Level I in Figure 1.3. A good understanding of the fundamental ageing mechanisms at the bitumen scale can provide useful information to further understand ageing at mastic, mixture and pavement scales, as illustrated in Figure 1.3.

## 1.2 Bituminous materials ageing mechanism

The process of ageing includes different mechanisms, such as physical hardening, loss of volatile components, and oxidation [30]. Physical hardening changes the rheological properties of bitumen due to a change in the orientation of molecules, Figure 1.4(a). This process is reversible because it alters the physical properties of bitumen without changing its chemical composition [31, 32]. Evaporation causes the loss of volatile components of bitumen [33, 34], Figure 1.4(b). This mechanism is also considered as one ageing mechanism, although the current penetration grade bitumen types are relatively not volatile. Oxidation is the principal process of ageing mechanisms, which represents an irreversible

phenomenon able to alter the chemical composition of bitumen. This mechanism occurs due to photo-oxidation and thermal-oxidation of bitumen. Photo-oxidation and thermal-oxidation are complex processes that depend upon the climate conditions, i.e. temperature, atmospheric pressure and Ultraviolet (UV) radiation [35, 36].

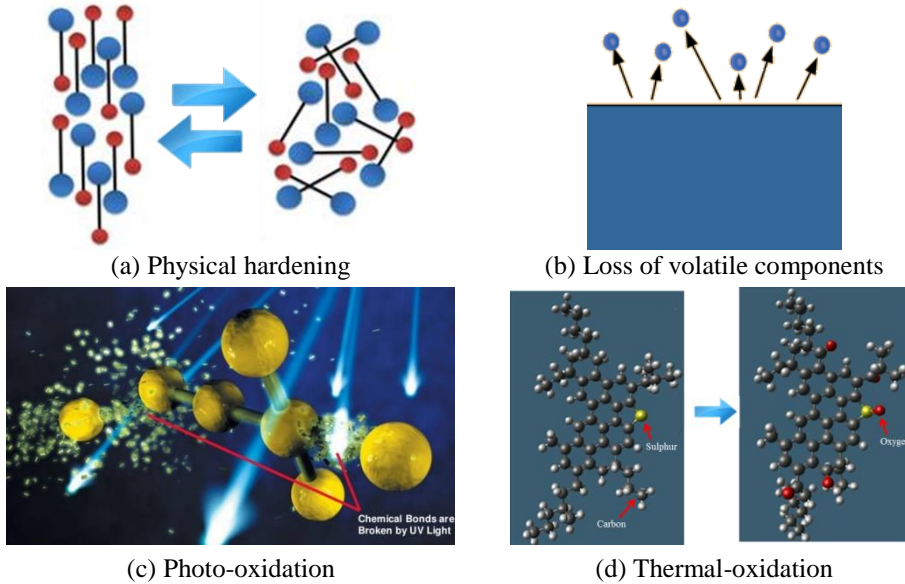


**Figure 1.4 Schematic of ageing mechanism.**

UV radiation is associated with bitumen ageing because it activates photo-oxidation reaction which is the degradation reaction of a bitumen surface in the presence of oxygen or ozone [37, 38], Figure 1.4(c). The effect is facilitated by radiant energy. As a consequence, the bitumen's molecular weight reduces and, the materials becomes more brittle and loses the smoothness of the surface [39]. Photo-oxidation generally takes place within the top 5  $\mu\text{m}$  of the exposed binder film, therefore UV ageing should not be ignored for the upper layer of pavement [40].

Nevertheless, the main ageing mechanism of asphalt pavements is still considered to be thermal oxidation [41, 42]. It is regarded as a chemical reaction process that leads to the transformation of one set of chemical substances to another [43], Figure 1.4(d). The reaction rate depends on

many environmental factors such as temperature, pressure and accessibility to oxygen [44]. Furthermore, it also depends on the characteristics of the asphalt mixture such as type of filler, sand and aggregate, percentage of voids content and layer thickness [45, 46]. All these factors can influence the process of deterioration throughout the service life of an asphalt pavement.

A greater understanding of the bitumen ageing mechanisms and how they changes the physicochemical properties of bitumen can help to accurately predict the service life of an asphalt pavement and develop high performance bituminous products that are less sensitive to ageing.

### **1.3 Research objective**

Even though the mechanisms related to bitumen ageing have been identified and studied for the past few decades, they are today still not understood to the extent that we have been able to mitigate the problem. Current ageing evaluation methods for bituminous materials are still primarily based on the empirical test methods and calculation models, and cannot make accurate ageing predictions.

Therefore, it is uppermost importance to understand the basic mechanisms in which oxygen diffuses into the asphalt binder, reacts with the active bituminous components, and changes the chemical and mechanical properties of bituminous materials, both over short- and long-term periods. For this reason, the objective of this thesis is to acquire an advanced understanding of the fundamental thermal ageing processes of bituminous materials, Figure 1.5. To achieve this, a series of experiments were conducted and computational models were developed. To this end, this research pursues the following objectives:

- (1) Develop an oxygen diffusion-reaction model that simulates oxygen diffusion into bitumen, reaction with active bitumen

component and production of the oxidation products, thus calculates the chemical change of bitumen due to ageing.

- (2) Investigate the effect of different ageing conditioning protocols on the chemical and mechanical characteristics of bitumen and their relationship with field ageing of asphalt mixtures.
- (3) Formulate a chemo-mechanical ageing model that links the chemical changing of bitumen to its mechanical responses due to ageing.

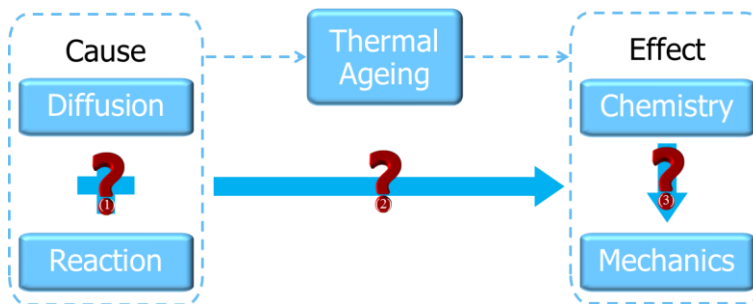


Figure 1.5 Thesis modules.

## 1.4 Thesis outline

This thesis consists of eight chapters that intend to study the most fundamental aspects of bitumen ageing. Chapter 2, 3 and 4 aim to develop a diffusion-reaction model to obtain the chemical changes of bitumen due to ageing. Chapter 5 and 6 investigate ageing effect on chemical and mechanical changing of bitumen at laboratory and field conditions. Chapter 7 dedicates to link the chemical changing of bitumen to its mechanical responses due to ageing. The content of each chapter is introduced in the following paragraphs.

Chapter 1 highlights the great interest on ageing of asphalt pavements, describes the basic ageing mechanisms, states the objective of this study and provides the outline of this thesis. A pertinent literature review is

provided in the start of each chapter according to the corresponding topic treated in the chapter.

Chapter 2 focuses on diffusion at bitumen level. First of all an overview of the main parameters that influence gas diffusion in bitumen is provided. Moreover, the mathematics of modelling gas diffusion are presented and formulated in a form suitable for implementation using three different mathematics approaches, i.e. the numerical integration method, the Laplace transform method and the finite element method.

Chapter 3 aims to understand the diffusion and reaction processes in bitumen. An overview of the main parameters that influence oxidation of bitumen is presented in the beginning of the chapter. Moreover, the mathematics of modelling gas diffusion and reaction are implemented using the theories presented in Chapter 2. In reality, the models developed in Chapter 2 are extended to include the oxygen reaction process.

Chapter 4 dedicates to the development of a methodology for the determination of the diffusion coefficient and reaction constant, discussed in Chapter 3. The method is based on the Fourier Transform Infrared (FTIR) tests. The diffusion and reaction model described in Chapter 3 is verified by the results of laboratory measurements.

Chapter 5 aims to investigate how bitumen properties change as a result of laboratory ageing. In particular, the change in the rheological properties of bitumen were evaluated by the means of dynamic shear rheometer (DSR). Moreover, FTIR was utilized for both the quantitative and qualitative analysis of functional groups during the ageing process.

Chapter 6 studies field ageing. Asphalt samples are cored from pavement test sections that are continuously exposed to environment since 2014. The results from the field cores are then linked to the results from the laboratory aged sample, presented in Chapter 5.

Chapter 7 focuses on linking the chemical characteristics of bitumen to its mechanical response during ageing and developing a framework on the chemo-mechanics of ageing. Specifically, two empirical models are established and one constitutive model is formulated and implemented to capture the viscoelastic response of the bituminous materials across the frequency spectrum.

Chapter 8 concludes this thesis by providing a brief summary of results, as well as the conclusions of this work and recommendations for future research.

## 1.5 References

1. Mo, L., *Damage development in the adhesive zone and mortar of porous asphalt concrete* (doctoral thesis). Delft University of Technology. 2010.
2. Van Der Zwan, J.T., et al., *Porous asphalt wearing courses in the Netherlands: State of the art review*. Transportation Research Record, 1990(1265): p. 95-110.
3. Swart, J., *Experiences with porous asphalt in the Netherlands. Ministry of transportation, public works and water management*. in *Proceedings of the European conference on porous asphalt*. Avon Books, Madrid, Spain, New York. 1997.
4. Hanson, D.I. and R.S. James, *Colorado DOT tire/pavement noise study*. No. CDOT-DTD-R-2004-5. Colorado Department of Transportation, Research Branch.2004.
5. Liu, M., X. Huang, and G. Xue, *Effects of double layer porous asphalt pavement of urban streets on noise reduction*. International Journal of Sustainable Built Environment, 2016. **5**(1): p. 183-196.
6. Ding, Y. and H. Wang, *FEM-BEM analysis of tyre-pavement noise on porous asphalt surfaces with different textures*. International Journal of Pavement Engineering, 2017: p. 1-8.
7. Barrett, M.E., P. Kearfott, and J.F. Malina, Jr., *Stormwater quality benefits of a porous friction course and its effect on pollutant removal by roadside shoulders*. Water Environment Research, 2006. **78**(11): p. 2177-85.
8. Hsu, T.W., S.C. Chen, and K.N. Hung, *Performance evaluation of asphalt rubber in porous asphalt-concrete mixtures*. Journal of Materials in Civil Engineering, 2011. **23**(3): p. 342-349.
9. Chen, J.S., S.F. Chen, and M.C. Liao, *Laboratory and field evaluation of porous asphalt concrete*. Asian Transport Studies, 2015. **3**(3): p. 298-311.
10. Isenring, T., H. Koster, and I. Scazziga, *Experiences with porous asphalt in Switzerland*. Transportation Research Record, 1990(1265): p. 41-53.

11. Takahashi, S., *Comprehensive study on the porous asphalt effects on expressways in Japan: based on field data analysis in the last decade*. Road Materials and Pavement Design, 2013. **14**(2): p. 239-255.
12. Huurman, R.M., L. Mo, and M.F. Woldekidan, *Unravelling porous asphalt concrete towards a mechanistic material design tool*. Road Materials and Pavement Design, 2010. **11**(3): p. 583-612.
13. Ma, X., et al., *Performance of porous asphalt mixture with various additives*. International Journal of Pavement Engineering, 2018. **19**(4): p. 355-361.
14. Lu, X. and U. Isacson, *Chemical and rheological evaluation of ageing properties of SBS polymer modified bitumens*. Fuel, 1998. **77**(9): p. 961-972.
15. Miradi, M., *Knowledge discovery and pavement performance: intelligent data mining* (doctoral thesis). Delft University of Technology. 2009.
16. Molenaar, A., et al., *Performance of porous asphalt concrete*. Journal of the Association of Asphalt Paving Technologists, 2006. **75**: p. 1053-1094.
17. Hagos, E.T., *The effect of aging on binder properties of porous asphalt concrete* (doctoral thesis). Delft University of Technology. 2008.
18. Huber, G., *Performance survey on open-graded friction course mixes*. Synthesis of highway practice 284. National Cooperative Highway Research Program. Transportation Research Board, National Research Council, Washington, DC, 2000.
19. Yildirim, Y., et al., *Winter maintenance issues associated with new generation with new generation open-graded friction courses*. Center for Transportation Research, The University of Texas at Austin, Austin, Texas, 2006.
20. Huurman, M., L. Mo, and M.F. Woldekidan, *Porous asphalt ravelling in cold weather conditions*. International Journal of Pavement Research and Technology, 2010. **3**(3): p. 110-118.
21. Airey, G.D. and Y.K. Choi, *State of the art report on moisture sensitivity test methods for bituminous pavement materials*. Road Materials and Pavement Design, 2002. **3**(4): p. 355-372.
22. Saoula, S., et al., *Analysis of the rheological behavior of aging bitumen and predicting the risk of permanent deformation of asphalt*. Materials Sciences and Applications, 2013. **4**(05): p. 312-318.
23. Siddiqui, M.N. and M.F. Ali, *Investigation of chemical transformations by NMR and GPC during the laboratory aging of Arabian asphalt*. Fuel, 1999. **78**(12): p. 1407-1416.
24. Kliewer, J.E., C.A. Bell, and D.A. Sosnovske, *Investigation of the relationship between field performance and laboratory aging properties of asphalt mixtures*, in *Engineering Properties of Asphalt Mixtures and the Relationship to Their Performance*. 1995, ASTM International. p. 3-20.
25. Das, P.K., et al., *Coupling of oxidative ageing and moisture damage in asphalt mixtures*. Road Materials and Pavement Design, 2015. **16**(sup1): p. 265-279.
26. Das, P.K., et al., *On the oxidative ageing mechanism and its effect on asphalt mixtures morphology*. Materials and Structures, 2015. **48**(10): p. 3113-3127.
27. Moore, L., R. Hicks, and D. Rogge, *Design, construction, and maintenance guidelines for porous asphalt pavements*. Transportation Research Record: Journal of the Transportation Research Board, 2001(1778): p. 91-99.



28. Alvarez, A., *Synthesis of current practice on the design, construction, and maintenance of porous friction courses*. Texas Transportation Institute-Texas A&M University: College Station, TX, 2006.
29. Mo, L.T., et al., *2D and 3D meso-scale finite element models for ravelling analysis of porous asphalt concrete*. *Finite Elements in Analysis and Design*, 2008. **44**(4): p. 186-196.
30. Lu, X., Y. Talon, and P. Redelius, *Ageing of bituminous binders-laboratory tests and field data*. in *Proceedings of the 4th Eurasphalt & Eurobitume Congress, Copenhagen*. 2008. p. 21-23.
31. Struik, L.C.E., *Physical aging in amorphous polymers and other materials* (doctoral thesis). Delft University of Technology. 1977.
32. Ferry, J.D., *Viscoelastic properties of polymers*. 1980: John Wiley & Sons.
33. Nie, F., et al., *Oil sand pyrolysis: Evolution of volatiles and contributions from mineral, bitumen, maltene, and SARA fractions*. *Fuel*, 2018. **224**: p. 726-739.
34. Petersen, J.C., *Chemical composition of asphalt as related to asphalt durability: state of the art*. Transportation research record, 1984(999): p. 13-30.
35. Petersen, J.C., *Asphalt oxidation -- An overview including a new model for oxidation proposing that physicochemical factors dominate the oxidation kinetics*. *Fuel Science and Technology International*, 1993. **11**(1): p. 57-87.
36. Petersen, J.C. and R. Glaser, *Asphalt oxidation mechanisms and the role of oxidation products on age hardening revisited*. *Road Materials and Pavement Design*, 2011. **12**(4): p. 795-819.
37. Lesueur, D., *The colloidal structure of bitumen: Consequences on the rheology and on the mechanisms of bitumen modification*. *Advances in Colloid and Interface Science*, 2009. **145**(1-2): p. 42-82.
38. Hu, J., et al., *Effect of ultraviolet radiation in different wavebands on bitumen*. *Construction and Building Materials*, 2018. **159**: p. 479-485.
39. Feng, Z.-g., et al., *FTIR analysis of UV aging on bitumen and its fractions*. *Materials and Structures*, 2016. **49**(4): p. 1381-1389.
40. Durrieu, F., F. Farcas, and V. Mouillet, *The influence of UV aging of a Styrene/Butadiene/Styrene modified bitumen: Comparison between laboratory and on site aging*. *Fuel*, 2007. **86**(10): p. 1446-1451.
41. Soenen, H., X. Lu, and O.-V. Laukkanen, *Oxidation of bitumen: molecular characterization and influence on rheological properties*. *Rheologica Acta*, 2016. **55**(4): p. 315-326.
42. Petersen, J.C., *A review of the fundamentals of asphalt oxidation: chemical, physicochemical, physical property, and durability relationships*. Transportation Research E-Circular, 2009(E-C140).
43. Wilkinson, A. and A. McNaught, *IUPAC Compendium of chemical terminology, (the "Gold Book")*. 1997, Blackwell Scientific Publications, Oxford.
44. Lopes, M., et al., *Characterisation of ageing processes on the asphalt mixture surface*. *Road Materials and Pavement Design*, 2014. **15**(3): p. 477-487.
45. Das, P.K., N. Kringos, and B. Birgisson, *Numerical study on the effect of mixture morphology on long-term asphalt mixture ageing*. *International Journal of Pavement Engineering*, 2015. **16**(8): p. 710-720.
46. Yin, F., et al., *Long-term ageing of asphalt mixtures*. *Road Materials and Pavement Design*, 2017. **18**(sup1): p. 2-27.

# 2

## **GAS DIFFUSION IN BITUMINOUS MATERIALS**

---

## 2.1 Introduction

Compared with dense asphalt pavement, porous asphalt (PA) pavement has a lower service life due to the fact that PA has no good resistance to raveling which is the main concern for road authorities and operators. Ageing of bitumen due to oxygen diffusion and oxidation is believed to be one of the major causes of raveling in PA. In order to let oxidation occur, air should enter into the pavement through the pore structure and, then it has to be dissolved into the bitumen through molecular diffusion. In other words, bitumen oxidation is controlled by diffusion.

In this chapter, research focuses on diffusion at bitumen level and transport of air into pavements is not included. First of all, an overview of the main parameters that influence gas diffusion in bitumen is presented. Then, three different mathematical approaches of modelling of gas diffusion are presented and implemented. A comparison among the various modelling techniques is made and the validation of the models is presented. At the end, a finite element (FE) model is presented to demonstrate gas diffusion phenomena in porous asphalt mixtures using microscale FE meshes.

### 2.1.1 Factors affecting gas diffusion

Gas diffusion in bituminous materials is a long term and slow process and is controlled by various physicochemical factors such as the chemical composition of bitumen and environmental temperature [1].

#### *Temperature*

Temperature has a strong influence on the diffusion coefficients of gas in solid, liquid and gas phases, because the movement of diffusive gas molecules is accelerated with increasing temperature [2, 3].

The influence of temperature on the diffusion characteristics of gases in different material phases is different. In solid phase, the diffusion

coefficients at different temperatures is generally found to be well predicted by the Arrhenius equation [4]:

$$D(T) = D_0 e^{\frac{-E_A}{kT}} \quad (2.1)$$

where,  $D_0$  is the maximal diffusion coefficient (at infinite temperature),  $E_A$  is the activation energy,  $T$  is the absolute temperature, and  $k$  is the Boltzmann constant ( $1.38 \times 10^{-23}$  J/K).

In liquid phase, an approximate dependence of the diffusion coefficient on temperature can be described by the Stokes-Einstein equation [5], on the basis of the assumption that molecular size of solute is larger than that of the solvent:

$$\frac{D_{T_1}}{D_{T_2}} = \frac{T_1 \eta_{T_2}}{T_2 \eta_{T_1}} \quad (2.2)$$

where  $T_1$  and  $T_2$  are the absolute temperatures,  $D_{T_1}$  and  $D_{T_2}$  are the diffusion coefficients at the corresponding temperatures,  $\eta_{T_1}$  and  $\eta_{T_2}$  are the dynamic viscosities of the liquid.

### *Bitumen type*

Bitumen is composed of complex hydrocarbons, and contains chemical components such as calcium, iron, sulphur, and oxygen [6]. The chemical compositions of bitumen are dependent on the source and type of crude oil, and they have strong influence on the gas diffusion coefficients of bitumen.

Han [7, 8] studied eight different types of bitumen (five base bitumen and three polymer-modified bitumen) at three different temperatures, which are shown in Figure 2.1. The study clearly concluded that both, environmental temperature and chemical composition of the bitumen have a significant effect on the oxygen diffusion coefficient, especially the temperature.

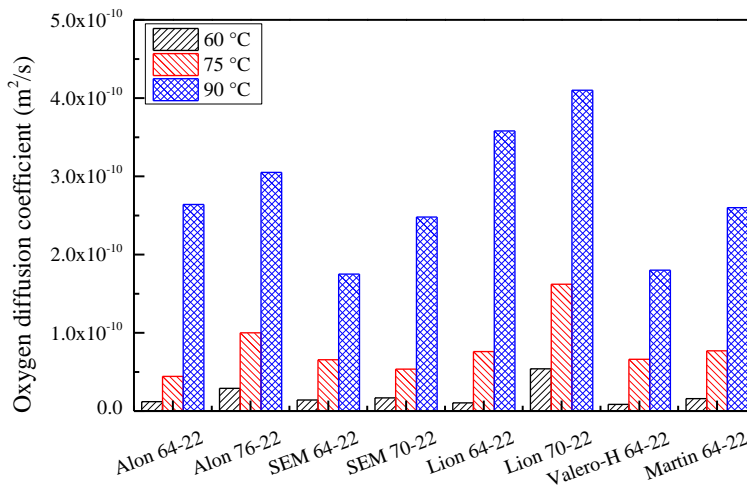


**Figure 2.1 Effect of temperature on gas diffusion coefficient of different bitumen (Han [7])**

### 2.1.2 Gas diffusion coefficients of bituminous materials

In the past, several experiments have been carried out to measure diffusion properties of bitumen [9-12]. The researchers focused primarily on the diffusion of inert gases, which do not undergo chemical reactions with bitumen. Besides temperature and bitumen type, gas diffusion coefficients of bitumen are highly depended on the test method and gas type [13-15]. From the literature, an overview of gas diffusion coefficient of several bitumen types and gas types can be found and it is shown in Table 2.1.

Table 2.1 shows that diffusion coefficients can be significantly different for different types of gas or bitumen at different temperature. Another observation from Table 2.1 is that only few studies have focused on the determination of oxygen diffusion. This is because oxygen not only diffuses into bitumen but also reacts with the constituents of the bitumen simultaneously. Thus, bitumen is gradually depleted. This depletion process masks the actual diffusion process and complicates the determination of the diffusion coefficient.

**Table 2.1 Gas diffusion coefficients for various bitumen**

Diffusion coefficient (m <sup>2</sup> /s)	Gas type	Bitumen type	Temperature (°C)	Reference
5×10 <sup>-15</sup>	O <sub>2</sub>	PEN 40/60 from Middle east	50	van Oort. W.P (1956) [16]
8×10 <sup>-15</sup>	O <sub>2</sub>	PEN 70/100 from Middle east	50	
7×10 <sup>-15</sup>	O <sub>2</sub>	PEN 40/60 from Venezuelan	50	
5×10 <sup>-10</sup>	CO <sub>2</sub>	Athabasca bitumen	50	T. Schmidt (1982) [17]
7.1×10 <sup>-10</sup>	CO <sub>2</sub>		75	
9.2×10 <sup>-10</sup>	CO <sub>2</sub>		100	
(4~7.5)×10 <sup>-10</sup>	CH <sub>4</sub>	Athabasca bitumen	50	T. Schmidt (1984) [18]
1.74×10 <sup>-10</sup>	C <sub>2</sub> H <sub>6</sub>		50	
3.37×10 <sup>-10</sup>	C <sub>2</sub> H <sub>6</sub>		75	
2.2×10 <sup>-10</sup>	CO <sub>2</sub>	Athabasca bitumen	25	S. R. Upreti et al. (2000) [19]
4.7×10 <sup>-10</sup>			90	
8.6×10 <sup>-9</sup>	CO <sub>2</sub>	Heavy oil	21	Y. P. Zhang et al. (2000) [20]
4.8×10 <sup>-9</sup>	CH <sub>4</sub>		21	
2.5×10 <sup>-10</sup>	CO <sub>2</sub>	SYN Bitumen	50	S. R. Upreti et al. (2002) [21]
2.8×10 <sup>-10</sup>	CH <sub>4</sub>		75	
4.0×10 <sup>-10</sup>	C <sub>2</sub> H <sub>6</sub>		75	
5.0×10 <sup>-11</sup>	N <sub>2</sub>		50	
1.828×10 <sup>-10</sup>	O <sub>2</sub>	PEN 180/200	50	P. R. Herrington (2012) [15]
(1.6~12.1)×10 <sup>-10</sup>	CO <sub>2</sub>	Athabasca bitumen	20	S. P. Cadogan et al. (2015) [22]
6.0×10 <sup>-11</sup>	O <sub>2</sub>	AAC-1	70	R. R. Glaser et al. (2015) [23]
1.7×10 <sup>-11</sup>	O <sub>2</sub>	AAK-1	70	
5.1×10 <sup>-16</sup>	N <sub>2</sub>	PEN 70/100	20	R. Jing et al. (2017) [24]
4.5×10 <sup>-14</sup>	N <sub>2</sub>		60	

## 2.2 Gas diffusion model

### 2.2.1 Description of gas diffusion equation

Consider a differential cubic volume element  $dx \, dy \, dz$ , Figure 2.2, in which  $c$  denotes the concentration of gas molecules and  $\mathbf{J}$  is the corresponding flux.

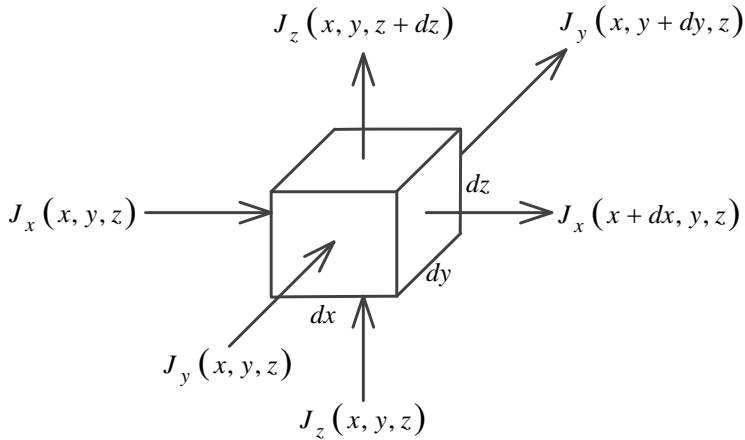


**Figure 2.2 Flux through a cubic volume element**

Then the change of the number of molecules in this volume element is given by the sum of all incoming and outgoing fluxes:

$$\begin{aligned}
 & \frac{\partial c}{\partial t} dx dy dz \\
 &= (J_x(x, y, z) - J_x(x + dx, y, z)) dy dz \\
 &+ (J_y(x, y, z) - J_y(x, y + dy, z)) dx dz \\
 &+ (J_z(x, y, z) - J_z(x, y, z + dz)) dx dy
 \end{aligned} \tag{2.3}$$

From Eq. (2.3), the continuity equation can be written as:

$$\frac{\partial c}{\partial t} = -\frac{\partial J_x}{\partial x} - \frac{\partial J_y}{\partial y} - \frac{\partial J_z}{\partial z} = -\text{div} \mathbf{J} \tag{2.4}$$

Within the framework of linear response theory the flux is proportional to the gradient of  $c$

$$\mathbf{J} = -D\text{grad}c \quad (2.5)$$

where,  $D$  is the diffusion coefficient.

The derivative of Eq. (2.5) is written as:

$$\text{div}(D\text{grad}c) = -\text{div}\mathbf{J} = \frac{\partial c}{\partial t} \quad (2.6)$$

In the special case of constant  $D$ , it simplifies to

$$\frac{\partial c}{\partial t} = D\nabla^2 c \quad (2.7)$$

### 2.2.2 Boundary conditions

In this study, the following two types of boundary conditions are considered:

#### a) Dirichlet boundary condition

The Dirichlet boundary condition specifies that the amount of gas available at boundary is equal to a prescribed value. In mathematical terms,  $c(t)$  at the boundary is specified. In an one dimensional space, for example, it can be realized that the material points  $x_0$  and  $x_N$  at boundary with given  $c(x_0, t)$  and  $c(x_N, t)$ .

#### b) No-flow boundary condition

A no-flow boundary condition specifies that there is no gas flow through the boundary. In mathematical terms, it can be realized by a reflection at the boundary. In an one dimensional space, for instance, additional points  $x_{-1}$  and  $x_{N+1}$  are added at boundary with  $c(x_{-1}, t) = c(x_1, t)$  and  $c(x_{N+1}, t) = c(x_{N-1}, t)$  which compensate for the flux through the boundary.



## 2.2.3 Solution procedure

### 2.2.3.1 Numerical integration method

#### 2.2.3.1.1 Discretization in space and time

The basic idea of the numerical integration method for the diffusion equation is to replace spatial (one dimensional for now) and time derivatives by suitable approximations. Specifically, instead of solving for  $c(x(t))$  with  $x$  and  $t$  continuous,  $c(x_i(t_j))$  is solved, where:

$$x_i = i\delta x \quad (2.8)$$

$$t_j = j\delta t \quad (2.9)$$

Derivatives of  $c$  are approximated by using the  $c$  value of each point. For example:

$$\frac{\partial c}{\partial x} = \lim_{\Delta x \rightarrow 0} \frac{\Delta c}{\Delta x} \quad (2.10)$$

The derivative at the point  $x(t) = x_i(t_j)$  can be evaluated approximately in various ways, of which the simplest are the following:

Forward difference method:

$$\left. \frac{\partial c}{\partial x} \right|_{x_i, t_j} \approx \frac{c(x_{i+1}(t_j)) - c(x_i(t_j))}{x_{i+1} - x_i} = \frac{c(x_{i+1}(t_j)) - c(x_i(t_j))}{\delta x} \quad (2.11)$$

Backward difference method:

$$\left. \frac{\partial c}{\partial x} \right|_{x_i, t_j} \approx \frac{c(x_i(t_j)) - c(x_{i-1}(t_j))}{x_i - x_{i-1}} = \frac{c(x_i(t_j)) - c(x_{i-1}(t_j))}{\delta x} \quad (2.12)$$

Central difference method:

$$\left. \frac{\partial c}{\partial x} \right|_{x_i, t_j} \approx \frac{c(x_{i+1}(t_j)) - c(x_{i-1}(t_j))}{x_{i+1} - x_{i-1}} = \frac{c(x_{i+1}(t_j)) - c(x_{i-1}(t_j))}{2\delta x} \quad (2.13)$$

The second space derivative at the point  $x_i(t_j)$  is approximated by using the following equation

$$\frac{\partial^2 c}{\partial x^2} = \lim_{\Delta x \rightarrow 0} \frac{\Delta \left( \frac{\partial c}{\partial x} \right)}{\Delta x} \quad (2.14)$$

In order to solve Eq. (2.14), firstly the term of  $\frac{\partial c}{\partial x}$  has to be obtained by using the central difference method at fictitious points  $x_{i+\frac{1}{2}}$  and  $x_{i-\frac{1}{2}}$ .

$$\left. \frac{\partial c}{\partial x} \right|_{x_{i+\frac{1}{2}}, t_j} \approx \frac{c(x_{i+1}(t_j)) - c(x_i(t_j))}{x_{i+1} - x_i} \quad (2.15)$$

$$\begin{aligned} &= \frac{c(x_{i+1}(t_j)) - c(x_i(t_j))}{\delta x} \\ \left. \frac{\partial c}{\partial x} \right|_{x_{i-\frac{1}{2}}, t_j} &\approx \frac{c(x_i(t_j)) - c(x_{i-1}(t_j))}{x_{i+1} - x_i} \\ &= \frac{c(x_i(t_j)) - c(x_{i-1}(t_j))}{\delta x} \end{aligned} \quad (2.16)$$

Then, Eq. (2.14) can be written as

$$\begin{aligned} \left. \frac{\partial^2 c}{\partial x^2} \right|_{x_i, t_j} &\approx \frac{\left. \frac{\partial c}{\partial x} \right|_{x_{i+\frac{1}{2}}, t_j} - \left. \frac{\partial c}{\partial x} \right|_{x_{i-\frac{1}{2}}, t_j}}{x_{i+\frac{1}{2}} - x_{i-\frac{1}{2}}} \\ &= \frac{c(x_{i+1}(t_j)) - 2c(x_i(t_j)) + c(x_{i-1}(t_j))}{(\delta x)^2} \end{aligned} \quad (2.17)$$

The approximations of the time derivatives are solved in the same way.

For example, the forward difference approximation for  $\frac{\partial c}{\partial t}$  at the point

$x_i(t_j)$  is as follows

$$\left. \frac{\partial c}{\partial t} \right|_{x_i, t_j} \approx \frac{c(x_i(t_{j+1})) - c(x_i(t_j))}{t_{j+1} - t_j} = \frac{c(x_i(t_{j+1})) - c(x_i(t_j))}{\delta t} \quad (2.18)$$

Using Eq. (2.17) and Eq. (2.18), Eq. (2.7) can be found by solving in an iterative way for the approximate solution via the following equation.

$$c(x_i(t_{j+1})) = c(x_i(t_j)) + D \frac{\delta t}{(\delta x)^2} (c(x_{i+1}(t_j)) - 2c(x_i(t_j)) + c(x_{i-1}(t_j))) \quad (2.19)$$

### 2.2.3.1.2 Stability analysis

In matrix notation the one-dimensional algorithm with boundary condition  $c = 0$  is given by

$$\begin{pmatrix} c(x_1(t_{j+1})) \\ \vdots \\ c(x_N(t_{j+1})) \end{pmatrix} = A \begin{pmatrix} c(x_1(t_j)) \\ \vdots \\ c(x_N(t_j)) \end{pmatrix} \quad (2.20)$$

where  $A$  is described as a tridiagonal matrix as following

$$A = \begin{pmatrix} 1-2r & r & & & \\ r & 1-2r & r & & \\ & \ddots & \ddots & \ddots & \\ & & r & 1-2r & r \\ & & & r & 1-2r \end{pmatrix} \quad (2.21)$$

where

$$r = D \frac{\delta t}{(\delta x)^2} \quad (2.22)$$

or by defining  $A$  as

$$A = 1 + rM \quad (2.23)$$

where  $M$  is a tridiagonal matrix

$$M = \begin{pmatrix} -2 & 1 & & & \\ 1 & -2 & 1 & & \\ & \ddots & \ddots & \ddots & \\ & & & 1 & -2 & 1 \\ & & & & 1 & -2 \end{pmatrix} \quad (2.24)$$

The eigenvalues of  $M$  in which is defined in reference [25] are

$$\lambda = -4 \sin^2 \left( \frac{k}{2} \right) \text{ with } k = \frac{\pi}{N+1}, \frac{2\pi}{N+1}, \dots, \frac{N\pi}{N+1} \quad (2.25)$$

Hence, the eigenvalues of  $A$  are given by

$$1 + r\lambda = 1 - 4r \sin^2 \left( \frac{k}{2} \right) \quad (2.26)$$

For stability of algorithm, the following requirement should be satisfied.

$$|1 + r\lambda| < 1 \text{ for all } \lambda \quad (2.27)$$

In other words

$$-1 < 1 - 4r \sin^2 \left( \frac{k}{2} \right) < 1 \quad (2.28)$$

The maximum value of the sine function  $\sin \left( \frac{k}{2} \right)$  in Eq. (2.28) is equal to 1. Hence, the right hand side of the equation is fulfilled and for the left part it should hold that

$$-1 < 1 - 4r \quad (2.29)$$

Finally, the stability condition of Eq. (2.20) is obtained

$$r = D \frac{\delta t}{(\delta x)^2} < \frac{1}{2} \quad (2.30)$$

### 2.2.3.2 Laplace transform method

The Laplace transform method is a technique for solving linear differential equations with initial conditions. By applying the Laplace transform, an ordinary differential equation is changed into an algebraic

equation which is generally easier to deal with than the original differential equation.

Assume that the diffusion coefficient is constant and there is not flow out of bottom boundary. According to Eq. (2.7), the one dimensional differential equation of gas diffusion can be written as

$$D \frac{\partial^2 c}{\partial x^2} = \frac{\partial c}{\partial t} \quad (2.31)$$

with following boundary conditions

$$x = 0 \quad \frac{\partial c}{\partial x} = 0 \quad (2.32)$$

$$t = 0, x > 0 \quad c = 0 \quad (2.33)$$

and

$$x = x_0 \quad c = c_0 \quad (2.34)$$

where  $x_0$  is the layer thickness and  $c_0$  is the concentration of free gas at the boundary. It means that a constant gas concentration  $c_0$  was applied on the boundary  $x_0$ .

When the Laplace transform method is applied on the diffusion equation with the boundary condition Eq. (2.33), the transform of the diffusion equation (2.31) is found to be:

$$D \frac{\partial^2 \bar{c}}{\partial x^2} = p \bar{c} \quad (2.35)$$

where,  $p$  is the Laplace transform variable.

The boundary conditions Eq. (2.32) and Eq. (2.34) are transformed into:

$$x = 0 \quad \frac{\partial \bar{c}}{\partial x} = 0 \quad (2.36)$$

$$x = x_0 \quad \bar{c} = \frac{c_0}{p} \quad (2.37)$$

Assume that

$$\bar{c}(x, p) = F(x)G(p) \quad (2.38)$$

Combining Eq. (2.35) and Eq. (2.38) gives

$$F(x) = c_1 e^{\sqrt{\frac{p}{D}}x} + c_2 e^{-\sqrt{\frac{p}{D}}x} \quad (2.39)$$

By substituting Eq. (2.39) into Eq. (2.38) provides

$$\bar{c}(x, p) = \left( c_1 e^{\sqrt{\frac{p}{D}}x} + c_2 e^{-\sqrt{\frac{p}{D}}x} \right) G(p) \quad (2.40)$$

Applying the boundary condition Eq. (2.36) into Eq. (2.40) one gets

$$\left. \frac{\partial \bar{c}}{\partial x} \right|_{x=0} = G(p) \sqrt{\frac{p}{D}} (c_1 - c_2) = 0 \quad (2.41)$$

Thus

$$c_1 = c_2 \quad (2.42)$$

Together Eq. (2.40) and Eq. (2.42) gives

$$\bar{c}(x, p) = c_1 G(p) \left( e^{\sqrt{\frac{p}{D}}x} + e^{-\sqrt{\frac{p}{D}}x} \right) = 2c_1 G(p) \cosh \left( \sqrt{\frac{p}{D}}x \right) \quad (2.43)$$

By introducing

$$H(p) = 2c_1 G(p) \quad (2.44)$$

Eq. (2.43) transforms to

$$\bar{c}(x, p) = H(p) \cosh \left( \sqrt{\frac{p}{D}}x \right) \quad (2.45)$$

Applying the boundary condition Eq. (2.37) into Eq. (2.45) gives

$$\bar{c}(x, p) \Big|_{x=a} = H(p) \cosh \left( \sqrt{\frac{p}{D}}a \right) = \frac{c_0}{p} \quad (2.46)$$

Thus

$$H(p) = \frac{c_0}{p} \frac{1}{\cosh\left(\sqrt{\frac{p}{D}}a\right)} \quad (2.47)$$

Combining Eq. (2.45) and Eq. (2.47) results in

$$\bar{c}(x, p) = \frac{c_0}{p} \frac{\cosh\left(\sqrt{\frac{p}{D}}x\right)}{\cosh\left(\sqrt{\frac{p}{D}}a\right)} \quad (2.48)$$

Applying inverse Laplace transformation into Eq. (2.48) gives

$$c = \frac{1}{2\pi i} \int_{e-i\infty}^{e+i\infty} \frac{c_0}{p} \frac{\cosh\left(\sqrt{\frac{p}{D}}x\right)}{\cosh\left(\sqrt{\frac{p}{D}}a\right)} e^{pt} dp \quad (2.49)$$

The singularities of the integrand are the singularity of the first order  $p=0$  and the zeros of  $\cosh\left(\sqrt{\frac{p}{D}}x_0\right)$ , yielding the first order singularities:

$$\sqrt{\frac{p}{D}}x_0 = n\pi i + \frac{\pi}{2}i \quad (2.50)$$

Thus

$$p_n = -\frac{D}{x_0^2} \left(n + \frac{1}{2}\right)^2 \pi^2 \quad (2.51)$$

Such a value of  $c$ , which is purely real, must be chosen such that the path of integration in the  $p$ -plane takes a course which leaves the singularity of the integrand at the left side. The line integral can be evaluated by transforming it into a closed contour and applying the theorem of residues hence:

$$\begin{aligned}
 c &= 2\pi i \sum_{n=0}^{\infty} \text{Res} \left( \frac{1}{2\pi i} \frac{c_0}{p} \frac{\cosh\left(\sqrt{\frac{p}{D}}x\right)}{\cosh\left(\sqrt{\frac{p}{D}}x_0\right)} e^{pt}, p=0 \text{ \& } p=p_n \right) \\
 &= \sum_{n=0}^{\infty} \text{Res} \left( \frac{c_0}{p} \frac{\cosh\left(\sqrt{\frac{p}{D}}x\right)}{\cosh\left(\sqrt{\frac{p}{D}}x_0\right)} e^{pt}, p=0 \text{ \& } p=p_n \right) \\
 &= \text{Res}(p=0) + \sum_{n=0}^{\infty} \text{Res}(p=p_n)
 \end{aligned} \tag{2.52}$$

It follows that:

$$\text{Res}(p=0) = c_0 \tag{2.53}$$

For the other singularities  $p = p_n$ , introduce:

$$r_n = \frac{D}{x_0^2} \left( n + \frac{1}{2} \right)^2 \pi^2 \tag{2.54}$$

which leads to

$$\sqrt{p_n} = i\sqrt{r_n} \tag{2.55}$$

Now assume that

$$f(r) = -\frac{c_0}{r} \frac{\cosh\left(i\sqrt{\frac{r}{D}}x\right)}{\cosh\left(i\sqrt{\frac{r}{D}}x_0\right)} e^{-rt} = -\frac{c_0}{r} \frac{\cos\left(\sqrt{\frac{r}{D}}x\right)}{\cos\left(\sqrt{\frac{r}{D}}x_0\right)} e^{-rt} \tag{2.56}$$

Thus

$$\begin{aligned}
 \text{Res}(f(r), r_n) &= \lim_{r \rightarrow r_n} (r_n - r) f(r) \\
 &= -\frac{c_0}{r_n} \cos\left(\sqrt{\frac{r_n}{D}}x\right) e^{-r_n t} \lim_{r \rightarrow r_n} \frac{r_n - r}{\cos\left(\sqrt{\frac{r}{D}}x_0\right)}
 \end{aligned} \tag{2.57}$$



Based on the L'Hôpital's rule, Eq. (2.57) is transformed into:

$$\begin{aligned}
 \text{Res}(f(r), r_n) &= -\frac{c_0}{r_n} \cos\left(\sqrt{\frac{r_n}{D}}x\right) e^{-r_n t} \lim_{r \rightarrow r_n} \frac{-1}{-\sin\left(\sqrt{\frac{r}{D}}x_0\right) \frac{x_0}{2\sqrt{Dr}}} \\
 &= -\frac{c_0}{r_n} \cos\left(\sqrt{\frac{r_n}{D}}x\right) e^{-r_n t} \frac{-1}{-\sin\left(\sqrt{\frac{r_n}{D}}x_0\right) \frac{x_0}{2\sqrt{Dr_n}}} \quad (2.58) \\
 &= -\frac{2c_0}{x_0} \sqrt{\frac{D}{r_n}} \cos\left(\sqrt{\frac{r_n}{D}}x\right) e^{-r_n t} \frac{1}{\sin\left(\sqrt{\frac{r_n}{D}}x_0\right)}
 \end{aligned}$$

Substituting Eq. (2.54) into Eq. (2.58) gives

$$\text{Res}(f(r), r_n) = -\frac{2c_0(-1)^n}{\left(n + \frac{1}{2}\right)\pi} \cos\left(\left(n + \frac{1}{2}\right)\pi \frac{x}{x_0}\right) e^{-\frac{D}{x_0^2}\left(n + \frac{1}{2}\right)^2 \pi^2 t} \quad (2.59)$$

Thus

$$\begin{aligned}
 \text{Res}(p = p_n) &= \text{Res}(f(r), r_n) \\
 &= \frac{2c_0(-1)^{n+1}}{\left(n + \frac{1}{2}\right)\pi} \cos\left(\left(n + \frac{1}{2}\right)\pi \frac{x}{x_0}\right) e^{-\frac{D}{x_0^2}\left(n + \frac{1}{2}\right)^2 \pi^2 t} \quad (2.60)
 \end{aligned}$$

Combining Eq. (2.52), Eq. (2.53) and Eq. (2.60), so that

$$c = c_0 + \sum_{n=0}^{\infty} \frac{2c_0(-1)^{n+1}}{\left(n + \frac{1}{2}\right)\pi} e^{-\frac{D}{x_0^2}\left(n + \frac{1}{2}\right)^2 \pi^2 t} \cos\left(\left(n + \frac{1}{2}\right)\pi \frac{x}{x_0}\right) \quad (2.61)$$

It can easily be verified that Eq. (2.61) satisfies the differential equation Eq. (2.31) and the boundary conditions Eq. (2.32) and Eq. (2.34).

Applying the initial condition Eq. (2.33) into Eq. (2.61) gives

$$c|_{t=0} = c_0 + \sum_{n=0}^{\infty} \frac{2c_0(-1)^{n+1}}{\left(n + \frac{1}{2}\right)\pi} \cos\left(\left(n + \frac{1}{2}\right)\pi \frac{x}{x_0}\right) = 0 \quad (2.62)$$

Thus

$$c_0 = -\sum_{n=0}^{\infty} \frac{2c_0(-1)^{n+1}}{\left(n + \frac{1}{2}\right)\pi} \cos\left(\left(n + \frac{1}{2}\right)\pi \frac{x}{x_0}\right) \quad (2.63)$$

Finally, combining Eq. (2.61) and Eq. (2.63) results to

$$c = -\sum_{n=0}^{\infty} \frac{2c_0(-1)^{n+1}}{\left(n + \frac{1}{2}\right)\pi} \cos\left(\left(n + \frac{1}{2}\right)\pi \frac{x}{x_0}\right) \left(1 - e^{-\frac{D}{x_0^2}\left(n + \frac{1}{2}\right)^2 \pi^2 t}\right) \quad (2.64)$$

### 2.2.3.3 Finite element method

#### 2.2.3.3.1 Discretization in space

A boundary values problem has to be solved which requires that the governing equations are satisfied within the domain  $\Omega$  and the boundary conditions are satisfied on the boundary  $\Gamma$  of the domain (Dirichlet boundary condition). The condition that the gas transport applies throughout the continuum and boundary requires that:

$$\int_{\Omega} \mathbf{a}^T \bar{\mathbf{A}}^T d\Omega + \int_{\Gamma} \mathbf{b}^T \bar{\mathbf{B}} d\Gamma = 0 \quad (2.65)$$

where  $\mathbf{a}$  and  $\mathbf{b}$  are a set of arbitrary functions, and

$$\bar{\mathbf{A}} = \frac{\partial c}{\partial t} - \nabla^T \mathbf{D} \nabla c \quad (2.66)$$

$$\bar{\mathbf{B}} = -\mathbf{n}^T \mathbf{D} \nabla c - q_c \quad (2.67)$$

where  $\mathbf{n}$  is the unit normal vector and  $q_c$  is the gas flow rate per unit area of the boundary surface. The Eq. (2.65) can be expanded as:

$$\begin{aligned} \int_{\Omega} \mathbf{a}^T \left( \frac{\partial c}{\partial t} \right) d\Omega - \int_{\Omega} \mathbf{a}^T (\nabla^T \mathbf{D} \nabla c) d\Omega \\ + \int_{\Gamma} \mathbf{b}^T (-\mathbf{n}^T \mathbf{D} \nabla c - q_c) d\Gamma = 0 \end{aligned} \quad (2.68)$$

The second derivatives in Eq. (2.68) can be eliminated by means of Green's theorem, which states that:

$$\int_{\Omega} \varpi \frac{\partial \psi}{\partial x} d\Omega = - \int_{\Omega} \frac{\partial \varpi}{\partial x} \psi d\Omega + \int_{\Gamma} (\varpi \psi) \cdot n_x d\Gamma \quad (2.69)$$

$$\int_{\Omega} \varpi \frac{\partial \psi}{\partial y} d\Omega = - \int_{\Omega} \frac{\partial \varpi}{\partial y} \psi d\Omega + \int_{\Gamma} (\varpi \psi) \cdot n_y d\Gamma \quad (2.70)$$

$$\int_{\Omega} \varpi \frac{\partial \psi}{\partial z} d\Omega = - \int_{\Omega} \frac{\partial \varpi}{\partial z} \psi d\Omega + \int_{\Gamma} (\varpi \psi) \cdot n_z d\Gamma \quad (2.71)$$

where  $\varpi$  and  $\psi$  are suitable differentiable functions,  $n_x$ ,  $n_y$  and  $n_z$  are the directional cosines of the outward normal to boundary  $\Gamma$ .

Applying this theorem to the integrals in Eq. (2.68) results to:

$$\begin{aligned} \int_{\Omega} \mathbf{a}^T \left( \frac{\partial c}{\partial t} \right) d\Omega \\ + \int_{\Omega} (\nabla \mathbf{a})^T \mathbf{D} \nabla c d\Omega - \int_{\Gamma} \mathbf{a}^T \mathbf{n}^T \mathbf{D} \nabla c d\Gamma \\ + \int_{\Gamma} \mathbf{b}^T (-\mathbf{n}^T \mathbf{D} \nabla c - q_c) d\Gamma = 0 \end{aligned} \quad (2.72)$$

Since the values of  $\mathbf{a}$  and  $\mathbf{b}$  are arbitrary, it can make  $\mathbf{b} = -\mathbf{a}$ , thus some terms of the boundary integrals can be cancelled out in Eq. (2.72) and it reduces to:

$$\int_{\Omega} \mathbf{a}^T \left( \frac{\partial c}{\partial t} \right) d\Omega + \int_{\Omega} (\nabla \mathbf{a})^T \mathbf{D} \nabla c d\Omega + \int_{\Gamma} \mathbf{a}^T q_c d\Gamma = 0 \quad (2.73)$$

The finite element approximation is applied to Eq. (2.73). The concentration  $c$  is expressed in terms of the nodal value  $\bar{\mathbf{c}}$  and the shape function  $\mathbf{N}$  as follow

$$c = \mathbf{N} \bar{\mathbf{c}} \quad (2.74)$$

Finally the Galerkin method is applied where  $\mathbf{a} = \mathbf{N}$ . The finite element discretization of Eq. (2.73) gives the result

$$\int_{\Omega} (\nabla \mathbf{N})^T \mathbf{D} \nabla \mathbf{N} d\Omega \bar{\mathbf{c}} + \int_{\Omega} \mathbf{N}^T \mathbf{N} d\Omega \frac{\partial \bar{\mathbf{c}}}{\partial t} = - \int_{\Gamma} \mathbf{N}^T q_c d\Gamma \quad (2.75)$$

The abbreviation of Eq. (2.75) can be written as

$$\mathbf{TR}\bar{\mathbf{c}} + \mathbf{TS} \frac{\partial \bar{\mathbf{c}}}{\partial t} = \mathbf{TG} \quad (2.76)$$

where

$$\mathbf{TR} = \int_{\Omega} (\nabla \mathbf{N})^T \mathbf{D} \nabla \mathbf{N} d\Omega \quad (2.77)$$

$$\mathbf{TS} = \int_{\Omega} \mathbf{N}^T \mathbf{N} d\Omega \quad (2.78)$$

$$\mathbf{TG} = - \int_{\Gamma} \mathbf{N}^T q_c d\Gamma \quad (2.79)$$

### 2.2.3.3.2 Discretization in time

The discretization in time may be regarded as an one dimensional finite difference scheme as distinct from the spatial discretization [26, 27]. The time domain is divided into a number of steps and integration is carried out for each step to obtain the change of parameter  $\bar{\mathbf{c}}$ . The step-by-step integrations are cumulatively summed to determine the total change. The integration takes the same form as used for the spatial integration, i.e. if  $F = 0$  then  $\int \bar{g} F dt = 0$ , where  $\bar{g}$  is an arbitrary function of time. When applied to Eq. (2.76), this method requires the solution of the following equation

$$\int_{t_k}^{t_k + \Delta t_k} \bar{g} \mathbf{TR} \bar{\mathbf{c}} dt + \int_{t_k}^{t_k + \Delta t_k} \bar{g} \mathbf{TS} \frac{d\bar{\mathbf{c}}}{dt} dt = \int_{t_k}^{t_k + \Delta t_k} \bar{g} \mathbf{TG} dt \quad (2.80)$$

where  $\Delta t_k$  is the duration of the  $k$  th time step.

The first order time derivatives of  $\bar{\mathbf{c}}$  may be approximated by assuming a linear variation of  $\bar{\mathbf{c}}$  within each time step  $\Delta t$

$$\bar{\mathbf{c}} = \begin{bmatrix} N_1^t & N_2^t \end{bmatrix} \begin{bmatrix} \bar{\mathbf{c}}^t \\ \bar{\mathbf{c}}^{t+\Delta t} \end{bmatrix} \quad (2.81)$$

where  $N_1 = 1 - \alpha$ ,  $N_2 = \alpha$  and  $\alpha = \frac{(t - t_k)}{\Delta t_k}$ ,  $0 \leq \alpha \leq 1$

The time derivatives of  $N_1$  and  $N_2$  are given as

$$\frac{d}{dt} \begin{bmatrix} N_1^t & N_2^t \end{bmatrix} = \begin{bmatrix} -\frac{1}{\Delta t_k} & \frac{1}{\Delta t_k} \end{bmatrix} \quad (2.82)$$

After substitution Eq. (2.81) and Eq. (2.82) into Eq. (2.80), it results:

$$\begin{aligned} & \int_{t_k}^{t_k + \Delta t_k} \bar{g} \mathbf{TR} \left[ (1 - \alpha) \bar{\mathbf{c}}_{t_k} + \alpha \bar{\mathbf{c}}_{t_k + \Delta t_k} \right] dt \\ & + \int_{t_k}^{t_k + \Delta t_k} \bar{g} \mathbf{TS} \left[ -\frac{1}{\Delta t_k} \bar{\mathbf{c}}_{t_k} + \frac{1}{\Delta t_k} \bar{\mathbf{c}}_{t_k + \Delta t_k} \right] dt \\ & = \int_{t_k}^{t_k + \Delta t_k} \bar{g} \mathbf{TG} dt \end{aligned} \quad (2.83)$$

Eq. (2.83) may now be integrated, after which  $\bar{g}$  is eliminated. Finally it is rearranged in the form

$$(\mathbf{TS} + \alpha \mathbf{TR} \Delta t_k) \bar{\mathbf{c}}_{t_k + \Delta t_k} = (\mathbf{TS} - \mathbf{TR} (1 - \alpha) \Delta t_k) \bar{\mathbf{c}}_{t_k} + \mathbf{TG} \Delta t_k \quad (2.84)$$

### 2.2.3.3.3 Oscillation and stability

Numerical stability was considered for the case of free response, i.e. when the right-hand of Eq. (2.76) is zero [28].

$$\mathbf{TR} \bar{\mathbf{c}} + \mathbf{TS} \frac{\partial \bar{\mathbf{c}}}{\partial t} = 0 \quad (2.85)$$

The standard solution for linear equations of this form is given by the sum of set modes of variation

$$\bar{\mathbf{c}} = [\mathbf{a}_1 \quad \mathbf{a}_2 \quad \cdots] [y_1 \quad y_2 \quad \cdots]^T \quad (2.86)$$

where

$$y_i = e^{\alpha_i t} \quad (2.87)$$

and

$$\alpha_i = \text{constant} \quad (2.88)$$

Substituting  $\bar{\mathbf{c}}$  from Eq. (2.86) into Eq. (2.85), and pre-multiplying by  $\mathbf{a}^T$  gives

$$\mathbf{a}^T \mathbf{TR} \mathbf{a} \mathbf{y} + \mathbf{a}^T \mathbf{TS} \mathbf{a} \frac{\partial \mathbf{y}}{\partial t} = 0 \quad (2.89)$$

It may be shown [26] that for eigenvalue solutions of equations such as Eq. (2.86)

$$\mathbf{a}_i^T \mathbf{TR} \mathbf{a}_j = \mathbf{a}_i^T \mathbf{TS} \mathbf{a}_j = 0, \quad i \neq j \quad (2.90)$$

so that Eq. (2.89) reduces to a set of scalar independent equations of the form

$$n_i y_i + m_i \frac{\partial y_i}{\partial t} = 0 \quad (2.91)$$

Application of the same argument to Eq. (2.84) also reduces these to a set of independent equations.

$$(\mathbf{TS} + \alpha \mathbf{TR} \Delta t_k) \bar{\mathbf{c}}_{t_k + \Delta t_k} = (\mathbf{TS} - \mathbf{TR} (1 - \alpha) \Delta t_k) \bar{\mathbf{c}}_{t_k} \quad (2.92)$$

and by substituting for  $\bar{\mathbf{c}}$  by means of Eq. (2.86), and pre-multiplying by  $\mathbf{a}^T$  the following expression is derived

$$(y_i)_{t_k + \Delta t_k} (m_i + n_i \alpha \Delta t_k) = (y_i)_{t_k} (m_i - n_i (1 - \alpha) \Delta t_k) \quad (2.93)$$

In order to prevent instability it is necessary that

$$\left| (y_i)_{t_k + \Delta t_k} \right| \leq \left| (y_i)_{t_k} \right| \quad (2.94)$$

that is

$$|\lambda| = \left| \frac{m_i - n_i (1 - \alpha) \Delta t_k}{m_i + n_i \alpha \Delta t_k} \right| \leq 1 \quad (2.95)$$

and hence

$$m_i - n_i (1 - \alpha) \Delta t_k \geq -(m_i + n_i \alpha \Delta t_k) \quad (2.96)$$

or

$$n_i(2\alpha - 1)\Delta t_k \geq -2m_i \quad (2.97)$$

The stability of the solution can easily be ensured by setting  $\alpha \geq \frac{1}{2}$  rather than checking Eq. (2.97) for every value of  $i$ .

## 2.2.4 Comparison between different methods

In order to compare the solutions of Eq. (2.7) by the different methods, the numerical integration method and the Laplace transform method were implemented in Matlab, while the finite element method was implemented in the CAPA-3D FE system. A commercial FE software, Comsol Multiphysics was also utilised.

### 2.2.4.1 Geometry and material properties

Simulations of gas diffusion into a 3D thin bitumen film were performed for a 200 hours' time period. The geometry of the film was modelled as a block with a thickness of 2mm, length of 10mm and a width of 5mm, as shown in Figure 2.3. The bituminous film was assumed to be an isotropic material. The diffusion coefficient was assumed to be  $1 \times 10^{-11}$  m<sup>2</sup>/s, based on the overview of gas diffusion coefficient in Table 2.1.

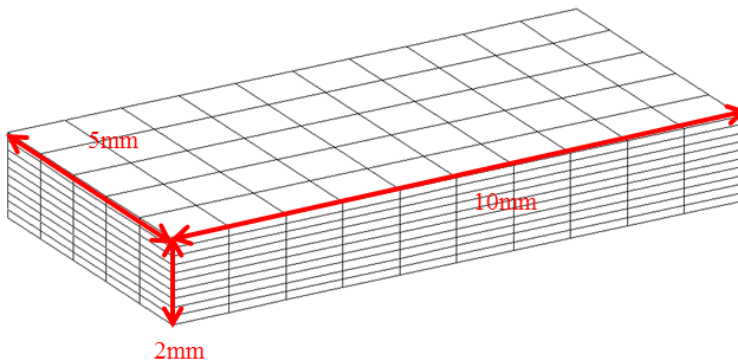


**Figure 2.3** Geometry of the thin bituminous film

#### 2.2.4.2 Initial values and boundary conditions

The initial concentration of the gas in the film was assumed to be equal to zero. During the simulations, a constant gas concentration boundary condition (assumed as  $1 \text{ mol/m}^3$ ) was applied on the top boundary, Figure 2.4, while there was no flux out of the four sides and the bottom boundaries. In other words, Dirichlet boundary condition was applied on the top, while the four sides and the bottom had a no-flow boundary condition.

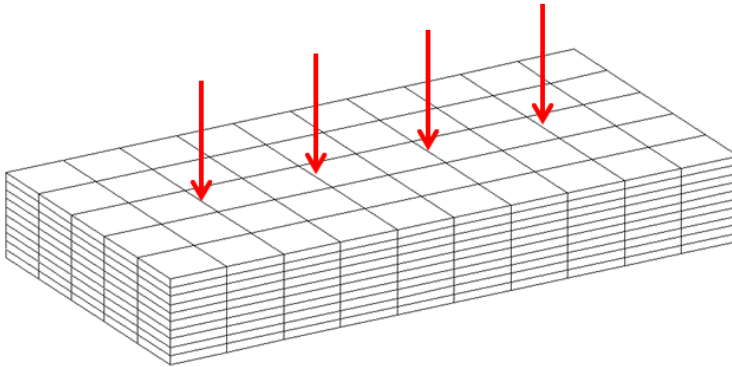


**Figure 2.4 Schematic of applied loading conditions**

#### 2.2.4.3 Results and discussion

For validation of the gas diffusion FE model implemented in the CAPA-3D FE system, a comparison of the results obtained by the different methods is given in Figure 2.5. The results show that there is a good agreement between the results by the different methods.



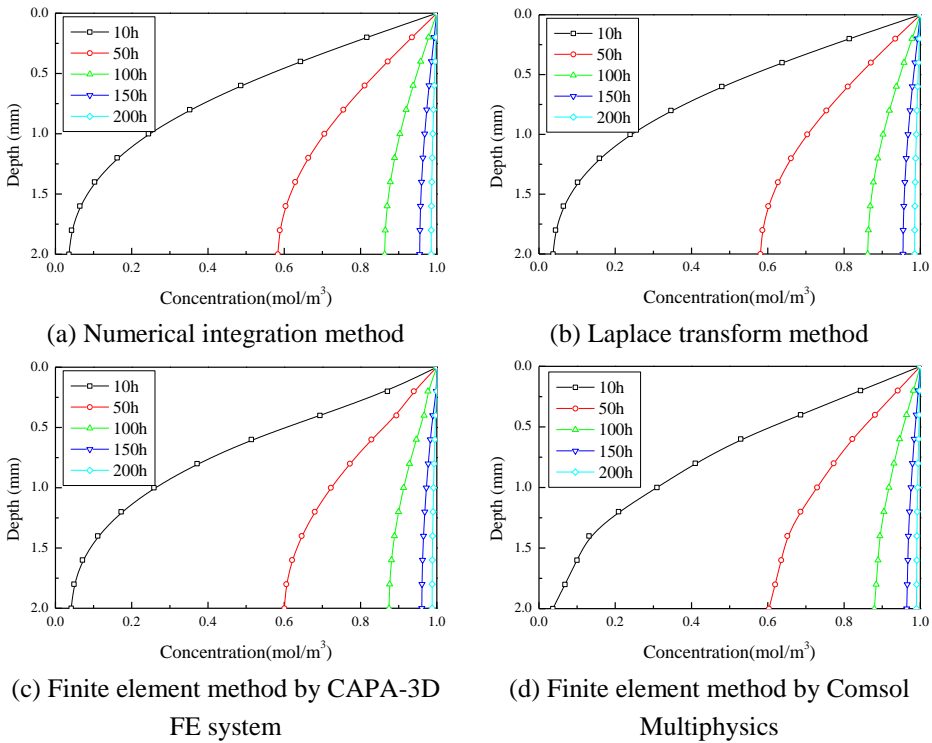


**Figure 2.5 Simulation results by different methods**

However, every coin has two sides. In this study, both the numerical integration method and the Laplace transform method were only applied for solving one dimensional diffusion problems, while the finite element method provides three dimensional solution. Due to the large number of elements utilized in FEM, longer calculation time is needed than the other two methods. Both the numerical integration method and the finite element method are numerical methods, while the Laplace transform method is an analytical method.

In this research, the Laplace transform method is used to determine the model parameters, whereas the finite element method is used to solve complex problems such as diffusion in three dimensional highly heterogeneous objects, and numerical integration method is used as an additional check of the previous two methods.

## 2.3 Application

### 2.3.1 Development of 3-D microscale FE meshes

The importance of an accurate representation of the internal structure of an asphalt mix is quite significant in modelling of diffusion since each mixture component has its particular gas diffusion characteristics and, therefore, the geometry of every phase plays an important role in the transport of gas. To address this issue, a 3-D microscale FE mesh was produced from X-ray CT scans by means of ScanIP, a specialized 3D-image-based processing software package. In this study, a FE mesh obtained from a porous asphalt mixture was used.

A sample 60 mm in height and 100 mm in diameter was prepared in the laboratory by using a roller compactor, and then used for X-ray CT scanning. The PA mixture had a nominal maximum aggregate size of 10 mm; the particle size distribution and physical properties of the mixture are given in Figure 2.6. The connectivity of the pores is critical in determining the susceptibility of asphalt mixtures to gas diffusion. For the PA, pore connectivity reached almost 90% of the total volume of the air void phase.

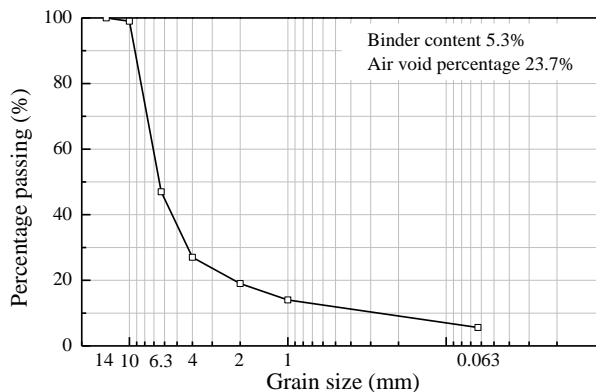


**Figure 2.6 Aggregate gradation and physical properties of PA mixture**

After the segmented data were cropped to the desired dimensions, a robust meshing algorithm was applied to enable the conversion of the

2D images into FE meshes, which were used for computational analysis via the CAPA-3D FE system. A region of 39.6 mm in height, 39.6 mm in length and 9.85 mm in width of PA mesh was selected for analysis. This area was discretized by using 3D linear four-node tetrahedral elements and consists of 312,304 elements in total, Figure 2.7.

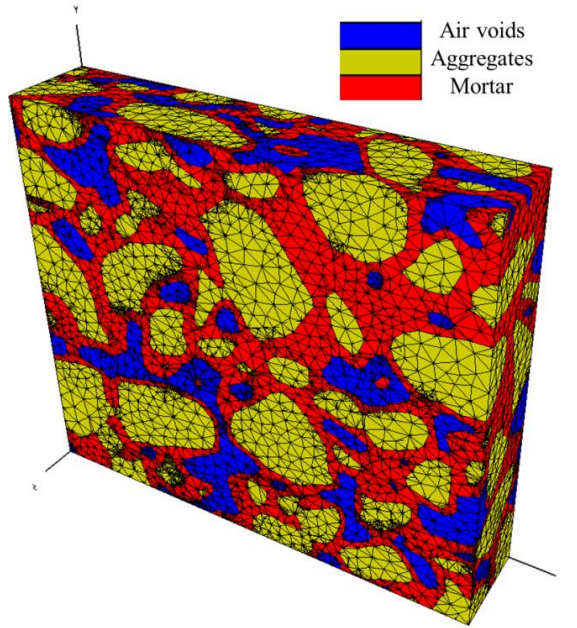


**Figure 2.7** Volume rendering of FE mesh for PA mixture

### 2.3.2 Microscale finite element gas diffusion simulations

Gas diffusion through the asphalt mixture components is considered to be a process that occurs at molecular level. During the simulations, gas was not allowed to diffuse into the aggregates, but it was defined to diffuse into the air voids with a relatively high diffusion coefficient. By making the simplification that the gas diffusion coefficients of mortar are the same as those of bitumen diffusion coefficients of  $5.108 \times 10^{-16}$  and  $4.463 \times 10^{-14} \text{ m}^2/\text{s}$  at  $20 \text{ }^\circ\text{C}$  and  $60 \text{ }^\circ\text{C}$  were utilized for the mortar films [24]. The diffusion coefficients of aggregates were set at 0 at both temperatures. The gas diffusion coefficients in a gaseous medium were

assumed to be  $7.753 \times 10^{-5}$  and  $9.45 \times 10^{-5}$   $\text{m}^2/\text{s}$  at  $20^\circ\text{C}$  and  $60^\circ\text{C}$ , respectively, as reported in the study by Marrero et al [29].

During the simulations, a constant gas concentration boundary condition ( $41.60$  and  $36.60$   $\text{mol}/\text{m}^3$  at  $20^\circ\text{C}$  and  $60^\circ\text{C}$ , respectively) was applied on the top, while no flux out of the four sides and bottom boundary was considered, in order to approximately simulate the condition of an asphalt pavement in the field.

The finite element results of the gas concentration in the mortar at different time intervals are shown in Figure 2.8. Results from the gas diffusion simulations at various days clearly show greater values of gas concentration at  $60^\circ\text{C}$  compared with those at  $20^\circ\text{C}$ .

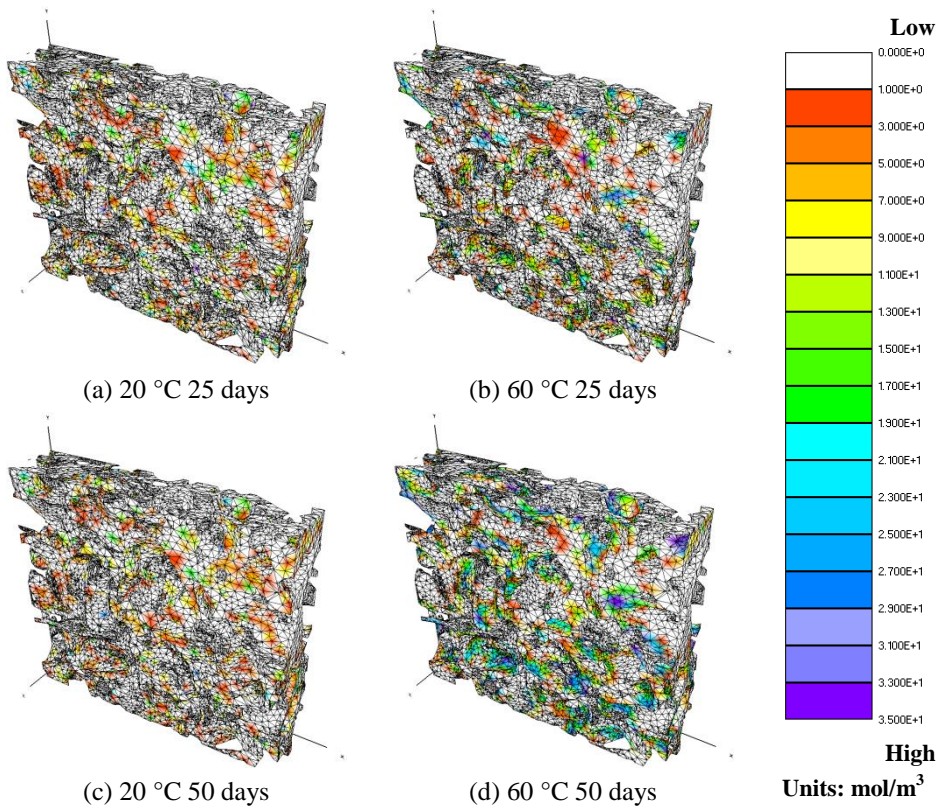


**Figure 2.8 Gas concentration in the mortar phase of PA mixture after different days of gas diffusion at different temperatures**

## 2.4 Summary

Oxygen diffusion is an important process for bitumen ageing. Gas transport in bitumen is influenced by a number of parameters such as bitumen type and environmental temperature. Given the strong relation between gas diffusion and ageing, knowledge of the gas concentration profile in thin films and asphalt mixtures is of outermost importance.

So far, there is no standard test method to determine the diffusion coefficients of oxygen in bituminous materials. Due to the fact that oxygen reacts with bitumen, researchers had to use inert gas such as CO<sub>2</sub>, CH<sub>4</sub>, C<sub>2</sub>H<sub>6</sub> and N<sub>2</sub> for the diffusion tests. However, the results of diffusion coefficients were highly depended on the test method. In Chapter 4, a new testing method for the determination of oxygen diffusion coefficient based on FTIR measurements is presented.

The diffusion models, presented in this chapter contributes to improved understanding of gas diffusion processes in bitumen. Based on this model, a diffusion and reaction model is developed in Chapter 3.

## 2.5 References

1. Liu, M., et al., *The kinetics of carbonyl formation in asphalt*. AIChE Journal, 1996. **42**(4): p. 1069-1076.
2. Juristyarini, P., R. Davison, and C.J. Glover, *Oxidation hardening kinetics of the rheological function  $G' / (\eta' / G')$  in asphalts*. Petroleum Science and Technology, 2011. **29**(19): p. 2027-2036.
3. Jin, X., et al., *Fast-rate–constant-rate oxidation kinetics model for asphalt binders*. Industrial & Engineering Chemistry Research, 2011. **50**(23): p. 13373-13379.
4. Laidler, K.J., *Chemical kinetics*. 1987, New York: Harper & Row.
5. Dill, K. and S. Bromberg, *Molecular driving forces: statistical thermodynamics in biology, chemistry, physics, and nanoscience*. 2010: Garland Science.
6. Speight, J.G., *Asphalt materials science and technology*. 2015: Butterworth-Heinemann.
7. Han, R., X. Jin, and C.J. Glover, *Oxygen diffusivity in asphalts and mastics*. Petroleum Science and Technology, 2013. **31**(15): p. 1563-1573.
8. Prapaitrakul, N., et al., *A transport model of asphalt binder oxidation in pavements*. Road Materials and Pavement Design, 2009. **10**(sup1): p. 95-113.

9. Anderson, A.P. and K.A. Wright, *Permeability and absorption properties of bituminous coatings*. Industrial & Engineering Chemistry, 1941. **33**(8): p. 991-995.
10. Beckman, A.O., et al., *Bituminous coatings*. Industrial & Engineering Chemistry, 1941. **33**(8): p. 984-990.
11. Karlsson, R. and U. Isacsson, *Application of FTIR-ATR to characterization of bitumen rejuvenator diffusion*. Journal of Materials in Civil Engineering, 2003. **15**(2): p. 157-165.
12. Petersen, J.C., *A review of the fundamentals of asphalt oxidation: chemical, physicochemical, physical property, and durability relationships*. Transportation Research E-Circular, 2009(E-C140).
13. Dickinson, E.J., J.H. Nicholas, and S. Boas Traube, *Physical factors affecting the absorption of oxygen by thin films of bituminous road binders*. Journal of Applied Chemistry, 1958. **8**(10): p. 673-687.
14. Petersen, J.C., P.M. Harnsberger, and R.E. Robertson, *Factors affecting the kinetics and mechanisms of asphalt oxidation and the relative effects of oxidation products on age hardening*. Preprints of Papers, American Chemical Society, Division of Fuel Chemistry, 1996. **41**(CONF-960807-).
15. Herrington, P.R., *Diffusion and reaction of oxygen in bitumen films*. Fuel, 2012. **94**: p. 86-92.
16. Oort, W.P.V., *Durability of asphalt - It's aging in the dark*. Industrial & Engineering Chemistry, 1956. **48**(7): p. 1196-1201.
17. Schmidt, T., T. Leshchyshyn, and V. Puttagunta, *Diffusivity of CO<sub>2</sub> into reservoir fluids*. in *33rd Annual technical meeting of the petroleum society of CIM, Calgary, Canada*. 1982. p. 6-9.
18. Schmidt, T., E. Jossy, and V.R. Puttagunta, *Mass transfer studies*. Final Report of project 188, Alberta Research Council, Edmonton, 1986.
19. Upreti, S.R. and A.K. Mehrotra, *Experimental measurement of gas diffusivity in bitumen: results for carbon dioxide*. Industrial & Engineering Chemistry Research, 2000. **39**(4): p. 1080-1087.
20. Zhang, Y.P., C.L. Hyndman, and B.B. Maini, *Measurement of gas diffusivity in heavy oils*. Journal of Petroleum Science and Engineering, 2000. **25**(1-2): p. 37-47.
21. Upreti, S.R. and A.K. Mehrotra, *Diffusivity of CO<sub>2</sub>, CH<sub>4</sub>, C<sub>2</sub>H<sub>6</sub> and N<sub>2</sub> in athabasca bitumen*. The Canadian Journal of Chemical Engineering, 2002. **80**(1): p. 116-125.
22. Cadogan, S., *Diffusion of CO<sub>2</sub> in fluids relevant to carbon capture, utilisation and storage* (doctoral thesis). Imperial College London. 2015.
23. Glaser, R.R., et al., *Asphalt film aging model*. Technical White Paper-WRI. 2015, Laramie, WY: Western Research Institute.
24. Jing, R., et al., *Experimental and computational investigation of gas diffusion in bitumen*. in *Proceedings of the Transportation Research Board 96th Annual Meeting Transportation Research Board, Washington, DC, USA*. 2017. p. 8-12.
25. Scherer, P.O., *Diffusion*, in *Computational physics*. 2013, Springer. p. 351-362.
26. Zienkiewicz, O.C., et al., *The finite element method*. Vol. 3. 1977: McGraw-hill London.
27. Norris, V., *The elastoplastic analysis of soil consolidation, with special reference to kinematic hardening* (doctoral thesis). University College of Swansea. 1981.
28. Lewis, R.W. and B.A. Schrefler, *The finite element method in the deformation and consolidation of porous media*. 1987: John Wiley and Sons Inc., New York, NY.

29. Marrero, T.R. and E.A. Mason, *Gaseous diffusion coefficients*. Journal of Physical and Chemical Reference Data, 1972. **1**(1): p. 3-118.

# 3

## **OXYGEN DIFFUSION AND REACTION**

---



### **3.1 Introduction**

As a consequence of oxygen diffusion, bitumen is subjected to chemical oxidation through reaction with the dissolved oxygen originating from the atmosphere. Bitumen oxidation results in hardening of the bitumen and an increase in its brittleness. Consequently, the propensity of asphalt pavements to cracking and ravelling increases.

This Chapter focuses upon the diffusion and reaction processes in bitumen. First, an overview of the main parameters that influence oxidation of bitumen is presented. Then three different mathematical models of the oxygen diffusion and reaction are presented and implemented. In reality, the models presented in Chapter 2 are extended to include the oxygen reaction process. A comparison among the three models is also presented. Finally, micromechanical finite element simulations are carried out to demonstrate the oxygen diffusion and reaction in porous asphalt mixtures.

### **3.2 Factors affecting bitumen oxidation**

Bitumen oxidation as a chemical reaction is a process that leads to the transformation of one set of chemical substances to another [1]. The substance (or substances) initially involved in a chemical reaction are called reactants. The chemical reaction rate is influenced by a number of factors such as concentration of reactants, temperature and pressure.

#### *Temperature*

Increasing the temperature of a system increases the average kinetic energy of its constituent molecules. As the average kinetic energy increases, the molecules move faster and collide more frequently per unit time. As a result, the number of effective collisions between reactant molecules also increases. Hence the reaction rate of virtually all reactions increases with increasing temperature. The relationship

between temperature and reaction constant is generally expressed by the Arrhenius equation:

$$k = Ae^{-\frac{E_a}{RT}} \quad (3.1)$$

where  $k$  is the rate constant,  $T$  is the absolute temperature,  $A$  is the pre-exponential factor,  $E_a$  is the activation energy of the reaction and  $R$  is the universal gas constant (8.314 J/(mol·K)).

Much research in the past has studied the importance of temperature on bitumen ageing [2-5]. Petersen (1989) obtained the effect of temperature on kinetic data (viscosity at 1 rad/sec, 60 °C) of bitumen by means of Thin Film Accelerated Ageing Test (TFAAT), see Figure 3.1[6]. It shows the effects of temperature on the ageing hardening kinetics of two different bitumen, AAD-1 and AAG-1.

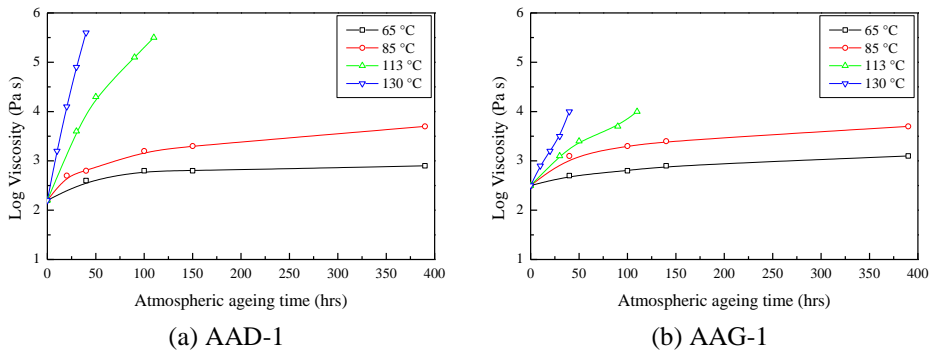


**Figure 3.1 Effects of temperature on age hardening kinetics (Peterson [6])**

### Pressure

In order to accurately predict the performance of bitumen after long-term ageing, researchers combined the thin film oven test (TFOT) with pressure oxidative ageing. For example, Lee (1973) used a standard TFOT in a pressure vessel at 2.07 MPa using pure oxygen at a temperature of 65 °C for up to 1000h [7]. Later, Edler (1985) developed a pressure oxidation bomb (PMB) based on the approach that was used by Lee [8]. In the 1990s, the SHRP-A-002A research team developed a method using the pressure ageing vessel (PAV) to simulate the long-

term in field oxidative ageing of bitumen [9, 10]. Hayton (1999) developed the high pressure ageing test (HiPAT) on the basis of PAV, which is using a lower temperature [11]. All these research results have shown high pressure ageing is an efficient way of accelerating ageing.

Actually, pressure is another way of expressing the concentration for gases. Under higher pressure or at a higher concentration, more oxygen molecules are dissolved in bitumen. This relation can be best described by Henry's law [12-14], as shown in Eq. (3.2). Henry's law dictates that when temperature is constant, the solubility of the gas corresponds to its partial pressure.

$$c_{O_2} = h \left( \frac{P_{O_2}}{RT} \right) \quad (3.2)$$

where,  $c_{O_2}$  is the concentration of oxygen,  $P_{O_2}$  is the oxygen gas phase partial pressure,  $T$  is the temperature,  $R$  is the universal gas constant and  $h$  is the dimensionless Henry's law constant. This dimensionless constant  $h$  has been estimated by Blokker and Hoorn as a function of temperature [12]:

$$h = h_r (1 + 0.0215(T - T_r)) \quad (3.3)$$

where  $T_r$  is the reference temperature which is 303.15 K, and  $h_r$  is the dimensionless Henry's law constant at the reference temperature which is 0.0076.

#### *Bitumen type*

The components of bitumen include four main classes of compounds: saturates, aromatics, resins and asphaltenes. The percentage of each component in bitumen is highly dependent on the source and type of crude oil. Different bitumen have different activation energies and different concentrations of reactants.

For a chemical reaction, two substances cannot possibly react with each other unless their constituent particles (molecules, atoms or ions) come into contact. Increasing the concentration of a reactant increases the number of collisions between the reacting species per unit of time. Consequently, the reaction rate usually increases when the concentration of the reactants increases.

A study from X. Jin (2011) presented the activation energy values of fifteen different bitumen (six base bitumen and nine SBS modified bitumen) for the fast-rate period and the constant-rate period of asphalt oxidative ageing, as show in Table 3.1. The results clearly confirm the fact that different bitumen types have different values of activation energy [15].

**Table 3.1 Activation energy for fifteen different bitumen**

Bitumen type	Activation energy (KJ/ mol)	
	Fast-rate period	Constant-rate period
Alon PG 64-22	58.4	83.4
Alon PG 70-22	60.8	78.3
Alon PG 76-22	52.6	77.0
Lion PG 64-22	68.5	90.6
Martin PG 64-22	51.9	72.5
Martin PG 70-22	60.9	88.0
SEM PG 64-22	47.6	68.8
SEM PG 70-22	54.4	79.9
SEM PG 70-28	49.1	72.5
SEM PG 76-22	45.2	64.9
Valero-C PG 64-22	67.2	87.4
Valero-C PG 70-22	75.4	103.8
Valero-C PG 76-22	47.2	68.1
Valero-H PG 76-22	68.6	86.9
Valero-O PG 64-22	57.3	81.3

### 3.3 Oxidation model

A chemical equation is used to describe the chemical reactions. Symbolically it shows the starting materials, end products and, in some cases, the intermediate products and the reaction conditions.

#### 3.3.1 Chemical equation

Chemical equation consists of chemical or structural formulae of the reactants on the left side and those of the products on the right. They are separated by an arrow ( $\rightarrow$ ) which indicates the direction and type of the reaction; the arrow is interpreted as "leads to" [16]. Reaction equations should be balanced according to concept of stoichiometry which the total number of atoms should be the same on both sides of the equation [1]. Correspondingly, the chemical equation of bitumen oxidation can be assumed and written as:



where  $B$  indicates the reactive components in bitumen,  $O_2$  is the oxygen,  $OP$  indicates the oxidation product and,  $a$ ,  $b$  and  $d$  indicate the stoichiometry of the individual components. Due to the complexity of the bitumen itself, there is more than one reactive component in bitumen. On a molecular scale, each reactive component in bitumen has its own chemical equation with its own stoichiometry and reaction rate. Therefore, Eq. (3.4) is a general chemical equation for a multicomponent system such as bitumen.

#### 3.3.2 Reaction rate

Chemical reactions happen at a characteristic reaction rate at a given temperature and chemical concentration. Typically, reaction rates increase with increasing temperature because there is more thermal

energy available to attain the activation energy of the reactants. For the general reaction in Eq. (3.4), the reaction rate can be expressed in terms of the change in concentration of any of its reactant components, as follows:

$$r = -\frac{\Delta c_B}{a\Delta t} = -\frac{\Delta c_{O_2}}{b\Delta t} = \frac{\Delta c_{OP}}{d\Delta t} \quad (3.5)$$

where  $r$  is the reaction rate,  $t$  is the time,  $c_B$ ,  $c_{O_2}$  and  $c_{OP}$  are the concentration of the reactive components in bitumen, oxygen and oxidation product, respectively.

Based on the rate law for a chemical reaction, which relates the rate of a reaction to the rate constant and the concentrations of the reactants [1], the reaction rate of Eq. (3.4) can also be given by a power law as:

$$r = kc_B^m c_{O_2}^n \quad (3.6)$$

where  $k$  is the rate constant,  $m$  and  $n$  are the partial reaction orders.

The reaction orders  $m$  and  $n$  depend on the reaction mechanism. For single-step reactions, the order with respect to each reactant is equal to its stoichiometric coefficient which means  $a = m$ ,  $b = n$ . For complex multistep reactions, this is often not true, and even the form of Eq. (3.6) may not be applicable. The bitumen oxidation process belongs to the category of complex reactions [17, 18], since a wide variety of molecules are involved. Considering that the reaction mechanism of bitumen ageing is still not that clear, the general expression of reaction rate, Eq. (3.6), is employed in this study to simplify the model.

### 3.4 Oxygen diffusion and reaction model

Diffusion and reaction processes correlate to several physical phenomena. The most common is the change in space and time of the concentration of one or more chemical substances; in the meanwhile, local chemical reactions occur in which the substances are transformed

into others, and diffusion takes place that causes the substances to spread out in space.

### 3.4.1 Basic diffusion and reaction equation

In Chapter 2, a diffusion model able to show the oxygen concentration gradient as a function of time inside the bitumen film was formulated. Here a diffusion-oxidation model is developed. The general form of the equation of diffusion and reaction can be represented as:

$$\frac{\partial c_{O_2}}{\partial t} = D\nabla^2 c_{O_2} - br \quad (3.7)$$

where  $b$  is the stoichiometry of the oxygen component and  $r$  is the reaction rate.

By substituting Eq. (3.6), Eq. (3.7) can be rewritten as:

$$\frac{\partial c_{O_2}}{\partial t} = D\nabla^2 c_{O_2} - bkc_B^m c_{O_2}^n \quad (3.8)$$

### 3.4.2 Boundary condition

Three substances are considered in the diffusion-reaction system: oxygen, reactive components in bitumen and oxidation product. In this system, oxygen is involved in both diffusion and reaction, while the bitumen and the oxidation product are involved in reaction only. Therefore, the boundary conditions for oxygen were set as the same as those in Chapter 2. For the bitumen and the oxidation product, certain initial values need to be assigned.

### 3.4.3 Solution of the diffusion and reaction equation

Similarly to Chapter 2, three mathematical methods were explored for the solution of the diffusion and reaction equations. Specially, the

numerical integration method, the Laplace transform method and the finite element method.

### 3.4.3.1 Numerical integration method

#### 3.4.3.1.1 Discretization in space and time

Based on the solution of the diffusion equation by the numerical integration method in Chapter 2, the solution of the one-dimensional diffusion-reaction equation Eq. (3.8) can be expressed as:

$$\begin{aligned}
 & c_{O_2}(x_i(t_{j+1})) \\
 & = c_{O_2}(x_i(t_j)) \\
 & + D \frac{\delta t}{(\delta x)^2} (c_{O_2}(x_{i+1}(t_j)) - 2c_{O_2}(x_i(t_j)) + c_{O_2}(x_{i-1}(t_j))) \\
 & - bkc_B^m(x_i(t_j))c_{O_2}^n(x_i(t_j))\Delta t
 \end{aligned} \tag{3.9}$$

Then, the equation of concentration of reactive components in bitumen is written as:

$$c_B(x_i(t_{j+1})) = c_B(x_i(t_j)) - akc_B^m(x_i(t_j))c_{O_2}^n(x_i(t_j))\Delta t \tag{3.10}$$

The schematic of the solving process of the diffusion-reaction model is shown in Figure 3.2. Due to the coupling of the diffusion and reaction phenomena, the values of oxygen concentration (left side in Figure 3.2) are always determined by the values of oxygen concentration and concentration of reactive components in bitumen at previous calculation step. The right side in Figure 3.2 shows the similar calculation process for the concentration of reactive components in bitumen.



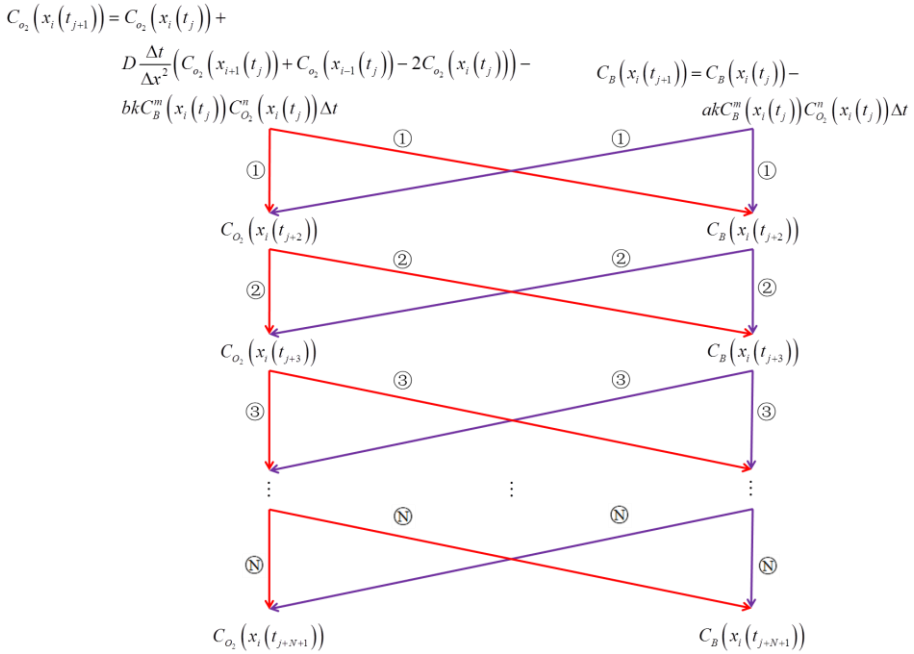


Figure 3.2 Schematic of the calculation process on diffusion and reaction model

### 3.4.3.1.2 Stability analysis

The diffusion-reaction system is a nonlinear coupled system. For such a nonlinear coupled system, the stability condition cannot be expressed by formulate. However this does not mean that the stability conditions do not affect the solution of a diffusion-reaction system.

### 3.4.3.2 Laplace transform method

By assuming the diffusion coefficient to be independent of the amount of gas locally bound, based on Eq. (3.8), the one dimensional differential equation of oxygen diffusion and reaction in a layer can be written as:

$$D \frac{\partial^2 c_{O_2}}{\partial x^2} = \frac{\partial c_{O_2}}{\partial t} + bkC_B^m c_{O_2}^n \quad (3.11)$$

The boundary conditions are

$$x = 0 \quad \frac{\partial c_{O_2}}{\partial x} = 0 \quad (3.12)$$

$$x = x_0 \quad c_{O_2} = c_0 \quad (3.13)$$

$$t = 0, x > 0 \quad c_{O_2} = 0 \quad (3.14)$$

$$t = 0, x > 0 \quad c_B = c_{B_0} \quad (3.15)$$

where  $x_0$  is the layer thickness,  $c_0$  is the concentration of oxygen at the boundary and  $c_{B_0}$  is the initial concentration of reactive components in bitumen.

The diffusion-reaction equation Eq.(3.11) can be solved with the Laplace transformation method, the transform of equation can be expressed as:

$$D \frac{\partial^2 \bar{c}_{O_2}}{\partial x^2} = p \bar{c}_{O_2} + b k c_B^m \bar{c}_{O_2}^n \quad (3.16)$$

Where  $p$  is the Laplace transform variable.

The boundary conditions (3.12) and (3.13) are transformed into:

$$x = 0 \quad \frac{\partial \bar{c}_{O_2}}{\partial x} = 0 \quad (3.17)$$

$$x = x_0 \quad \bar{c}_{O_2} = \frac{c_0}{p} \quad (3.18)$$

Introducing

$$\bar{c}_{O_2}(x, p) = F(x)G(p) \quad (3.19)$$

and substituting it into Eq. (3.16) gives

$$\frac{\partial^2 F(x)}{\partial x^2} - \frac{p}{D} F(x) - b \frac{k}{D} c_B^m F(x)^n G(p)^{n-1} = 0 \quad (3.20)$$

Eq. (3.20) is an nonlinear differential equation for  $n \neq 0$  or 1, while it is an linear differential equation for  $n = 0$  or 1. Since the Laplace transform method cannot be used to solve the nonlinear differential equations, only option of  $n = 0$  or 1 should be considered. For  $n = 0$ , the equation states that the concentration of oxygen does not influence the

oxidation rate, which is obviously incorrect. Therefore,  $n = 1$  was selected for further analysis, which assumed that bitumen ageing is the first order for oxygen. Then Eq. (3.20) gives:

$$F(x) = c_1 e^{\sqrt{\frac{p}{D} + b \frac{k}{D} c_B^m x}} + c_2 e^{-\sqrt{\frac{p}{D} + b \frac{k}{D} c_B^m x}} \quad (3.21)$$

Combining Eq. (3.19) and Eq. (3.21) results to:

$$\bar{c}_{O_2}(x, p) = \left( c_1 e^{\sqrt{\frac{p}{D} + b \frac{k}{D} c_B^m x}} + c_2 e^{-\sqrt{\frac{p}{D} + b \frac{k}{D} c_B^m x}} \right) G(p) \quad (3.22)$$

Applying the boundary condition Eq. (3.17) to Eq. (3.22), it results

$$c_1 = c_2 \quad (3.23)$$

Combining Eq. (3.22) and Eq. (3.23), it gives

$$\bar{c}_{O_2}(x, p) = 2c_1 G(p) \cosh \left( \sqrt{\frac{p}{D} + b \frac{k}{D} c_B^m x} \right) \quad (3.24)$$

By introducing

$$H(p) = 2c_1 G(p) \quad (3.25)$$

Eq. (3.24) transforms to

$$\bar{c}_{O_2}(x, p) = H(p) \cosh \left( \sqrt{\frac{p}{D} + b \frac{k}{D} c_B^m x} \right) \quad (3.26)$$

By applying the boundary condition Eq. (3.18) to Eq.(3.24) results to

$$\bar{c}_{O_2}(x, p) \Big|_{x=x_0} = H(p) \cosh \left( \sqrt{\frac{p}{D} + b \frac{k}{D} c_B^m x_0} \right) = \frac{c_0}{p} \quad (3.27)$$

Hence

$$H(p) = \frac{c_0}{p} \frac{1}{\cosh \left( \sqrt{\frac{p}{D} + b \frac{k}{D} c_B^m x_0} \right)} \quad (3.28)$$

Combing Eq. (3.26) and Eq. (3.28) gives

$$\bar{c}_{O_2}(x, p) = \frac{c_0}{p} \frac{\cosh\left(\sqrt{\frac{p}{D} + b \frac{k}{D}} c_B^m x\right)}{\cosh\left(\sqrt{\frac{p}{D} + b \frac{k}{D}} c_B^m x_0\right)} \quad (3.29)$$

Applying inverse Laplace transformation in to Eq. (3.29) gives

$$c_{O_2} = \frac{1}{2\pi i} \int_{e^{-i\infty}}^{e^{+i\infty}} \frac{c_0}{p} \frac{\cosh\left(\sqrt{\frac{p}{D} + b \frac{k}{D}} c_B^m x\right)}{\cosh\left(\sqrt{\frac{p}{D} + b \frac{k}{D}} c_B^m x_0\right)} e^{pt} dp \quad (3.30)$$

The singularities of the integrand are the pole of the first order (only appear on time)  $p = 0$  and the zeros of  $\cosh\left(\sqrt{\frac{p}{D} + b \frac{k}{D}} c_B^m x_0\right)$ , yielding the first order poles:

$$\sqrt{\frac{p}{D} + b \frac{k}{D}} c_B^m x_0 = n\pi i + \frac{\pi}{2} i \quad (3.31)$$

Hence

$$p_n = -\frac{D}{x_0^2} \left(n + \frac{1}{2}\right)^2 \pi^2 - bkc_B^m \quad (3.32)$$

Such a value of  $c_{O_2}$ , which is purely real, must be chosen such that the path of integration in the p-plane takes a course which leaves the pole of the integrand at the left side. The line integral can be evaluated by transforming it into a closed contour and applying the theorem of residues [19] hence:

$$\begin{aligned} c_{O_2} &= \sum_{n=0}^{\infty} \text{Res} \left( \frac{c_0}{p} \frac{\cosh\left(\sqrt{\frac{p}{D} + b \frac{k}{D}} c_B^m x\right)}{\cosh\left(\sqrt{\frac{p}{D} + b \frac{k}{D}} c_B^m x_0\right)} e^{pt}, p = 0 \& p = p_n \right) \\ &= \text{Res}(p = 0) + \sum_{n=0}^{\infty} \text{Res}(p = p_n) \end{aligned} \quad (3.33)$$

It follows that:

$$\text{Res}(p=0) = c_0 \frac{\cosh\left(\sqrt{b\frac{k}{D}c_B^m x}\right)}{\cosh\left(\sqrt{b\frac{k}{D}c_B^m x_0}\right)} \quad (3.34)$$

For the other singularities  $p = p_n$  introduce:

$$r_n = \frac{D}{x_0^2} \left(n + \frac{1}{2}\right)^2 \pi^2 + bkc_B^m \quad (3.35)$$

so that

$$\sqrt{p_n} = i\sqrt{r_n} \quad (3.36)$$

Now assume that

$$\begin{aligned} f(r) &= -\frac{c_0}{r} \frac{\cosh\left(i\sqrt{\frac{r}{D} - b\frac{k}{D}c_B^m x}\right)}{\cosh\left(i\sqrt{\frac{r}{D} - b\frac{k}{D}c_B^m x_0}\right)} e^{-rt} \\ &= -\frac{c_0}{r} \frac{\cos\left(\sqrt{\frac{r}{D} - b\frac{k}{D}c_B^m x}\right)}{\cos\left(\sqrt{\frac{r}{D} - b\frac{k}{D}c_B^m x_0}\right)} e^{-rt} \end{aligned} \quad (3.37)$$

Hence

$$\begin{aligned} &\text{Res}(f(r), r_n) \\ &= \lim_{r \rightarrow r_n} (r_n - r) f(r) \\ &= -\frac{c_0}{r_n} \cos\left(\sqrt{\frac{r_n}{D} - b\frac{k}{D}c_B^m x}\right) e^{-r_n t} \cdot \lim_{r \rightarrow r_n} \frac{r_n - r}{\cos\left(\sqrt{\frac{r}{D} - b\frac{k}{D}c_B^m x_0}\right)} \end{aligned} \quad (3.38)$$

Based on the L'Hôpital's rule, Eq.(3.38) is transformed to:

$$\text{Res}(f(r), r_n) = -\frac{2Dc_0 \sqrt{\frac{r_n}{D} - b \frac{k}{D} c_B^m}}{ar_n} \cdot \cos\left(\sqrt{\frac{r_n}{D} - b \frac{k}{D} c_B^m} x\right) e^{-r_n t} \frac{1}{\sin\left(\sqrt{\frac{r_n}{D} - b \frac{k}{D} c_B^m} x_0\right)} \quad (3.39)$$

Applying Eq. (3.35) to Eq. (3.39) gives

$$\text{Res}(f(r), r_n) = -\frac{2Dc_0(n+\frac{1}{2})\pi(-1)^n}{\left(D\left(n+\frac{1}{2}\right)^2 \pi^2 + x_0^2 bkc_B^m\right)} \cdot \cos\left(\left(n+\frac{1}{2}\right)\pi \frac{x}{x_0}\right) e^{-\left(\frac{D}{x_0^2}\left(n+\frac{1}{2}\right)^2 \pi^2 + bkc_B^m\right)t} \quad (3.40)$$

Hence

$$\begin{aligned} \text{Res}(p = p_n) &= \text{Res}(f(r), r_n) \\ &= \frac{2Dc_0(n+\frac{1}{2})\pi(-1)^{n+1}}{D\left(n+\frac{1}{2}\right)^2 \pi^2 + x_0^2 bkc_B^m} \cdot \cos\left(\left(n+\frac{1}{2}\right)\pi \frac{x}{x_0}\right) e^{-\left(\frac{D}{x_0^2}\left(n+\frac{1}{2}\right)^2 \pi^2 + bkc_B^m\right)t} \end{aligned} \quad (3.41)$$

Combining Eq.(3.33), (3.34) and (3.41) yields:

$$c_{O_2} = c_0 \frac{\cosh\left(\sqrt{b \frac{k}{D}} c_B^m x\right)}{\cosh\left(\sqrt{b \frac{k}{D}} c_B^m x_0\right)} + \sum_{n=0}^{\infty} \left( \frac{2Dc_0(n+\frac{1}{2})\pi(-1)^{n+1}}{D\left(n+\frac{1}{2}\right)^2 \pi^2 + x_0^2 b k c_B^m} \cdot \cos\left((n+\frac{1}{2})\pi \frac{x}{x_0}\right) e^{-\left(\frac{D}{x_0^2}\left(n+\frac{1}{2}\right)^2 \pi^2 + b k c_B^m\right)t} \right) \quad (3.42)$$

It can be easily verified that Eq. (3.42) is the solution of the Eq. (3.11) with the boundary conditions Eq. (3.12) and Eq. (3.13). Applying the initial condition Eq. (3.14) to Eq. (3.42):

$$c_{O_2}|_{t=0} = c_0 \frac{\cosh\left(\sqrt{b \frac{k}{D}} c_B^m x\right)}{\cosh\left(\sqrt{b \frac{k}{D}} c_B^m x_0\right)} + \sum_{n=0}^{\infty} \frac{2Dc_0(n+\frac{1}{2})\pi(-1)^{n+1}}{D\left(n+\frac{1}{2}\right)^2 \pi^2 + x_0^2 b k c_B^m} \cos\left((n+\frac{1}{2})\pi \frac{x}{x_0}\right) = 0 \quad (3.43)$$

Hence

$$c_0 = - \frac{\cosh\left(\sqrt{b \frac{k}{D}} c_B^m x_0\right)}{\cosh\left(\sqrt{b \frac{k}{D}} c_B^m x\right)} \cdot \sum_{n=0}^{\infty} \frac{2Dc_0(n+\frac{1}{2})\pi(-1)^{n+1}}{D\left(n+\frac{1}{2}\right)^2 \pi^2 + x_0^2 b k c_B^m} \cos\left((n+\frac{1}{2})\pi \frac{x}{x_0}\right) \quad (3.44)$$

and substitution into Eq. (3.42) gives

$$c_{O_2} = - \sum_{n=0}^{\infty} \left( \frac{2Dc_0(n+\frac{1}{2})\pi(-1)^{n+1}}{D\left(n+\frac{1}{2}\right)^2\pi^2+x_0^2bkc_B^m} \cdot \cos\left((n+\frac{1}{2})\pi\frac{x}{x_0}\right) \left(1 - e^{-\left(\frac{D}{x_0^2}\left(n+\frac{1}{2}\right)^2\pi^2+bkc_B^m\right)t}\right) \right) \quad (3.45)$$

The solution of  $c_B$  can be obtained as follow:

$$\frac{\partial c_B}{\partial t} = -akc_B^m c_{O_2} \quad (3.46)$$

Similar to Eq. (3.20), Eq. (3.46) is a nonlinear differential equation for  $m \neq 0$  or 1, while it is a linear differential equation for  $m = 0$  or 1. Since it is difficult to get the analytical solution for a nonlinear differential equation, only option of  $m = 0$  or 1 was considered. For  $m = 0$ , the equation states the concentration of reactive components in bitumen does not influence the oxidation rate, which is obviously incorrect. Therefore,  $m = 1$  was selected to do further analysis, which assumed that bitumen ageing is the first order for reactive components in bitumen. Then Eq. (3.46) can be rewritten as follows

$$\frac{\partial c_B}{\partial t} = -akc_B c_{O_2} \quad (3.47)$$

Hence

$$c_B = c_{B0} e^{-akc_{O_2}t} \quad (3.48)$$

Combining Eq. (3.45) and Eq. (3.48) results to



$$c_{O_2} = - \sum_{n=0}^{\infty} \left( \frac{2Dc_0(n+\frac{1}{2})\pi(-1)^{n+1}}{D\left(n+\frac{1}{2}\right)^2 \pi^2 + x_0^2 bkc_{B0} e^{-akc_{O_2}t}} \cdot \cos\left(\left(n+\frac{1}{2}\right)\pi \frac{x}{x_0}\right) \left(1 - e^{-\left(\frac{D}{x_0^2}\left(n+\frac{1}{2}\right)^2 \pi^2 + bkc_{B0} e^{-akc_{O_2}t}\right)t}\right) \right) \quad (3.49)$$

By defining

$$A_n = 2Dc_0(n+\frac{1}{2})\pi(-1)^{n+1} \cos\left(\left(n+\frac{1}{2}\right)\pi \frac{x}{x_0}\right) \quad (3.50)$$

$$F_n = D\left(n+\frac{1}{2}\right)^2 \pi^2 \quad (3.51)$$

Eq. (3.49) can be rewritten as follows

$$c_{O_2} + \sum_{n=0}^{\infty} \frac{A_n}{F_n + x_0^2 bkc_{B0} e^{-akc_{O_2}t}} \left(1 - e^{-\left(\frac{F_n}{x_0^2} + bkc_{B0} e^{-akc_{O_2}t}\right)t}\right) = 0 \quad (3.52)$$

Introducing

$$G(c_{O_2}) = c_{O_2} + \sum_{n=0}^{\infty} \frac{A_n}{F_n + x_0^2 bkc_{B0} e^{-akc_{O_2}t}} \left(1 - e^{-\left(\frac{F_n}{x_0^2} + bkc_{B0} e^{-akc_{O_2}t}\right)t}\right) \quad (3.53)$$

Then

$$G'(c_{O_2}) = 1 - abk^2 tc_{B0} e^{-akc_{O_2}t}.$$

$$\sum_{n=0}^{\infty} A_n \frac{\left(F_n + x_0^2 bkc_{B0} e^{-akc_{O_2}t} + x_0^2\right) e^{-\left(\frac{F_n}{x_0^2} + bkc_{B0} e^{-akc_{O_2}t}\right)t}}{\left(F_n + x_0^2 bkc_{B0} e^{-akc_{O_2}t}\right)^2} t - x_0^2 \quad (3.54)$$

and defining

$$E_n = F_n + x_0^2 bkc_{B0} e^{-akc_{O_2}t} \quad (3.55)$$

$$H_n = A_n abk^2 tc_{B0} e^{-akc_{O_2}t} \quad (3.56)$$

Then Eq. (3.53) and Eq. (3.54) can be rewritten as follows

$$G(c_{O_2}) = c_{O_2} + \sum_{n=0}^{\infty} \frac{A_n}{E_n} \left( 1 - e^{-\frac{E_n t}{x_0^2}} \right) \quad (3.57)$$

$$G'(c_{O_2}) = 1 - \sum_{n=0}^{\infty} H_n \left( \frac{(E_n + x_0^2) t e^{-\frac{E_n t}{x_0^2}} - x_0^2}{E_n^2} \right) \quad (3.58)$$

By applying the Newton-Raphson iterative solution method it holds that

$$c_{O_2} \Big|_{i+1} = c_{O_2} \Big|_i - \frac{G(c_{O_2})}{G'(c_{O_2})} \quad (3.59)$$

Substituting the solution of Eq. (3.59) into Eq. (3.48) gives the solution of the concentration of reactive components in bitumen.

### 3.4.3.3 Finite element method

#### 3.4.3.3.1 Discretization in space

A boundary value problem has to be solved which requires that the governing equations are satisfied within the domain  $\Omega$  and the boundary conditions are satisfied on the boundary  $\Gamma$  of the domain. The condition that the gas transport applies throughout the continuum and boundary [20] requires that:

$$\int_{\Omega} \mathbf{a}^T \bar{\mathbf{A}}^T d\Omega + \int_{\Gamma} \mathbf{b}^T \bar{\mathbf{B}} d\Gamma = 0 \quad (3.60)$$

where  $\mathbf{a}$  and  $\mathbf{b}$  are a set of arbitrary functions, and

$$\bar{\mathbf{A}} = \frac{\partial c_{O_2}}{\partial t} - \nabla^T \mathbf{D} \nabla c_{O_2} + br = 0 \quad (3.61)$$

$$\bar{\mathbf{B}} = -\mathbf{n}^T \mathbf{D} \nabla c_{O_2} - q_c \quad (3.62)$$

where  $\mathbf{n}$  is the unit normal vector and  $q_c$  is the gas flow rate per unit area of the boundary surface. This allows Eq. (3.60) to be written as:

$$\begin{aligned} & \int_{\Omega} \mathbf{a}^T \left( \frac{\partial c_{o_2}}{\partial t} \right) d\Omega - \int_{\Omega} \mathbf{a}^T (\nabla^T \mathbf{D} \nabla c_{o_2}) d\Omega + \int_{\Omega} \mathbf{a}^T (br) d\Omega \\ & + \int_{\Gamma} \mathbf{b}^T (-\mathbf{n}^T \mathbf{D} \nabla c_{o_2} - q_c) d\Gamma = 0 \end{aligned} \quad (3.63)$$

The second derivatives appearing in Eq. (3.63) are eliminated by means of Green's theorem, which states that:

$$\int_{\Omega} \varpi \frac{\partial \psi}{\partial x} d\Omega = - \int_{\Omega} \frac{\partial \varpi}{\partial x} \psi d\Omega + \int_{\Gamma} (\varpi \psi) \cdot n_x d\Gamma \quad (3.64)$$

$$\int_{\Omega} \varpi \frac{\partial \psi}{\partial y} d\Omega = - \int_{\Omega} \frac{\partial \varpi}{\partial y} \psi d\Omega + \int_{\Gamma} (\varpi \psi) \cdot n_y d\Gamma \quad (3.65)$$

$$\int_{\Omega} \varpi \frac{\partial \psi}{\partial z} d\Omega = - \int_{\Omega} \frac{\partial \varpi}{\partial z} \psi d\Omega + \int_{\Gamma} (\varpi \psi) \cdot n_z d\Gamma \quad (3.66)$$

where  $\varpi$  and  $\psi$  are suitable differentiable functions,  $n_x$ ,  $n_y$ , and  $n_z$  are the directional cosines of the outward normal to boundary  $\Gamma$ .

Applying this theorem to the integrals in Eq. (3.63) results to:

$$\begin{aligned} & \int_{\Omega} \mathbf{a}^T \left( \frac{\partial c_{o_2}}{\partial t} \right) d\Omega + \int_{\Omega} \mathbf{a}^T (br) d\Omega + \\ & \int_{\Omega} (\nabla \mathbf{a})^T \mathbf{D} \nabla c_{o_2} d\Omega - \int_{\Gamma} \mathbf{a}^T \mathbf{n}^T \mathbf{D} \nabla c_{o_2} d\Gamma + \\ & \int_{\Gamma} \mathbf{b}^T (-\mathbf{n}^T \mathbf{D} \nabla c_{o_2} - q_c) d\Gamma = 0 \end{aligned} \quad (3.67)$$

Since the values of  $\mathbf{a}$  and  $\mathbf{b}$  are arbitrary, it can make  $\mathbf{b} = -\mathbf{a}$  some terms of the boundary integrals cancel out and Eq. (3.67) therefore reduces to

$$\begin{aligned} & \int_{\Omega} \mathbf{a}^T \left( \frac{\partial c_{o_2}}{\partial t} \right) d\Omega + \int_{\Omega} \mathbf{a}^T (br) d\Omega + \\ & \int_{\Omega} (\nabla \mathbf{a})^T \mathbf{D} \nabla c_{o_2} d\Omega + \int_{\Gamma} \mathbf{a}^T q_c d\Gamma = 0 \end{aligned} \quad (3.68)$$

The finite element approximation is applied to Eq. (3.68). The variation of concentration  $c$  can be expressed in terms of the nodal value  $\bar{c}$  and the shape functions  $\mathbf{N}$ , as follows

$$c_{O_2} = \mathbf{N}\bar{\mathbf{c}}_{O_2} \quad (3.69)$$

$$c_B = \mathbf{N}\bar{\mathbf{c}}_B \quad (3.70)$$

Finally the Galerkin method is applied in which  $\mathbf{a} = \mathbf{N}$ . The finite element discretization of Eq. (3.68) gives

$$\begin{aligned} \int_{\Omega} (\nabla \mathbf{N})^T \mathbf{D} \nabla \mathbf{N} d\Omega \bar{\mathbf{c}}_{O_2} + \int_{\Omega} \mathbf{N}^T \mathbf{N} d\Omega \frac{\partial \bar{\mathbf{c}}_{O_2}}{\partial t} = \\ - \int_{\Gamma} \mathbf{N}^T q_c d\Gamma - \int_{\Omega} \mathbf{N}^T (br) d\Omega \end{aligned} \quad (3.71)$$

An abbreviation of Eq. (3.71) can be written as

$$\mathbf{TR}\bar{\mathbf{c}}_{O_2} + \mathbf{TS} \frac{\partial \bar{\mathbf{c}}_{O_2}}{\partial t} = \mathbf{TG} - b\mathbf{R} \quad (3.72)$$

where

$$\mathbf{R} = \int_{\Omega} \mathbf{N}^T r d\Omega \quad (3.73)$$

$$\mathbf{TR} = \int_{\Omega} (\nabla \mathbf{N})^T \mathbf{D} \nabla \mathbf{N} d\Omega \quad (3.74)$$

$$\mathbf{TS} = \int_{\Omega} \mathbf{N}^T \mathbf{N} d\Omega \quad (3.75)$$

$$\mathbf{TG} = - \int_{\Gamma} \mathbf{N}^T q_c d\Gamma \quad (3.76)$$

The solution of  $c_B$  can be obtained as follow:

$$\frac{\partial c_B}{\partial t} = -ar \quad (3.77)$$

$$\int_{\Omega} \frac{\partial c_B}{\partial t} d\Omega + \int_{\Omega} ar d\Omega = 0 \quad (3.78)$$

$$\int_{\Omega} \mathbf{N}^T d\Omega \frac{\partial \bar{\mathbf{c}}_B}{\partial t} + \int_{\Omega} \mathbf{N}^T ar d\Omega = 0 \quad (3.79)$$

$$\mathbf{TJ} \frac{\partial \bar{\mathbf{c}}_B}{\partial t} = -a\mathbf{R} \quad (3.80)$$

where

$$\mathbf{TJ} = \int_{\Omega} \mathbf{N}^T d\Omega \quad (3.81)$$

Finally, the governing equation of the diffusion and reaction system can be written as follows:

$$\begin{bmatrix} \mathbf{TR} & 0 \\ 0 & 0 \end{bmatrix} \begin{Bmatrix} \bar{\mathbf{c}}_{\text{O}_2} \\ \bar{\mathbf{c}}_{\text{B}} \end{Bmatrix} + \begin{bmatrix} \mathbf{TS} & 0 \\ 0 & \mathbf{TJ} \end{bmatrix} \frac{d}{dt} \begin{Bmatrix} \bar{\mathbf{c}}_{\text{O}_2} \\ \bar{\mathbf{c}}_{\text{B}} \end{Bmatrix} = \begin{Bmatrix} \mathbf{TG} - b\mathbf{R} \\ -a\mathbf{R} \end{Bmatrix} \quad (3.82)$$

### 3.4.3.3.2 Discretization in time

The discretization in time may be regarded as an one dimensional finite difference scheme as distinct from the spatial discretization [21, 22]. The time domain is divided into a number of elements or steps and integration is carried out for each step to obtain the change of the parameter  $\bar{\mathbf{c}}_{\text{O}_2}$ . The step-by-step integrations may then be summed to determine the total change of the parameter. The integration takes the same form as used for the spatial integration, if  $F = 0$  then  $\int \bar{g}F dt = 0$ , where  $\bar{g}$  is an arbitrary function of time. When applied to Eq. (3.72), this method requires the solution of the equations

$$\int_{t_k}^{t_k + \Delta t_k} \bar{g} \mathbf{TR} \bar{\mathbf{c}}_{\text{O}_2} dt + \int_{t_k}^{t_k + \Delta t_k} \bar{g} \mathbf{TS} \frac{d\bar{\mathbf{c}}_{\text{O}_2}}{dt} dt = \int_{t_k}^{t_k + \Delta t_k} \bar{g} (\mathbf{TG} - b\mathbf{R}) dt \quad (3.83)$$

where  $\Delta t_k$  is the duration of the  $k$  th time step

The first order time derivatives of  $\bar{\mathbf{c}}$  may be approximated by assuming a linear variation of  $\bar{\mathbf{c}}$  within each time step  $\Delta t$

$$\bar{\mathbf{c}} = \begin{bmatrix} N_1^t & N_2^t \end{bmatrix} \begin{Bmatrix} \bar{\mathbf{c}}^t \\ \bar{\mathbf{c}}^{t+\Delta t} \end{Bmatrix} \quad (3.84)$$

where  $N_1 = 1 - \alpha$ ,  $N_2 = \alpha$  and  $\alpha = \frac{(t - t_k)}{\Delta t_k}$

The time derivatives of  $N_1$  and  $N_2$  are given by

$$\frac{d}{dt} \begin{bmatrix} N_1^t & N_2^t \end{bmatrix} = \begin{bmatrix} -\frac{1}{\Delta t_k} & \frac{1}{\Delta t_k} \end{bmatrix} \quad (3.85)$$

After substitution of Eq. (3.84) and Eq. (3.85), Eq. (3.83) takes the form

$$\begin{bmatrix} \mathbf{TS} + \alpha \mathbf{TR} \Delta t_k & 0 \\ 0 & 0 \end{bmatrix} \begin{Bmatrix} \bar{\mathbf{c}}_{\mathbf{O}_2}^{t+\Delta t_k} \\ \bar{\mathbf{c}}_{\mathbf{B}}^{t+\Delta t_k} \end{Bmatrix} = \begin{bmatrix} \mathbf{TS} - (1-\alpha) \mathbf{TR} \Delta t_k & 0 \\ 0 & \mathbf{TJ} \end{bmatrix} \begin{Bmatrix} \bar{\mathbf{c}}_{\mathbf{O}_2}^t \\ \bar{\mathbf{c}}_{\mathbf{B}}^t \end{Bmatrix} + \Delta t_k \begin{Bmatrix} \mathbf{TG} - b\mathbf{R} \\ -a\mathbf{R} \end{Bmatrix} \quad (3.86)$$

### 3.4.3.3.3 Oscillation and stability

Numerical stability was considered for the case of free response, i.e. when the right-hand side of Eq. (3.72) is zero [20], it becomes

$$\mathbf{TR} \bar{\mathbf{c}}_{\mathbf{O}_2} + \mathbf{TS} \frac{\partial \bar{\mathbf{c}}_{\mathbf{O}_2}}{\partial t} = 0 \quad (3.87)$$

The standard solution for linear equations of this form is given by the sum of a set of modes of variation

$$\bar{\mathbf{c}}_{\mathbf{O}_2} = [\mathbf{a}_1 \quad \mathbf{a}_2 \quad \cdots] [y_1 \quad y_2 \quad \cdots]^T \quad (3.88)$$

where

$$y_i = e^{\alpha_i t} \quad (3.89)$$

in which

$$\alpha_i = \text{constant} \quad (3.90)$$

Substituting Eq. (3.88) into Eq. (3.87), and pre-multiplying by  $\mathbf{a}^T$ , gives

$$\mathbf{a}^T \mathbf{TR} \mathbf{a} \mathbf{y} + \mathbf{a}^T \mathbf{TS} \mathbf{a} \frac{\partial \mathbf{y}}{\partial t} = 0 \quad (3.91)$$

It was shown that for eigenvalue solutions of Eq. (3.88) it holds

$$\mathbf{a}_i^T \mathbf{TR} \mathbf{a}_j = \mathbf{a}_i^T \mathbf{TS} \mathbf{a}_j = 0, \quad i \neq j \quad (3.92)$$

so that Eq. (3.91) reduces to a set of scalar independent equations

$$n_i y_i + m_i \frac{\partial y_i}{\partial t} = 0 \quad (3.93)$$

Application of the same argument to Eq. (3.86) also reduces these to a set of independent equations.

$$(\mathbf{TS} + \alpha \mathbf{TR} \Delta t_k) \bar{\mathbf{c}}_{\mathbf{O}_2} \Big|_{t_k + \Delta t_k} = (\mathbf{TS} - \mathbf{TR} (1 - \alpha) \Delta t_k) \bar{\mathbf{c}}_{\mathbf{O}_2} \Big|_{t_k} \quad (3.94)$$

and by substituting  $\bar{\mathbf{c}}$  from Eq. (3.88), and pre-multiplying by  $\mathbf{a}^T$  the following expression results:

$$(y_i)_{t_k + \Delta t_k} (m_i + n_i \alpha \Delta t_k) = (y_i)_{t_k} (m_i - n_i (1 - \alpha) \Delta t_k) \quad (3.95)$$

In order to prevent instability [20] it is necessary that

$$\left| (y_i)_{t_k + \Delta t_k} \right| \leq \left| (y_i)_{t_k} \right| \quad (3.96)$$

which means that the value of  $y_i$  monotonically decreases in time and it is always link the value of  $y_i$  at  $t = 0$ . Therefore, combining Eq. (3.95) and Eq. (3.96) gives

$$|\lambda| = \left| \frac{m_i - n_i (1 - \alpha) \Delta t_k}{m_i + n_i \alpha \Delta t_k} \right| \leq 1 \quad (3.97)$$

and hence

$$m_i - n_i (1 - \alpha) \Delta t_k \geq -(m_i + n_i \alpha \Delta t_k) \quad (3.98)$$

or

$$n_i (2\alpha - 1) \Delta t_k \geq -2m_i \quad (3.99)$$

The stability of the solution can easily be ensured by setting  $\alpha \geq \frac{1}{2}$  rather than checking Eq. (3.99) for every value of  $i$ .

### 3.4.4 Comparison between different methods

In order to compare the solutions of the diffusion-reaction system obtained by applying different methods, the numerical integration method and the Laplace transform method were implemented in Matlab, while the CAPA-3D FE system was used for implementation of the finite element solution.

### 3.4.4.1 Geometry and material properties

Simulations of oxygen diffusion and reaction in a 3D thin film were performed for a 200 hours' time period. The geometry of the film is modelled as a block with a thickness of 2 mm, length of 10 mm and a width of 5 mm, similar to Chapter 2, Figure 3.3. The bituminous film was assumed to be an isotropic material. The material properties are shown in Table 3.2.

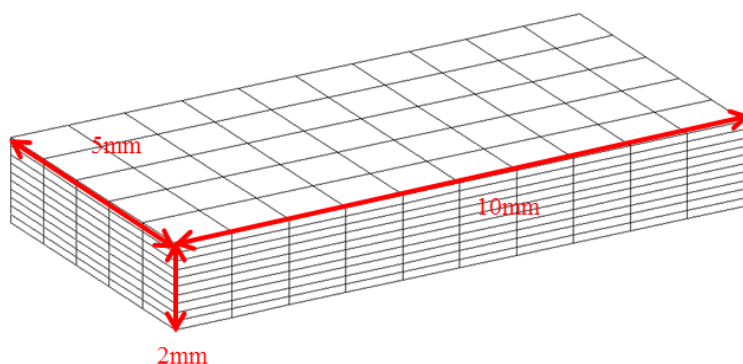


**Figure 3.3 Geometry of thin bituminous film**

**Table 3.2 Material properties of bituminous materials**

Gas diffusion coefficient $D$ ( $\text{m}^2/\text{s}$ )	Reaction constant $k$ ( $\text{m}^3/(\text{mol} \cdot \text{s})$ )	Reaction order $m, n$	Stoichiometry $a, b, d$	Initial reactive components in bitumen ( $\text{mol}/\text{m}^3$ )
$1 \times 10^{-11}$	$1 \times 10^{-6}$	1	1	1

### 3.4.4.2 Initial values and boundary conditions

The initial concentration of oxygen in the film was assumed to be 0. During the simulations, oxygen was allowed to flow into the film from the top, while there was no flow going out of the four sides and the bottom boundaries, as illustrated in Figure 3.4. The oxygen concentration loading on the top boundary was kept at a constant value of  $1 \text{ mol}/\text{m}^3$ .



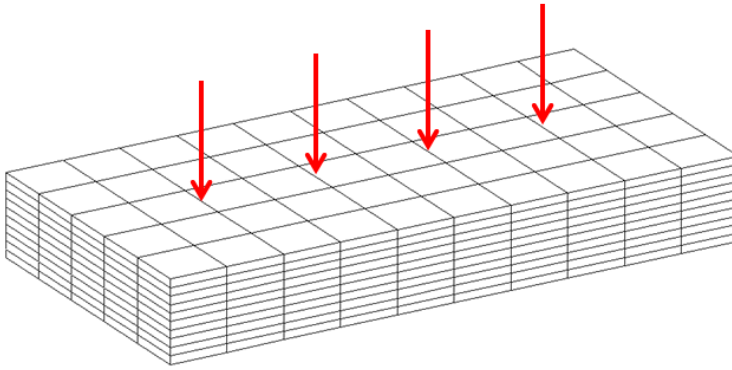


**Figure 3.4 Schematic of applied loading conditions**

### 3.4.4.3 Results and discussion

A comparison of the results obtained by the different solution methods is given in Figure 3.5. The result shows an overall agreement between the results by the different solution methods.

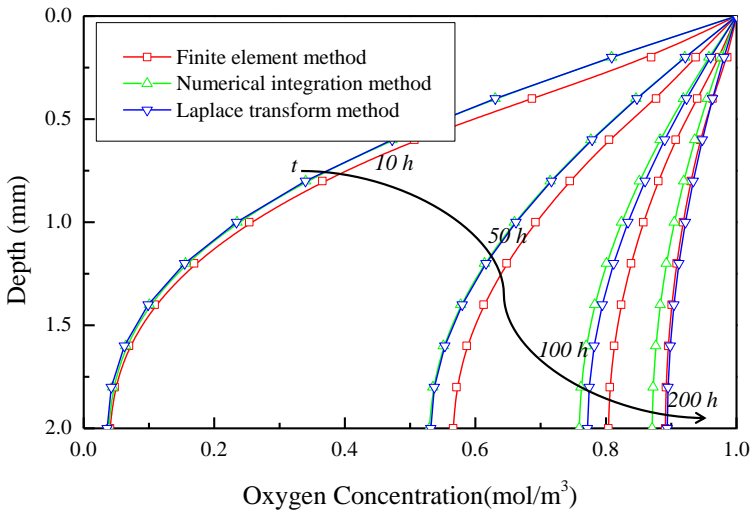


**Figure 3.5 Simulation results of different solution methods**

As described in Chapter 2, each method has its own advantages and disadvantages. In this study, the numerical integration method can only solve one dimensional diffusion and reaction by posing a strict stability condition. The Laplace transform method can only solve the linear

differential equations (reaction order  $m = n = 1$ ) in one dimension. The finite element method can solve complex problems at the cost of longer computation times. In this research, the Laplace transform method is used to determine the model parameters on the basis of experimental results. The finite element method is used to solve complex problems such as diffusion in three dimensional space and highly heterogeneous materials. The numerical integration method is used to verify the other two methods.

### 3.4.5 Comparison between diffusion and diffusion-reaction

In order to quantify the difference between the diffusion system and the diffusion-reaction system, simulations were performed for a thin film. The geometry of the film is the same as that in previous section. The Laplace transform method was selected to be used. Five different cases were analysed. Specifically, for case 1 the reaction constant is 0, which means only diffusion. Moreover, for case 2, 3, 4 and 5 the simulations were done by means of the coupled diffusion-reaction system using different reaction constants. The material properties for the various cases are presented in Table 3.3.

**Table 3.3 Material properties of different case**

Case	Gas diffusion coefficient $D$ ( $m^2/s$ )	Reaction constant $k$ ( $m^3/(mol \cdot s)$ )	Reaction order $m, n$	Stoichiometry $a, b, d$	Initial reactive components in bitumen ( $mol/m^3$ )
1		0			
2		$1 \times 10^{-6}$			
3	$1 \times 10^{-11}$	$5 \times 10^{-6}$	1	1	1
4		$1 \times 10^{-5}$			
5		$5 \times 10^{-5}$			

The initial concentration of oxygen in the film was assumed to be equal to 0. Section 3.4.4.2 describes the boundary conditions set during the simulation. The oxygen concentration loading on the top boundary was

kept at a constant value of  $1 \text{ mol/m}^3$ . The profiles of oxygen and oxidation product are plotted in Figure 3.6 and Figure 3.7 respectively.

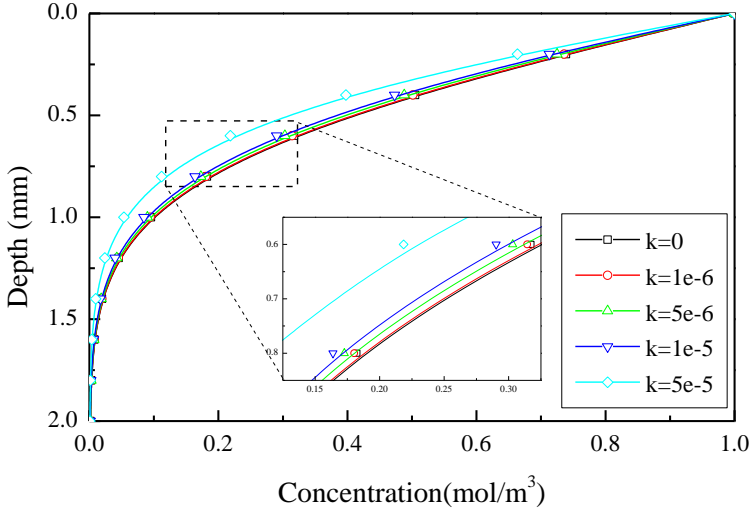


**Figure 3.6** Oxygen concentration profiles at 5 hours for different cases

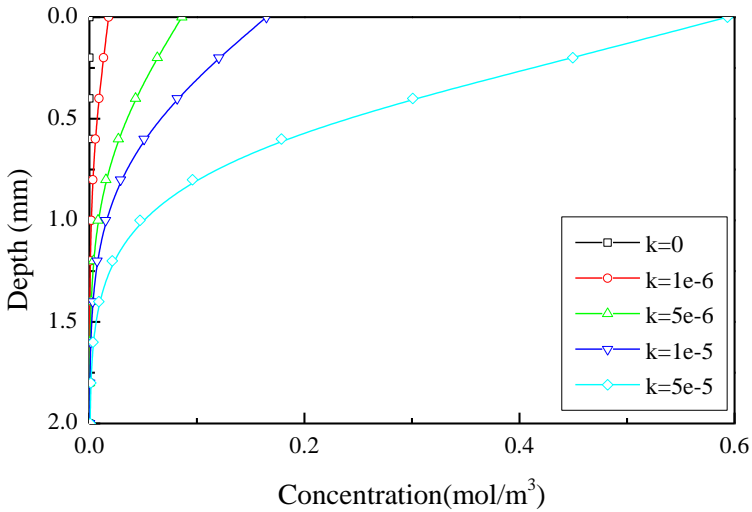


**Figure 3.7** Oxidation product concentration profiles at 5 hours for different cases

From Figure 3.6, it can be found that the reaction rate has a significant effect on the oxygen distribution in the bitumen film. A higher reaction rate can cause the consumption rate of oxygen to increase. That is the reason why the oxygen concentration profile curves move to the upper

left corner in Figure 3.6 with increasing reaction rate. Figure 3.7 shows that more oxidation products were produced with higher reaction rate.

### 3.4.6 Parametric analysis of diffusion-reaction system

In order to find out the effect of reaction parameters on diffusion-reaction system, parametric analysis was discussed in this section. The same geometry, loading and boundary conditions were used during the simulations, in which the diffusion coefficient and reaction constant were set equal to  $1 \times 10^{-11} \text{ m}^2/\text{s}$  and  $1 \times 10^{-5} \left( s \cdot (\text{mol}/\text{m}^3)^{m+n-1} \right)^{-1}$ . In order to clearly show the role of the reaction part in a coupled system, the profile of oxygen concentration in time only due to diffusion was also added into Figure 3.8 to Figure 3.12.

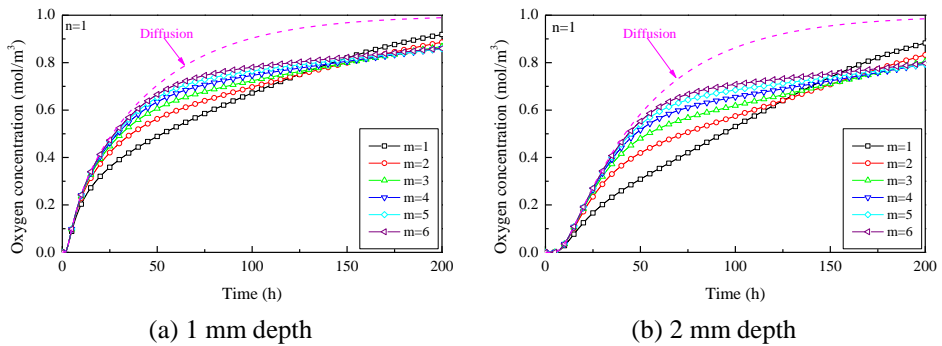


**Figure 3.8 Oxygen concentration profiles in time using different reaction order  $m$  value at (a) 1 mm depth and (b) 2 mm depth**

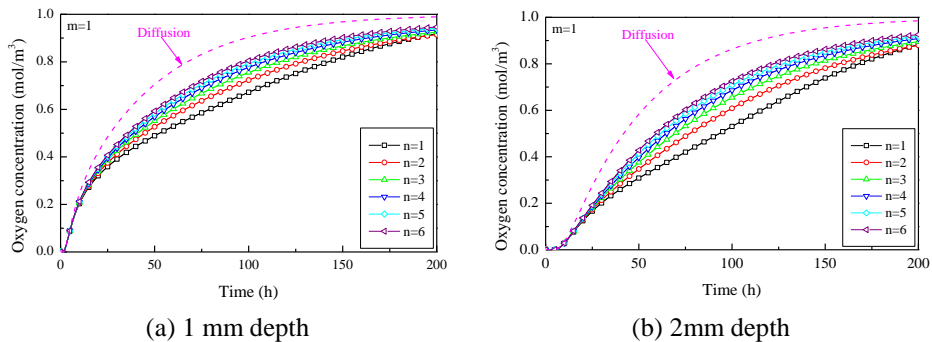


**Figure 3.9 Oxygen concentration profiles in time using different reaction order  $n$  value at (a) 1 mm depth and (b) 2 mm depth**

As shown in Figure 3.8 and Figure 3.9, the profile of oxygen concentration in time at specific positions is affected by the values of parameters  $m$  and  $n$  that describe the reaction order in Eq. (3.6). Since the values of  $c_B$  and  $c_{O_2}$  are always smaller than 1, the higher value of reaction order denote slower reaction rate. With a higher value of reaction order ( $m$  or  $n$ ), the profiles of oxygen concentration significant increases for the short term (before 100 hours) due to the lower reaction rate.

The difference in Figure 3.8 and Figure 3.9 happens for the long term profiles of oxygen concentration. The reason is that, for smaller values of  $m$  (which corresponds to the reaction order of reactive components in bitumen) more bitumen is consumed. As more bitumen is consumed, the reaction rate decreases more significantly and profiles of oxygen increase. For smaller values of  $n$  (which corresponds to the reaction order of oxygen) more oxygen is consumed. Although oxygen is consumed, it is supplemented due to diffusion. Hence, the reaction rate decreases but not as such as that at high  $m$  value.

Simulations were performed by varying the parameters  $a$  and  $b$  that describes the stoichiometry of reactive components in bitumen and oxygen, respectively, in Eq. (3.4). The results were shown in Figure 3.10 and Figure 3.11.

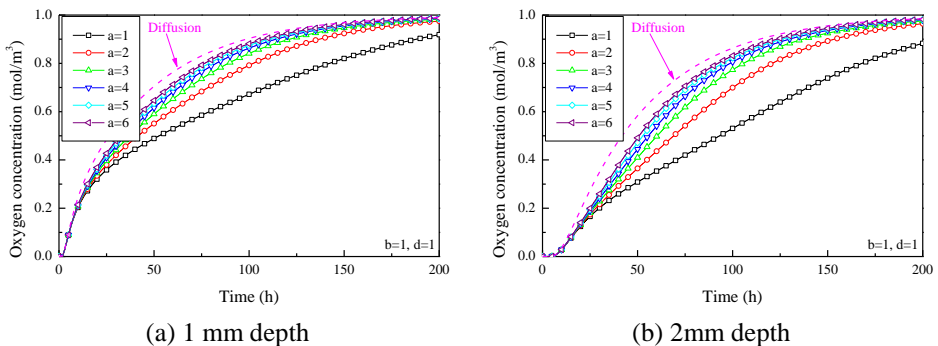
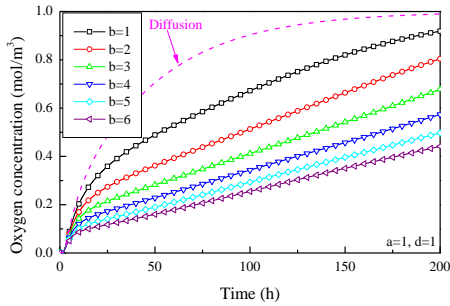
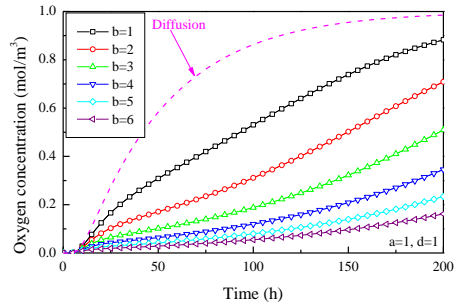


**Figure 3.10 Oxygen concentration profiles in time using different stoichiometry a value at (a) 1 mm depth and (b) 2 mm depth**



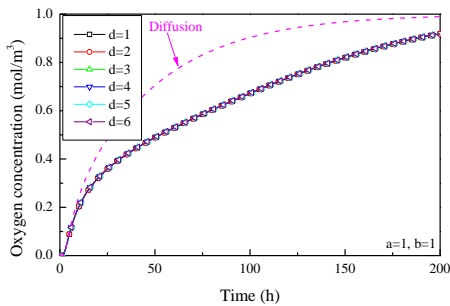
(a) 1 mm depth



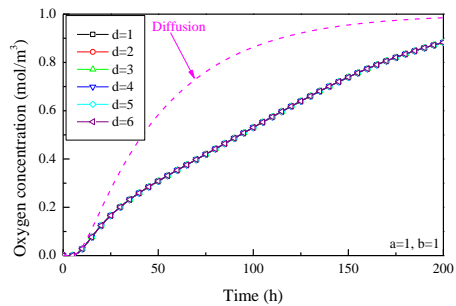
(b) 2 mm depth

**Figure 3.11 Oxygen concentration profiles in time using different stoichiometry  $b$  value at (a) 1 mm depth and (b) 2 mm depth**

Figure 3.10 shows that it take less time for the bitumen film to be saturated due to higher consumption rate of bitumen. On the contrary, it take more time for the bitumen film to be saturated due to higher consumption rate of oxygen in Figure 3.11. However, in Figure 3.12, the profile of oxygen concentration in time do not changed by changing the value of  $d$  that describe the stoichiometry of the oxidation product. It is because the oxidation product is the end product of the reaction, which has no effect on the reaction rate. But, it has a large influence on the amount of oxidation production, as shown in Figure 3.13.



(a) 1 mm depth



(b) 2 mm depth

**Figure 3.12 Oxygen concentration profiles in time using different stoichiometry  $d$  value at (a) 1 mm depth and (b) 2 mm depth**

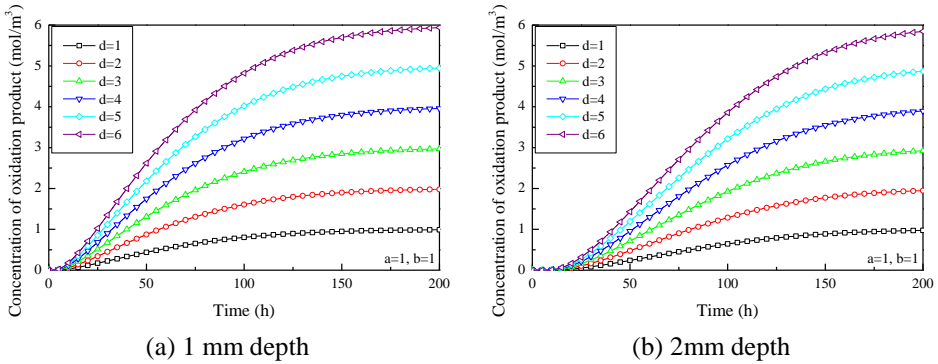


**Figure 3.13 Oxidation product concentration profiles in time using different stoichiometry  $d$  value at (a) 1 mm depth and (b) 2 mm depth**

In summary, because of the important role of reaction in couple system, the oxygen concentration profile curves are all below the one which is only have pure diffusion without reaction, Figure 3.8 to Figure 3.12. In addition, through the parametric analysis, it is realized that the importance of a proper definition for all reaction parameters. The further discussion and determination on all reaction parameters were conducted in next chapter.

### 3.5 Application

In order to demonstrate the capabilities of the FE method in simulating oxygen diffusion-reaction in asphalt mixtures, a 3D micromechanical FE mesh was generated by CT scanning of a porous asphalt mixture (more details explained in the section of application in Chapter 2).

In this study, oxygen was set not to diffuse into nor react with the aggregates. In addition, oxygen was allowed to diffuse into the air voids with a relatively high diffusion coefficient. The oxidation reaction of the mortar was assumed to be a first order for each reactant and a second order over all. In chemistry terms, this means that all stoichiometric coefficients and reaction orders were set equal to 1. The concentration of the reactive components in mortar was set equal to 1 mol/m<sup>3</sup> as well.

During the simulations, a constant oxygen concentration boundary was applied on the top, while no flow out of the four sides and bottom

boundaries was considered, in order to approximately simulate the condition of an asphalt pavement in the field. Table 3.4 illustrates the input materials parameters of each component in the PA mixtures for the FE simulation. Simulation results were shown in Figure 3.14.

**Table 3.4 Material properties of each component in mixture**

Component	Oxygen diffusion coefficient $D$ ( $m^2/s$ )	Reaction constant $k$
Mortar	$1 \times 10^{-11}$	$1 \times 10^4 \text{ m}^3 / (\text{mol} \cdot \text{s})$
Aggregate	0	0
Air void	$1 \times 10^{-4}$	0

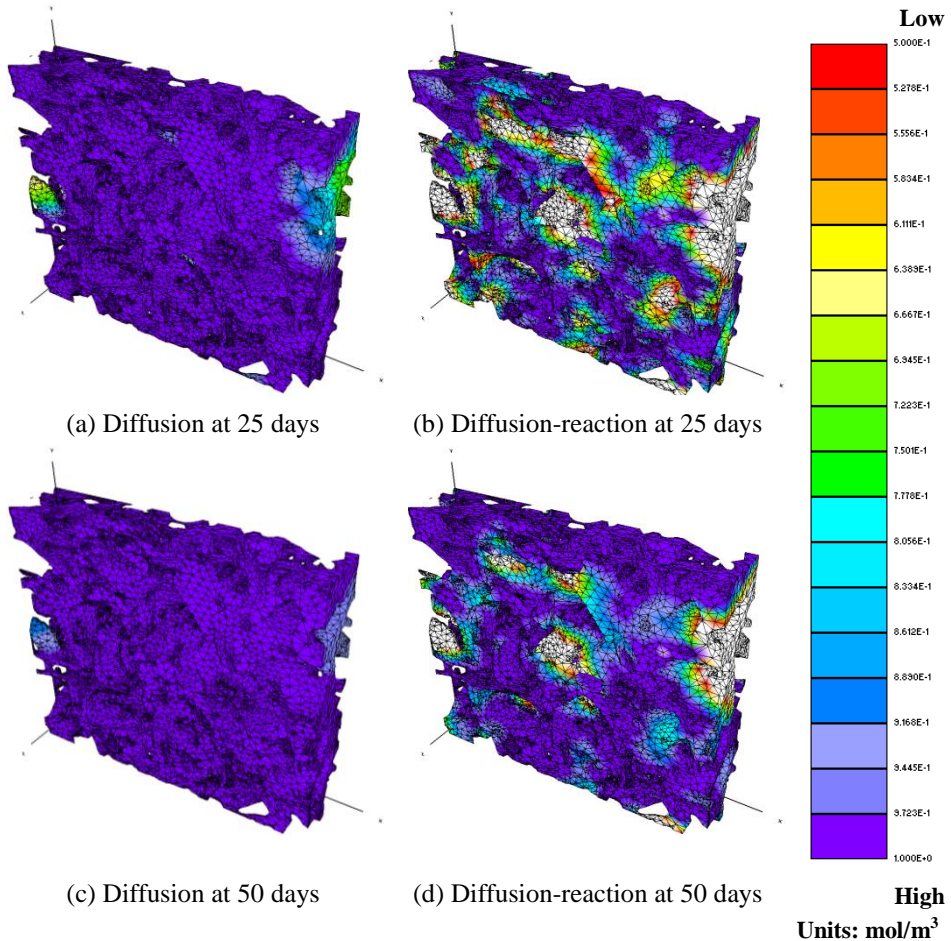


**Figure 3.14 Oxygen concentration in the mortar phase of a PA mixture after various days of diffusion (Left) and diffusion-reaction (Right)**



Figure 3.14 shows the oxygen concentration in the mortar at various time intervals. The left column is the diffusion only case, while the right column shows the coupled diffusion-reaction case. From Figure 3.14, it can be seen that the oxidation of mortar affects significantly the oxygen concentration, since oxygen consumption occurs during the reaction.

### **3.6 Summary**

Bitumen oxidation is a long-term process that causes a stiffening of the material, a loss in ductility and an increase in brittleness. Consequently, the pavement is more susceptible to ravelling and cracking. In order to evaluate the long-term performance of a pavement, the chemical changes in bitumen and the profile of the oxidation products within the bituminous layers must be first understood.

Based on the diffusion model of Chapter 2, a diffusion-reaction model was developed to simulate oxidation in bitumen. The diffusion-reaction model was solved by means of three different mathematical methods, on the basis of the assumption that diffusion is independent of the oxygen concentration and the physical state of the bitumen. Comparing the results of the diffusion and the diffusion-reaction models show that, in the latter case, it takes more time for the bituminous film to be saturated by oxygen because of the depletion of oxygen due to the reaction with the oxidizing bitumen components. Parametric analysis demonstrated the critical roles of reaction order and stoichiometry in the coupled diffusion-reaction model.

The model especially contributes to improved understanding of bitumen oxidation and the effect of the various parameters on this. In Chapter 4, parameter determinations and verification of the model are presented.

### 3.7 References

1. Wilkinson, A. and A. McNaught, *IUPAC Compendium of chemical terminology, (the "Gold Book")*. 1997, Blackwell Scientific Publications, Oxford.
2. Dickinson, E.J., J.H. Nicholas, and S. Boas Traube, *Physical factors affecting the absorption of oxygen by thin films of bituminous road binders*. Journal of Applied Chemistry, 1958. **8**(10): p. 673-687.
3. Benson, P.E., *Low temperature transverse cracking of asphalt concrete pavements in central and west texas*. TTI-2-9-72-1752-2F Final Report. 1976.
4. Liu, M., et al., *The kinetics of carbonyl formation in asphalt*. AIChE Journal, 1996. **42**(4): p. 1069-1076.
5. Xiao, F., et al., *Model developments of long-term aged asphalt binders*. Construction and Building Materials, 2012. **37**: p. 248-256.
6. Petersen, J.C., *A thin film accelerated aging test for evaluating asphalt oxidative aging*. Transportation Research Board, Washington, DC, 1989. **58**: p. 220-237.
7. Lee, D.-Y., *Asphalt durability correlation in LOWA*. Transportation Research Record, 1973. **468**: p. 43-60.
8. Edler, A., et al., *Use of aging tests to determine the efficacy of hydrated lime additions to asphalt in retarding its oxidative hardening*. in *Proceedings, Association of Asphalt Paving Technologists*. 1985. p. 118-139.
9. Christensen, D.W. and D.A. Anderson, *Interpretation of dynamic mechanical test data for paving grade asphalt cements (with discussion)*. Journal of the Association of Asphalt Paving Technologists, 1992. **61**: p. 67-116.
10. Petersen, J.C., et al., *Binder characterization and evaluation: Volume 1*. Rep. No. SHRP-A-367, Strategic Highway Research Program, National Research Council, Washington, DC, 1994.
11. Hayton, B., et al., *Long term ageing of bituminous binders hayton*. Proc. EurobitumeWorkshop, 1999. **99**(126).
12. Hoorn, C.B., *Durability of bitumen in theory and practice*, in *5th World Petroleum Congress*. 1959, World Petroleum Congress: New York, USA. p. 16.
13. Dickinson, E., *The diffusion controlled reaction of oxygen with films of bituminous binders*. Australian Road Research, 1984. **14**(3): p. 121-132.
14. Prapaitrakul, N., et al., *A transport model of asphalt binder oxidation in pavements*. Road Materials and Pavement Design, 2009. **10**(sup1): p. 95-113.
15. Jin, X., et al., *Fast-rate-constant-rate oxidation kinetics model for asphalt binders*. Industrial & Engineering Chemistry Research, 2011. **50**(23): p. 13373-13379.
16. Myers, R., *The basics of chemistry*. 2003: Greenwood Publishing Group.
17. Thyron, F.C., *Chapter 16 Asphalt oxidation*, in *Developments in Petroleum Science*, T.F. Yen and G.V. Chilingarian, Editors. 2000, Elsevier. p. 445-474.
18. Navarro González, M., *Rheology and engineering parameters of bitumen modified with polyolefins, elastomers and reactive polymers*. 2010, Berlin: Univ.-Verl. der TU Berlin.
19. Krantz, S.G., *Handbook of complex variables*. 2012: Springer Science & Business Media.
20. Lewis, R.W. and B.A. Schrefler, *The finite element method in the deformation and consolidation of porous media*. 1987: John Wiley and Sons Inc., New York, NY.

21. Zienkiewicz, O.C., et al., *The finite element method*. Vol. 3. 1977: McGraw-hill London.
22. Norris, V., *The elastoplastic analysis of soil consolidation, with special reference to kinematic hardening* (doctoral thesis). University College of Swansea. 1981.

# 4

## **PARAMETER DETERMINATION AND VERIFICATION OF OXYGEN DIFFUSION- REACTION MODEL**

---

## 4.1 Introduction

An accurate simulation of a process does not only depend on the capabilities of the model, but also on the quality of the associated input parameters like material properties. In this Chapter, firstly, an overview of the experimental determination of the diffusion coefficient and the reaction rate of bituminous materials is presented. Then, a methodology is presented which has been developed on the basis of Fourier Transform Infrared (FTIR) tests for the determination of the diffusion coefficient and the reaction constant which were discussed in Chapter 3. By using the corresponding model parameters, the diffusion and reaction model described in Chapter 3 is verified by the results of laboratory measurements.

## 4.2 Review on the experimental determination of diffusion coefficient and reaction rate of bituminous materials

Anderson and Wright (1941) measured oxygen diffusion through bitumen films by means of a permeability cell, Figure 4.1 [1]. Oxygen gas at atmospheric pressure diffuses through a bituminous film. The pressure of the diffused gas after a certain time interval was registered by the connected manometer. By measuring the volume and pressure changes of the diffused gas, the weight of the diffused oxygen can be calculated and this, together with the area and the thickness of the diaphragm, were used to calculate the permeability constant by the following equation:

$$W = \frac{KAPt}{L} \quad (4.1)$$

where  $W$  is the weight of oxygen diffused,  $K$  is the permeability constant,  $A$  is the area of the film,  $L$  is the thickness of the film,  $P$  is the pressure differential and  $t$  is time of diffusion.

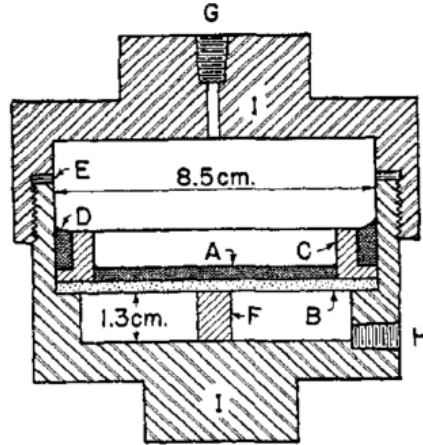


**Figure 4.1** Cross section of the measuring cell (A. bitumen film, B. porous aluminum disk, C. stainless steel diaphragm ring, D. hard wax seal, E. greased lead gasket, F. metal block support, G. Tapped hole to gas supply, H. Tapped hole to manometer, I. Hexagonal stainless steel shell) (Anderson & Wright [1])

van Oort (1954) performed absorption experiments of a bitumen sample in order to determine the diffusion coefficients of oxygen in bitumen [2]. The instrument, Figure 4.2, consists of a gas burette, a mercury pressure gauge and a flask which contains the bitumen as a coating. Based on the Laplace transform method, the diffusion coefficient and the reaction constant were obtained by means of the absorption function, Eq. (4.2).

$$\frac{M}{ac_0} = \frac{\tanh \varphi}{\varphi} + \frac{1}{2 \cosh^2 \varphi} + \frac{\tanh \varphi}{\varphi} \tau \left[ 1 + \frac{\left( \left( n + \frac{1}{2} \right)^2 \pi^2 \right)}{\varphi^2} \right] - 2 \sum_{n=0}^{\infty} \frac{\left( n + \frac{1}{2} \right)^2 \pi^2 e^{-\left( \left( n + \frac{1}{2} \right)^2 \pi^2 + \varphi^2 \right) \tau}}{\left( \left( n + \frac{1}{2} \right)^2 \pi^2 + \varphi^2 \right)^2} \quad (4.2)$$

in which

$$\varphi = a \sqrt{\frac{kG_0}{D_0}} \quad (4.3)$$

$$\tau = kG_0 t \quad (4.3)$$

where  $M$  is the total quantity of oxygen absorbed,  $c_0$  is the solubility of oxygen,  $a$  is the film thickness,  $k$  is reaction constant,  $G_0$  is the maximum concentration of bound gas,  $D_0$  is the diffusion coefficient of fresh material,  $t$  is the time and  $n$  is an integer between 0 to  $\infty$ .

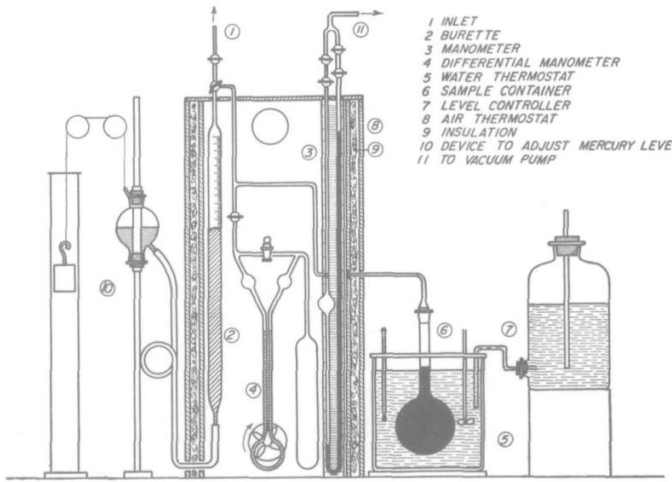


**Figure 4.2 Absorption apparatus (van Oort [2])**

Dickinson et al. (1958) performed experiments for measuring the absorption of oxygen into bitumen films by using a semi-micro gas burette [3]. Measurements were made by adjusting the burette to balance the manometer. The design of this apparatus is shown in Figure 4.3. The initial absorption rate is related to the film thickness by the expression:

$$R_d = \frac{\sqrt{R'K}}{d} \tanh \sqrt{\frac{R'}{K}} d \quad (4.3)$$

where,  $R_d$  is the initial rate of absorption per unit of liquid for a film of thickness  $d$ ,  $R'$  is the rate of absorption when the whole film is saturated with gas and  $K$  is the permeability constant for the diffusion of oxygen through the bitumen.

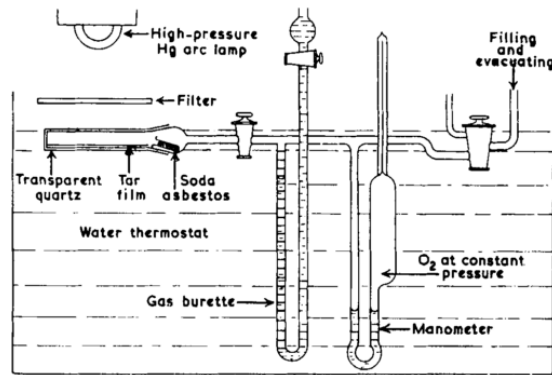


**Figure 4.3** Apparatus for measuring the absorption of oxygen by bitumen films (Dickinson et al. [3])

Dorrence et al. (1974) provided direct evidence for the formation of significant amounts of carbonyl on ageing of asphalts by means of infrared spectra [4]. Later Petersen discussed the kinetics of bitumen oxidation in terms of the formation of ketones/carbonyl and sulfoxide components [5-7]. The study showed that there are two different phases of oxidation and kinetic mechanisms, consisting of an initial large increase of the sulfoxides and a second phase in which the ketone components increase, Figure 4.4. The results were supported extensively by other experiments [8-12].

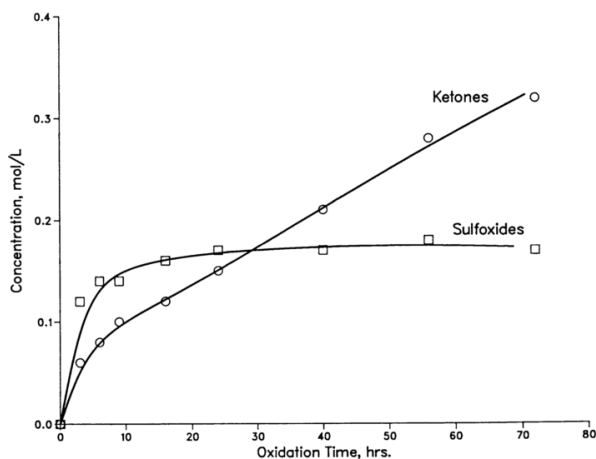


**Figure 4.4** Kinetic oxidation data for TFAAT oxidation of SHRP asphalt AAG-1 at 113 °C (Petersen et al. [10])



Domke et al. (2000) oxidized eight types of bitumen at various temperatures and pressures to determine how the ageing condition affected the oxidation kinetics by means of FTIR [13]. The results are shown in Figure 4.5. Then an oxidation kinetics model was developed based on the Arrhenius equation to predict the rate of oxidation in the constant-rate region.

$$r_{ca} = A'e^{\frac{-E}{RT}} \quad (4.4)$$

where  $r_{ca}$  is the carbonyl rate,  $A'$  is the pressure dependent variable,  $E$  is the activation energy,  $R$  is the universal gas constant and  $T$  is the absolute temperature.

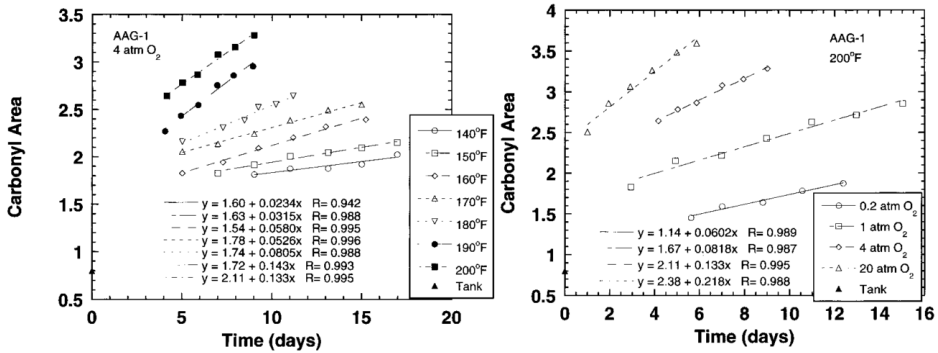
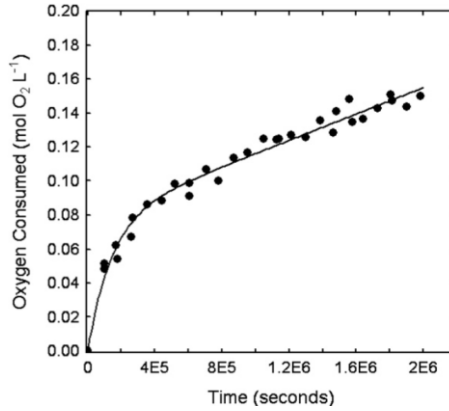


Figure 4.5 Oxidation rates of AAG-1 bitumen at various temperature (left) and pressure (right) (Domke et al. [13])

Herrington (2012) developed a numerical model to simulate the diffusion and reaction of oxygen in bitumen films [14]. The diffusion coefficient was calculated by Eq. (4.5), based on the studies of Dickinson and Blokker [15, 16].

$$\log D = -12.3083 - 0.3351 \log \eta + \log RT \quad (4.5)$$

where  $D$  is the oxygen diffusion coefficient ( $\text{m}^2/\text{s}$ ),  $\eta$  is the bitumen viscosity (Pa s),  $R$  is the universal gas constant ( $8.3143 \text{ J}/(\text{K mol})$ ) and  $T$  is the temperature (K). The reaction rate was obtained by the curve of oxygen consumption, Figure 4.6.



**Figure 4.6 Oxygen consumption (per liter of bitumen) for oxidation in toluene solution at 50 °C for 555 h with constant oxygen concentration (Herrington [14])**

Han et al. (2013) determined the oxygen diffusivity in bitumen by comparing the oxidation rates at the exposed surface and the substrate surface using an oxygen diffusion and reaction model, Eq. (4.6), with known reaction kinetics [17].

$$\frac{\partial P}{\partial t} = \frac{\partial D_{O_2}}{\partial x} \frac{\partial P}{\partial x} + D_{O_2} \frac{\partial^2 P}{\partial x^2} - \frac{cRT}{h} r_{CA} \quad (4.6)$$

where,  $P$  is the oxygen pressure,  $t$  is the time,  $D_{O_2}$  is the oxygen diffusion coefficient,  $x$  is the depth into the film,  $c$  is the asphalt dependent factor,  $R$  is the universal gas constant,  $T$  is the temperature,  $h$  is the Henry's law constant and  $r_{CA}$  is the carbonyl rate which is described by the Arrhenius expression, according to Eq. (4.4).

In summary, there are limited data and test methodology on the determination of the diffusion coefficients and oxidative rates of oxygen in bitumen. Due to the fact that the solubility of oxygen in bitumen is so low, the absorption of oxygen requires high precision measurements and therefore the test apparatus can be quite complicated, as shown by the instrument setups in Figure 4.1 to Figure 4.3. In addition, due to the fact that the bitumen film may deform during the test, especially at high temperatures, it is difficult to control the thickness of the bitumen film. Another difficulty is that to make sure the diffusion process is always

under the same air pressure during the measurement. All these factors make the test apparatus even more complicated.

In the 1970s, researchers found that the amounts of carbonyls and sulfoxides significantly increases in aged bitumen by means of FTIR tests. After that, several oxygen diffusion and reaction models were developed, but they mainly focused on the prediction of carbonyls, such as Eq.(4.4) and Eq.(4.6). As described in Chapter 3, because diffusion and reaction are coupled, researchers have to develop diffusion-reaction model with known one of these two process first. Hence, Herrington's model assumes a known diffusion coefficient, while Han's model assumes known reaction kinetics. Then, based on the their test results, the other process is calculated. In other words, these tests cannot obtain two parameters, the diffusion coefficient and the reaction kinetics, through a single test setup.

Considering the limitations of the above experimental methods, a new methodology was developed in this thesis based on FTIR testing. The benefits of the methodology include: firstly the ease of its implementation in the lab, secondly its capability to determine both, the diffusion coefficient and the reaction constant and, thirdly the consideration of both, carbonyl and sulfoxide as the oxidation products.

### **4.3 Methodology to determine the diffusion coefficient and reaction constant of bituminous materials**

In the followings, the development of oxygen diffusion and oxidation product in two fresh bitumen films with different thickness,  $h$  and  $2h$ , as shown in Figure 4.7, is presented schematically in five time instants (i. e.  $0 < t_1 < t_2 < t_3 < t_4 < t_\infty$ ). Oxygen is only allowed to diffuse into the bitumen from the top, while no flow is going out from the bottom. At time zero, diffusion has not started yet, thus no new oxidation product

exists inside the bitumen films. In reality, an initial amount of sulfoxides can be present in bitumen because of sample preparation, slow oxidation due to storage, etc. For this reason, the relative change in the oxidation products is used for the determination of the diffusion coefficients presented in section 4.6.3.

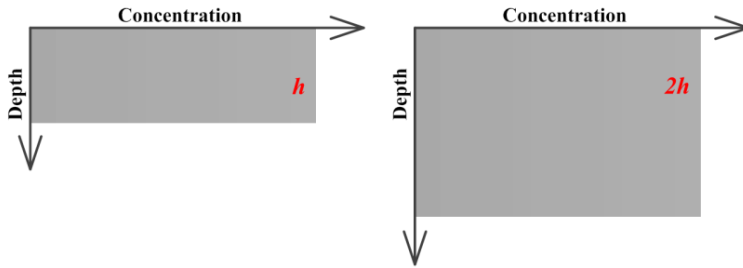
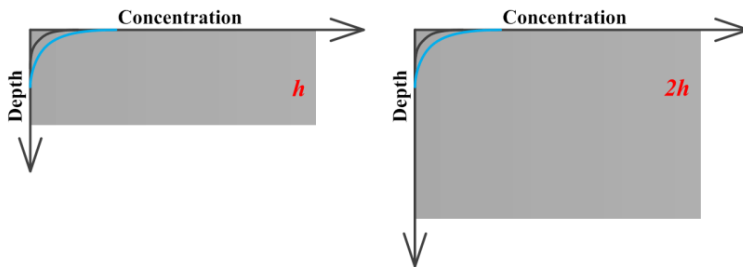


**Figure 4.7** Schematic of two bitumen films with different thickness (fresh stage).

As diffusion progresses, until time  $t_2$ , the diffusion process can be considered similar to diffusion into an infinite medium. This is the reason why in Figure 4.8(a) and Figure 4.8(b) the profile of the oxygen in the two films is the same. Hence, the profile of the oxidation products in the films is the same as well. Moreover, diffusion is always one step earlier than reaction and considering that the diffusion rate is generally much larger than the reaction rate, the blue curve (profile of oxygen) is always below black curve (profile of oxidation products), Figure 4.8.



(a)  $t = t_1$

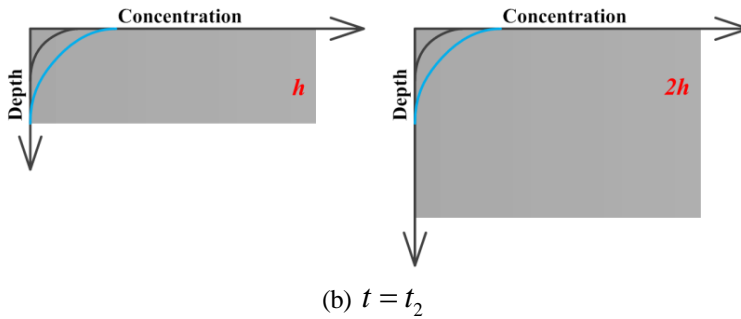


**Figure 4.8** Schematic of two bitumen films at different aged state,  $t = t_1$  &  $t_2$   
(Blue curve is oxygen, while black curve is oxidation product).

At time  $t = t_2$ , oxygen has reached the bottom of the thin film, while it has reached at depth  $h$  in the thick film. Oxygen diffusion into the thick film is still similar to diffusion into an infinite medium. However, for the thin film, diffusion is now affected by the bottom boundary. Therefore, the development of oxygen profile in the two films starts to differ. Correspondingly, the concentration of the oxidation product will also be different at time  $t = t_3$ , Figure 4.9. It can be observed that the concentration of oxygen (or of oxidation products) in the two films is always different until both films are fully oxidized.

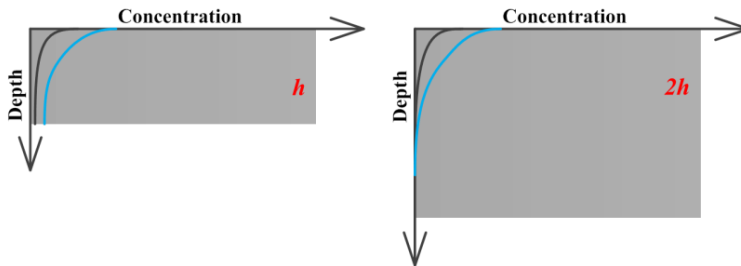


**Figure 4.9** Schematic of two bitumen flimes at aged state,  $t = t_3$

When time is equal to  $t_4$ , the concentration of oxygen (or of oxidation products) at any position of the films has reached the maximum value, since both bitumen films are fully oxidized. After this point in time, the concentration profiles do not change anymore, Figure 4.10.

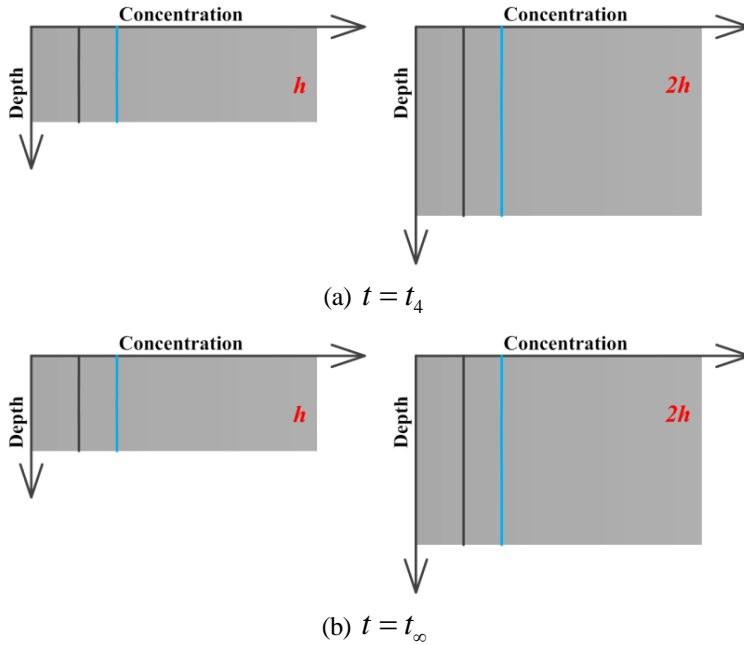


**Figure 4.10** Schematic of two bitumen films at different aged state,  $t = t_4$  &  $t_\infty$

At the period before time  $t_2$ , one can accept that the volume average concentration of the oxidation products in the thin film is twice as that of the thick film, as the profile of the oxidation products in the two films is the same and the thickness of the thick film is twice than that of the thin film, as shown in the left part of the Figure 4.11. After time  $t_4$ , because both films are fully oxidized, the volume average concentration of the oxidation products in the thin film is the same as this in the thick film, as shown in the right part of the Figure 4.11. Between  $t_2$  and  $t_4$ , the ratio of the volume average concentration of the oxidation products between the thin and the thick film is between 2 and 1, as shown at time equals  $t_3$  in Figure 4.11.

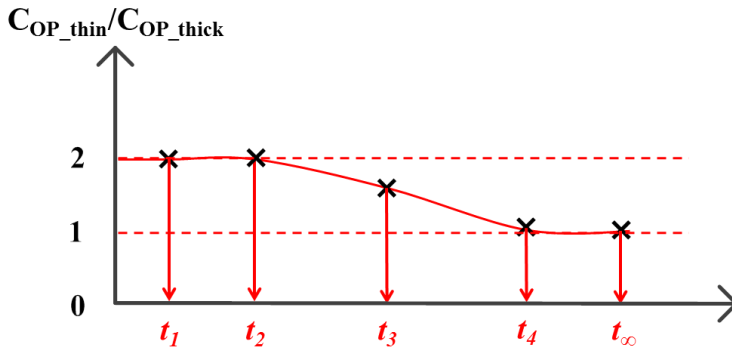


**Figure 4.11 Schematic of oxidation production volume average concentration ratio between thin and thick films ( $C_{OP\_thin}$  and  $C_{OP\_thick}$  is volume average concentration of oxidation product in thin and thick film, respectively)**

From Figure 4.11, it can be observed that the ratio of the volume average concentration of the oxidation products at  $t_2$  is a special point. At the time  $t_2$ , oxygen molecules have just reached the bottom of the thin film with thickness of  $h$ . By knowing that the oxygen needs time of  $t_2$  to reach depth  $h$  in the film, the diffusion coefficient of oxygen in the bituminous materials can be calculated. Then by using the relationship between the concentration of oxidation products and ageing time, the reaction constant can be determined as well.

#### 4.4 Overview of experimental program

Based on the methodology presented above, bitumen films with two different thicknesses were aged at four different temperatures for various time periods. The FTIR test method was employed for evaluating the changes in the chemical behavior (oxidation products) of bitumen due to oxidative ageing.

#### 4.4.1 Materials

The PEN 70/100 bitumen, which is one of the most commonly used bitumen in the Netherlands, was used in this study. Table 4.1 shows the main physical and rheological properties of the examined bitumen from Q8 Oils.

**Table 4.1 Specifications of PEN 70/100 at fresh (unaged) state**

Property	Unit	PEN 70/ 100
Penetration at 25 °C	0.1 mm	70-100
Softening point	°C	43-51
Dynamic viscosity at 60 °C	Pa·s	160
Complex shear modulus at 1.6 Hz & 60 °C	kPa	1.8
Phase angle at 1.6 Hz & 60 °C	°	88

#### 4.4.2 Ageing method

In this study, bitumen film samples with two different thicknesses were aged by oven for various ageing times and temperatures. Table 4.2 summarizes the various ageing conditions that were considered. After ageing, in order to uniform the distribution of oxidation product inside, the bitumen film was stirred before the measurement.

**Table 4.2 Ageing program**

Thickness (µm)	Temperature (°C)	Ageing time(h)
200, 400	50, 75, 100, 125	1, 2, 5, 10, 20, 40, 80, 160

#### 4.4.3 Experimental method

The tests were performed using the Spectrum 100 FT-IR spectrometer of Perkin-Elmer available at the Section of Pavement Engineering at TU Delft, Figure 4.12. A single-beam configuration was used. The sample was scanned 20 times, with a fixed instrument resolution of 4 cm<sup>-1</sup>. The wavenumbers were set to vary from 600 to 4000 cm<sup>-1</sup>.





**Figure 4.12** Spectrum 100 FT-IR spectrometer of Perkin-Elmer.

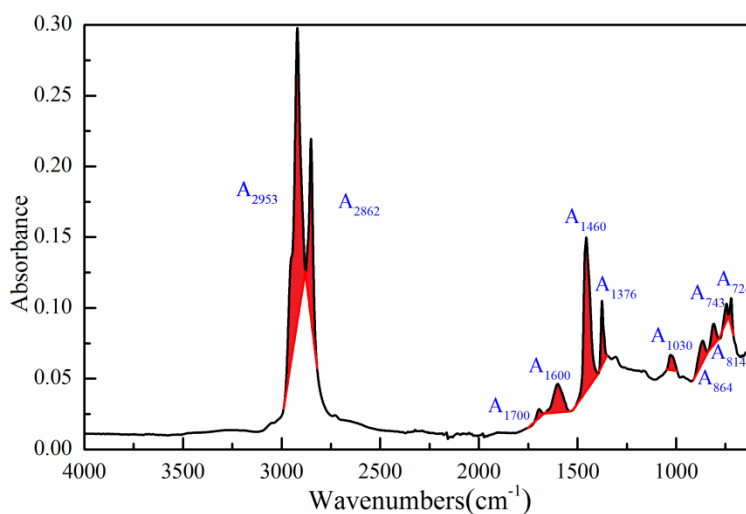
The chemical composition of bitumen is very complex. Therefore specific peaks at selected wavenumbers were used to investigate the changes in the functional groups due to bitumen ageing. In this study, the effects of ageing were studied considering specific bands of wavenumbers and the corresponding area under those bands. Using the area values, the ageing indices were calculated. The characteristic regions were adopted from a previous study [18].

The most important infrared region is between wavenumbers of 1800-600  $\text{cm}^{-1}$ . This region provides information about the functional chemical groups which contain oxidation products such as carbonyls (1753-1660  $\text{cm}^{-1}$ ) and sulfoxides (1047-995  $\text{cm}^{-1}$ ). This region is also called the fingerprint region. The functional groups that are normally used to characterize the effects of ageing on bitumen chemistry are summarized in Table 4.3.

**Table 4.3 Vertical Limit Bands with the Corresponding Functional Groups (Lamontagne et al. [19])**

Area	Vertical band limit (cm <sup>-1</sup> )	Functional groups
A <sub>724</sub>	734-710	Long chains
A <sub>743</sub>	783-734	Out of plane adjacent
A <sub>814</sub>	838-783	Out of plane adjacent
A <sub>864</sub>	912-838	Out of plane singlet
A <sub>1030</sub>	1047-995	Oxygenated functions - sulfoxide
A <sub>1376</sub>	1390-1350	Branched aliphatic structures
A <sub>1460</sub>	1525-1395	Aliphatic structures
A <sub>1600</sub>	1670-1535	Aromatic structures
A <sub>1700</sub>	1753-1660	Oxygenated functions - carbonyl
A <sub>2862</sub>	2880-2820	Stretching symmetric
A <sub>2953</sub>	2990-2880	Stretching aromatic

On the basis of these bandwidths the ageing indices, carbonyl and sulfoxide index were calculated as defined by Lamontagne et al. [19]. The calculation is performed by dividing the area under a specific location of the spectrum by the sum of others specific areas, Figure 4.13. The analytical expressions to determine the ageing indices are shown in Eq.(4.7) to Eq. (4.9).

**Figure 4.13 Schematic of bitumen infrared spectrum**

$$\text{Carbonyl index} = \frac{A_{1700}}{\sum A} \quad (4.7)$$

$$\text{Sulfoxide index} = \frac{A_{1030}}{\sum A} \quad (4.8)$$

$$\sum A = A_{(2953,2862)} + A_{1700} + A_{1600} + A_{1460} + A_{1376} + A_{1030} + A_{864} + A_{814} + A_{743} + A_{724} \quad (4.9)$$

## 4.5 Results and discussion

Bitumen samples subjected to different ageing conditions were tested by means of FTIR. At least five replicate samples were tested at each condition. Figure 4.14 shows a typical FTIR spectrum with wavenumbers less than 2000  $\text{cm}^{-1}$  at various ageing times. The presented wavenumbers region corresponds to functional groups related to the bitumen oxidation.

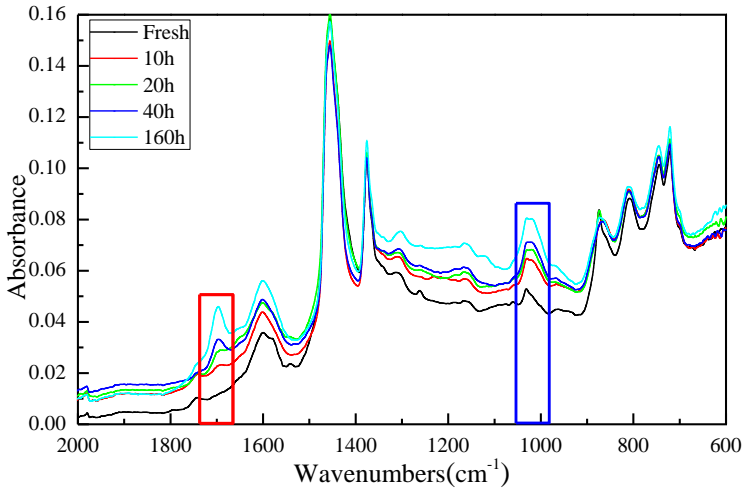


**Figure 4.14** Detail of the FTIR spectra of 0.2 mm thickness bitumen film at different ageing time (oven ageing at 100 °C).

Figure 4.14 shows the high variability of the carbonyl (right column at left) and sulfoxide (blue column at right) functional groups. Both groups increase with ageing. Figure 4.15 shows the variation of the carbonyl

and sulfoxide indices (average value of three measurements), which were calculated based on Eq. (4.7) to (4.9).

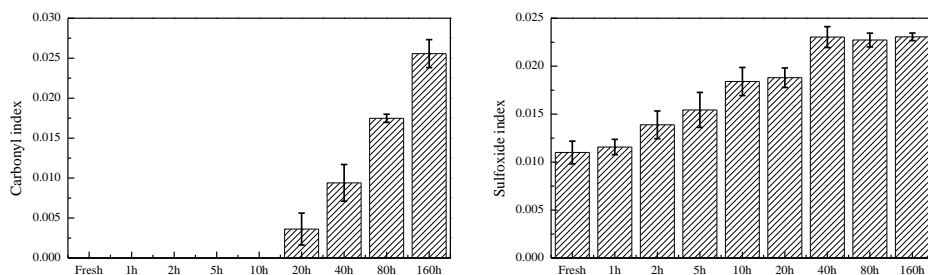


**Figure 4.15 Ageing indices of 0.2 mm thickness bitumen film at different ageing time (oven ageing at 100 °C).**

The results showed that oven ageing at 100 °C causes an increase of the carbonyl and sulfoxide indices with time. It is interesting to note that carbonyls start forming after 10 hours of ageing and then increase with time, while the sulfoxide index increases progressively. In other words, sulfoxides are formed earlier than carbonyls, because sulphur is more reactive than carbon in bitumen. The results show that during short time ageing only sulfoxides are formed and no (or few) carbonyls exist. On the contrary, carbonyls increase under long time ageing, whereas the sulfoxide index stabilises probably due to full consumption of sulphur. In this study, both short and long time ageing were considered. Therefore a Combined Ageing Index (CAI) consisting of carbonyl index and sulfoxide index was used to describe the volume average concentration of oxidation products in aged bitumen.

By using the same analytical method, the combined ageing indices of different thickness bitumen films at various ageing conditions were obtained and illustrated in Figure 4.16. The results showed that temperature plays an important role in bitumen ageing. With higher temperature, the ageing rate is higher.

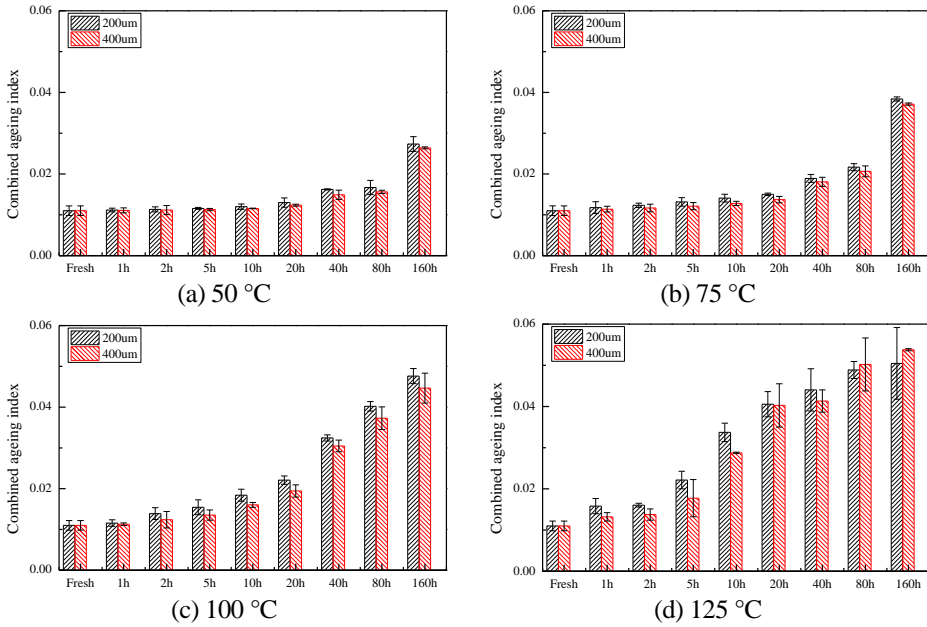


**Figure 4.16** Combined ageing index of different thickness bitumen film at various ageing conditions.

## 4.6 Model parameters determination

As described in Chapter 3, the governing equations of the diffusion and reaction systems are represented by Eq. (4.10) to Eq. (4.12).

$$\frac{\partial c_{O_2}}{\partial t} = D\nabla^2 c_{O_2} - bkc_B^m c_{O_2}^n \quad (4.10)$$

$$\frac{\partial c_B}{\partial t} = -akc_B^m c_{O_2}^n \quad (4.11)$$

$$\frac{\partial c_{op}}{\partial t} = -dkc_B^m c_{O_2}^n \quad (4.12)$$

The meaning of the notations in Eq. (4.10) to Eq. (4.12) were explained in Chapter 3, The boundary conditions for solving the governing equations are:

$$x = 0 \quad \frac{\partial c_{O_2}}{\partial x} = 0 \quad (4.13)$$

$$x = x_0 \quad c_{O_2} = c_0 \quad (4.14)$$

$$t = 0, x > 0 \quad c_{O_2} = 0 \quad (4.15)$$

$$t = 0, x > 0 \quad c_B = c_{B_0} \quad (4.16)$$

In the above equations (Eq. (4.10) to Eq. (4.16)), the following parameters need to be determined.

- Stoichiometry  $a, b, d$  and reaction order  $m, n$
- Initial concentration of reactive components  $c_0$  and  $c_{B_0}$
- Diffusion coefficient  $D$
- Reaction constant  $k$

#### 4.6.1 Stoichiometry and reaction order

Dickinson [3] and Tuffour [20] assumed the reaction between bitumen and oxygen to be first order with respect to both oxygen concentration and the concentration of reactive bitumen species. This assumption is supported by Gooswilligen et al. who found a first order dependence on concentration of bitumen [21]. Knoterus reported a reaction order of 1.6 for Venezuelan bitumen based on rates measured in a solution (toluene) after 20 hours at 50 °C [22]. In Herrington's studies on the oxidation rate of reactive bitumen species derived from two types of Venezuelan bitumen, the order of reaction was found to be slightly higher than unity (1.39 and 1.14, respectively) for short time oxidation. But for both bitumen, at longer reaction times, the reaction became first-order [23]. Recently, research from the Western Research Institute (WRI) also defined both the stoichiometry and the reaction order to be one [24, 25].

Based on the above research, an assumption that it is first order for each reactant is reasonable. Then the chemical equation and its reaction rate in Chapter 3 are rewritten as Eq. (4.17) and Eq. (4.18):



$$r = kc_Bc_{O_2} = -\frac{dc_B}{dt} = -\frac{dc_{O_2}}{dt} = -\frac{dc_{OP}}{dt} \quad (4.18)$$

Then diffusion and reaction system formulation can be rewritten as:

$$\frac{\partial c_{O_2}}{\partial t} = D\nabla^2 c_{O_2} - kc_Bc_{O_2} \quad (4.19)$$

## 4.6.2 Initial concentration of reactive components

### 4.6.2.1 Concentration of oxygen at the boundary at $t = 0$

The initial concentration of oxygen at the boundary is determined by the solubility of oxygen in bitumen. As described in Chapter 3, the solubility of the gas can be described by Henry's Law. Combining it with the Ideal Gas Law, the solubility of oxygen in bitumen (or the initial concentration of oxygen at the boundary) is written as follows:

$$c_0 = h \left( \frac{P_{O_2}}{RT} \right) \quad (4.20)$$

where,  $c_0$  is the initial concentration of oxygen at the boundary,  $P_{O_2}$  is the oxygen partial pressure at gas phase,  $T$  is the temperature,  $R$  is the universal gas constant (0.08206 atm/(K·mol/L)) and  $h$  is the dimensionless Henry's law constant. This constant  $h$  has been estimated as a function of temperature based on literature [16, 26, 27]:

$$h = h_r (1 + 0.0215(T - T_r)) \quad (4.21)$$

where,  $T_r$  is the reference temperature which is 303.15 K and,  $h_r$  is the Henry's law constant at reference temperature which is 0.0076.

For example, the Pavement Engineering laboratory of TUD is located in Delft, the Netherlands, at zero elevation, so the air pressure is nominally one atmosphere. Detailed atmospheric pressure data from our weather station were presented in Chapter 6. As 21% of air is oxygen, the oxygen

pressure is 0.21 atm. If a bitumen sample is aged in oven at 100 °C, the initial concentration of oxygen at the boundary is:

$$\begin{aligned} h &= h_r (1 + 0.0215(T - T_r)) \\ &= 0.0076 \times (1 + 0.0215 \times (100 - 30)) \\ &= 0.0190 \end{aligned} \quad (4.22)$$

$$\begin{aligned} c_0 &= h \left( \frac{P_{O_2}}{RT} \right) \\ &= 0.0190 \times \left( \frac{0.21}{0.08206 \times (100 + 273.15)} \right) \\ &= 1.31 \times 10^{-4} \text{ mol/L} \end{aligned} \quad (4.23)$$

#### 4.6.2.2 Concentration of reactive components in bitumen at $t = 0$

The initial concentration of reactive components in bitumen is defined as the concentration of reactive components in bitumen before the bitumen oxidation occurs, which is bitumen type dependent. Both in the laboratory and the field, the volume of air is sufficiently large compared with that of bitumen film. And, the diffusion rate, is much faster than the rate of bitumen oxidation in general. On the basis of the above two facts, one can assume that the concentration of oxygen in a very thin bitumen film is a constant value,  $c_{O_2}$  [14, 28]. To find the initial concentration of reactive components in bitumen, the reaction rate Eq. (4.18) can be written as below:

$$-\frac{dc_B}{dt} = k'c_B \quad (4.24)$$

where,  $k' = kc_{O_2}$  is a pseudo-first rate constant and integrating from  $t = 0$ , where  $c_B = c_{B_0}$  to time  $t$  gives

$$c_B = c_{B_0} e^{-k't} \quad (4.25)$$



From the stoichiometry of Eq. (4.17), one can note that  $c_{B_0} = c_B + c_{OP} = c_{OP_\infty}$ , where  $c_{OP_\infty}$  is the concentration of oxidation products at completion of the reaction. In other words, the concentration of reactive components in bitumen is at maximum level before bitumen oxidation starts; while no oxidation products are formed. During bitumen oxidation, the reactive components in bitumen react and form oxidation products, such as carbonyls and sulfoxides. The oxidation process stops when all the reactive components in bitumen have reacted with the oxygen available and are transformed into oxidation products. Substituting for  $c_{B_0}$  and  $c_B$  in Eq.(4.25), then

$$c_{OP} = c_{OP_\infty} (1 - e^{-kt}) \quad (4.26)$$

Since the value of  $c_{OP}$  cannot be measured directly, it can be expressed as a function of  $\Delta CAI$  (changed value of combined ageing index) as shown below:

$$c_{OP} = \alpha \Delta CAI \quad (4.27)$$

In order to verify above linear relationship between  $c_{OP}$  and  $\Delta CAI$ , samples in Table 4.4 with various ratio of fresh and aged bitumen were prepared and measured by FTIR.

**Table 4.4 Samples with various ratio of fresh and aged bitumen**

Bitumen Sample	Fresh (%)	Aged (%)
Fresh	100	0
F3A1	75	25
F1A1	50	50
F1A3	25	75
Aged	0	100

Sample preparation is a physical mixing process. Hence, the concentration of oxidation products in each sample relates to the ratio of fresh and aged bitumen inside the sample. In Table 4.4, the fraction of fresh/aged bitumen in each sample changes linearly, thus the

concentration of oxidation products in each sample changes linearly as well. If the relationship in Eq.(4.27) is valid, the combined ageing index value of each sample would satisfy a linear relationship.

By using the same analytical process in the Section 4.5, the combined ageing index of each sample was obtained by means of FTIR and plotted in Figure 4.17. It can be seen that there is a good linear relationship between the CAI value of each sample and their fresh/aged bitumen ratio, which verifies Eq. (4.27).

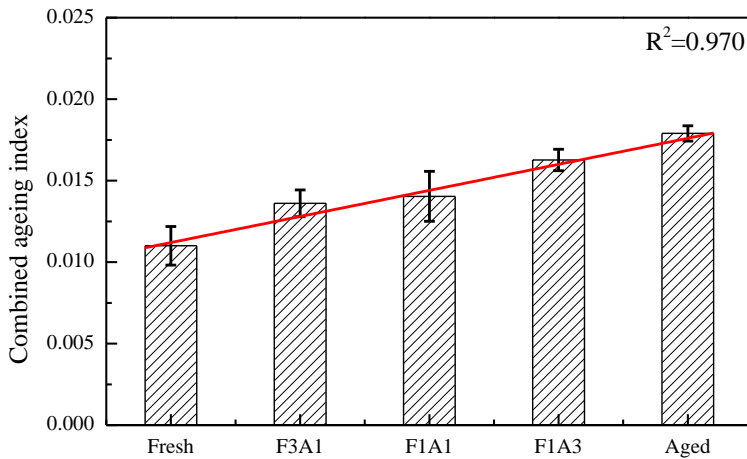


**Figure 4.17 Combined ageing index of samples with various ratio of fresh and aged bitumen.**

By applying Eq. (4.27) into Eq. (4.26), the following equation is obtained:

$$\Delta CAI = \Delta CAI_{\infty} (1 - e^{-kt}) \quad (4.28)$$

where  $\Delta CAI_{\infty}$  is the combined ageing index at completion of the reaction. Due to the fact that the value of  $\Delta CAI_{\infty}$  is only bitumen type dependent, Eq. (4.28) can be used to fit the  $\Delta CAI$  (changed value of the combined ageing index) vs time curve of 200  $\mu\text{m}$  bitumen films at various ageing temperatures with the same  $\Delta CAI_{\infty}$  value. The fitting results are shown in Figure 4.18.

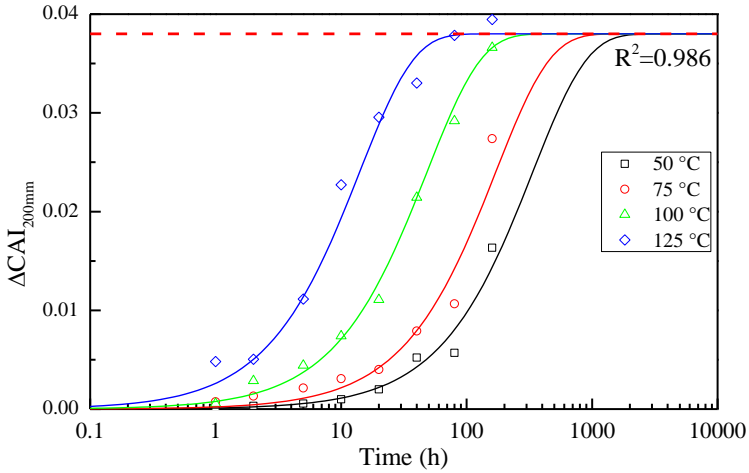


**Figure 4.18 Fitting results of Eq. (4.28) on 200  $\mu\text{m}$  bitumen films at various ageing temperatures.**

Figure 4.18 shows that the  $\Delta CAI_{\infty}$  is 0.038 for the studied bitumen. Because of  $c_{B_0} = c_{OP_{\infty}} = \alpha \Delta CAI_{\infty}$ ,  $c_{B_0}$  is  $0.038\alpha$ . For the value of  $\alpha$ , there is a further discussion in the section of the reaction constant.

### 4.6.3 Diffusion coefficient

From the FTIR results in the previous section, the changed value of the combined ageing index ( $\Delta CAI$ ) for the films with various thickness aged at 100 °C were calculated and presented in Table 4.5. The last column of the table shows their ratio.

**Table 4.5 Changed value of combined ageing index under 100 °C ageing**

Ageing time	$\Delta CAI_{200\mu\text{m}}$	$\Delta CAI_{400\mu\text{m}}$	$\Delta CAI_{200\mu\text{m}} / \Delta CAI_{400\mu\text{m}}$
Fresh	-	-	-
1	0.00027	0.00029	1.966
2	0.00260	0.00140	1.857
5	0.00444	0.00253	1.755
10	0.00740	0.00503	1.471
20	0.01108	0.00844	1.313
40	0.02144	0.01948	1.101
80	0.02920	0.02628	1.111
160	0.03459	0.03365	1.028

Table 4.5 shows that the ratio of  $\Delta CAI$  between 200  $\mu\text{m}$  and 400  $\mu\text{m}$  films was reduced from two to one, which was anticipated as described in the methodology section. Figure 4.19 illustrates the ratio of  $\Delta CAI$  between 200  $\mu\text{m}$  and 400  $\mu\text{m}$  films with increasing ageing time.

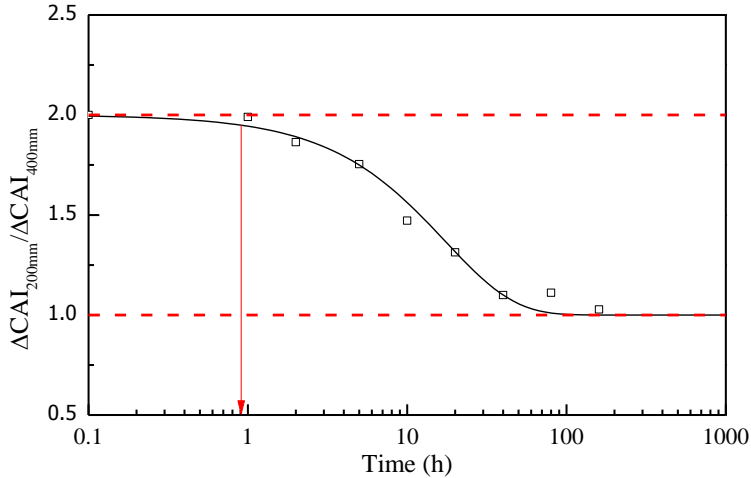


**Figure 4.19 Ratio of  $\Delta CAI$  between 200  $\mu\text{m}$  and 400  $\mu\text{m}$  films under 100 °C ageing**

In Figure 4.19, the time  $t_2$  (mentioned in methodology section) was estimated as 0.9 hours. It means that oxygen reached at the bottom of the 200  $\mu\text{m}$  depth in 0.9 hours. Utilizing this information into the Laplace transform method, in Chapter 2 (Eq. 2.64), the diffusion coefficient of oxygen was calculated to be  $5.13 \times 10^{-13} \text{ m}^2/\text{s}$ .

By using the same analysis procedure, the ratios of  $\Delta CAI$  between 200 and 400  $\mu\text{m}$  films at different ageing temperatures were summarized and plotted in Figure 4.20.

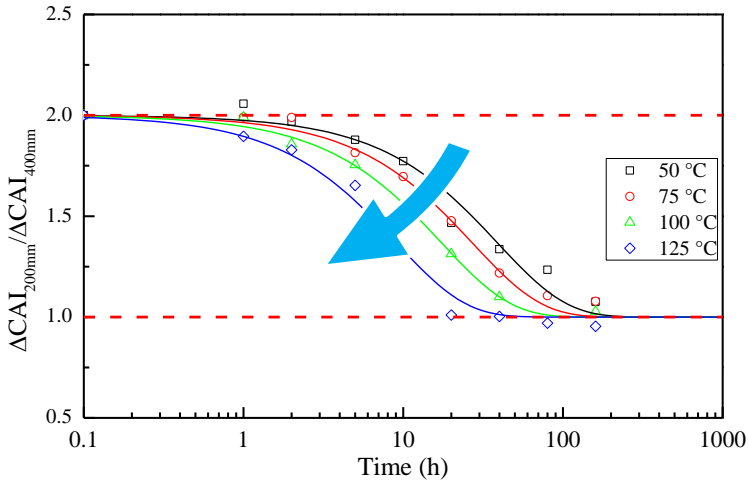


**Figure 4.20 Ratio of  $\Delta\text{CAI}$  between 200  $\mu\text{m}$  and 400  $\mu\text{m}$  films at various ageing temperature**

In Figure 4.20, the ratio of  $\Delta\text{CAI}$  between the two films at various ageing temperatures varied from two to one. The ratio curve moved from right to left with increasing temperature, as indicated by the blue arrow in the figure. This can be explained by considering that the diffusion coefficient is significantly increased with increasing temperature and oxygen needs less time to reach 200  $\mu\text{m}$  at a higher temperature. From Figure 4.20, the time  $t_2$  at each temperature was determined, thus the diffusion coefficient of oxygen was calculated, as shown in Table 4.6.

**Table 4.6 Summary of time  $t_2$  and diffusion coefficient for studied bitumen**

Ageing temperature ( $^{\circ}\text{C}$ )	Time $t_2$ (h)	Diffusion coefficient ( $\text{m}^2/\text{s}$ )
50	2.0	$2.32 \times 10^{-13}$
75	1.4	$3.31 \times 10^{-13}$
100	0.9	$5.13 \times 10^{-13}$
125	0.5	$9.25 \times 10^{-13}$

The values of oxygen diffusion coefficient obtained above have similar order of magnitude with the values reported in literatures (Table 2.1). The differences between of the obtained diffusion coefficients and the

values in literatures are caused by lots of factors, such as bitumen type, gas type and test method. In order to verify the methodology and results in this study, bitumen films with 600  $\mu\text{m}$  thickness were made and aged at 100  $^{\circ}\text{C}$  (ageing time is as same as that in Table 4.2). After ageing, the combined ageing index of bitumen was obtained by means of FTIR. Then the ratios of  $\Delta\text{CAI}$  between 200  $\mu\text{m}$  and 600  $\mu\text{m}$  films were calculated and plotted in Figure 4.21.

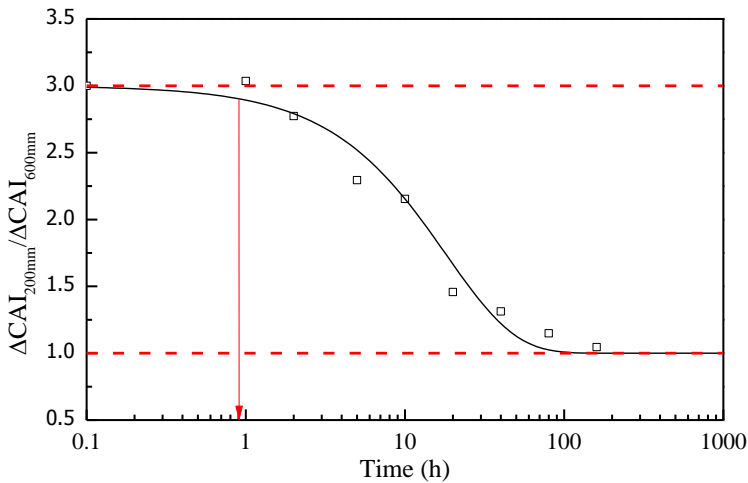


**Figure 4.21** Ratio of  $\Delta\text{CAI}$  between 200  $\mu\text{m}$  and 600  $\mu\text{m}$  films under 100  $^{\circ}\text{C}$  ageing

In Figure 4.21, the ratio of  $\Delta\text{CAI}$  between 200  $\mu\text{m}$  and 600  $\mu\text{m}$  films reduced from three to one. The time  $t_2$  is 0.93 h which is similar to that in Figure 4.19. Thus the diffusion coefficients obtained by the two experiments are similar as well. In addition, it is also confirmed that the methodology developed in this study is consistent.

### *Discussion*

Considering that the diffusion and reaction process are coupled, the question arises as to which equation should be used to calculate the diffusion coefficient, the diffusion equation (Eq. (2.7)) in Chapter 2 or the diffusion and reaction equation (Eq. (3.11)) in Chapter 3. Below are

the solutions of these two equations based on the Laplace transform method. More detailed information can be found in Chapter 2 and 3.

The solution of the diffusion equation is:

$$c = -\sum_{n=0}^{\infty} \frac{2C_0(-1)^{n+1}}{\left(n + \frac{1}{2}\right)\pi} \cos\left(\left(n + \frac{1}{2}\right)\pi \frac{x_0 - x}{x_0}\right) \left(1 - e^{-\frac{D}{x_0^2}\left(n + \frac{1}{2}\right)^2 \pi^2 t}\right) \quad (4.29)$$

The solution of the diffusion and reaction equation is:

$$c_{O_2} = -\sum_{n=0}^{\infty} \left( \frac{2DC_0\left(n + \frac{1}{2}\right)\pi(-1)^{n+1}}{D\left(n + \frac{1}{2}\right)^2 \pi^2 + x_0^2 bkc_{B_0} e^{-akc_{O_2} t}} \cdot \cos\left(\left(n + \frac{1}{2}\right)\pi \frac{x_0 - x}{x_0}\right) \left(1 - e^{-\left(\frac{D}{x_0^2}\left(n + \frac{1}{2}\right)^2 \pi^2 + bkc_{B_0} e^{-akc_{O_2} t}\right)t}\right) \right) \quad (4.30)$$

Substituting the condition at time  $t_2$  into the above equations, they give

$$c = -\sum_{n=0}^{\infty} \frac{2DC_0\left(n + \frac{1}{2}\right)\pi(-1)^{n+1}}{D\left(n + \frac{1}{2}\right)^2 \pi^2} \left(1 - e^{-\frac{D}{x_0^2}\left(n + \frac{1}{2}\right)^2 \pi^2 t_2}\right) = 0 \quad (4.31)$$

$$c_{O_2} = -\sum_{n=0}^{\infty} \frac{2DC_0\left(n + \frac{1}{2}\right)\pi(-1)^{n+1}}{D\left(n + \frac{1}{2}\right)^2 \pi^2 + h^2 bkc_{B_0}} \left(1 - e^{-\frac{1}{h^2}\left(D\left(n + \frac{1}{2}\right)^2 \pi^2 + h^2 bkc_{B_0}\right)t_2}\right) = 0 \quad (4.32)$$

In comparison with Eq. (4.31), because of the reaction part, there is an extra term (in blue colour) in Eq. (4.32), which is  $h^2 bkc_{B_0}$ . In this extra term, there are a total of four parameters, namely film thickness  $h$ , stoichiometry  $b$ , reaction constant  $k$  and initial concentration of reactive components in bitumen  $C_{B_0}$ . As the film thickness  $h$  always relates to the time  $t_2$  and the stoichiometry  $b$  is assumed to be equal to one as

discussed earlier, the sensitivity analyses were done only for the parameters  $k$  and  $C_{B0}$ .

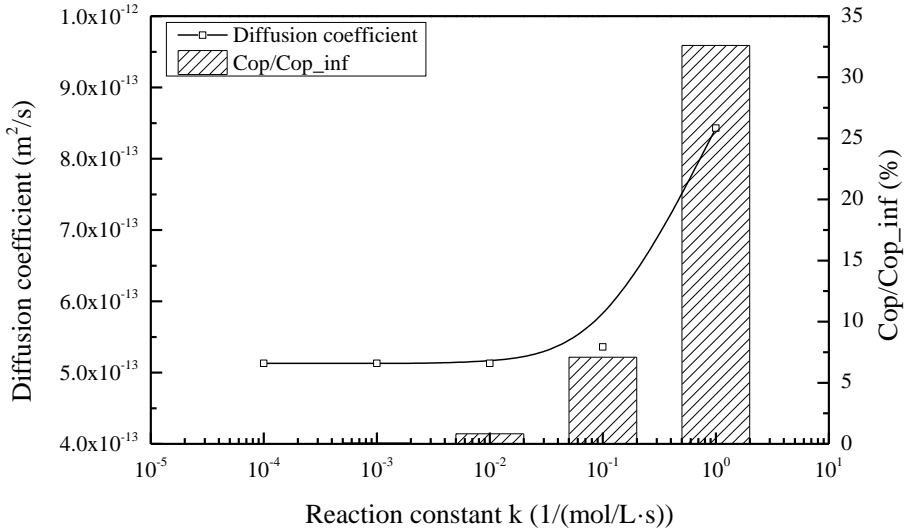


**Figure 4.22 Parameter sensitivity analysis for reaction constant**

Figure 4.22 shows the sensitivity analysis for the reaction constant  $k$  at 100 °C and assuming  $c_{B0}$  is equal to 1 mol/L. The results show that the reaction constant only has a significant influence on the results of diffusion coefficients when its value is larger than 1 (mol/L·s)<sup>-1</sup>. However, in this case, more than 30% of bitumen were aged at the same time (right column in Figure 4.22), which is in conflict with reality. In Figure 4.16 (c), it was observed that the bitumen was not aged as much as that after 1 hour of oven ageing. Therefore, the reaction constant value should be smaller than 1 (mol/L·s)<sup>-1</sup> to simulate realistic ageing times. When the reaction constant is less than 1 (mol/L·s)<sup>-1</sup>, it can be seen from Figure 4.22 that similar diffusion coefficients are obtained.



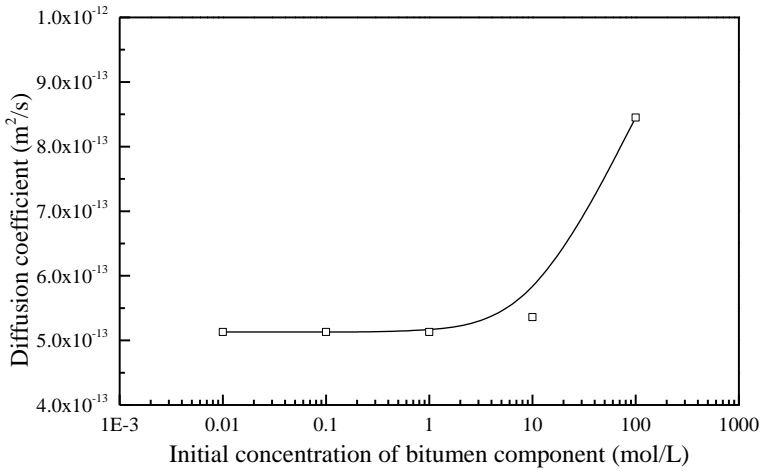


**Figure 4.23 Parameter sensitivity analysis for initial concentration of reactive components in bitumen.**

Figure 4.23 shows the results from the sensitivity analysis for the initial concentration of reactive components in bitumen at 100 °C with a reaction constant  $k$  equal to  $0.01 \text{ (mol/L}\cdot\text{s)}^{-1}$ . The results show that the initial concentration of the reactive components in bitumen has a huge effect only on the values of the diffusion coefficient when its value is larger than  $1 \text{ mol/L}$ . However, such large concentrations are in conflict with reality [29]. For example, Eq. (4.33) provides a rough calculation of bitumen concentration when the molar mass of bitumen is selected as  $750 \text{ g/mol}$ . The initial concentration of reactive components in bitumen represents the concentration of the species of bitumen that can react with oxygen. Therefore  $c_{B0}$  is much smaller than  $1.33 \text{ mol/L}$  and the diffusion coefficient values does not change at these values of  $c_{B0}$ .

$$\frac{1 \text{ mol}}{750 \text{ g}} \cdot \frac{1 \text{ g}}{1 \text{ cm}^3} \cdot \frac{1000 \text{ cm}^3}{1 \text{ L}} = 1.33 \text{ mol/L} \quad (4.33)$$

In summary, the extra term in Eq. (4.32) (in blue colour) can be neglected. Hence, Eq. (4.32) is simplified and matches Eq. (4.31). In other words, the diffusion equation can be used to calculate the diffusion coefficient.

#### 4.6.4 Reaction constant

By using all the model parameters derived from the previous sections, the reaction constant at each temperature can be obtained (Table 4.7) by fitting the  $\Delta CAI$  of 200  $\mu\text{m}$  bitumen film vs time at various ageing temperatures, as shown in Figure 4.24.

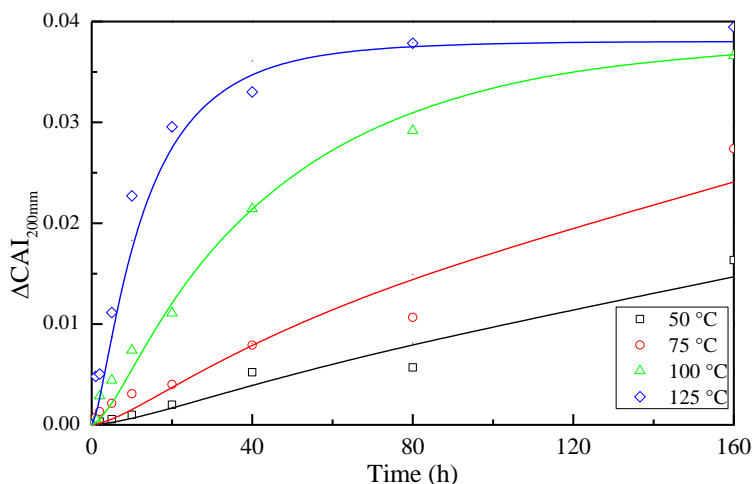


**Figure 4.24** Fitting results of diffusion and reaction system on 200  $\mu\text{m}$  bitumen films at various ageing temperatures.

**Table 4.7** Summary of reaction constant for studied bitumen

Ageing temperature (°C)	Initial concentration of oxygen (mol/L)	Initial reactive components in bitumen (mol/L)	Diffusion coefficient ( $\text{m}^2/\text{s}$ )	Reaction constant ( $1/(\text{mol/L}\cdot\text{s})$ )	$R^2$
50	$0.86 \times 10^{-4}$	$0.038\alpha$	$2.32 \times 10^{-13}$	$1.0 \times 10^{-2}$	0.951
75	$1.10 \times 10^{-4}$	$0.038\alpha$	$3.31 \times 10^{-13}$	$1.6 \times 10^{-2}$	0.938
100	$1.31 \times 10^{-4}$	$0.038\alpha$	$5.13 \times 10^{-13}$	$4.5 \times 10^{-2}$	0.993
125	$1.49 \times 10^{-4}$	$0.038\alpha$	$9.25 \times 10^{-13}$	$14.0 \times 10^{-2}$	0.985

As mentioned in Chapter 3, the relationship between reaction constant and temperature is generally expressed using the Arrhenius equation. Arrhenius plot in Figure 4.25 confirms this relationship for a 200  $\mu\text{m}$  bitumen film.

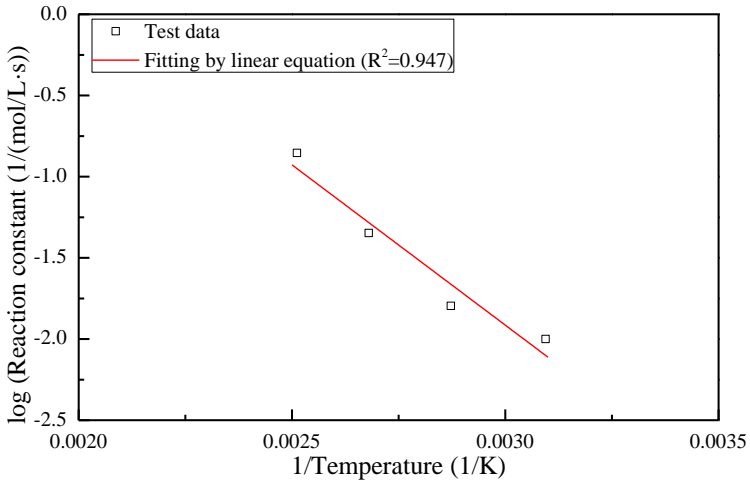


**Figure 4.25 Arrhenius plot.**

### Discussion

Here is the discussion about  $\alpha$  in the term of the initial concentration of the reactive components in bitumen.  $\alpha$  is the linear relationship factor between the concentration of the oxidation products and the combined ageing index, Eq. (4.27). Figure 4.26 is the schematic of the calculation process of the diffusion and reaction system. It shows that the combined ageing index needs to be converted to concentration in the input stage, while it is converted back in the output stage. Therefore the pre-multiplying constant  $\alpha$  is canceled out and does not influence the calculated values.

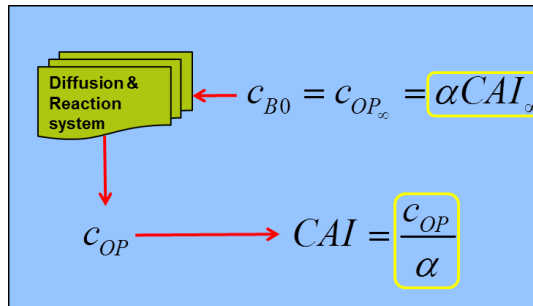


**Figure 4.26 Schematic of the calculation process of the diffusion and reaction system.**

## 4.7 Model verification

In order to verify the diffusion and reaction model, the model parameters obtained from 200  $\mu\text{m}$  bitumen films (Table 4.7) were used to calculate the values of  $\Delta\text{CAI}$  in 400  $\mu\text{m}$  bitumen films at various temperatures. By comparing the calculated results and test results, Figure 4.27 shows the overall agreement between the test results and the calculations.

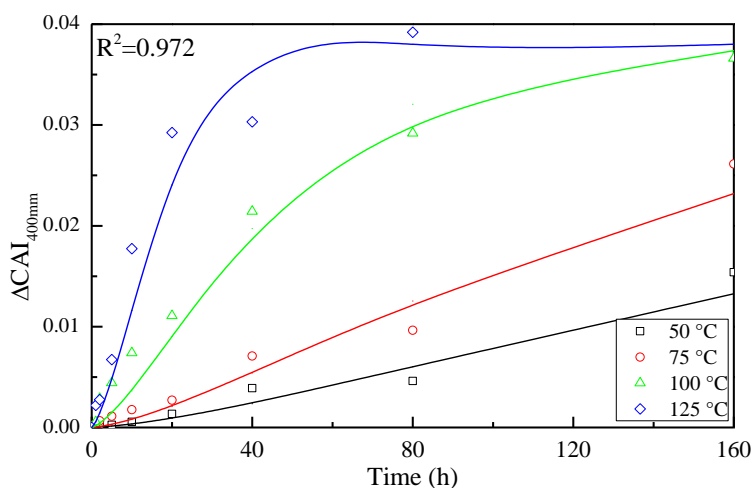


**Figure 4.27 Comparison of test results and diffusion-reaction model calculated results for a 400  $\mu\text{m}$  bitumen films at various ageing temperatures.**

## 4.8 Summary

In this Chapter, a more simple and efficient methodology has been developed, using FTIR measurements, for the determination of the parameters in the diffusion-reaction model presented in Chapter 3. By measuring the difference in chemical changes between two bitumen films with different thickness, the diffusion time that oxygen through a film can be obtained. Based on some necessary and reasonable assumptions on stoichiometry and reaction order, the diffusion coefficient and reaction constant were determined. The diffusion-

reaction model was verified using experimental results of 400  $\mu\text{m}$  bitumen films at different temperatures.

The diffusion and reaction model is used for predicting the changes of the chemical composition of bitumen. These changes are important as they dictate the performance of the bitumen. The laboratory and field tests, presented in Chapter 5 and 6, attempted to correlate the changes in the chemical properties of bitumen with its mechanical response.

## 4.9 References

1. Anderson, A.P. and K.A. Wright, *Permeability and absorption properties of bituminous coatings*. Industrial & Engineering Chemistry, 1941. **33**(8): p. 991-995.
2. Oort, W.P.V., *Durability of asphalt - It's aging in the dark*. Industrial & Engineering Chemistry, 1956. **48**(7): p. 1196-1201.
3. Dickinson, E.J., J.H. Nicholas, and S. Boas Traube, *Physical factors affecting the absorption of oxygen by thin films of bituminous road binders*. Journal of Applied Chemistry, 1958. **8**(10): p. 673-687.
4. Dorrence, S.M., F.A. Barbour, and J.C. Petersen, *Direct evidence of ketones in oxidized asphalts*. Analytical Chemistry, 1974. **46**(14): p. 2242-2244.
5. Branthaver, J.F., et al., *Binder characterization and evaluation. Volume 2: Chemistry*. 1993 [SHRP-A-368].
6. Petersen, J.C., *Asphalt oxidation -- An overview including a new model for oxidation proposing that physicochemical factors dominate the oxidation kinetics*. Fuel Science and Technology International, 1993. **11**(1): p. 57-87.
7. Petersen, J.C., P.M. Harnsberger, and R.E. Robertson, *Factors affecting the kinetics and mechanisms of asphalt oxidation and the relative effects of oxidation products on age hardening*. Preprints of Papers, American Chemical Society, Division of Fuel Chemistry, 1996. **41**(CONF-960807-).
8. Liu, M., et al., *The kinetics of carbonyl formation in asphalt*. AIChE Journal, 1996. **42**(4): p. 1069-1076.
9. Herrington, P.R., *Oxidation of bitumen in the presence of a constant concentration of oxygen*. Petroleum Science and Technology, 1998. **16**(9-10): p. 1061-1084.
10. Petersen, J.C., *A review of the fundamentals of asphalt oxidation: chemical, physicochemical, physical property, and durability relationships*. Transportation Research E-Circular, 2009(E-C140).
11. Jin, X., et al., *Fast-rate-constant-rate oxidation kinetics model for asphalt binders*. Industrial & Engineering Chemistry Research, 2011. **50**(23): p. 13373-13379.
12. Glaser, R., et al., *Low-temperature oxidation kinetics of asphalt binders*. Transportation Research Record: Journal of the Transportation Research Board, 2013. **2370**: p. 63-68.

13. Domke, C.H., R.R. Davison, and C.J. Glover, *Effect of oxygen pressure on asphalt oxidation kinetics*. Industrial & Engineering Chemistry Research, 2000. **39**(3): p. 592-598.
14. Herrington, P.R., *Diffusion and reaction of oxygen in bitumen films*. Fuel, 2012. **94**: p. 86-92.
15. Hoorn, C.B., *Durability of bitumen in theory and practice*, in *5th World Petroleum Congress*. 1959, World Petroleum Congress: New York, USA. p. 16.
16. Dickinson, E., *The diffusion controlled reaction of oxygen with films of bituminous binders*. Australian Road Research, 1984. **14**(3): p. 121-132.
17. Han, R., X. Jin, and C.J. Glover, *Oxygen diffusivity in asphalts and mastics*. Petroleum Science and Technology, 2013. **31**(15): p. 1563-1573.
18. Van den Bergh, W., *The effect of ageing on the fatigue and healing properties of bituminous mortars* (doctoral thesis). Delft University of Technology. 2011.
19. Lamontagne, J., et al., *Comparison by Fourier transform infrared (FTIR) spectroscopy of different ageing techniques: application to road bitumens*. Fuel, 2001. **80**(4): p. 483-488.
20. Tuffour, Y.A. and I. Ishai, *The diffusion model and asphalt age-hardening*. Asphalt Paving Technology, 1990. **59**: p. 73-92.
21. van Gooswilligen E. H., B.H., de Bats F. Th., *Oxidations of bitumens in various tests*. Proc. European Bitumen Conference, 1985: p. 95-101.
22. Knotnerus, J., *Bitumen durability-measurement by oxygen absorption*. Industrial & Engineering Chemistry Product Research and Development, 1972. **11**(4): p. 411-422.
23. Herrington, P.R., *Effect of concentration on the rate of reaction of asphaltenes with oxygen*. Energy & Fuels, 2004. **18**(5): p. 1573-1577.
24. Glaser, R.R., et al., *Asphalt film aging model*. Technical White Paper-WRI. 2015, Laramie, WY: Western Research Institute.
25. Glaser, R.R., et al., *Ageing master curve and ageing rate model*. Technical White Paper-WRI. 2015, Laramie, WY: Western Research Institute.
26. Hoorn, C.B., *Durability of bitumen in theory and practice*. 1959, World Petroleum Congress.
27. Prapaitrakul, N., et al., *A transport model of asphalt binder oxidation in pavements*. Road Materials and Pavement Design, 2009. **10**(sup1): p. 95-113.
28. Cui, Y., et al., *Further exploration of the pavement oxidation model – Diffusion-reaction balance in asphalt*. Construction and Building Materials, 2018. **161**: p. 132-140.
29. Lesueur, D., *The colloidal structure of bitumen: Consequences on the rheology and on the mechanisms of bitumen modification*. Advances in Colloid and Interface Science, 2009. **145**(1–2): p. 42-82.



# 5

## **EFFECT OF AGEING ON BITUMEN CHEMISTRY AND RHEOLOGY**

---



## 5.1 Introduction

The chemical and mechanical properties of bitumen, as all other type of organic substances, evolve with time. Ageing of bitumen occurs during storage, mixing, transport, laying on the road, as well as during its service life [1]. It is well known that as bitumen ages its ductility and penetration index reduce while the softening point increases [2-4]. Ultimately, the viscosity of bitumen is increased and bitumen becomes stiffer. This may lead the mixture to become excessively brittle and susceptible to raveling and cracking at lower temperatures, especially for porous mixtures [5].

Typical physical parameters of bitumen such as viscosity, penetration, softening point and ductility were first recognized by researchers as having a good correlation with ageing [6-9]. At that time, the level of ageing was expressed as a reduction in penetration, an increase in softening point or as the ratio of viscosities, always in relation with the unaged (fresh) condition [10, 11]. Recently, more and more researchers use Dynamic Shear Rheometer (DSR) to investigate the effects of ageing on the rheological properties of bitumen [12-15]. Rheology involves the study and evaluation of the time-temperature dependent behavior of materials and leads to a better knowledge of bitumen behavior that occurs when subjected to different thermal and mechanical conditions.

Chemical changes of bitumen before and after ageing include the formation of functional groups, transformation of generic fractions and changing in molecular weight. The Fourier Transform Infrared spectrometer (FTIR) is commonly used to determine the chemical characteristics of bitumen by identifying specific chemical functional groups. In the infrared spectrogram of bitumen, the absorbance bands corresponding to carbonyls and sulfoxides show a significant increase with ageing [16-18]. The peak areas at those two bands are considered as concentration measures of carbonyls and sulfoxides, respectively. The components of bitumen include four main classes of compounds:

saturates, aromatics, resin and asphaltenes. It has been shown that ageing causes a decrease of the aromatics and at the same time increases the content of resins and asphaltenes. The content of saturates changes slightly due to their inert nature to oxygen [19, 20]. Another aspect, ageing increases the molecular weight, the amount of large molecules and polydispersity of bitumen [21]. By comparing with other chemical characterization methods, FTIR is a more efficient, convenient and inexpensive tool to determine the chemical changes of bitumen.

The main objective of this Chapter is to investigate how bitumen properties change as a result of laboratory ageing. In particular, the change in the rheological properties of bitumen were evaluated by means of DSR. FTIR was utilized for both the qualitative and quantitative analysis of functional groups during the ageing process.

## **5.2 Overview of experimental program**

### **5.2.1 Materials**

This study focuses on the characterization of the chemical and rheological properties of PEN 70/100 bitumen from Q8 Oils. This bitumen was used throughout this study, as it is the bitumen commonly used for porous asphalt pavements in the Netherlands. The product specifications for PEN 70/100 were given in Table 4.1 of Chapter 4.

### **5.2.2 Ageing method and testing matrix**

First, samples were tested without the application of any ageing protocol so as to define their properties at unaged (fresh) conditions. Then, the samples were subjected to three different ageing protocols: oven ageing, RTFOT (Rolling Thin Film Oven Test) and PAV (Pressure Ageing Vessel). Oven ageing was applied for various ageing times and

temperatures, while PAV was applied for various ageing pressures. Table 5.1 summarizes the various ageing protocols that were considered.

Short-term ageing (STA) was simulated by using the RTFOT at 163 °C for 75 minutes, in accordance with the EN 12607-1 test standard. This ageing steps is considered to represent the ageing of bitumen during plant mixing, production, transportation and construction. Long-term ageing (LTA) was simulated by using PAV at 100 °C and 2.1 MPa for 20 hours, according to the EN 14769 ageing standard. This protocol is thought to simulate age hardening of bitumen during the first 5-10 years of pavement service life [22].

**Table 5.1 Ageing test program**

Ageing method	Temperature (°C)	Pressure (atm)	Ageing time (h)
Oven	100	1	20, 40, 80, 160, 320
Oven	50, 150	1	40
PAV	100	5, 10, 15, 20	40
RTFOT (STA)	Standard conditions		
RTFOT+PAV (LTA)	Standard conditions		

In this study, the forced-air oven with circulation was used, since this type of oven has better temperature uniformity, Figure 5.1(a). The RTFOT equipment, Figure 5.1(b), can hold eight glass bottles in a horizontal position. During the test, the bottles rotate in a carousel and hot fresh air is periodically injected into the bottles at a rate of 4000 ml/min. The ATS Pressure Ageing Vessel was applied for ageing bitumen at specific values of temperature and pressure, Figure 5.1(c).

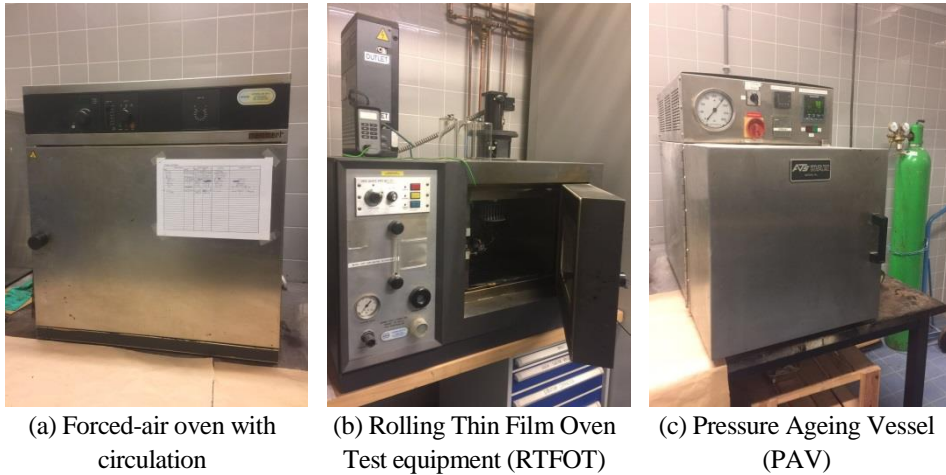


**Figure 5.1 Laboratory ageing equipment.**

### 5.2.3 Sample preparation

For each sample, 8.37 grams of bitumen were poured into an aluminium tray (73 mm in diameter) to form a thin film of 2 mm. Then the samples were placed into the oven or PAV to undergo thermal ageing, following the ageing matrix given in Table 5.1. For the standard RTFOT, 35 grams of bitumen is placed in each bottle. During the test, high temperatures lead the material to liquefy. Thus, liquid bitumen would cover the entire surface of each bottle forming a thin film. For the standard PAV tests, the bitumen firstly undergoes short-term ageing using the RTFOT. Then 50 grams of bitumen were poured into a PAV tray with a diameter of 140 mm. This quantity of bitumen forms a film of 3.2 mm thickness.

In the PAV aged samples, some bubbles may be entrapped in the surface of bitumen due to the applied high pressure. In order to remove any air bubbles and to ensure uniformity of the ageing process, the materials was stirred before been poured into a specific mould, Figure 5.2, which allows the preparation of 8 specimens with 27.5 mm diameter and 2 mm thickness. The samples were then cut into the specific geometries for the

DSR or FTIR tests. Because of the large number of samples to be tested, they were placed in the freezer during storage.



**Figure 5.2 Mould for samples preparation**

#### 5.2.4 Experimental method

The Fourier Transform Infrared Spectroscopy is able to offer quickly reliable data regarding the chemical functional groups. The tests were performed using the Spectrum 100 FT-IR spectrometer of Perkin-Elmer available in the Pavement Engineering laboratory at TU Delft. It is an attenuated total reflectance (ATR) spectrometer. The test method is based on the measurement of the beam reflected by the material. In this study, a single-beam configuration was used. The sample was scanned 20 times, with a fixed instrument resolution of  $4\text{ cm}^{-1}$ . The wavenumbers were set to vary from  $600$  to  $4000\text{ cm}^{-1}$ . The detailed analysis methodology was described in Chapter 4.

The changes in the mechanical properties of bitumen due to ageing were studied by using the DSR, Figure 5.3. The tests were performed using the Anton Paar Dynamic Shear Rheometer MCR 502 available in the Pavement Engineering laboratory at TU Delft. In order to fully characterise the mechanical response of aged bitumen, four kinds of tests were performed, namely, the amplitude sweep test, the frequency sweep

test, the relaxation test and the fatigue test. Detail information about each testing conditions, such as frequency, temperature and strain levels, is presented in the section 5.4.



**Figure 5.3 Dynamic Shear Rheometer MCR 502.**

## **5.3 Results and discussion: chemical properties**

### **5.3.1 Effect of ageing time**

The PEN 70/100 bitumen sample were aged in the oven for varying ageing periods at a temperature of 100 °C. At least three replicate samples were tested by means of FTIR at each condition to investigate the changes in their chemical properties. Figure 5.4 presents the FTIR spectra with wavenumbers less than 2000  $\text{cm}^{-1}$ , which correspond to functional groups related to the bitumen oxidation.

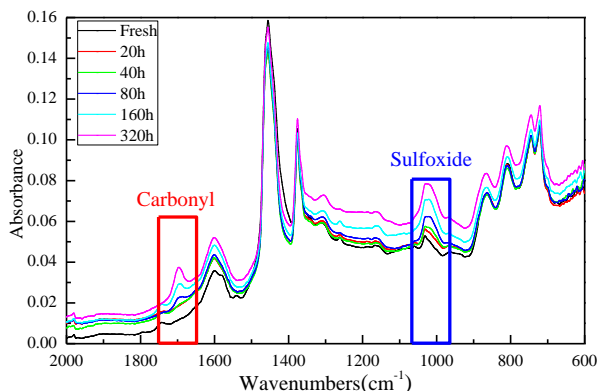


**Figure 5.4** Detail of the FTIR spectra of PEN 70/100 at different ageing times (oven ageing at 100 °C and 1 atm).

Figure 5.4 shows the high variability of the carbonyl (left red part) and sulfoxide (right blue part) functional groups. They are both increased with increasing ageing time. As explained in Chapter 4, the carbonyl and sulfoxide indices were calculated. Figure 5.5 shows the average value of three measurements.

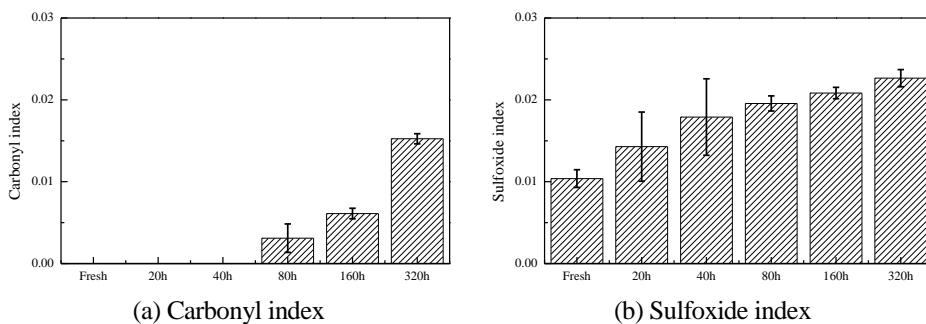


**Figure 5.5** Ageing indices of PEN 70/100 at various ageing times (oven ageing at 100 °C and 1 atm).

Figure 5.5 shows that, at the beginning of ageing (within 40 hours), the sulfoxide index significant increases with time, however no carbonyls are formed. After 40 hours of ageing, carbonyls start forming and increase with ageing time. On the other hand, the sulfoxide index increases slightly. This finding confirms previous studies that observed two different phases of ageing; a first phase were an initial increase of sulfoxides occurred and a second phase in which the increase of the

carbonyl took place [23, 24]. Figure 5.6 illustrates the evolution of the carbonyl index, sulfoxide index, and their summation (combined ageing index) with ageing time.

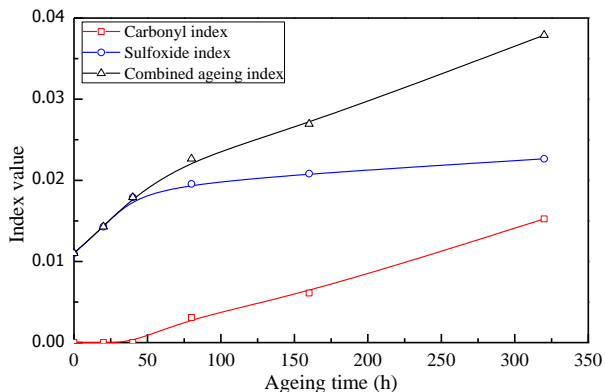


Figure 5.6 Ageing indices vs time of PEN 70/100 (oven ageing at 100 °C and 1 atm).

### 5.3.2 Effect of ageing pressure

PEN 70/100 bitumen samples subjected to PAV ageing at various pressures were tested by means of FTIR. At least three replicate samples were tested at each condition. Figure 5.7 shows the FTIR spectra of the bitumen at various ageing pressures.

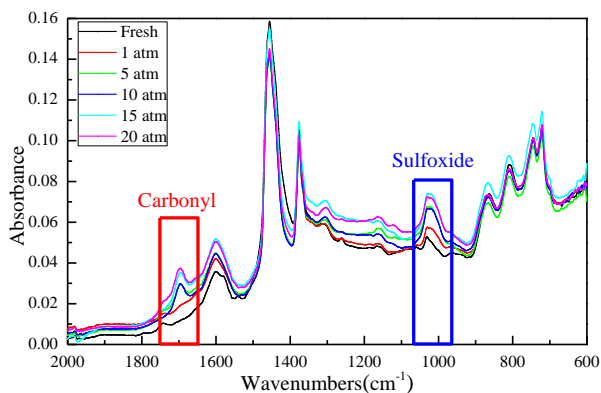
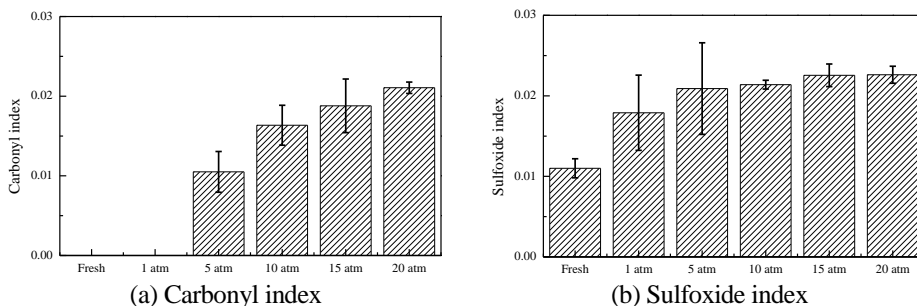


Figure 5.7 Detail of the FTIR spectra of PEN 70/100 at different ageing pressures (PAV ageing for 40 h at 100 °C).

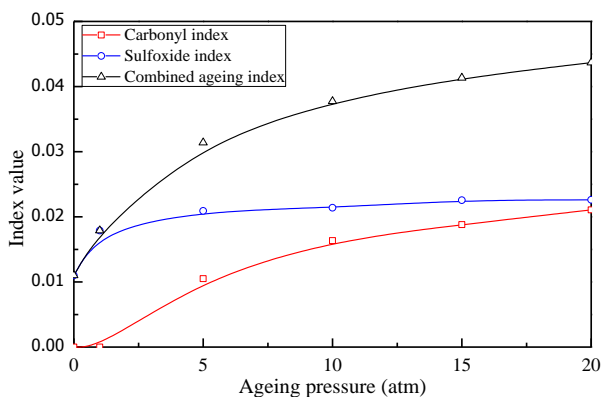


Both the carbonyl (left red part) and sulfoxide (right blue part) functional groups increased with rising pressure, Figure 5.7. The carbonyl and sulfoxide indices were calculated and shown in Figure 5.8.



**Figure 5.8 Ageing indices of PEN 70/100 at different ageing pressures (PAV ageing for 40 h at 100 °C).**

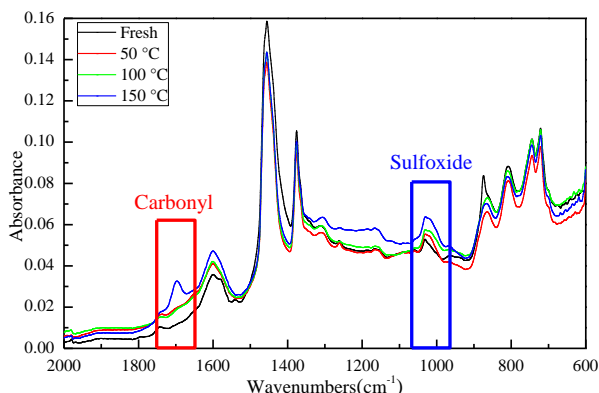
It can be observed that ageing pressure stimulates the formation of carbonyl compounds, possibly due to higher oxygen solubility in bitumen at higher pressure. The results show that no carbonyls are formed below 1 atm, while above 1 atm the carbonyls index increases with ageing pressure. In contrast, the sulfoxide index increases with ageing when at atmospheric pressure, but it shows no change in its value with increasing pressure. Figure 5.9 illustrates the carbonyl index, sulfoxide index and their summation (combined ageing index) with ageing pressure.



**Figure 5.9 Ageing indices vs pressure of PEN 70/100 (PAV ageing for 40 h at 100 °C)**

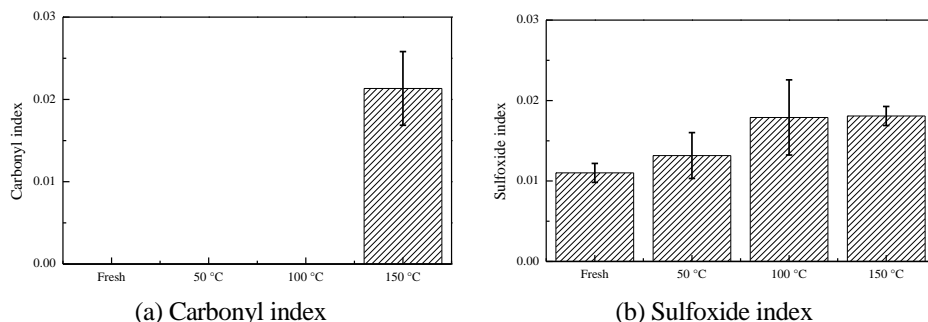
### 5.3.3 Effect of ageing temperature

Figure 5.10 shows the FTIR spectra of PEN 70/100 bitumen samples subjected to oven ageing at various temperatures for 40 hours. At least three replicate samples were tested at each condition.



**Figure 5.10 Detail of the FTIR spectra of PEN 70/100 at different ageing temperatures (oven ageing for 40 h and 1 atm).**

The results show high variability of the carbonyls (left red part) and sulfoxides (right blue part) functional groups. This can be explained by the fact that temperature has a significant influence not only on the oxidative rate but also on oxygen diffusivity and solubility in bitumen. All these parameters increase with higher temperatures, according to the Arrhenius equation and Henry's law (see Chapter 2 and 3, respectively). Figure 5.11 shows the calculated carbonyl and sulfoxide indices.



**Figure 5.11 Ageing indices of PEN 70/100 at different ageing temperatures (oven ageing for 40 h and 1 atm).**

The results show that the sulfoxide index increases with ageing temperature (at 1 atm and 40 hours), while no carbonyls are formed below 100 °C. When the temperature exceeds 100 °C the carbonyl index increases with ageing temperature, whereas the sulfoxide index remains stable. Figure 5.12 illustrates plots of the carbonyl index, sulfoxide index and their summation (combined ageing index) with ageing temperature.

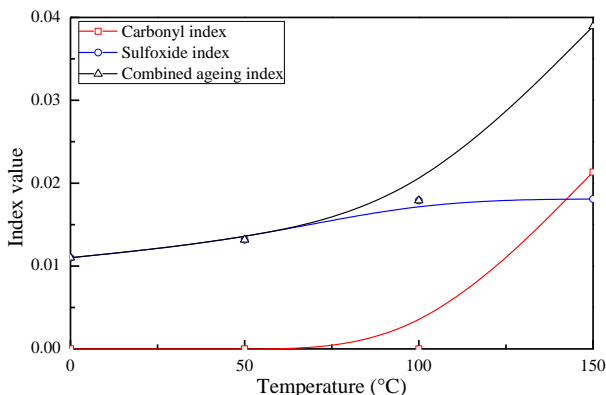


**Figure 5.12 Ageing indices vs temperature of PEN 70/100 (oven ageing for 40 h and 1 atm).**

From Figure 5.6, Figure 5.9 and Figure 5.12, it can be observed that sulfoxides are formed earlier than carbonyls at any ageing condition. This is because sulphur is more reactive than carbon in bitumen. Another observation is that under short-term ageing only sulfoxides are formed and increase further, while no (or few) carbonyls are formed. On the contrary, carbonyls increase under long-term ageing, whereas the sulfoxide index is stable probably due to the full consumption of sulphur. Comparing Figure 5.6, Figure 5.9 and Figure 5.12, it can be observed that temperature is the most influential parameters for ageing, because of the fact that the ageing reaction rate increases with temperature based on the Arrhenius equation.

The rate at which ageing occurs not only depends upon the rate of oxygen diffusion into bitumen but also on the rate at which bitumen oxidation takes place, according to the diffusion and reaction model.

Figure 5.13(a) and (b) illustrate the schematic of sensitivity analysis of each ageing factor (ageing time, pressure or temperature) for the diffusion rate and reaction rate, respectively. They clearly show that the ageing temperature dramatically changes the diffusion and the reaction rate, following an exponential growth trend following Arrhenius equation. Due to the fact that the diffusion rate is one of the basic physical properties of a material, it is not be affected by ageing time and ageing pressure, Figure 5.13(a). The reaction rate is a chemical property of the material. It increases linearly with ageing pressure following Henry's law, while it decreases exponentially with ageing time due to the consumption of the bitumen during ageing, Figure 5.13(b).

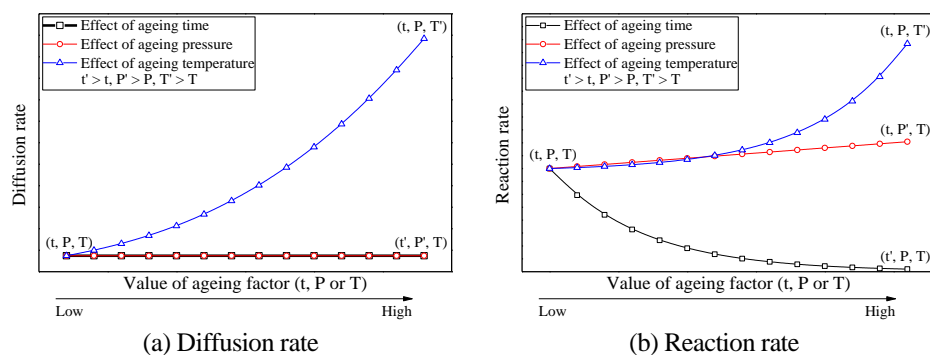


**Figure 5.13 Sensitivity analysis of ageing factor (time, pressure or temperature) for diffusion rate and reaction rate.**

### 5.3.4 Comparison and discussion

The PEN 70/100 bitumen samples were aged at standard ageing conditions, namely short-term ageing (STA) simulated by RTFOT and long-term ageing (LTA) simulated by RTFOT followed by PAV. Three replicate samples were tested by means of FTIR at each condition. Figure 5.14 shows the carbonyl and sulfoxide indices at fresh, short-term aged and long-term aged state.

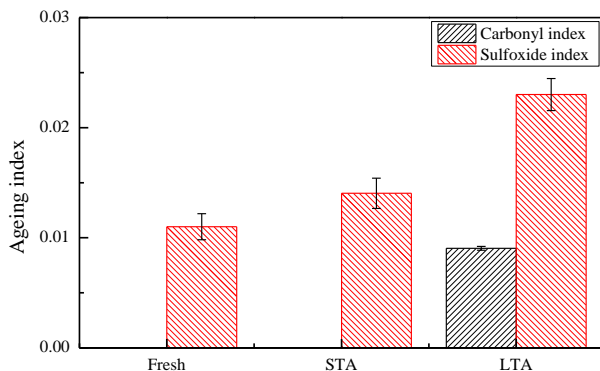
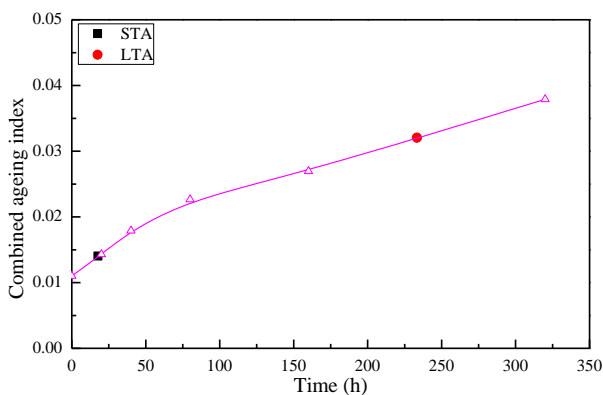
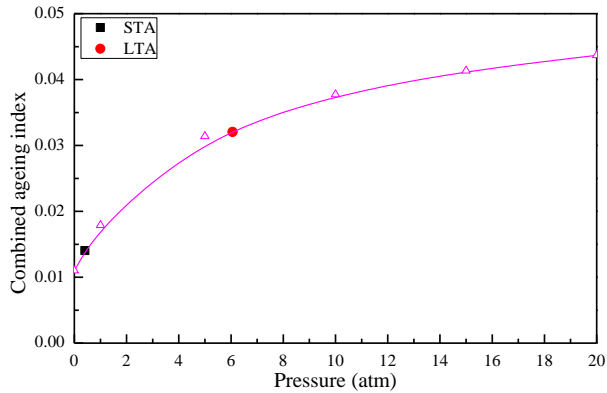


**Figure 5.14** Ageing indices of PEN 70/100 at standard ageing conditions.

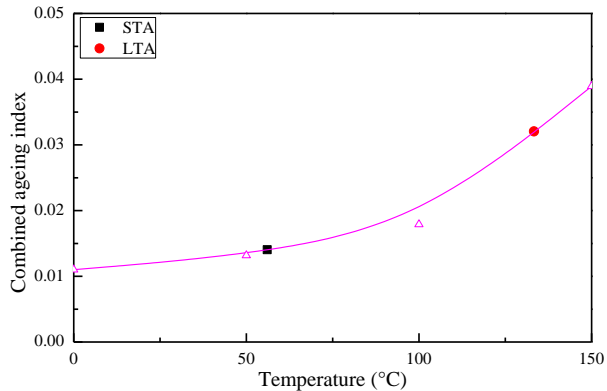
Figure 5.14 shows that the sulfoxide index slightly increases, while no carbonyls are formed after standard short-term ageing. However, both the carbonyl and sulfoxide indices increase significantly after standard long-term ageing. In order to compare the effect of the various ageing conditions on bitumen chemistry with that of the standard ageing protocols, the CAI (combined ageing index) value of STA and LTA aged samples is plotted in Figure 5.15.



(a) Different ageing time (oven ageing at 100 °C and 1 atm).



(b) Different ageing pressures (PAV ageing for 40 h at 100 °C).



(c) Different ageing temperatures (oven ageing for 40 h at 1 atm).

**Figure 5.15 Comparison of standard ageing protocols (STA and LTA) with various ageing conditions**

As mentioned in Chapter 3, the ageing rate of bitumen is influenced by a number of factors, such as time, pressure and temperature. In other words, different ageing conditions can be interrelated with each other. By using the different combinations of time, pressure and temperature, combined ageing index of bitumen can reach a specific value. Therefore, it is important to find some certain combinations that can simulate short/long-term field ageing well. And some of this combinations may provide an easier, cheaper and less time consuming options to replace the standard ageing by RTFOT and PAV. On observing the above results, the time, pressure and temperature required in each ageing condition to simulate STA and LTA ageing can be obtained, Table 5.2.

**Table 5.2 The requirement of time, pressure and temperature to simulate the standard STA and LTA**

Temperature (°C)	Pressure (atm)	Ageing time (h)	Standard ageing protocol
100	1	18	
100	0.4	40	STA
56	1	40	
100	1	233	
100	6	40	LTA
133	1	40	

The effect of STA on bitumen chemistry is equal to that of oven ageing at 100°C and 1 atm for 18 hours (Figure 5.15(a)) or ageing under the pressure of 0.4 atm at 100°C for 40 hours (Figure 5.15(b)), and or oven ageing at 56°C and 1 atm for 40 hours (Figure 5.15(c)). Similarly, the effect of LTA on bitumen chemistry is equal to that of oven ageing at 100°C and 1 atm for 233 hours (Figure 5.15(a)) or oven ageing at higher pressure of 6 atm at 100°C for 40 hours (Figure 5.15(b)), and or oven ageing 133°C and 1 atm for 40 hours (Figure 5.15(c)).

## 5.4 Results and discussion: mechanical properties

### 5.4.1 Amplitude sweep test

The amplitude sweep test is utilized in order to distinguish the linear and nonlinear viscoelastic response of bitumen. The test is conducted at constant temperature and frequency with an increasing amplitude (stress/strain). The relationship between stress and strain for typical bituminous materials is shown in Figure 5.16.

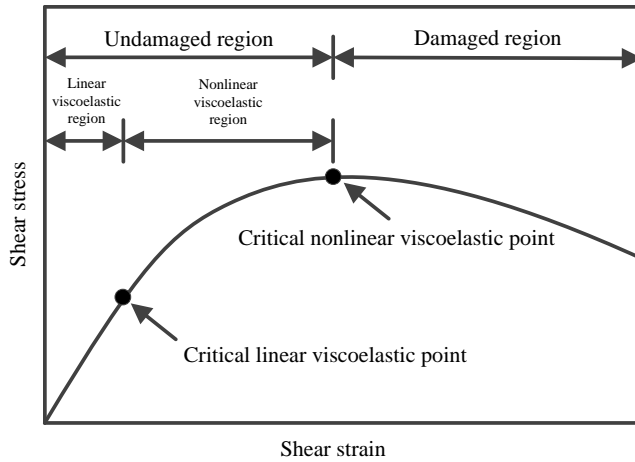


**Figure 5.16 Shear stress vs shear strain for typical bituminous materials**

As the stress/strain level increases, the bituminous material passes through the linear viscoelastic phase to the nonlinear viscoelastic phase and then to the damage phase. Beyond the critical nonlinear viscoelastic point, the mechanical properties of the bituminous materials change: the complex shear modulus decreases and the phase angle increases.

In this study, the stress/strain sweep was performed using the DSR at a fixed temperature of 20 °C and the frequency of 10 Hz. The shear stress varied linearly from 0 to 1000 kPa for the stress-controlled mode, while the shear strain varied linearly from 0 % to 100 % for the strain-controlled mode. The tests are stopped automatically when the complex shear modulus drops to 1 MPa. The bitumen samples were tested using the parallel-plates configuration with 8 mm plate diameter and 2 mm gap. Three repetition tests were done at each condition. The stress-strain curve of each aged sample is shown in Figure 5.17.



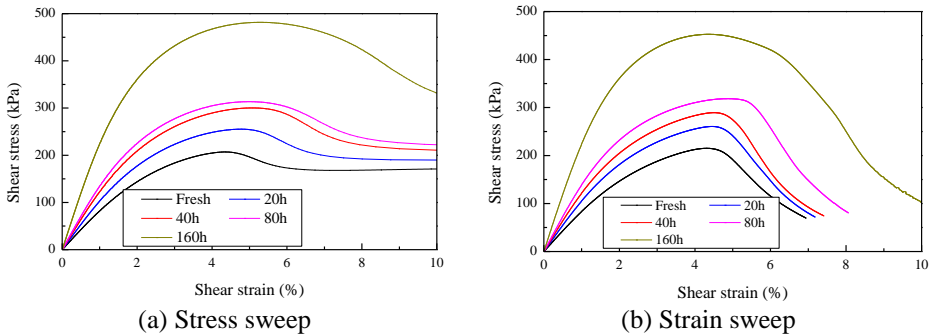


**Figure 5.17 Shear stress vs shear strain of PEN 70/100 with various ageing times**

From Figure 5.17, it can be observed that, in both control modes, the shear stress increases with increasing shear strain and reaches to a maximum value at about 5% shear strain. The slope within the 5% shear strain range increases with ageing.

By comparing Figure 5.17(a) and (b), a significant difference can be observed. For the stress-controlled mode, the shear strain increases linearly with shear stress at the beginning; then as the applied shear stress increases nonlinearity becomes more apparent after the applied shear stress attains a maximum value, it starts degrading due to the accumulation of progressive damage in the sample. For the strain-controlled mode, the shear stress increases linearly with shear strain at the beginning; then the shear stress increases slower and slower which indicates that the response of bituminous materials is in the nonlinear viscoelastic range; when the applied strain increases to a certain level, the shear stress of materials reaches a maximum; after that the shear stress decreases continuously due to the built up of damage.

Based on the stress-strain curve, the results of complex shear modulus and phase angle for the two control modes were calculated and shown in Figure 5.18 and Figure 5.19, respectively.

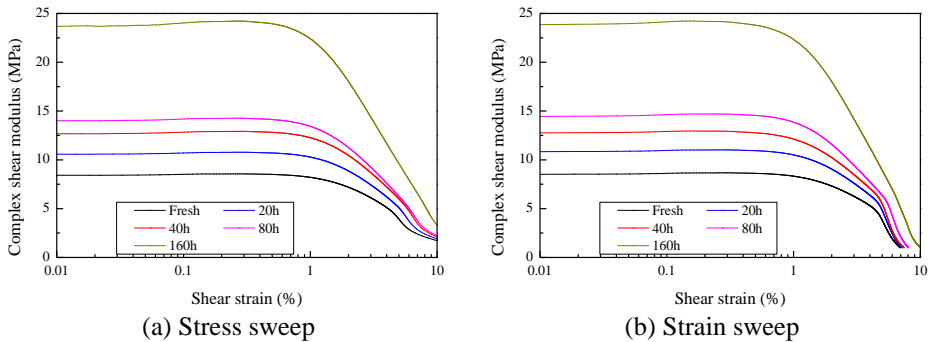


**Figure 5.18** Complex shear modulus vs shear strain of PEN 70/100 with various ageing times

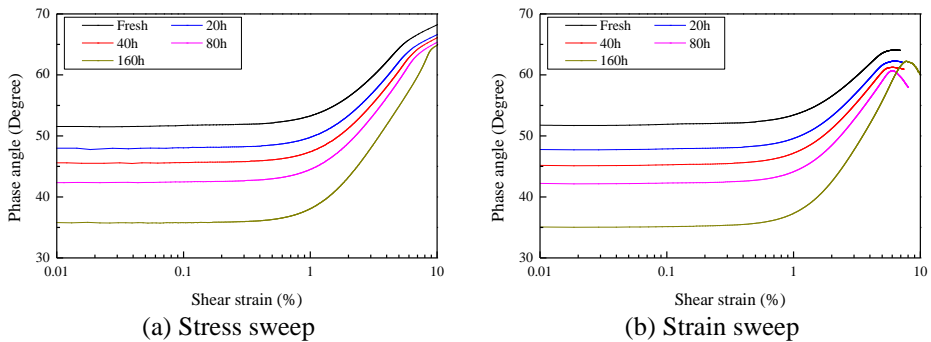


**Figure 5.19** Phase angle vs shear strain of PEN 70/100 with various ageing times

In Figure 5.18 and Figure 5.19, for both control modes, the strain amplitude of 1 % causes the bitumen to respond in the linear range of viscoelastic behaviour. The critical linear viscoelasticity point is defined as the point that a 95% reduction in the initial complex shear modulus occurs [25, 26]. After this point, the response of bitumen is in the nonlinear viscoelastic range, in which the complex shear modulus decreases and the phase angle increases, respectively. The changes of the critical linear viscoelasticity point after ageing in both control modes are shown below.

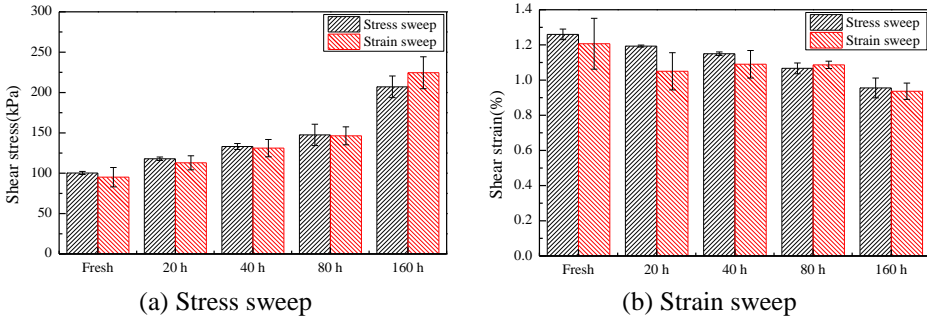


**Figure 5.20 Critical linear viscoelastic points at various ageing times**

Figure 5.20 shows that the values (stress or strain) of the critical linear viscoelasticity point at same ageing condition are similar for both control modes, which confirms the fact that that different control modes have no influence on the linear viscoelastic region [27]. The results show that ageing definitely has an effect on the linear visco-elastic limits of the material. Comparing with fresh bitumen, aged bitumen has lower linear limits for strain, whereas it has higher linear limits for stress. For the other two ageing conditions (different strain pressure and temperature), the same conclusion can be derived, Figure 5.21 and Figure 5.22.

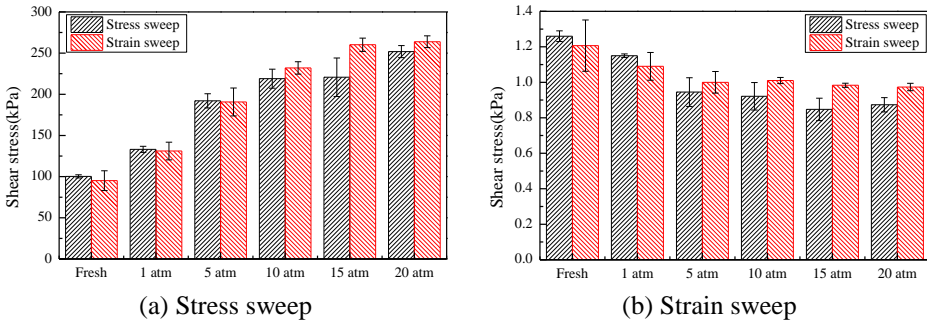


**Figure 5.21 Critical linear viscoelastic points at various ageing pressures**

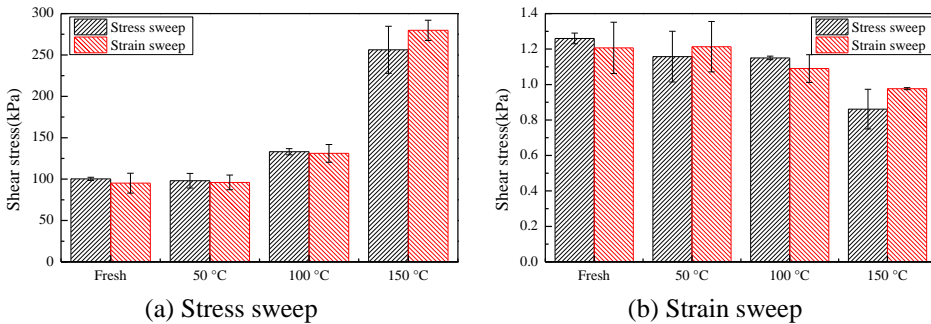
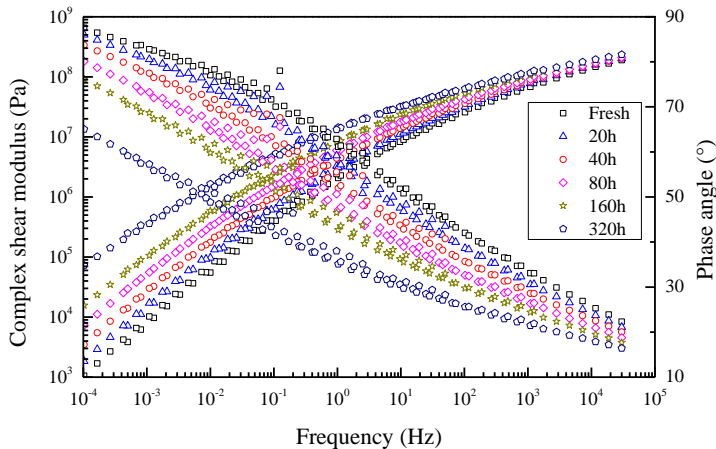


**Figure 5.22 Critical linear viscoelastic point at various ageing temperatures**

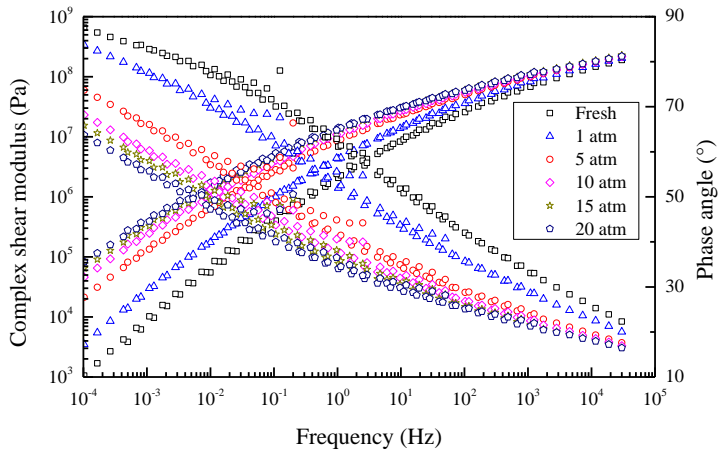
### 5.4.2 Frequency sweep test

The frequency sweep test is used to determine the rheological response of linear viscoelastic materials over a large range of temperatures and frequencies. Based on the linear viscoelastic strain range of bitumen samples, determined using the above mentioned amplitude sweep tests, the frequency sweep tests were performed at five different temperatures (0, 10, 20, 30 and 40 °C). During the tests the frequency varied in a logarithmic manner from 50 Hz to 0.01 Hz.

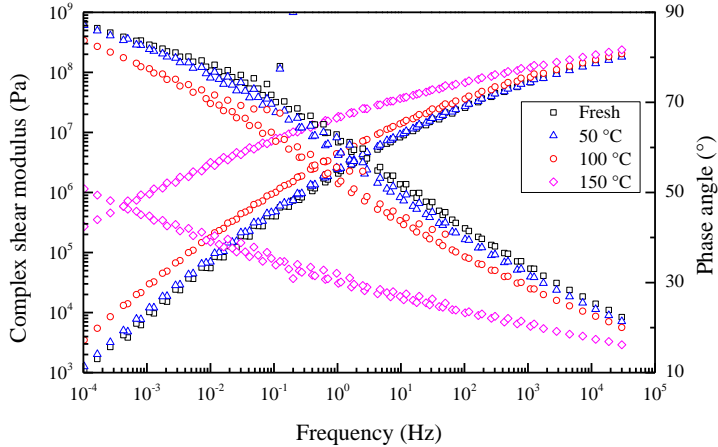
The PEN 70/100 bitumen samples were tested by means of the DSR after the application of the various ageing protocols. At least three replicate samples were tested at each condition. Based on the Time-Temperature Superposition (TTS) principle, master curves of the complex shear modulus and the phase angle were generated at a reference temperature of 20 °C. Figure 5.23 shows the evolution of the rheological characteristics of bitumen with increased ageing time, temperature and pressure.



(a) Different ageing times (oven ageing at 100 °C and 1 atm).



(b) Different ageing pressures (PAV ageing for 40 h at 100 °C).



(c) Different ageing temperatures (oven ageing for 40 h at 1 atm).

**Figure 5.23** Master curve at 20 °C of PEN 70/100 at different ageing conditions.

In Figure 5.23, the observed differences are more pronounced at low frequencies, while they become less pronounced at higher frequencies at which the material behaves more elastically. Specifically, the variation of complex modulus between fresh and aged materials was about two orders of magnitude at low frequencies. Moreover, at the highest frequency, all samples tend to reach a value of  $10^8$  Pa. On the contrary, the phase angle differs substantially for the whole frequency range. By comparing Figure 5.23(a), (b) and (c), it can be observed that small changes in the ageing time and pressure do not generate large differences

of the master curve. In the other words, the temperature is the most influential parameters for ageing.

Figure 5.24 and Figure 5.25 show a comparison between the effect of the various ageing protocols and standard ageing protocols on bitumen rheology. The corresponding relationship between standard ageing conditions and various other ageing conditions is similar to that given by aforementioned section of bitumen chemistry. In other words, similar chemical composition as a result of different ageing protocols results to similar mechanical properties. It is an important confirmation that the relationship between bitumen chemistry and rheology does exist. For example, in Figure 5.15(a) and Figure 5.24, STA and oven ageing at 100 °C for 20 hours give both similar combined ageing index (CAI) values and rheological results and, in Figure 5.15(b) and Figure 5.25, LTA and PAV ageing at 5 atm and 100 °C for 40 hours give both similar CAI values and rheological results. In addition, it is evident that different ageing methods can be used to appropriately obtain similar rheological results with the STA and LTA aged samples.

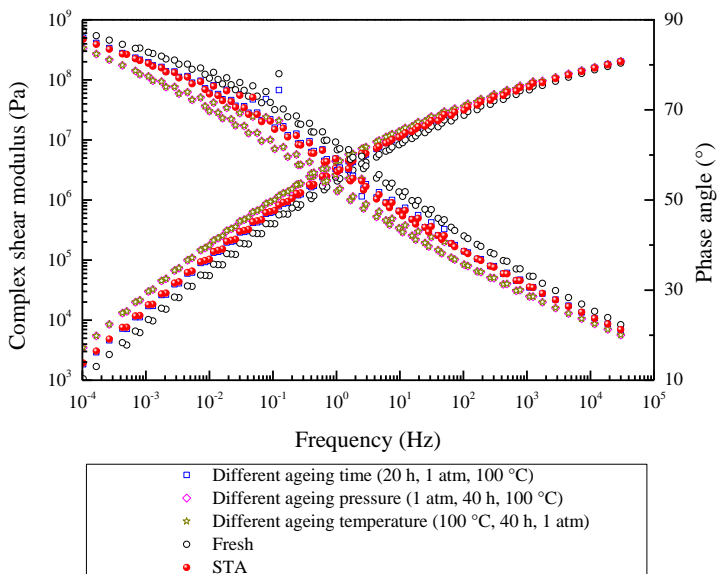


**Figure 5.24 Comparison between standard short term ageing (STA) with various ageing conditions.**

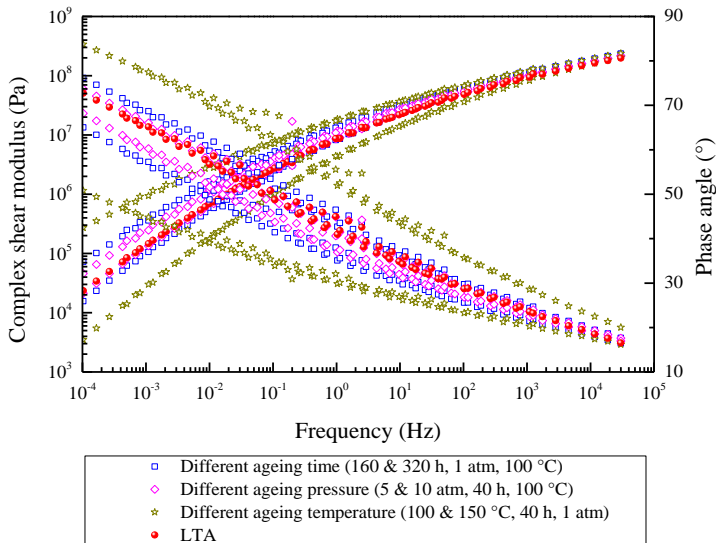
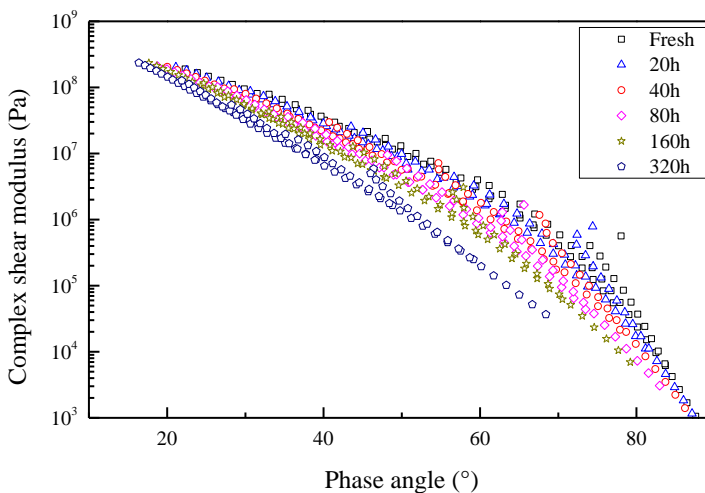
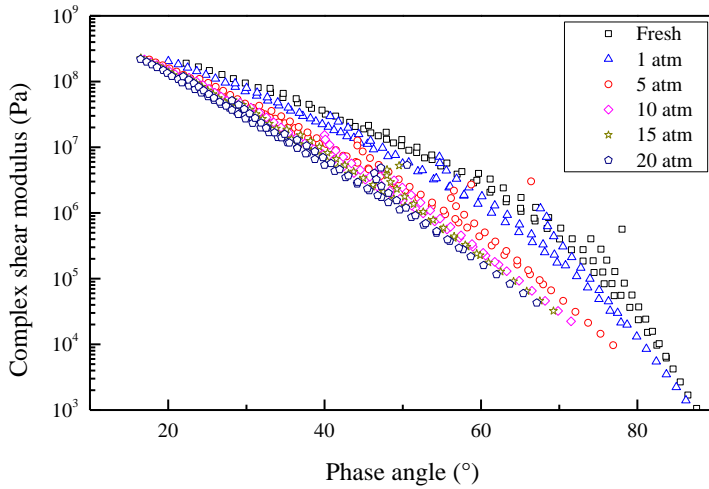


**Figure 5.25 Comparison between standard long term ageing (LTA) with various ageing conditions.**

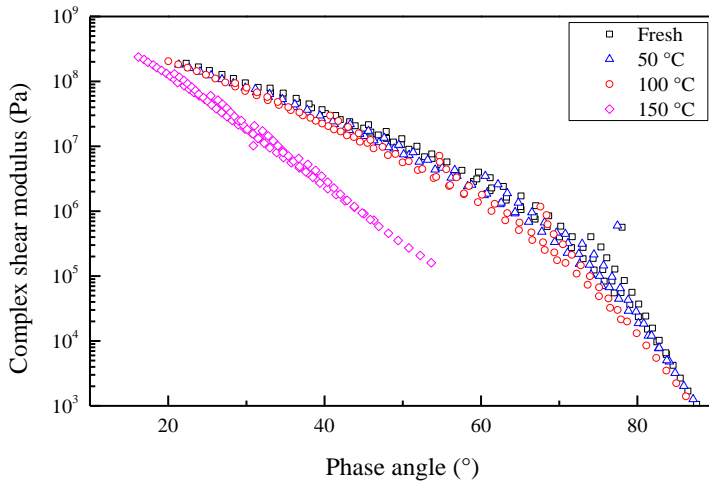
The rheological changes of bitumen due to ageing time were selected and plotted as Black diagrams [28] in Figure 5.26. The effect of ageing is seen as a shift of the Black diagram curves towards lower phase angles; in the meantime the shape of the curves changes to a straight line and the curvature reduces. The stiffness increases and phase angle decreases denote a tendency towards a more brittle material response.



(a) Different ageing times (oven ageing at 100 °C and 1 atm).



(b) Different ageing pressures (PAV ageing for 40 h at 100 °C).



(c) Different ageing temperatures (oven ageing for 40 h at 1 atm).

**Figure 5.26 Black diagram for bitumen at different ageing conditions.**

One of the most commonly used methods for characterizing the viscoelastic fluid to solid transitional behaviour is the crossover frequency, Figure 5.27(a), of the storage shear modulus and the loss shear modulus [29], that is the frequency when the phase angle is  $45^\circ$ . The complex shear modulus corresponding to the crossover frequency is named the crossover modulus, Figure 5.27(b). Lower crossover frequency suggests bitumen has higher molecular mass [30, 31], longer relaxation time and higher softening point [32], while lower crossover



modulus denotes it has wider molecular mass distribution and higher polydispersity [31, 33]. The crossover frequency and modulus for all samples are represented in Figure 5.28 and Figure 5.29, respectively. The results shows that aged bitumen has lower crossover frequency and lower crossover modulus than fresh bitumen at reference temperature

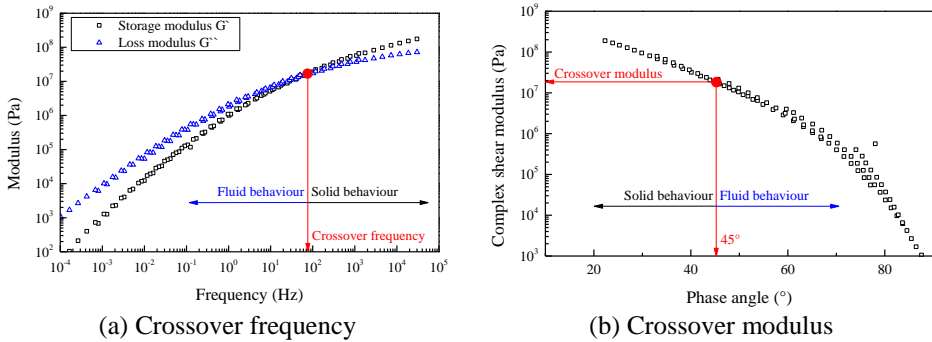


Figure 5.27 Schematic of crossover frequency and crossover modulus.

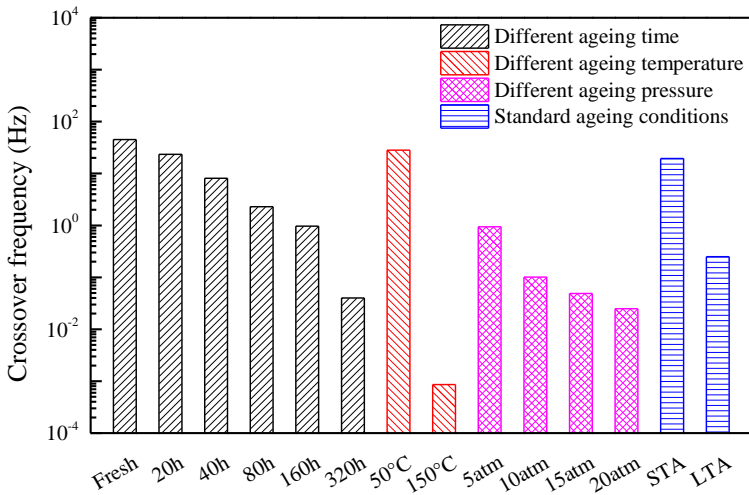
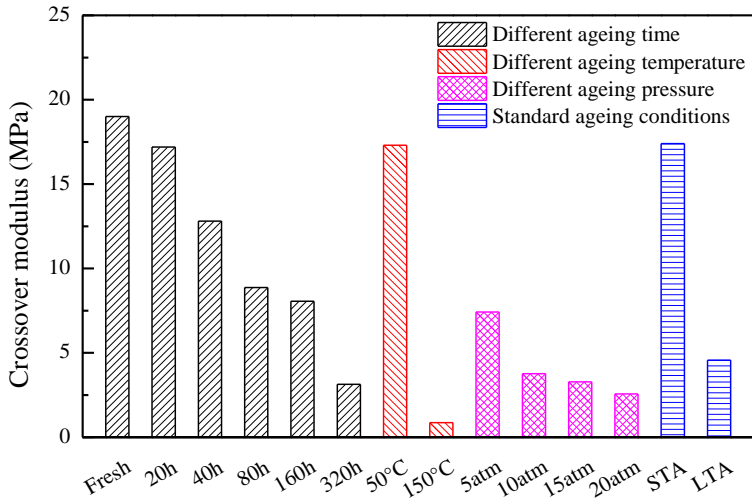
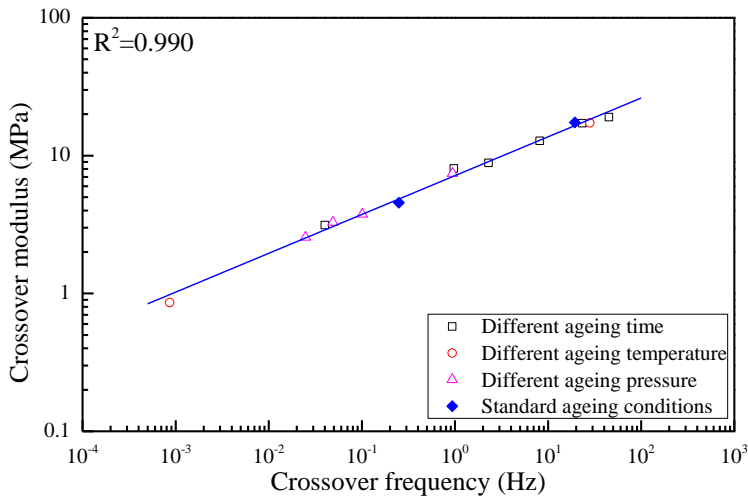


Figure 5.28 Crossover frequencies of bitumen at different ageing conditions.



**Figure 5.29 Crossover modulus of bitumen at different ageing conditions.**

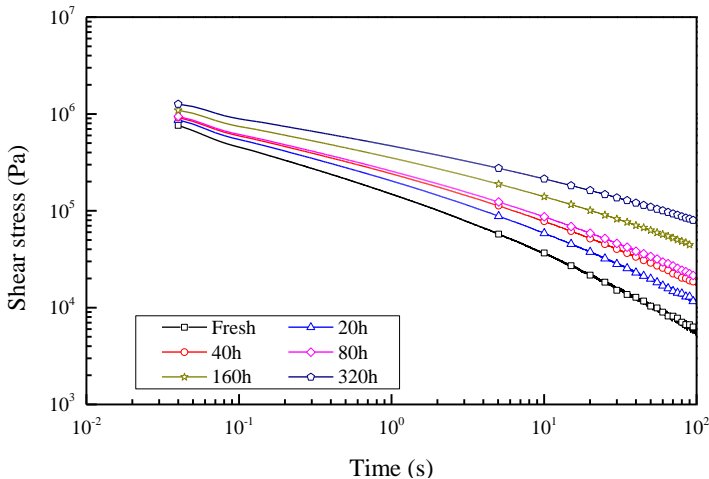
Chambon and Winter have shown that there exists a good logarithmic relationship between crossover frequency and crossover modulus for the same type of polymers [34, 35]. The findings of this research validate this statement for the studied bitumen, as shown in Figure 5.30.



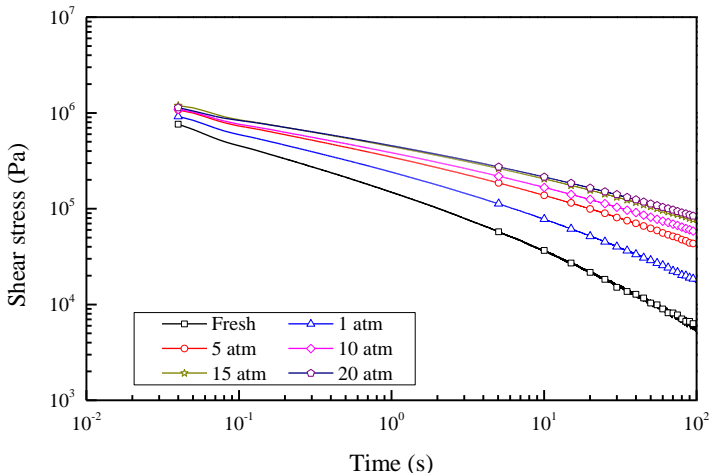
**Figure 5.30 Crossover modulus vs crossover frequency of bitumen at different ageing conditions.**

### 5.4.3 Relaxation test

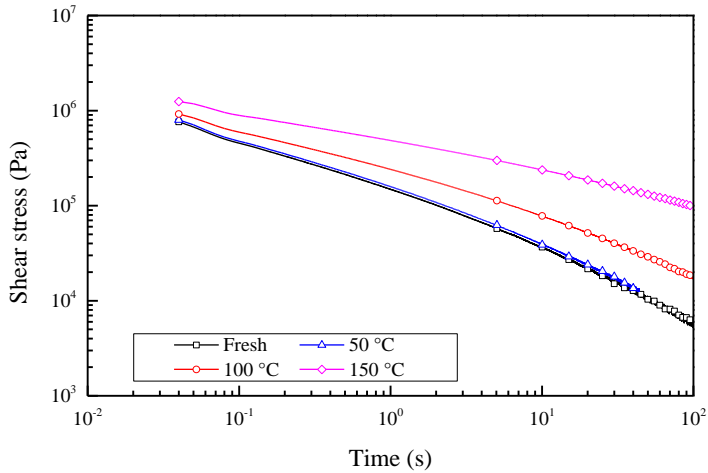
After the application of various ageing protocols, the bitumen samples were tested using the parallel-plates configuration with 8 mm plate diameter and 2 mm gap at 0 °C. The relaxation tests were performed with 1 % shear strain (in 0.04 seconds) at the beginning, followed by a relaxation period of 100 seconds. The frequency of data collection was 100 Hz. A minimum of three replicate samples for each ageing condition were tested. Figure 5.31 shows the relationship between shear stress and relaxation time with increased ageing time, temperature and pressure.



(a) Different ageing times (oven ageing at 100 °C and 1 atm).



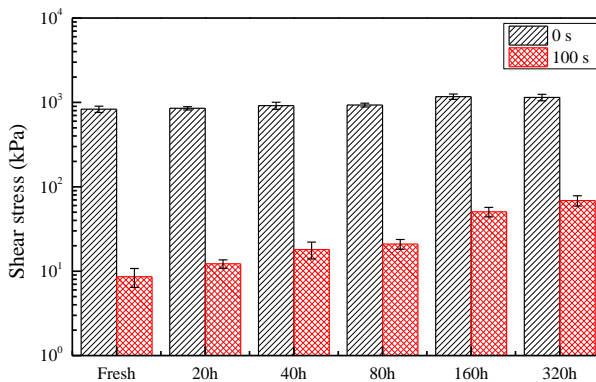
(b) Different ageing pressures (PAV ageing for 40 h at 100 °C).



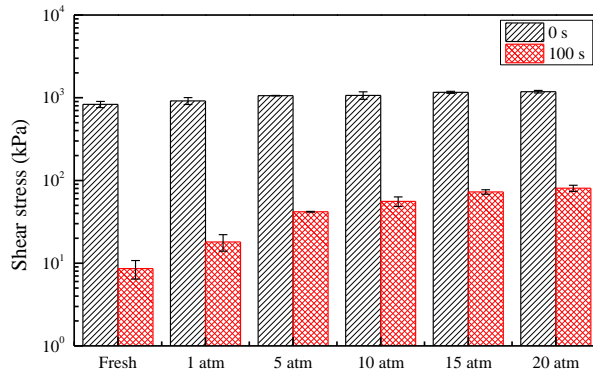
(c) Different ageing temperatures (oven ageing for 40 h at 1 atm).

**Figure 5.31 Relaxation curves of PEN 70/100 at different ageing conditions.**

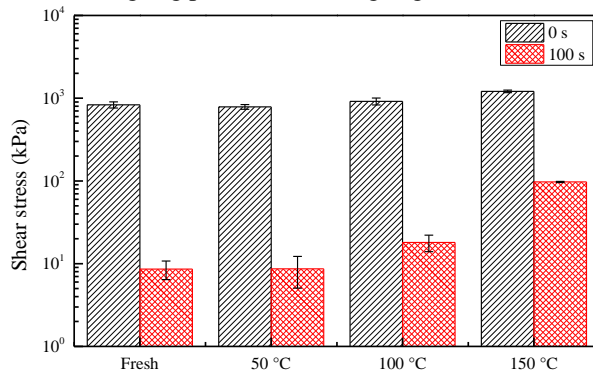
Figure 5.31 shows there is a good power law between shear stress and relaxation time. The relaxation curve moves up with ageing indicating that at the same relaxation time, the residual shear stress of bitumen increases with ageing as a result of the relaxation modulus increasing with ageing. In order to further analyse the relaxation properties of aged bitumen, the absolute values of shear stress at 0 s and 100 s are plotted in Figure 5.32, which denote the stress state of bitumen at the initial and at the end time.



(a) Different ageing times (oven ageing at 100 °C and 1 atm).



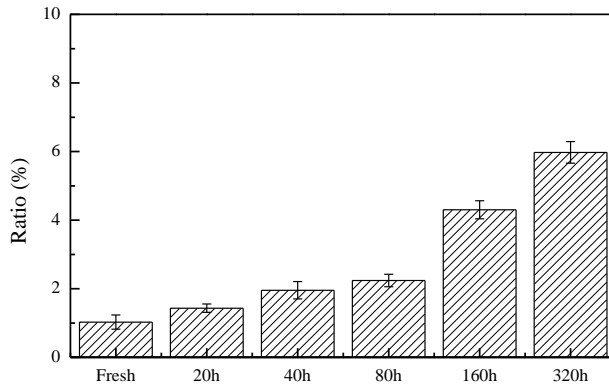
(b) Different ageing pressures (PAV ageing for 40 h at 100 °C).



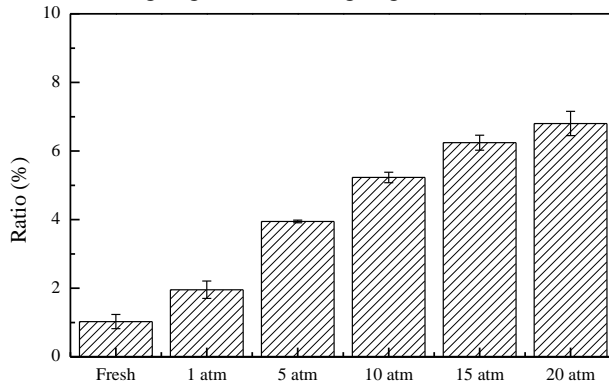
(c) Different ageing temperatures (oven ageing for 40 h at 1 atm).

**Figure 5.32 Shear stress of PEN 70/100 at 0 s and 100s.**

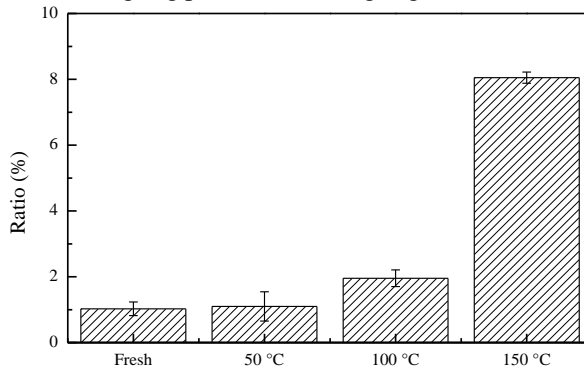
In Figure 5.32, the initial shear stress (at 0 s) of bitumen samples subjected to different ageing conditions are in the order of 1000 kPa. The initial shear stress of the most highly aged sample (320 h, 150 °C or 20 atm) is about 1.4 times larger than that of fresh bitumen. However, after a relaxation period of 100 s, the shear stress of the 320 h aged sample, the 150 °C aged sample and the 20 atm aged sample was still 68.73 kPa, 97.29 kPa and 80.63 kPa, respectively, which is more than 10 times larger than that of fresh bitumen. Hence, the residual shear stresses after the same relaxation time are higher for the aged samples. Figure 5.33 shows the ratio of residual shear stress (at 100 s) versus the initial shear stress (at 0 s).



(a) Different ageing times (oven ageing at 100 °C and 1 atm).



(b) Different ageing pressures (PAV ageing for 40 h at 100 °C).

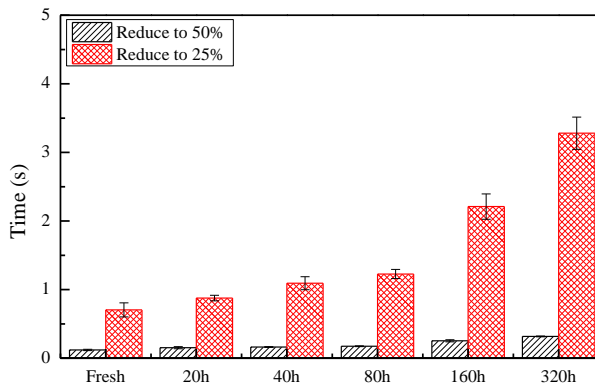


(c) Different ageing temperatures (oven ageing for 40 h at 1 atm).

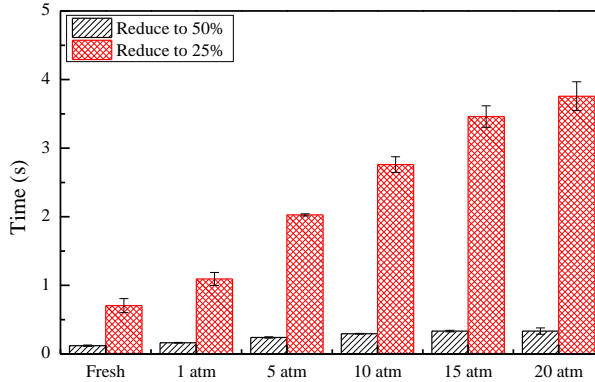
**Figure 5.33 Ratio of shear stress at 100 s vs 30 s.**

The results show that the shear stress ratio increases with ageing. For the fresh bitumen, 1.03 % of the initial shear stress remained after 100 s relaxation, however more than 6 % of the initial shear stress remained in

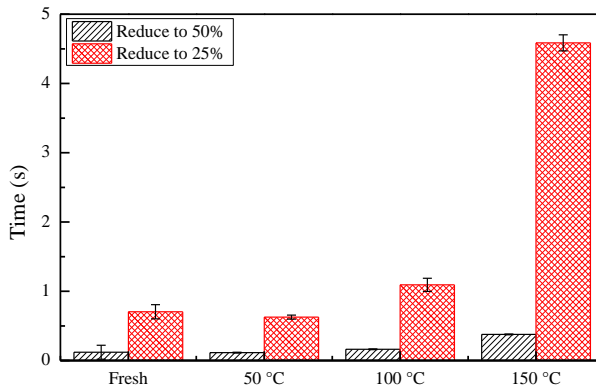
the aged sample after relaxation. Especially, for the sample aged at 150 °C, Figure 4(b), about 8 % of the initial shear stress remained after relaxation. The results show that aged bitumen results to higher stress ratios, suggesting that it can accumulate higher stress. Due to the fact that there is continuous traffic loading, the relaxation time of bitumen needs to be short so as to prevent stress accumulation in the pavement. Figure 5.34 shows the relaxation time, when the shear stress reduces to 50 % or 25 % of the initial stress.



(a) Different ageing times (oven ageing at 100 °C and 1 atm).



(b) Different ageing pressures (PAV ageing for 40 h at 100 °C).



(c) Different ageing temperatures (oven ageing for 40 h at 1 atm).

**Figure 5.34** Time that shear stress reduce to 50% and 25% of the initial.

The relaxation time, at which the shear stress reduces to 50 % or 25 % of the initial stress, increases with ageing. An increase of the relaxation time can be explained by the fact that the viscosity of bitumen increases due to ageing. For fresh bitumen, the shear stress reduces to 25% of its initial value in one second, however, for the 320 h aged sample and the 20 atm aged sample, they need 3.28 s and 3.76 s, respectively. For the bitumen aged in the oven at 150 °C, the relaxation time to reach 25 % decay in stress is 4.58 s. Longer relaxation times denote materials that are more susceptible to stress accumulation.

#### 5.4.4 Fatigue test

Considering that the selected control modes in a DSR tests can have a significant influence on the damaged behaviour of bitumen [36-39], fatigue tests were conducted at the temperature of 20 °C and at a frequency of 10 Hz under two different control modes, stress-controlled and strain-controlled. The bitumen samples were tested using the parallel-plates configuration with 8 mm plate diameter and 2 mm gap. Based on the results of the amplitude sweep tests, six different stress amplitudes and five different strain amplitudes were applied for each control mode. Fatigue tests were conducted on three bitumen samples



for each stress/strain level and ageing condition. For the fresh bitumen, the results of complex shear modulus vs number of cycles in both control modes are shown in Figure 5.35.

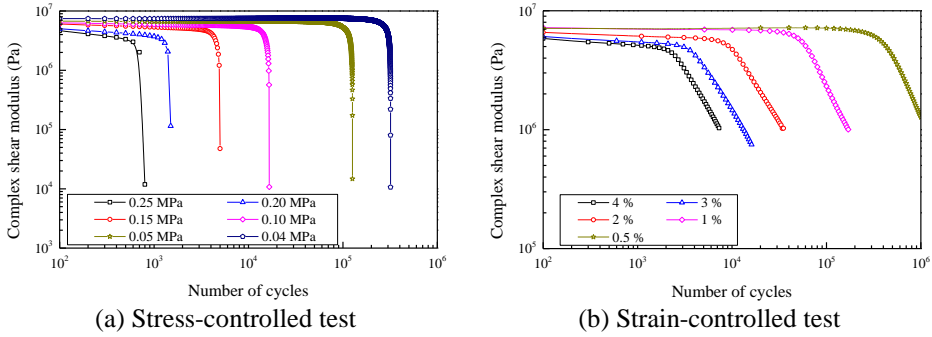


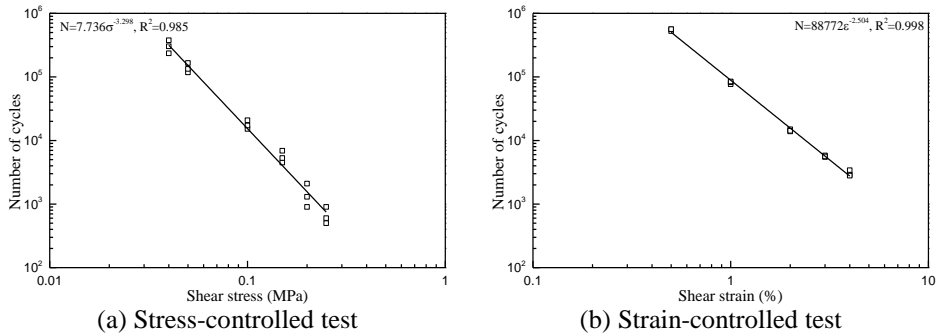
**Figure 5.35 Complex shear modulus vs number of cycles for fresh bitumen**

There is an obvious difference between the results of the stress-controlled and strain-controlled modes, as shown in Figure 5.35. After certain cycles of loading in the stress-controlled test the complex shear modulus suddenly drops, while it drops slowly for the strain-controlled tests. The fatigue criterion is defined as a 50% reduction in the value of the complex shear modulus. Then based on the concepts of viscoelastic continuum damage (VECD) theory [40], the fatigue life of bitumen can be fitted by Eq. (5.1) and Eq. (5.2).

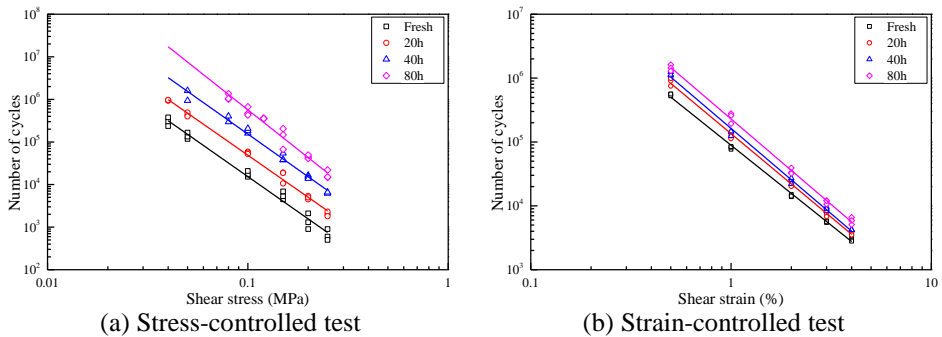
$$N_{\sigma} = A_{\sigma} \sigma^{B_{\sigma}} \quad (5.1)$$

$$N_{\varepsilon} = A_{\varepsilon} \varepsilon^{B_{\varepsilon}} \quad (5.2)$$

where,  $\sigma$  is shear stress and  $\varepsilon$  is shear strain.  $N_{\sigma}$  and  $N_{\varepsilon}$  are number of cycles to failure in stress-controlled and strain-controlled, respectively.  $A_{\sigma}$ ,  $B_{\sigma}$  and  $A_{\varepsilon}$ ,  $B_{\varepsilon}$  are fitting parameters derived from the experiment of stress sweep and strain sweep, respectively. The fatigue results and fitting results of fresh bitumen in both control modes are shown in Figure 5.36.


**Figure 5.36 Fatigue results of fresh bitumen**

The experimental results of the bitumen aged at various ageing times are fitted according to Eq. (5.1) and Eq. (5.2). The results of the fatigue and the fitting parameters in both control modes are shown in Figure 5.37 and Table 5.3, respectively.


**Figure 5.37 Fatigue results of bitumen with various ageing time**
**Table 5.3 Fitting parameters for fatigue results**

Name	$A_{\sigma}$	$B_{\sigma}$	$R^2$	$A_{\varepsilon}$	$B_{\varepsilon}$	$R^2$
Fresh	7.736	-3.298	0.985	88772	-2.054	0.998
20 h	25.581	-3.281	0.994	134938	-2.617	0.998
40 h	72.197	-3.327	0.988	162852	-2.671	0.997
80 h	106.99	-3.725	0.967	229202	-2.678	0.997

From Figure 5.37, it can be observed that the fatigue life increases after ageing. This result can also be found in Table 5.3, in which the fitting parameters  $A_{\sigma}$  and  $A_{\varepsilon}$  increase significantly with ageing (%), while the

parameters  $B_\sigma$  and  $B_\epsilon$  change slightly or not at all with ageing. Based on the VECD concepts, when there is no change on the value of the parameter  $B_\sigma$  or  $B_\epsilon$ , the larger the value of the parameter  $A_\sigma$  or  $A_\epsilon$ , the better its fatigue characteristic will be. It is an interesting observation that ageing seems to increase the pavement fatigue life, which conflicts with a common view that a pavement becomes susceptible to fatigue damage because of ageing [41-44]. One reason may be that the fatigue damage of a pavement due to ageing is not a cohesive damage but an adhesive damage, Figure 5.38. Ageing increases the fatigue life of bitumen itself but it may reduce the bonding between the bitumen and the aggregates. The other reason may be that the fatigue criterion defined as a 50% reduction in the values of complex shear modulus, is not suitable for data analysis of fatigue [45-47]. It is recommended to develop some new method for fatigue data analysis.

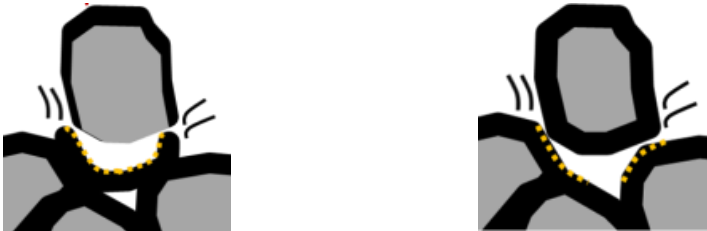


Figure 5.38 Schematic of adhesive damage (left) and cohesive damage (right)

## 5.5 Summary

Given the strong relationship between the material mechanical response and ageing, the knowledge of the evolution of the chemical and mechanical properties in bituminous materials is of uppermost importance. For this reason, a series of ageing experiments were conducted on 2 mm thickness bitumen films at different ageing times, temperatures and pressures. A series of FTIR and DSR tests were carried out to determine the changes in chemical properties and rheological response of aged bitumen.

The analysis of chemical properties showed the high variability of the carbonyl and sulfoxide functional groups with ageing. Furthermore, it confirmed two distinct phases of ageing, with an initial increase of sulfoxides and a second phase in which an increase of the carbonyls occurs. In addition, it has been shown that different ageing methods (or protocols) can achieve the same ageing effect. In other works, different ageing protocols can be interrelated with each other.

The analysis of rheological properties was conducted through DSR testing by looking at the range of the linear viscoelastic (LVE) region, the master curves of complex shear modulus and phase angle, as well as the relaxation and fatigue characteristics. Specifically, ageing definitely has an effect on the linear visco-elastic limits of the materials. In comparison with fresh bitumen, aged bitumen has lower linearity limits for strain, whereas it has higher linearity limits for stress. The fact that bitumen becomes stiffer with ageing was confirmed by the results of the frequency sweep tests at various temperatures. The results show a more significant increase in complex shear modulus and decrease in phase angle at low frequencies, corresponding to high testing temperatures. Results from the relaxation tests show that, in comparison with fresh bitumen, the aged samples had higher residual shear stress and were therefore more susceptible to stress accumulation and consequently cracking. On the basis of standard fatigue analysis criteria, it appears that ageing seems to have a positive effect on the fatigue life of bitumen. This observation contradicts field observations and raises question about the suitability of such criteria.

Based on the test results presented in this Chapter, a specific relationship between the chemical properties and rheological response of bitumen will be established in Chapter 7.

## 5.6 References

1. Airey, G.D., *State of the art report on ageing test methods for bituminous pavement materials*. International Journal of Pavement Engineering, 2003. **4**(3): p. 165-176.
2. Lesueur, D., *The colloidal structure of bitumen: Consequences on the rheology and on the mechanisms of bitumen modification*. Advances in Colloid and Interface Science, 2009. **145**(1–2): p. 42-82.
3. Siddiqui, M.N. and M.F. Ali, *Investigation of chemical transformations by NMR and GPC during the laboratory aging of Arabian asphalt*. Fuel, 1999. **78**(12): p. 1407-1416.
4. Saoula, S., et al., *Analysis of the rheological behavior of aging bitumen and predicting the risk of permanent deformation of asphalt*. Materials Sciences and Applications, 2013. **4**(05): p. 312-318.
5. Kliewer, J.E., C.A. Bell, and D.A. Sosnovske, *Investigation of the relationship between field performance and laboratory aging properties of asphalt mixtures, in Engineering Properties of Asphalt Mixtures and the Relationship to Their Performance*. 1995, ASTM International. p. 3-20.
6. Oort, W.P.V., *Durability of asphalt - It's aging in the dark*. Industrial & Engineering Chemistry, 1956. **48**(7): p. 1196-1201.
7. Benson, P.E., *Low temperature transverse cracking of asphalt concrete pavements in central and west texas*. TTI-2-9-72-1752-2F Final Report. 1976.
8. Branthaver, J.F., et al., *Binder characterization and evaluation. Volume 2: Chemistry*. 1993 [SHRP-A-368].
9. Huang, S.C., M. Tia, and B.E. Ruth, *Laboratory aging methods for simulation of field aging of asphalts*. Journal of Materials in Civil Engineering, 1996. **8**(3): p. 147-152.
10. Rostler, F.S. and R.M. White, *Influence of chemical composition of asphalts on performance, particularly durability*. ASTM STP, 1960. **277**: p. 64-88.
11. Petersen, J.C., *A thin film accelerated aging test for evaluating asphalt oxidative aging*. Transportation Research Board, Washington, DC, 1989. **58**: p. 220-237.
12. Kandhal, P. and S. Chakraborty, *Effect of asphalt film thickness on short-and long-term aging of asphalt paving mixtures*. Transportation Research Record: Journal of the Transportation Research Board, 1996(1535): p. 83-90.
13. Ruan, Y., R.R. Davison, and C.J. Glover, *An investigation of asphalt durability: Relationships between ductility and rheological properties for unmodified asphalts*. Petroleum Science and Technology, 2003. **21**(1-2): p. 231-254.
14. Van den Bergh, W., *The effect of ageing on the fatigue and healing properties of bituminous mortars* (doctoral thesis). Delft University of Technology. 2011.
15. Behera, P.K., A.K. Singh, and M. Amaranatha Reddy, *An alternative method for short- and long-term ageing for bitumen binders*. Road Materials and Pavement Design, 2013. **14**(2): p. 445-457.
16. Petersen, J.C., *Quantitative method using differential infrared spectrometry for the determination of compound types absorbing in the carbonyl region in asphalts*. Analytical Chemistry, 1975. **47**(1): p. 112-117.
17. Harnsberger, P., et al., *Comparison of oxidation of SHRP asphalts by two different methods*. Fuel science & technology international, 1993. **11**(1): p. 89-121.

18. Taylor, R., et al., *Rheological & structural analysis of recovered asphalt binders from the FHWA ALF rutting & fatigue experiments, Part III FTIR spectral analysis*. in *Abstracts of papers of the american chemical society*. 1998. p. U847-U847.
19. Feng, Z.G., J.Y. Yu, and Y.S. Liang, *The relationship between colloidal chemistry and ageing properties of bitumen*. *Petroleum Science and Technology*, 2012. **30**(14): p. 1453-1460.
20. Gamarra, A. and E.A. Ossa, *Thermo-oxidative aging of bitumen*. *International Journal of Pavement Engineering*, 2018. **19**(7): p. 641-650.
21. Lu, X. and U. Isacson, *Effect of ageing on bitumen chemistry and rheology*. *Construction and Building Materials*, 2002. **16**(1): p. 15-22.
22. Kandhal, P., et al., *Hot mix asphalt materials, mixture design and construction*. NAPA Education Foundation, Lanham, Md, 1996.
23. Petersen, J.C., *A review of the fundamentals of asphalt oxidation: chemical, physicochemical, physical property, and durability relationships*. *Transportation Research E-Circular*, 2009(E-C140).
24. Kanabar, A., *Physical and chemical aging behavior of asphalt cements from two northern ontario pavement trials* (doctoral thesis). Queen's University. 2010.
25. Bahia, H.U., et al., *Development of binder specification parameters based on characterization of damage behavior (With discussion)*. *Journal of the Association of Asphalt Paving Technologists*, 2001. **70**: p. 442-470.
26. Singh, B., N. Saboo, and P. Kumar, *Modelling the complex modulus strain relationship of asphalt binders*. *Petroleum Science and Technology*, 2016. **34**(13): p. 1137-1144.
27. Shan, L., et al., *Effect of load control mode on the fatigue performance of asphalt binder*. *Materials and Structures*, 2016. **49**(4): p. 1391-1402.
28. Airey, G.D., *Use of black diagrams to identify inconsistencies in rheological data*. *Road Materials and Pavement Design*, 2002. **3**(4): p. 403-424.
29. Rahalkar, R.R., *Correlation between the crossover modulus and the molecular weight distribution using the Doi-Edwards theory of reptation and the Rouse theory*. *Rheologica Acta*, 1989. **28**(2): p. 166-175.
30. Liu, C., et al., *Evaluation of different methods for the determination of the plateau modulus and the entanglement molecular weight*. *Polymer*, 2006. **47**(13): p. 4461-4479.
31. Mezger, T.G., *The rheology handbook: for users of rotational and oscillatory rheometers*. 2006: Vincentz Network GmbH & Co KG.
32. Nivitha, M.R. and J. Murali Krishnan, *What is transition temperature for bitumen and how to measure it?* *Transportation in Developing Economies*, 2016. **2**(1): p. 3.
33. Scarsella, M., et al., *Petroleum heavy ends stability: Evolution of residues macrostructure by aging*. *Energy & Fuels*, 1999. **13**(3): p. 739-747.
34. Winter, H.H., *Can the gel point of a cross-linking polymer be detected by the  $G' - G''$  crossover?* *Polymer Engineering & Science*, 1987. **27**(22): p. 1698-1702.
35. Chambon, F. and H.H. Winter, *Stopping of crosslinking reaction in a PDMS polymer at the gel point*. *Polymer Bulletin*, 1985. **13**(6): p. 499-503.
36. Monismith, C.L. and J.A. Deacon, *Fatigue of asphalt paving mixtures*. *Transportation Engineering Journal of ASCE*, 1969. **95**(2): p. 317-346.

37. Shen, S. and S. Carpenter, *Development of an asphalt fatigue model based on energy principles*. Asphalt Paving Technology-Proceedings, 2007. **76**: p. 525.
38. Kim, Y.R., H.-J. Lee, and D.N. Little, *Fatigue characterization of asphalt concrete using viscoelasticity and continuum damage theory (with discussion)*. Journal of the Association of Asphalt Paving Technologists, 1997. **66**: p. 520-569.
39. Masad, E., et al., *A unified method for the analysis of controlled-strain and controlled-stress fatigue testing*. International Journal of Pavement Engineering, 2008. **9**(4): p. 233-246.
40. Jafari, M. and A. Babazadeh, *Evaluation of polyphosphoric acid-modified binders using multiple stress creep and recovery and linear amplitude sweep tests*. Road Materials and Pavement Design, 2016. **17**(4): p. 859-876.
41. Van den bergh, W. and M.F.C. Van de Ven, *The influence of ageing on the fatigue and healing properties of bituminous mortars*. Procedia-Social and Behavioral Sciences, 2012. **53**: p. 256-265.
42. Liu, X., et al., *Fatigue properties of layered double hydroxides modified asphalt and its mixture*. Advances in Materials Science and Engineering, 2014. **2014**: p. 6.
43. Ouyang, C., et al., *Improving the aging resistance of asphalt by addition of Zinc dialkyldithiophosphate*. Fuel, 2006. **85**(7): p. 1060-1066.
44. Airey, G.D. and B. Rahimzadeh, *Combined bituminous binder and mixture linear rheological properties*. Construction and Building Materials, 2004. **18**(7): p. 535-548.
45. Bonnetti, K., K. Nam, and H. Bahia, *Measuring and defining fatigue behavior of asphalt binders*. Transportation Research Record: Journal of the Transportation Research Board, 2002. **1810**: p. 33-43.
46. Ghuzlan, K. and S. Carpenter, *Energy-Derived, Damage-Based failure criterion for fatigue testing*. Transportation Research Record: Journal of the Transportation Research Board, 2000. **1723**: p. 141-149.
47. Bhasin, A., et al., *Quantitative comparison of energy methods to characterize fatigue in asphalt materials*. Journal of Materials in Civil Engineering, 2009. **21**(2): p. 83-92.

# 6

## **AGEING IN THE FIELD**

---



## 6.1 Introduction

Bitumen ageing is one of the principal factors causing the deterioration of asphalt pavements. Because of bitumen ageing, asphalt pavements lose their ability to relax stresses during the cooling process, thus the risk of cracking increases [1]. Oxidation and ultraviolet (UV) radiation are believed to be the main reasons of bitumen ageing as the pavement is exposed to the atmosphere in the field [2]. In addition, other environmental variables such as moisture, wind, atmospheric pressure play a role [3, 4]. Also, ageing in the field is difficult to investigate because such studies are highly time-consuming and costly [5, 6]. Moreover, ageing is dependent on the mixture properties such as the void content and/or bitumen film thickness [7, 8].

For this work, one open (PA) and one dense (SMA) graded pavement sections were designed and constructed in the LINTRACK facility at TU Delft in October 2014. The test sections have been continuously exposed to the various environmental conditions similar to those an actual pavement experiences in the field. Since field ageing of pavements highly depends on the local weather conditions [9], the variations in weather data such as air temperature and UV index were constantly recorded via a weather station.

In order to study the deterioration of the asphalt mixtures, asphalt cores were collected from the test sections periodically (at one-year intervals). The volumetric and the mechanical properties of the asphalt cores were determined by means of X-ray CT scanner and Indirect Tensile Tests (ITT). To investigate the ageing propagation in the depth profile of the pavement, the core samples were cut into three slices. Next, bitumen was extracted from the different slices to evaluate the chemical and the rheological properties by utilizing Fourier Transform Infrared spectrometer (FTIR) and Dynamic Shear Rheometer (DSR) tests. The results were then linked to the results from the laboratory aged samples in Chapter 5.

## 6.2 Overview of the test sections

### 6.2.1 Asphalt mixture design

The asphalt mixtures were designed by Heijmans. Both PA and SMA mixtures used the same type of aggregate, Fjordstone, with a nominal maximum aggregate size of 16 mm. Fjordstone is a type of crushed stone from Norway, with density  $2740 \text{ kg/m}^3$ . The binder content was 5.0 % and 6.4% for the PA and the SMA mixture, respectively. The aggregate gradations of both mixtures are shown in Figure 6.1. The same type of PEN70/100 bitumen was used for the construction of the two test sections. Moreover, the WIGRO 60K filler (density is  $2780 \text{ kg/m}^3$ ) was used for both mixtures, which is a type of filler with hydroxide which contains hydrated lime.

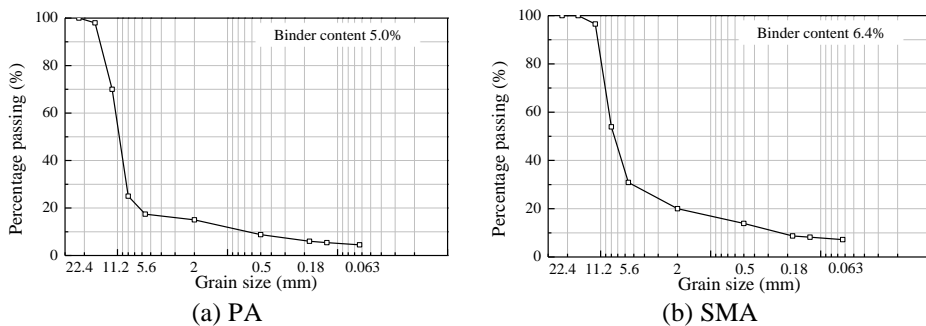


**Figure 6.1 Aggregate gradation and physical properties of mixture**

### 6.2.2 Construction

The construction phase started with the removal of the existing old pavement surface as shown in Figure 6.2. At first, the top 40 mm of existing SMA layer was removed and then the existing 60 mm of stone asphalt concrete (STAC) base layer was removed as well. STAC is a type of dense asphalt, which is commonly used as the base layer of pavements in the Netherlands.



**Figure 6.2 Existing pavement removal**

After the milling process, a bitumen emulsion tack coat layer was sprayed on the surface, Figure 6.3(a). Then the 60 mm thickness new STAC layer was laid first, Figure 6.3(b) and the 50 mm thickness top PA and SMA layers were placed on the left and right lanes separately, Figure 6.3(c). All layers were compacted using a roller compactor separately, Figure 6.3(d). The construction of the test sections was done on 9<sup>th</sup> of October, 2014. The profile of the new pavement structures is shown in Figure 6.4, where AGRAC is a type of cement bound asphalt granulate base which was laid more than 10 years ago.



(a) Tack coat spray



(b) Paving of the new STAC layer



(c) Paving of upper layers (PA and SMA)



(d) Compaction

**Figure 6.3 Construction of test sections**

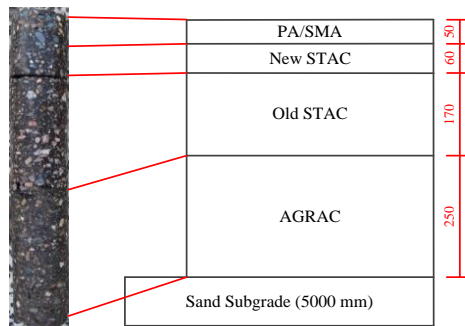


Figure 6.4 Profile of field test section (length unit: mm)

## 6.2.3 Instrumentation

### 6.2.3.1 Field condition monitoring

In order to monitor continuously the pavement temperature, the test sections were instrumented with thermal sensors, Figure 6.5. Thermal sensors were placed across the depth of the pavement cross section. In order to have proper positioning, the sections have been cut through, Figure 6.6, and the sensors were placed inside the pavement from the lateral surface through the cut. Extra care was taken during sensor placement so that all sensors were isolated by waterproof foam to avoid moisture effect from the open boundary along the side of the pavement. The frequency of data collection is 1 time every 5 minutes. The instrumentation was completed in the summer of 2016.

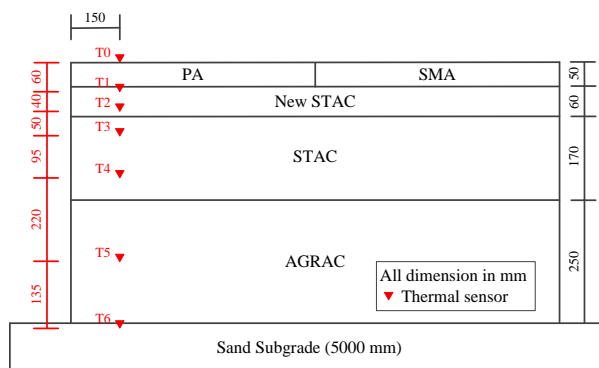


Figure 6.5 Cross section details and instrumentation plan



**Figure 6.6 Cutting through test section and sensor setup**

### 6.2.3.2 Weather station

A WeatherLink weather station was used to collect climate data. The station can collect continuously numerous climate parameters in all seasons. The collected parameters are the ambient temperature, humidity, wind speed and its direction, air pressure, precipitation amount, solar radiation, UV index etc. The frequency of data collection is once every 30 minutes. The weather station was fixed on the roof of a nearby building around 10 meters away from the LINTRACK test sections, Figure 6.7. The data collection started in July, 2014.



**Figure 6.7 Weather station next to LINTRACK in TU Delft**

### 6.2.4 UV reflective glass-plate

UV reflecting glass plates (1500mm×3880mm) were utilized to cover part of the pavement surface. The idea of installing UV reflecting glasses is that they would enable the comparison of ageing with and without the effect of UV radiation. It is noted here that the glass plate is capable of reflecting most of the UV radiation but it allows thermal waves to penetrate and to heat the pavement. The glass plate has been lifted up by pegs to allow the pavement to age due to other factors such as water and air, Figure 6.8. The glass plates were installed on 3<sup>rd</sup> of March, 2016.

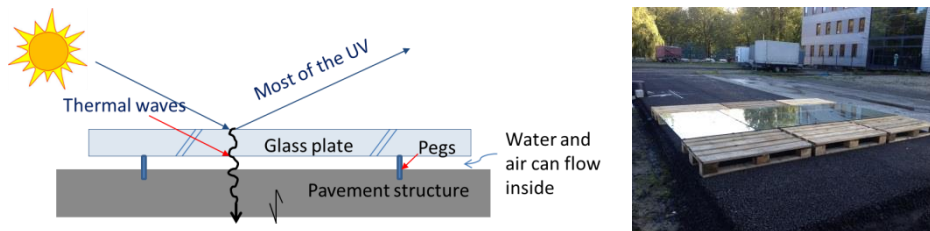


**Figure 6.8 Schematic representing the use of UV reflective glass-plate**

### 6.2.5 Drill core samples

Asphalt core samples with 100 mm diameter were cored from the pavement sections across the full depth of the PA/SMA layer. The core samples were cut off the bottom to a final height of around 45 mm. Four core samples have been taken from the top layer of the PA and SMA sections every October since 2014. Another eight core samples were taken from sections covered by the UV reflecting glass plate on 10<sup>th</sup> of October 2017. A schematic of the coring position is shown in Figure 6.9. After coring, the volumetric and mechanical characteristics of samples were determined by the means of X-Ray CT scans and ITT tests.

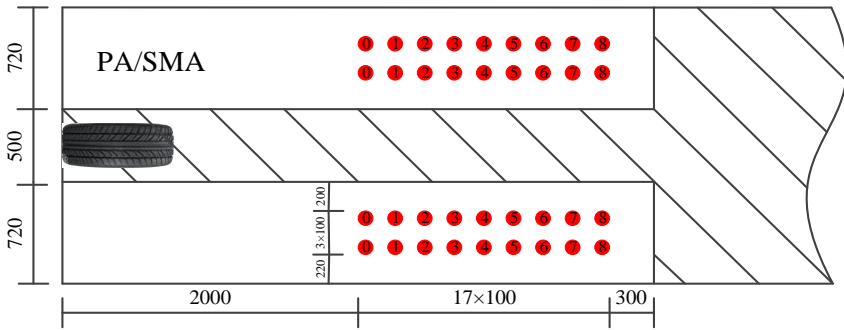


**Figure 6.9 Core sampling locations (Unit: mm)**

In order to investigate the ageing propagation into the pavement, PA core samples were cut into three slices with 12 mm thickness from top to bottom, Figure 6.10, and the remaining part was discarded. Bitumen was extracted from the different slices to evaluate the chemical and the rheological properties by utilizing FTIR and DSR tests.

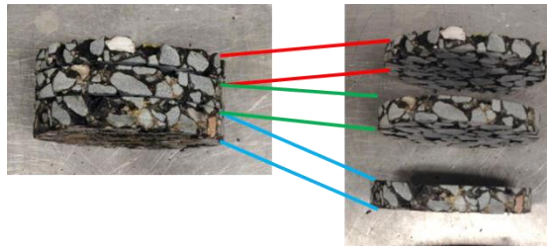


**Figure 6.10 Slices description**

In summary, the key dates and events of the test sections are summarized in Table 6.1. The symbols PA\_G and SMA\_G denote the core samples from the pavement covered by UV reflecting glass plate.

**Table 6.1 Key dates and events of test section**

Dates (YY. MM. DD)	Events	Explanation
2014.10.09	Pavement construction	
2014.10.24	Coring	4 PA
2015.10.01	Coring	4 PA, 4 SMA
2016.03.03	UV reflective glass-plate installation	
2016.08.05	Thermal sensor installation	
2016.10.07	Coring	4 PA, 4 SMA
2017.10.10	Coring	4 PA, 4 SMA, 4 PA_G, 4 SMA_G

## 6.3 Tests on asphalt mixtures

### 6.3.1 X-Ray CT scans

To get information on the volumetric composition, firstly the cores were scanned with a Siemens SOMATOM Plus4 Volume Zoom medical scanner, Figure 6.11. The cores were scanned along the height with a slice distance of 0.6 mm. Other settings are shown in Table 6.2.



Figure 6.11 Siemens medical scanner

Table 6.2 Settings of Siemens medical scanner

Scan mode	Beam voltage	Beam current	Scan area	Resolution
Spiral	140 kV	250 mA	$100 \times 100 \text{ mm}^2$	$0.294 \times 0.294 \text{ mm}^2$

Simpleware software was used to segment the different components in the pavement. Figure 6.12(a) and (b) show the CT scans of the PA and SMA mixtures, respectively. Figure 6.13(a) and (b) show the distribution of the air voids, mortar and aggregates (rock) over the height of the PA and SMA mixtures, respectively. It can be observed that PA has higher void content and lower mortar content in comparison with SMA.



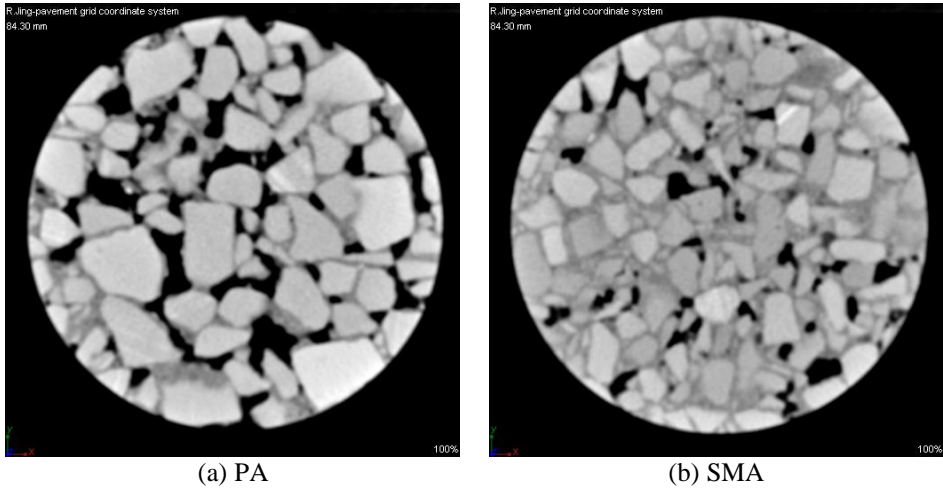


Figure 6.12 CT Scan results

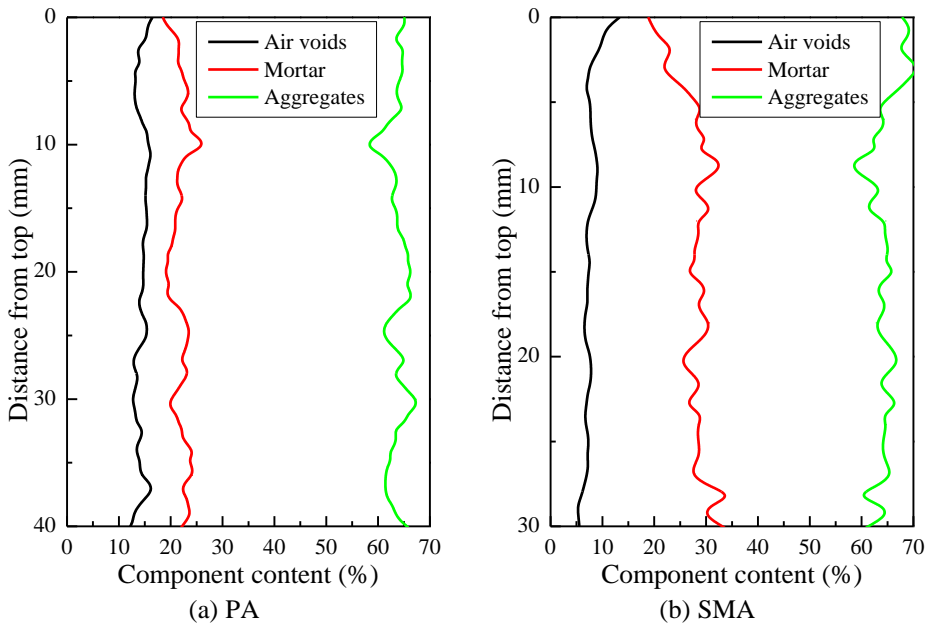


Figure 6.13 Distributions of voids, mortar and aggregates (rock) over the height

### 6.3.2 Indirect tensile test

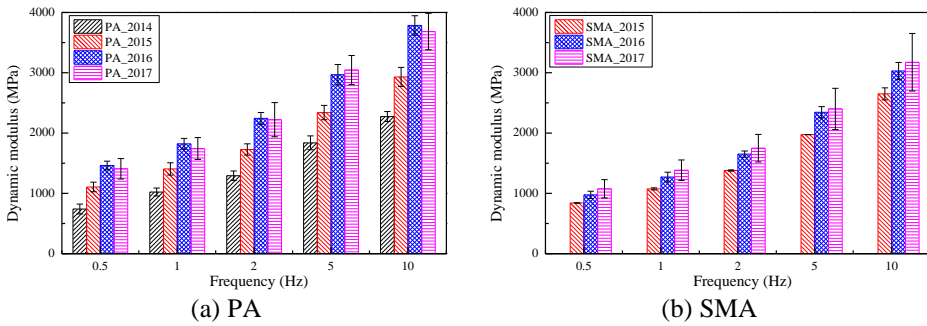
The dynamic moduli of the core samples were determined by means of dynamic indirect tensile tests (ITT) according to EN 12697-26. The test

setup is shown in Figure 6.14. Frequencies were 0.5, 1, 2, 5 and 10 Hz. Test temperature was set to 20 °C. Conditioning time was 30 minutes.



**Figure 6.14 ITT test setup**

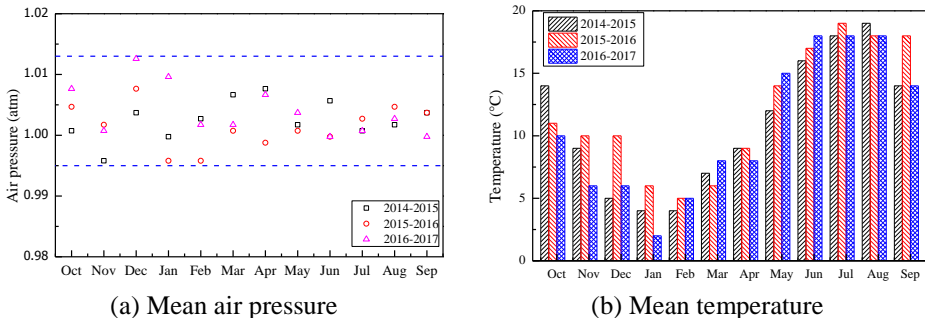
The dynamic moduli of the PA and SMA mixtures at 20°C are presented in Figure 6.15. It can be observed that the dynamic modulus of PA mixture increases with time. Unfortunately, there were no cores taken from the SMA section right after laying. However, it can be observed that the dynamic modulus of the SMA mixture increases with time. In addition, the change of the dynamic modulus of PA mixture is much more significant than that of the SMA mixture, possibly because of the high void content of the PA mixture. The results show that the dynamic moduli of PA\_2017 samples were relatively similar to that of 2016, while the SMA\_2017 samples displayed an increasing trend of the dynamic modulus. The reason for that may be that the mechanical properties of the PA mixture are becoming stable after three years due to the higher ageing rate compared to the SMA mixture. This hypothesis needs to be verified in the future by collecting data in subsequent years.



**Figure 6.15 Dynamic moduli of mixtures at 20 °C**

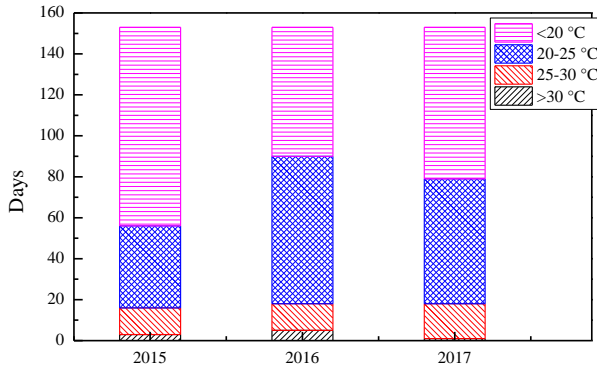
More interestingly though, it can be observed that the dynamic moduli of both mixtures have the highest increase rate from 2015 to 2016. As there is a lot of variation (temperature, air pressure and UV) associated with field ageing, it is important to find which one is the key factor.

Figure 6.16(a) and (b) illustrate the monthly mean air pressure and temperature from Oct 2014 to Oct 2017, respectively. The air pressure varies in a very small range (1 to 1.01 atm). Based on the results of the monthly mean temperature, the yearly mean temperature was calculated to be 10.92 °C, 11.92 °C and 10.67 °C from Oct 2014 to Oct 2017. It is clearly shown that the yearly mean temperature of 2015-2016 was 1 °C higher than other two years. The increase of the yearly mean temperature for the period 2015-2016 coincides with the highest increase rate of the dynamic moduli for both mixture samples from 2015 to 2016, as shown in Figure 6.15.



**Figure 6.16 Weather information from Oct 2014 to Oct 2017**

Furthermore, it is expected that longer periods with high temperature will have more significant impact on the ageing rate. Figure 6.16(b) shows that the higher temperatures were recorded from May to September every year. Moreover, Figure 6.17 shows the number of days corresponding to the daily maximum temperature from May to September of each year. Overall, the daily maximum temperature exceeded 20 °C for 90 days in 2016, while 56 and 79 days were recorded in 2015 and 2017, respectively. This can possibly also explain the high increase rate of the dynamic modulus from October of 2015 to October of 2016. The above observations imply that thermal ageing is the key mechanism for pavement ageing in the Netherlands.



**Figure 6.17 Highest temperature days from May to Sep since 2014**

So far, the discussion of the results was based on the data of ambient temperature. It is also interesting to understand the relationship between the ambient temperature and road surface temperature. Therefore, the ambient temperature collected from the weather station and the road surface temperature collected from thermal sensors are illustrated in Figure 6.18. The data collection was performed from 15<sup>th</sup> of August to 12<sup>th</sup> of September, 2016.

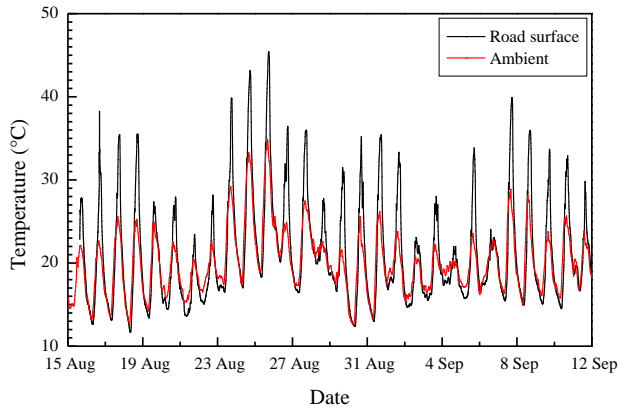


**Figure 6.18 Temperature along various pavement depths.**

It can be observed that the highest temperature of the road surface is always higher than the ambient temperature, Figure 6.18. The difference is about 10 °C [10-12]. Hence, it can be anticipated that the increase of 1 °C in the yearly mean temperature of 2015-2016 translates into a higher difference ( $>1$  °C) in the temperature of the road surface, which can cause large changes in the stiffness of the mixtures for this period.

In addition, the influence of UV radiation on ageing was investigated. Figure 6.19 illustrates the ITT results of the two mixtures with and without the effect of UV radiation. The UV reflecting glass-plate was installed on March 2016 and, therefore the sample was covered by glass (PA\_2017\_G, SMA\_2017\_G) only for a period of one and half years.

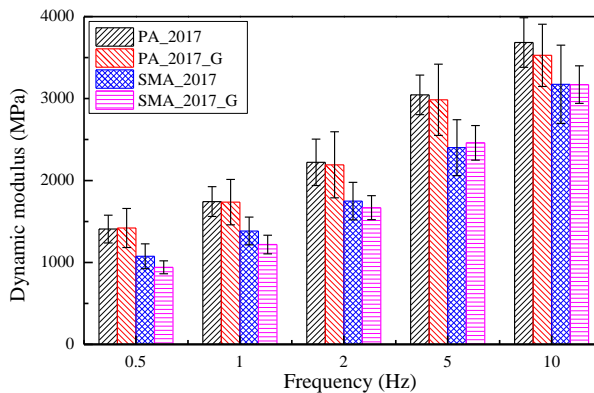


**Figure 6.19 Effect of UV on dynamic modulus of PA and SMA at 20 °C**

From Figure 6.19, it is observed that there is no significant difference for the samples with and without the UV radiation effect. However, it cannot be concluded that UV has no influence on ageing, as the data represent a short time period. Figure 6.20 shows the UV index information from the weather station from March 2016 to October 2017. The UV index represent the strength of ultraviolet radiation. Higher UV index means stronger UV radiation.

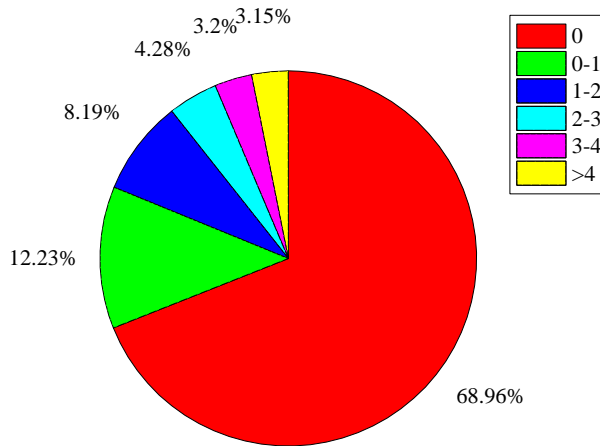


**Figure 6.20 UV index information**

The weather data show that the UV index is zero for nearly 70% of the time period, while for 93.65% of the time the UV index is very low, from 0.0 to 2.9, values that are considered to be of no or low danger for human health. Only for 3.15% of this period the UV index has values higher than 4. This data indicate that UV is expected to have no or slight influence on pavement ageing in the studied geographic region. Hence, it appears that UV ageing is not the main reason of pavement ageing in the Netherlands due to the low UV index, Figure 6.21.

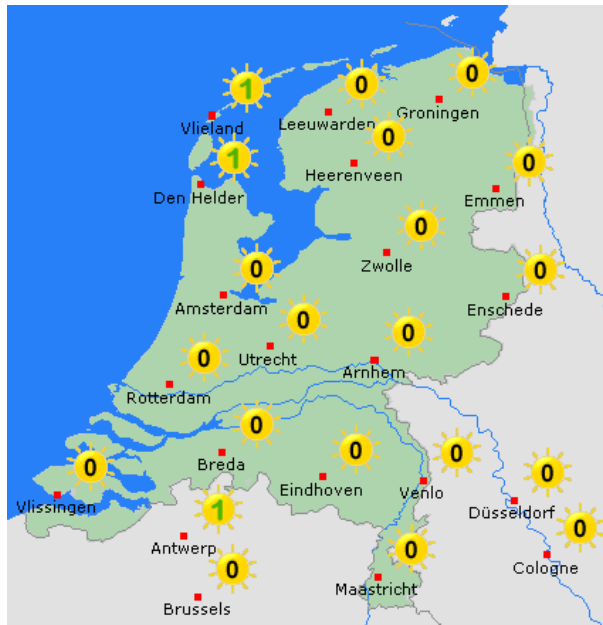


Figure 6.21 UV index value in the Netherlands (a sunny day)

## 6.4 Tests on recovered bitumen

In order to investigate the propagation of ageing across the depth of the profile of the pavement, the PA core samples were cut into three slices, Figure 6.10. Then the bitumen was extracted and tested by the means of FTIR and DSR to determine the changes in chemistry and rheology due to field ageing.

### 6.4.1 Bitumen extraction procedure

The steps of the extraction procedure are described below and shown in Figure 6.22.

- (a) Put the mixture slice into oven and heat it up at 60 °C for 30 minutes.
- (b) Take the mixture slice out and break it into small pieces.

(c) Water sieving of the mixture by using the 0.5 mm sieve to remove the dust inside.

(d) Place the mixture into the oven at 60 °C for another 30 minutes to evaporate the water.

(e) Place the mixture and 100 ml of Dichloromethane ( $\text{CH}_2\text{Cl}_2$ ) in a glass bottle, and let it dissolve for 30 minutes. After that, transfer the solution (solvent + bitumen + fines) to another bottle, leaving the aggregate and sand in the glass bottle.

(f) Separate the bitumen solution and fine particles by passing them through a filter with openings of 10 microns.

(g) Place the bitumen solution in a fume hood at room temperature until the Dichloromethane evaporates completely.

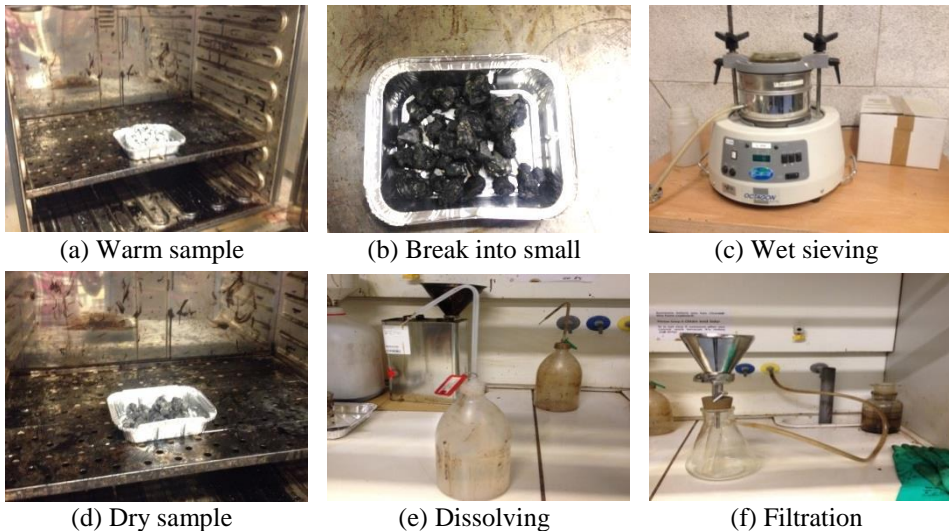
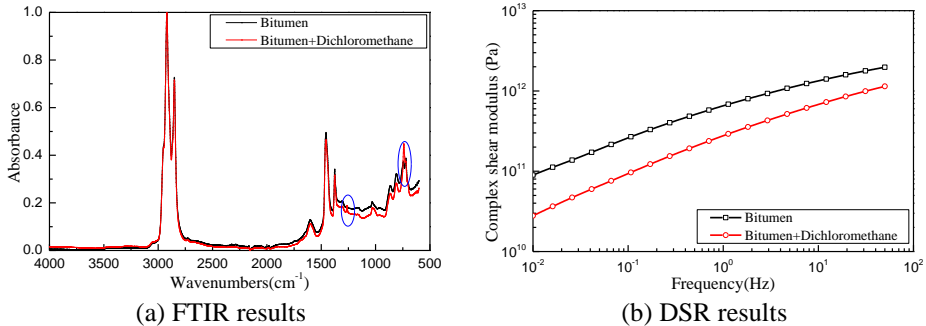


**Figure 6.22 Bitumen extraction procedure**

After the recovery of bitumen, DSR and FTIR tests were performed to check if the solvent was fully evaporated. If the solvent was still present in the sample, this would appear in the FTIR results as a special peak in spectrum (wavenumbers are 1250 and 750  $\text{cm}^{-1}$ ), Figure 6.23(a). The chemical expression of dichloromethane is  $\text{CH}_2\text{Cl}_2$ . The left new peak



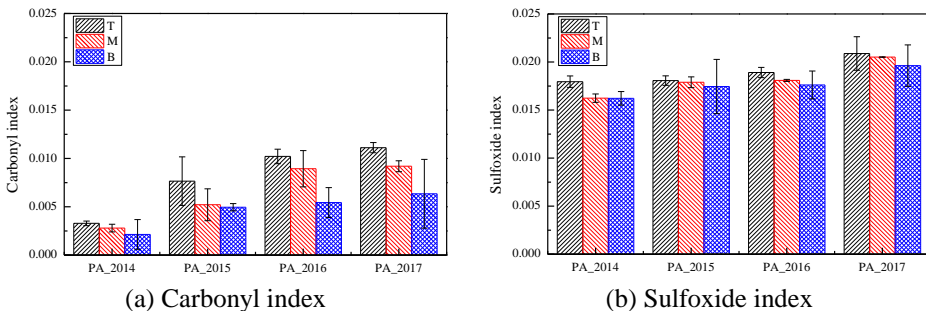
around  $1250\text{ cm}^{-1}$  is the functional group of H-C-H and the right new peak around  $750\text{ cm}^{-1}$  is the functional group of Cl-C-Cl. Therefore, with these two peak in FTIR result, it means there is still dichloromethane present in bitumen. Moreover, the DSR results should show that the material is much softer than the actual fresh material, Figure 6.23(b).



**Figure 6.23 Results of pure bitumen vs bitumen with residual Dichloromethane**

## 6.4.2 FTIR results

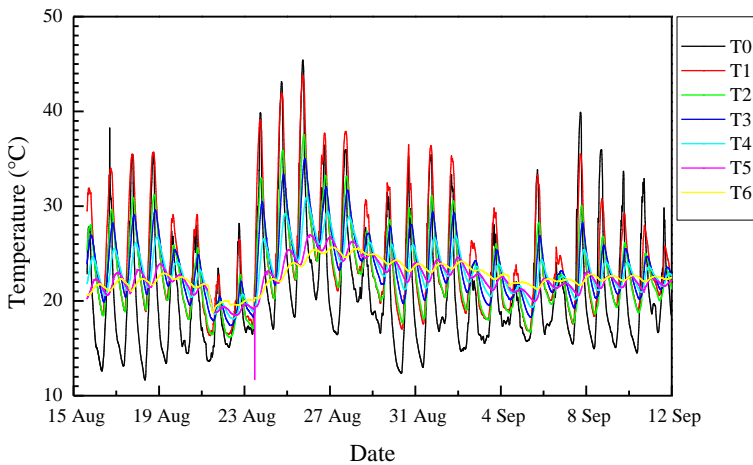
Based on the quantitative method of FTIR results described in the Chapter 4, the carbonyl index and sulfoxide index of the recovered bitumen were determined. The results of the bitumen extracted from the PA mixture are shown in Figure 6.24. T, M and B denote the bitumen samples from the top, middle and bottom slices of mixture respectively.



**Figure 6.24 Function group index of extracted bitumen from PA mixture**

The result show that the ageing indices (carbonyl index and sulfoxide index) increase with time and that the effect of ageing is more significant

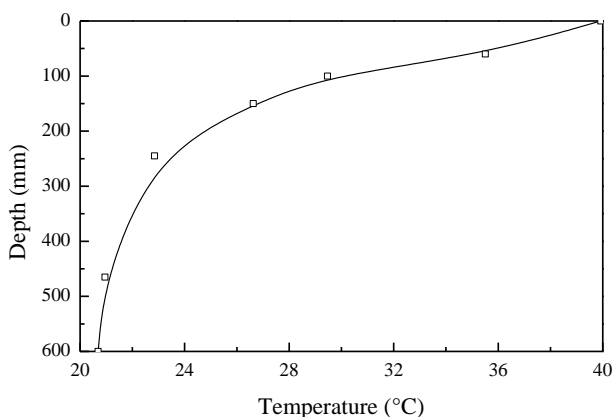
for the top part of the PA layer than for the bottom. This results confirm the fact that the top part of field cores is aged much more than the lower parts [13, 14]. This can be explained by the fact that the top part of the pavement layer is in direct contact with the atmosphere and, naturally, air flows and oxygen diffuses from surface to the bottom. In addition, another reason may be the temperature distribution in the pavement structure. Figure 6.25 shows the temperature data collected by thermal sensors at various depths. The position of each thermal sensor is shown in Figure 6.5. The measurement period is from 15<sup>th</sup> of August to 12<sup>th</sup> of September in 2016. It is clearly shown that the temperature changes are more distinct for the T0 sensor, which is located at the pavement surface, due to it is direct contact with the atmosphere.



**Figure 6.25 Temperature at various pavement depths from 15<sup>th</sup> of August to 12<sup>th</sup> of September 2016.**

As higher temperatures have larger effects on the ageing rate, the pavement temperature at various depths at the warmest time of 7<sup>th</sup> September was selected and illustrated in Figure 6.26. The results show the variation of the temperature along the depth of the pavement. The temperature difference between the pavement surface and the 600 mm depth is nearly 20 °C. Moreover, it can be observed that the larger variations in temperature were found among the locations near the

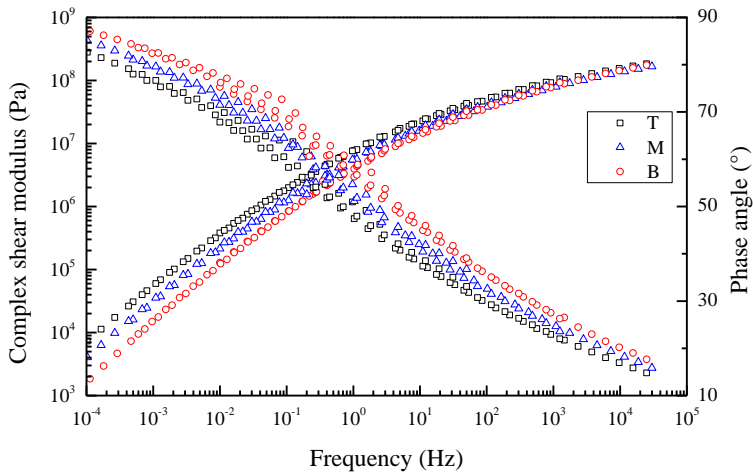
surface. For example, the difference between the pavement surface temperature and the temperature at 100 mm depth is 10 °C. If one considers a linear temperature distribution from the pavement surface to the 100 mm depth, then the temperature gradient is 0.1 °C/mm. In other words, for this case the temperature difference between each core slice is about 1.2 °C. Hence, the top slice always has the higher ageing rate, which leads to higher ageing indices.



**Figure 6.26 Temperature along the depth of the pavement at the warmest time of 7<sup>th</sup> September**

### 6.4.3 DSR results

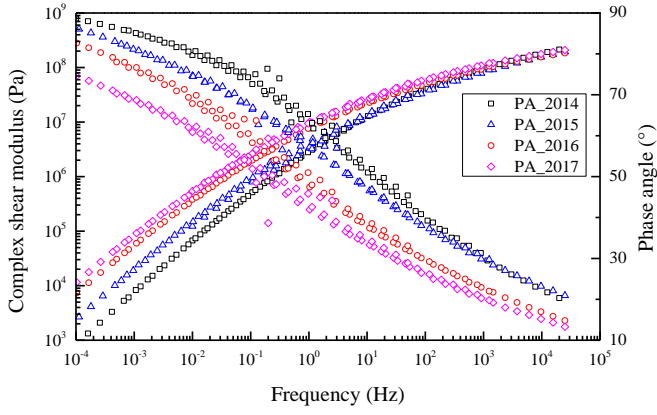
Dynamic Shear Rheometer (DSR) tests were carried out on the bitumen samples extracted from the PA mixtures. Frequency sweep tests were performed in a frequency range from 50 Hz to 0.01 Hz at five different temperatures (0, 10, 20, 30 and 40 °C). The master curve of the complex shear modulus and phase angle of the recovered bitumen from PA\_2016 is selected and illustrated in Figure 6.27, in which the reference temperature is 20 °C.



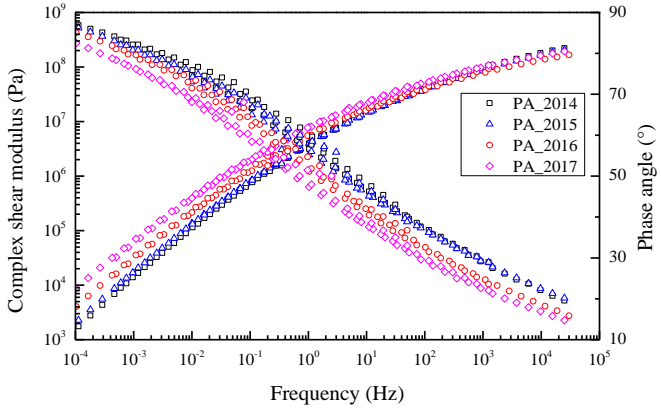
**Figure 6.27 Complex shear modulus and phase angle vs frequency at 20 °C of extracted bitumen from PA\_2016**

Figure 6.27 shows that the complex shear modulus increases from bottom to top, while the phase angle reduces from bottom to top. Similar to the explanation for the FTIR results, the effect of ageing is more significant for the top part of the pavement, as it is in contact with the atmospheric air directly and the temperature is higher.

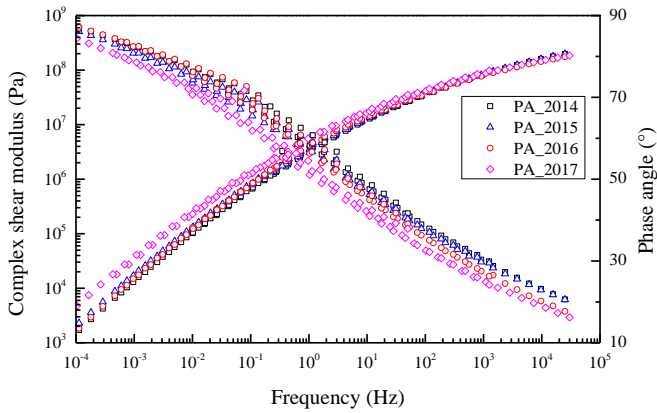
Figure 6.28 shows the evolution of the complex shear modulus and phase angle at each slice in time. The results show an increase in the complex shear modulus and a decrease in the phase angle for the top part. Especially the differences between 2015 and 2016 is larger than other years, possibly due to the higher yearly mean temperature in that period and the longer periods with high temperature, as discussed in Section 6.3. The changes are less obvious for the middle and bottom part, as the values indeed change with time but at a slower rate.



(a) Top slices



(b) Middle slices



(c) Bottom slices

**Figure 6.28 Evolution of complex shear modulus and phase angle at 20 °C with time at different slices of the PA mixture.**

#### 6.4.4 Comparison between laboratory and field ageing

In this section the results (in terms of chemistry and rheology) of the bitumen samples subjected to the laboratory ageing protocols, presented in Chapter 5, are compared to the results of the field aged bitumen. The results of standard ageing condition, provided in Chapter 5, were selected as the results of laboratory ageing. STA denotes standard short term ageing, while LTA denotes standard long term ageing.

The comparison of functional groups present in bitumen samples after field and laboratory ageing is shown in Figure 6.29. It is easily observed, in Figure 6.29(a) that carbonyl was not formed in the studied bitumen after STA ageing. However, carbonyls have been formed in the field ageing samples since paving in 2014. The combined ageing index, Figure 6.30, shows the same trend.

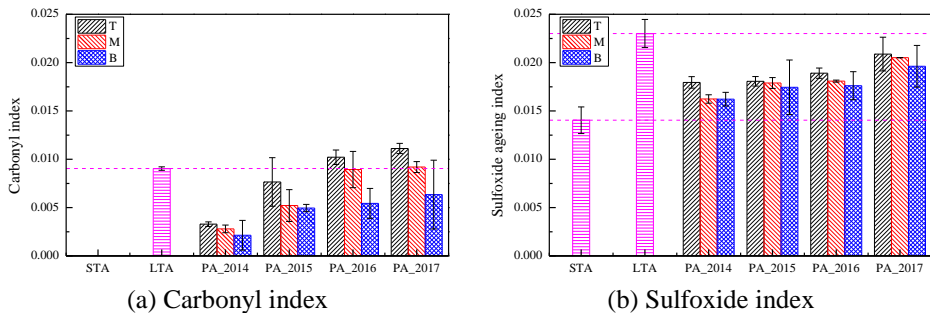


**Figure 6.29 Comparison of function group indices of the bitumen sample from field and laboratory standard ageing**

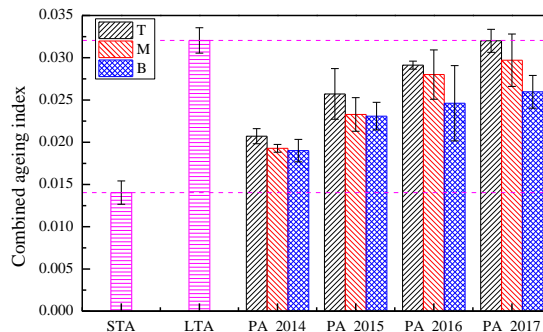


**Figure 6.30 Comparison of combined ageing index of the bitumen sample from field and laboratory standard ageing**

There may be more than more than one reason to explain the discrepancy between the results from the field and laboratory standard ageing [13-15]. RTFOT was developed by the state of California Department of Public Works in 1963 and gave a relatively good indication of ageing for a PEN 40/60 bitumen used in dense continuously graded mixes [16]. However, compared with dense asphalt, the thickness of the bitumen film around the aggregates in porous asphalt is thinner, as shown in the mortar distribution (in white colour) of the two types of mixture obtained from CT scans, Figure 6.31. Therefore the bitumen would have been more aged during mixing and in-service. Thus, standard short term ageing, RTFOT, may be not suitable for simulating the short term ageing of porous asphalt. In addition, it has been shown that RTFOT does not work for hard bitumen or polymer modified bitumen (PMB) [17].

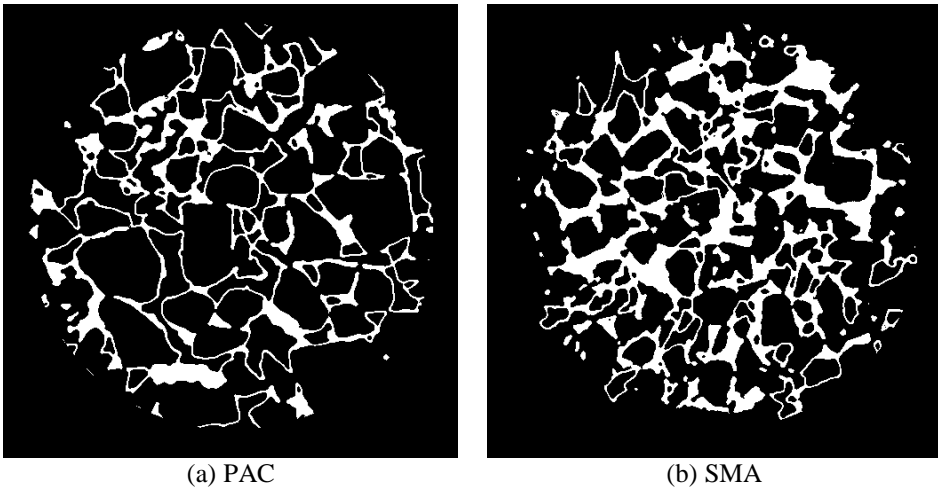


**Figure 6.31 Mortar in different mixtures**

Standard long term ageing is considered to simulate ageing of bitumen during the first five to ten years of pavement service life. However, Figure 6.29(a) clearly shows that, the carbonyl index of the bitumen sample from top and middle slices (in 2016) has been higher than that of LTA ageing in the laboratory.

Although the sulfoxide index of all field samples were still below that of the standard long term ageing, Figure 6.29(b), the combined ageing index in Figure 6.30 clearly shows that the ageing state of the bitumen recovered from the top slice in 2017 has already reached that of the long term standard ageing. In other words, after three years in the field, the ageing state of porous asphalt has reached that of standard long term ageing. Thus, standard long term ageing protocol, RTFOT + PAV, maybe not suitable for simulating the long term ageing of porous asphalt, mainly because of its the high voids content. In addition, both carbonyls and sulfoxides have different growth trends, indicating a discrepancy between the field and laboratory ageing conditions.

The rheological properties of bitumen after field and laboratory standard ageing are shown in Figure 6.32. The master curves show that the stiffness of the bitumen recovered from PA\_2014-B is slightly higher than that of STA aged bitumen. The bitumen extracted from PA\_2017-T has approximately the same stiffness and phase angle as the LTA aged bitumen. Based on the results, it appears that the ageing state of the bottom slice of the porous asphalt (PA\_2014-B) was slightly higher than that of bitumen after STA ageing, while the PA\_2017-T samples after three years of field ageing have similar rheological response as the LTA samples. These results again show that standard laboratory short and long term ageing methods cannot describe the short and long term ageing behaviour of porous asphalt very well.



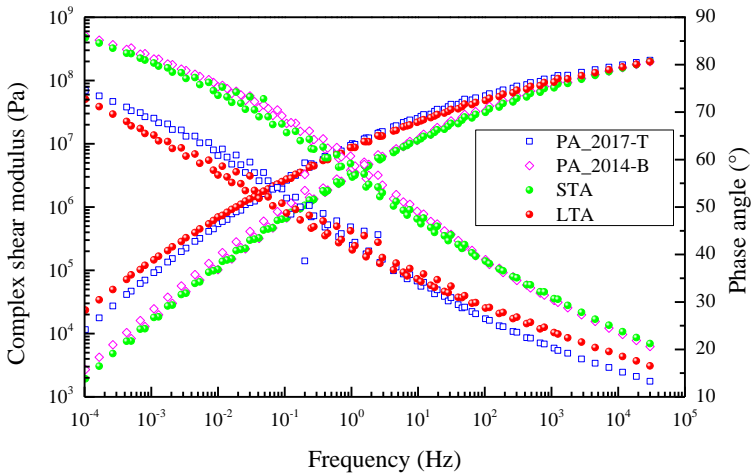


**Figure 6.32 Comparison of master curves (complex shear modulus and phase angle) of bitumen samples from field and laboratory standard ageing**

## 6.5 Summary

Although the amount of bitumen in asphalt mixtures is mostly 5-7% out of all components, it plays an important role in ensuring the performance and durability of the pavement. In this Chapter, the effect of field ageing on the properties of bitumen was studied. One open and one dense graded asphalt pavements were constructed in 2014 and continuously exposed to environmental conditions.

In the literature, ageing in the field is mainly considered to be caused by oxidation and ultraviolet (UV) radiation. In combination with weather data, the results of asphalt cores (yearly taken from the pavement section) show that thermal ageing is the main cause of pavement ageing in the Netherlands. The effect of the air-void distribution, their interconnectivity and the mineral aggregate packing have a significant effect on the resulting age hardening of the overall time. This fact is proven by the results of the tests on asphalt cores in which the change of the stiffness of PA mixtures was much more significant than that of

SMA mixtures, because of the high void content of the PA mixtures, which allows air to flow easier into the mixtures.

Bitumen ageing is more severe for the top part of the pavement, as it is in contact with the atmospheric air and the pavement temperature is higher. Therefore, there is a stiffness gradient across the depth of the pavement that could play a major role in the occurrence of top-down cracking [16]. The laboratory-aged bitumen following the standard long term ageing protocol, RTFOT+ PAV, is aged equivalently to the surface of a porous asphalt layer that has been in place for 3 years in the Netherlands. Field ageing at the pavement surface is far more severe than standard laboratory ageing protocols and cannot be simulated by RTFOT and PAV ageing. Therefore, the ageing protocols have to be re-examined and modified to account for the particularities of porous asphalt that undoubtedly exhibits higher ageing rates than dense asphalt mixtures due to their larger porosity. Finally, the rheological and chemical profiles of field-aged bitumen result from the synergistic effects of thermal-oxidative ageing, ultraviolet radiation and moisture. During laboratory ageing, though, bitumen is exposed only to combinations of temperature and pressure. To fully characterize the long-term behaviour of bitumen a turn in condition protocols that couple the various environmental factors seems necessary.

## 6.6 References

1. Isacson, U. and H. Zeng, *Relationships between bitumen chemistry and low temperature behaviour of asphalt*. Construction and Building Materials, 1997. **11**(2): p. 83-91.
2. Petersen, J.C. and R. Glaser, *Asphalt oxidation mechanisms and the role of oxidation products on age hardening revisited*. Road Materials and Pavement Design, 2011. **12**(4): p. 795-819.
3. Lopes, M., et al., *Characterisation of ageing processes on the asphalt mixture surface*. Road Materials and Pavement Design, 2014. **15**(3): p. 477-487.
4. Wu, S., et al., *Rheological properties for aged bitumen containing ultraviolet light resistant materials*. Construction and Building Materials, 2012. **33**(Supplement C): p. 133-138.

5. Zhang, H., et al., *The relationships between asphalt ageing in lab and field based on the neural network*. Road Materials and Pavement Design, 2015. **16**(2): p. 493-504.
6. Juristyarini, P., R. Davison, and C.J. Glover, *Development of an asphalt aging procedure to assess long-term binder performance*. Petroleum Science and Technology, 2011. **29**(21): p. 2258-2268.
7. Nicholls, C., *BitVal: Analysis of available data for validation of bitumen tests*. FEHRL Report on Phase 1 of the BiTVal Project, 2006.
8. Kandhal, P. and S. Chakraborty, *Effect of asphalt film thickness on short- and long-term aging of asphalt paving mixtures*. Transportation Research Record: Journal of the Transportation Research Board, 1996. **1535**: p. 83-90.
9. Huang, S.C., R. Glaser, and F. Turner, *Impact of water on asphalt aging*. Transportation Research Record: Journal of the Transportation Research Board, 2012. **2293**: p. 63-72.
10. Solaimanian, M. and T.W. Kennedy, *Predicting maximum pavement surface temperature using maximum air temperature and hourly solar radiation*. Transportation research record., 1993(1417).
11. Guan, K.K., *Surface and ambient air temperatures associated with different ground material: a case study at the University of California, Berkeley*. Environmental Science, 2011. **196**: p. 1-14.
12. Li, H., et al., *The use of reflective and permeable pavements as a potential practice for heat island mitigation and stormwater management*. Environmental Research Letters, 2013. **8**(1): p. 015023.
13. Choquet, F. and A. Verhasselt, *Ageing of bitumens: From the road to the laboratory and vice versa*. in *Proceedings of The Conference Strategic Highway Research Program (SHRP) and Traffic Safety on Two Continents*. 1994. Hague, Netherlands.
14. Farrar, M.J., et al., *Evaluation of oxidation in asphalt pavement test sections after four years of service*. in *International Conference on Perpetual Pavement*. Western Research Institute. 2006.
15. Shalaby, A., *Modelling short-term aging of asphalt binders using the rolling thin film oven test*. Canadian Journal of Civil Engineering, 2002. **29**(1): p. 135-144.
16. O'Connell, J. and W. Steyn, *An overview of the ageing of bituminous binders*. in *36th Southern African Transport Conference (SATC 2017)*, July. 2017. p. 308-324.
17. Li, X., et al., *Evaluation of field aging effects on asphalt binder properties*. Road Materials and Pavement Design, 2006. **7**(sup1): p. 57-73.

# 7

## **CHEMO-MECHANICS OF AGEING**

---

## 7.1 Introduction

Ageing of bituminous materials is a physico-chemical process. Past research has shown that typical bitumen properties such as viscosity, penetration, softening point and ductility have a good correlation with ageing [1]. At that time the level of ageing was expressed as a reduction in penetration, an increase in softening point or as the ratio of the aged and the unaged viscosities [2, 3]. Based on large datasets of recovered bitumen from the field, several empirical models were reported to predict the long-term performance of bituminous materials [4-6].

Recently, more researchers have attempted to correlate the chemical composition of bituminous materials with their performance [7, 8]. Studies have indicated that the ageing mechanism affects the chemical composition of bitumen and it was clear that the rheological properties would change as well [9, 10]. Unfortunately, the specific relationship between the chemical properties and mechanical response of bitumen is still unclear. If this relationship is established, then predictions of pavement performance over longer time periods can be made possible.

In the previous chapters (Chapter 2 to 4), the chemical change of bituminous materials can be calculated by the diffusion and reaction model. Chapters 5 and 6 contribute to the understanding of the chemical and mechanical change of bitumen materials due to lab and field ageing. The main objective of this Chapter is to link the changes in the chemical properties of bitumen to its mechanical response due to ageing. On the basis of the experimental results presented in Chapter 5, two empirical models are established and validated using results of field aged samples presented in Chapter 6. Moreover, another objective is to determine the influence of ageing on the parameters of five different viscoelastic models. Finally, the Huet model was modified to include the chemo-mechanics ageing model and implemented to capture the viscoelastic response of the bituminous materials across the frequency spectrum.

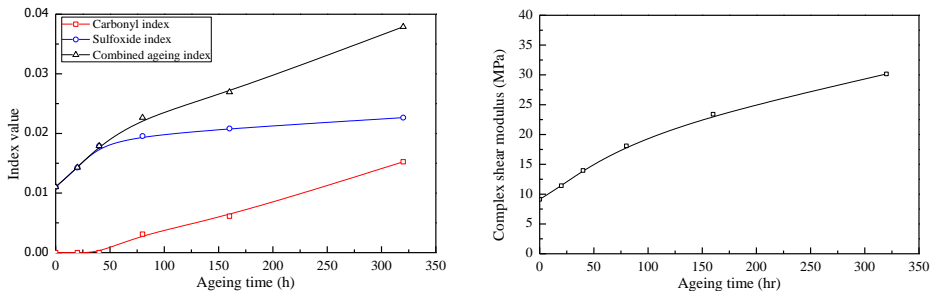
## 7.2 Chemo-mechanics of ageing model: Empirical model

### 7.2.1 Complex modulus at 20 °C and 10 Hz

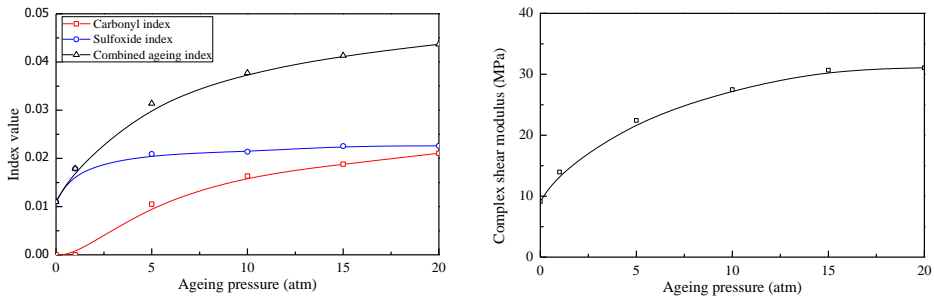
Based on the results of frequency sweep tests in Chapter 5, the complex shear modulus at 20 °C and 10 Hz of studied bitumen at different ageing conditions were selected and related with corresponding combined ageing index. The reason of choosing shear moduli at 10 Hz and 20 °C is that 10 Hz is the common used frequency in a dynamic test and 20 °C is considered to be room temperature [11, 12].

#### 7.2.1.1 Model development

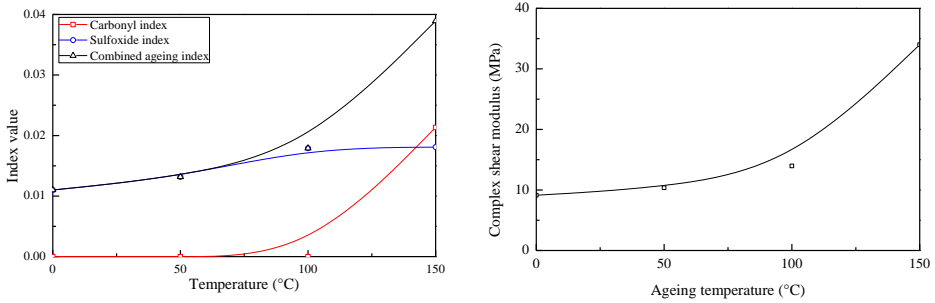
Figure 7.1 illustrates plots of the carbonyl index, the sulfoxide index and their summation with increasing ageing time, Figure 7.1(a), ageing pressure, Figure 7.1(b), and ageing temperature, Figure 7.1(c). Also, the variation of the complex shear moduli at 10 Hz and 20 °C are shown in the right hand side of Figure 7.1. Each point in the graph represents the average measurement value of the three replicate samples.



(a) Different ageing time (oven ageing at 100 °C and 1 atm).



(b) Different ageing pressures (PAV ageing for 40 h at 100 °C).



(c) Different ageing temperatures (oven ageing for 40 h at 1 atm).

**Figure 7.1** Ageing indices (left column) and complex shear moduli at 20 °C and 10Hz (right column) of PEN 70/100 at different ageing conditions.

Figure 7.1 shows that the combined ageing index and the complex shear modulus follow the same trend when varying the ageing conditions. Plotting the combined ageing index against the complex shear modulus at 10 Hz, 20 °C, one can observe that there is a linear relationship between the two properties, Figure 7.2. It is interesting to note that this relationship does not depend on the ageing method. In another words, the different ageing conditions can be interrelated.

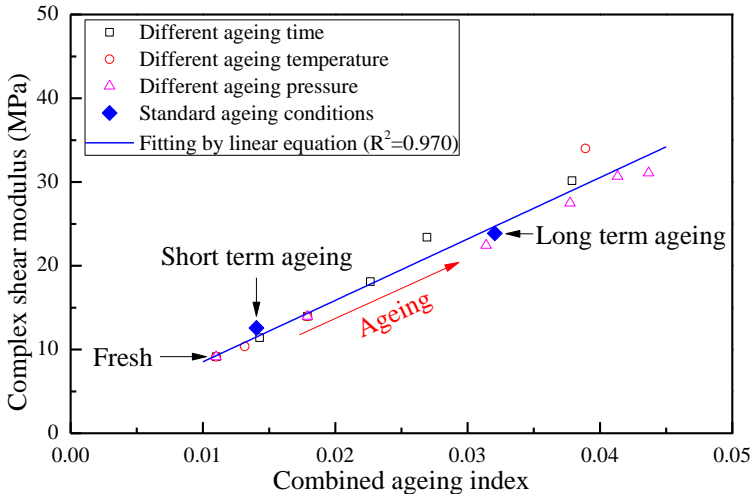


**Figure 7.2** Complex shear modulus at 10 Hz, 20 °C vs the combined ageing index at different ageing conditions.

### 7.2.1.2 Model validation

In order to correlate laboratory ageing to field ageing, bitumen was extracted from pavement test sections and tested for its rheological and chemical properties, as presented in Chapter 6. Following the methodology of Section 7.2.1.1, the relationship between the combined ageing index and the complex shear modulus (10 Hz, 20 °C) was found. The results after laboratory and field ageing are plotted in Figure 7.3. The black points in the graph are the results from the laboratory aged samples and the coloured symbols are from field aged samples.

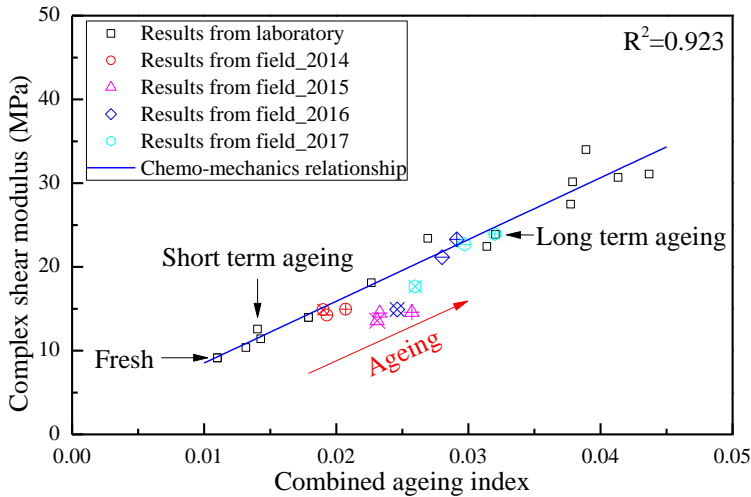


**Figure 7.3 Comparison of laboratory and field results.**

Figure 7.3 shows an overall agreement between field results and the predictions of the chemo-mechanics of ageing model. The deviation of some field results may be caused by the discrepancy between the field and laboratory ageing conditions. Furthermore, for the field results, the symbols with '+', '-' and 'x' correspond to the results of bitumen samples from top, middle and bottom slices respectively. It can be observed that the effect of ageing is more pronounced on the top of the pavement and decreases with increasing pavement depth. Also, the differences in ageing among the three depths increase with ageing time.



## 7.2.2 Crossover model and crossover modulus

In the previous section, the empirical model is limited to consider only the complex shear modulus at specific frequency and temperature. In this section, a new model was developed to correlate the phase change behaviour (bitumen change from viscoelastic fluid to solid) with ageing.

### 7.2.2.1 Model development

As described in Chapter 5, there was a good logarithmic relationship between crossover frequency and crossover modulus for the studied bitumen. Figure 7.4 plots the crossover frequency against the crossover modulus of the studied bitumen subjected to the various ageing protocols and, for the convenience of description, it is referred hereinafter as the crossover map.

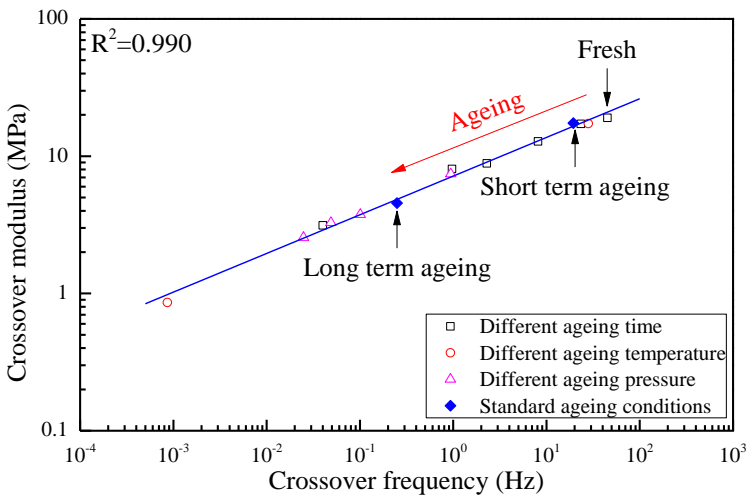


**Figure 7.4 Crossover frequency vs crossover modulus of bitumen at different ageing conditions.**

In Figure 7.4, due to ageing, the points move from the top right corner down towards the left corner along the indicated blue line. The ageing state of bitumen, which can be described by the changes in the values of the combined ageing index, determines how far a point can move. Then the relationship between chemical and mechanical properties of aged

bitumen (for each ageing condition) can be described by using normalized distance in the crossover map and change in the combined ageing index (carbonyl index + sulfoxide index). The unit distance is defined as the length between the Fresh point and the Long term ageing point in Figure 7.4. Figure 7.5 shows that there is a good linear relationship between these two parameters for the specific bitumen type. Interestingly it appears that this relationship does not depend on the ageing methods. In another words, the results indicate that the different ageing conditions can be used interchangeably.

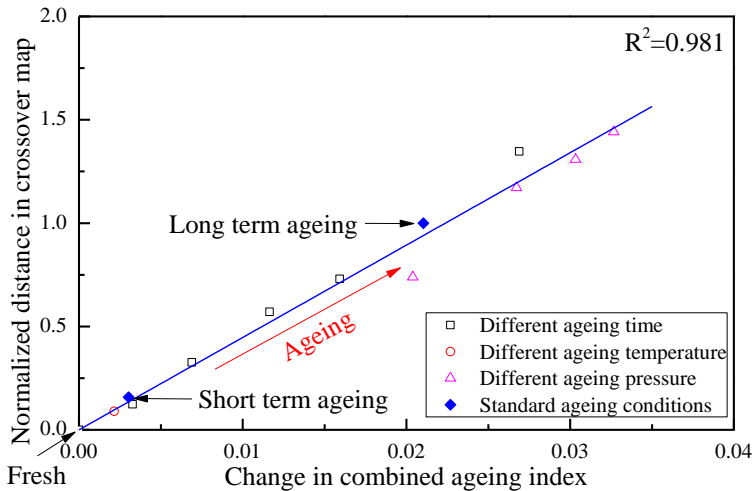


**Figure 7.5 Normalized distance in the crossover map vs change in combined ageing index of bitumen at different ageing conditions.**

### 7.2.2.2 Model validation

Based on the test results in Chapter 6, the crossover frequency and crossover modulus of field aged sample were found, Figure 7.6. The black points in the graph are the results from the laboratory aged samples and the coloured symbols are from field aged samples. The good logarithmic relationship between crossover frequency and crossover modulus for the studied bitumen, presented in Chapter 5, was well validated by the field ageing data.

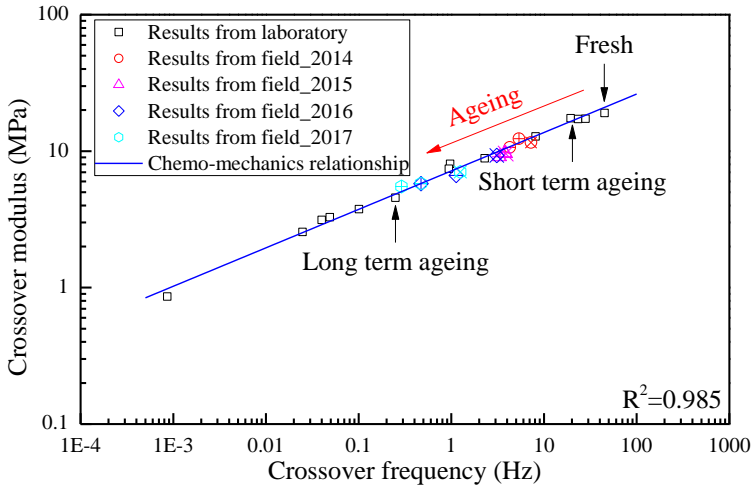


**Figure 7.6 Crossover frequency vs crossover modulus of bitumen at laboratory and field ageing conditions.**

Following the aforementioned methodology, the relationship between the combined ageing index and the distance in crossover map was found. The results after laboratory and field ageing are plotted in Figure 7.7. Considering the test error, Figure 7.7 shows an overall agreement between field results and the predictions of the chemo-mechanics of ageing model.

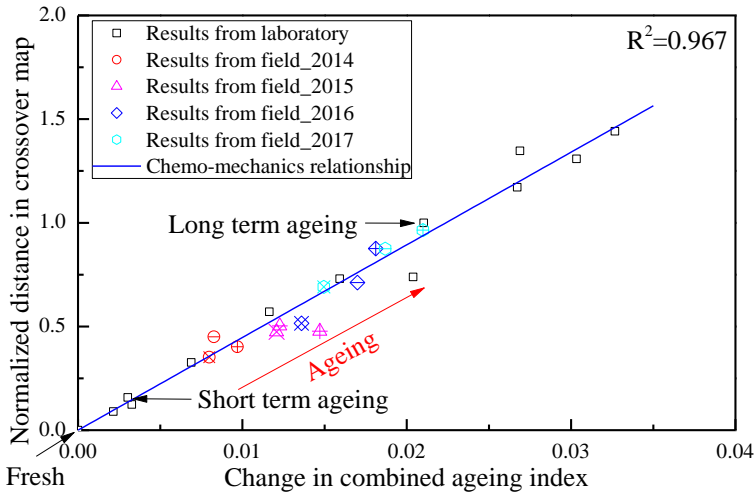


**Figure 7.7 Normalized distance in the crossover map vs change in combined ageing index of bitumen at laboratory and field ageing conditions.**

### 7.3 Ageing effect on constitutive models

#### 7.3.1 Maxwell model

The Maxwell model [13-15] is one of the basic constitutive models for viscoelastic materials. It is represented by a spring and a dashpot connected in series, Figure 7.8.

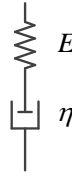


Figure 7.8 Schematic of the Maxwell model.

The constitutive equation of the Maxwell model is defined as

$$\frac{d\varepsilon}{dt} = \frac{1}{E} \frac{d\sigma}{dt} + \frac{\sigma}{\eta} \quad (7.1)$$

where  $E$  is the elastic modulus of the spring and  $\eta$  is the viscosity parameter of the dashpot. Under sinusoidal loading, the complex modulus, the storage modulus, the loss modulus, the absolute value of the complex modulus and the phase angle can be written as

$$E^*(i\omega) = \frac{E\omega^2\eta^2 + iE^2\omega\eta}{E^2 + \omega^2\eta^2} \quad (7.2)$$

$$E'(i\omega) = \frac{E\omega^2\eta^2}{E^2 + \omega^2\eta^2} \quad (7.3)$$

$$E''(i\omega) = \frac{E^2\omega\eta}{E^2 + \omega^2\eta^2} \quad (7.4)$$

$$|E^*(i\omega)| = \sqrt{(E'(i\omega))^2 + (E''(i\omega))^2} \quad (7.5)$$

$$\delta = \arctan \frac{E''(i\omega)}{E'(i\omega)} \quad (7.6)$$

Since there is a relationship between  $E$  and  $G$  ( $E=2G(1+\nu)$ ), the master curves (reference temperature is 20 °C) of the complex modulus and

phase angle can be fitted to the Maxwell model using Eq. (7.3) to Eq.(7.6). All model parameters can be obtained by minimizing the mean relative error (*MRE*), as defined in Eq. (7.7).

$$MRE = \sum \frac{|G_c^* - G_t^*|}{G_t^*} + \sum \frac{|\delta_c - \delta_t|}{\delta_t} \quad (7.7)$$

where  $G_c^*$  is the calculated value and  $G_t^*$  is the test value of the complex shear modulus,  $\delta_c$  is the calculated value and  $\delta_t$  is the test value of the phase angle.

The model parameters are presented in Table 7.1, where the CAI stands for combined ageing index (summation of the carbonyl and the sulfoxide indices). From Table 7.1, a difference between fresh and aged materials can be clearly observed. It is clearly shown that the value of viscosity  $\eta$  increases with increasing ageing time, temperature and pressure. It validates the fact that bitumen would have higher viscosity after ageing. The shear modulus  $G$  seems to change with ageing as well, but it is not that obvious.

**Table 7.1 Maxwell model fitting parameters**

Ageing condition				Maxwell model parameters			CAI
No.	t (h)	T (°C)	P (atm)	$G$ (MPa)	$\eta$ (MPa s)	<i>MRE</i>	
1	Fresh			15.25	2.52	87.01	0.010
2	STA			14.23	5.96	97.68	0.014
3	LTA			19.00	18.79	112.90	0.032
4	20	100	1	16.11	4.08	91.46	0.014
5	40	100	1	18.46	6.10	96.94	0.018
6	80	100	1	18.67	9.85	103.08	0.023
7	160	100	1	23.88	15.48	109.19	0.027
8	320	100	1	20.63	43.41	122.40	0.038
9	40	50	1	15.84	2.75	88.98	0.013
10	40	150	1	11.79	252.43	134.29	0.039
11	40	100	5	19.90	19.94	112.35	0.035
12	40	100	10	14.38	41.41	119.07	0.038
13	40	100	15	16.61	49.03	121.60	0.041
14	40	100	20	16.93	55.99	124.16	0.042

The model was validated using three sets of data, at fresh (unaged) condition, after STA and LTA ageing. Figure 7.9 shows that the Maxwell model cannot properly describe the response of the material across the frequency spectrum. The high values of MRE in Table 7.1 support this point as well.

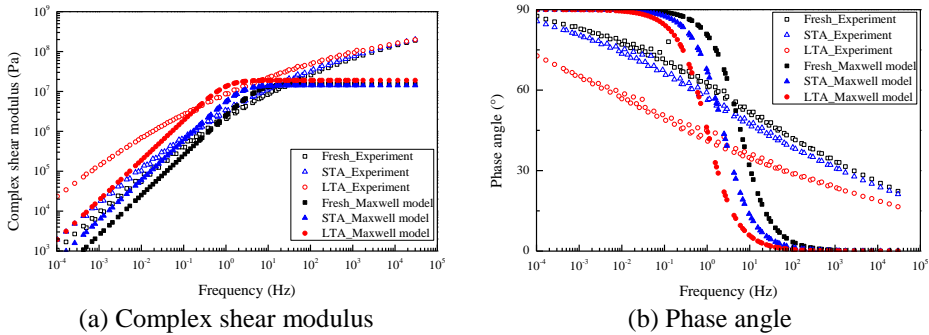


**Figure 7.9 Validation of the Maxwell model.**

### 7.3.2 Kelvin model

The Kelvin model [16, 17] is another basic constitutive model for viscoelastic materials. It consists of a spring and a dashpot element in parallel, Figure 7.10.

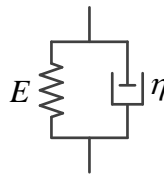


**Figure 7.10 Schematic of the Kelvin model.**

The constitutive equation of the Kelvin model is defined as

$$\sigma = E\varepsilon + \eta \frac{d\varepsilon}{dt} \quad (7.8)$$

where  $E$  is the elastic modulus of the spring and  $\eta$  is the viscosity parameter of the dashpot. Under sinusoidal loading, the complex

modulus, the storage modulus, the loss modulus, the absolute value of the complex modulus and the phase angle can be written as

$$E^*(i\omega) = E + i\eta\omega \quad (7.9)$$

$$E'(i\omega) = E \quad (7.10)$$

$$E''(i\omega) = \omega\eta \quad (7.11)$$

$$|E^*(i\omega)| = \sqrt{(E'(i\omega))^2 + (E''(i\omega))^2} \quad (7.12)$$

$$\delta = \arctan \frac{E''(i\omega)}{E'(i\omega)} \quad (7.13)$$

By minimizing the mean relative error, Eq. (7.7), the model parameters were obtained and presented in Table 7.2.

**Table 7.2 Kelvin model fitting parameters**

Ageing condition				Kelvin model parameters			CAI
No.	t (h)	T (°C)	P (atm)	$G$ (Pa)	$\eta$ (Pa s)	$MRE$	
1	Fresh			9.22E-04	1.26E+04	154.08	0.010
2	STA			3.25E-04	1.21E+04	177.41	0.014
3	LTA			2.35E+04	3.98E-01	181.11	0.032
4	20	100	1	3.14E-04	1.37E+04	164.56	0.014
5	40	100	1	8.22E-02	1.40E+04	176.20	0.018
6	80	100	1	5.53E+03	1.07E-01	191.47	0.023
7	160	100	1	1.57E+04	2.83E-01	182.26	0.027
8	320	100	1	7.27E+04	3.16E-01	179.19	0.038
9	40	50	1	6.03E-04	1.21E+04	160.92	0.013
10	40	150	1	4.57E+05	3.98E-01	175.79	0.039
11	40	100	5	2.13E+04	3.78E-01	181.33	0.035
12	40	100	10	4.58E+04	8.43E-01	179.73	0.038
13	40	100	15	6.53E+04	1.08E+00	179.29	0.041
14	40	100	20	8.32E+04	1.38E+00	178.92	0.042

From Table 7.2, it is clearly observed that, for the weak ageing conditions (short time, low temperature and low pressure ageing conditions), the value of the viscosity  $\eta$  is much bigger than the value of the shear modulus  $G$ , the difference is about 8 orders of magnitude. On the contrary, for the strong ageing conditions (long time, high

temperature and high pressure ageing conditions ), the value of the shear modulus  $G$  is much bigger than the value of the viscosity  $\eta$  , the difference is about 5 orders of magnitude. In the other words, the Kelvin model physically describes the soft bitumen as a viscous dashpot and the hard bitumen as an elastic spring. Moreover, all the values of MRE are too high, which means that the Kelvin model cannot capture the response of the materials across the frequency spectrum at any ageing conditions, Figure 7.11.

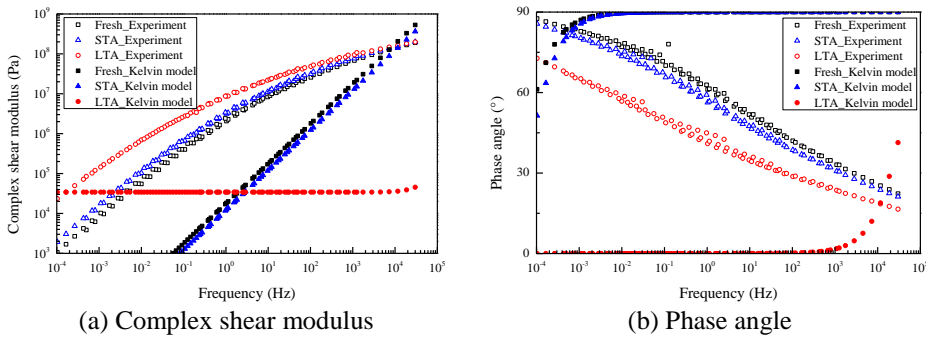


Figure 7.11 Validation of the Kelvin model.

### 7.3.3 Burgers model

Burgers model [18-20] consists of a Maxwell element and a Kelvin element, Figure 7.12.

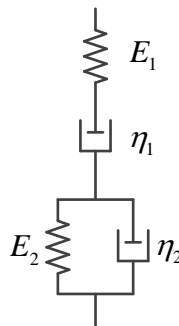


Figure 7.12 Schematic of the Burgers model.



The constitutive equation of the Burgers model is defined as

$$\sigma + p_1 \frac{d\sigma}{dt} + p_2 \frac{d^2\sigma}{dt^2} = q_1 \frac{d\varepsilon}{dt} + q_2 \frac{d^2\varepsilon}{dt^2} \quad (7.14)$$

where,

$$p_1 = \frac{\eta_1 E_1 + \eta_1 E_2 + \eta_2 E_1}{E_1 E_2} \quad (7.15)$$

$$p_2 = \frac{\eta_1 \eta_2}{E_1 E_2} \quad (7.16)$$

$$q_1 = \eta_1 \quad (7.17)$$

$$q_2 = \frac{\eta_1 \eta_2}{E_2} \quad (7.18)$$

and  $E_1$  and  $E_2$  are the elastic moduli of the spring in the Maxwell and the Kelvin elements, respectively.  $\eta_1$  and  $\eta_2$  are the viscosities of the dashpot in the Maxwell and the Kelvin elements, respectively. Under sinusoidal loading, the complex modulus can be written as

$$E^*(i\omega) = \frac{1}{\left(\frac{1}{E_1} + \frac{E_2}{E_2^2 + \eta_2^2 \omega^2}\right) - \left(\frac{1}{\eta_1 \omega} + \frac{\eta_2 \omega}{E_2^2 + \eta_2^2 \omega^2}\right) i} \quad (7.19)$$

making

$$E^*(i\omega) = \frac{1}{\alpha - i\beta} \quad (7.20)$$

$$\alpha = \frac{1}{E_1} + \frac{E_2}{E_2^2 + \eta_2^2 \omega^2} \quad (7.21)$$

$$\beta = \frac{1}{\eta_1 \omega} + \frac{\eta_2 \omega}{E_2^2 + \eta_2^2 \omega^2} \quad (7.22)$$

Thus, the storage modulus, the loss modulus, the absolute value of the complex modulus and the phase angle can be written as

$$E'(i\omega) = \frac{\alpha}{\alpha^2 + \beta^2} \quad (7.23)$$

$$E''(i\omega) = \frac{\beta}{\alpha^2 + \beta^2} \quad (7.24)$$

$$|E^*(i\omega)| = \sqrt{(E'(i\omega))^2 + (E''(i\omega))^2} \quad (7.25)$$

$$\delta = \arctan \frac{E''(i\omega)}{E'(i\omega)} \quad (7.26)$$

By minimizing the mean relative error, Eq. (7.7), the model parameters were obtained and presented in Table 7.3. It can be observed that the values of viscosity in both the Maxwell and the Kelvin element increase with ageing. However, the values of the shear modulus in both Maxwell and Kelvin elements do not change significantly with ageing.

**Table 7.3 Burgers model fitting parameters**

Ageing condition				Burgers model parameters				MRE	CAI
No.	t (h)	T (°C)	P (atm)	$G_1$ (MPa)	$\eta_1$ (MPa s)	$G_2$ (MPa)	$\eta_2$ (MPa s)		
1	Fresh			46.58	4.52	3.93	0.70	53.07	0.010
2	STA			44.19	10.81	4.71	1.16	61.34	0.014
3	LTA			43.85	54.61	5.46	3.85	72.98	0.032
4	20	100	1	52.99	6.79	5.25	0.85	56.41	0.014
5	40	100	1	55.78	10.96	6.94	1.04	61.00	0.018
6	80	100	1	48.43	21.95	5.68	2.08	66.00	0.023
7	160	100	1	55.41	37.23	7.12	3.14	70.40	0.027
8	320	100	1	48.61	163.93	6.44	9.45	79.59	0.038
9	40	50	1	45.50	5.52	4.27	0.73	54.56	0.013
10	40	150	1	53.37	418.84	8.46	10.65	89.19	0.039
11	40	100	5	47.33	50.42	6.57	3.48	72.70	0.035
12	40	100	10	44.88	100.43	5.56	6.85	77.13	0.038
13	40	100	15	51.99	123.41	7.50	5.93	79.28	0.041
14	40	100	20	46.01	172.13	6.14	8.55	80.87	0.042

Moreover, it can be observed that the values of MRE in Table 7.3 are smaller than those in Table 7.1 and Table 7.2. The validation of the model for three sets of data, Figure 7.13(a), shows that Burgers model can only describe the master curve of the complex shear modulus satisfactorily over a limited frequency range and the maximum stiffness

modulus reaches an asymptotic value corresponding to the parameter  $G_1$ . However, it cannot capture the master curve of the phase angle for any frequency spectrum at all, Figure 7.13(b).

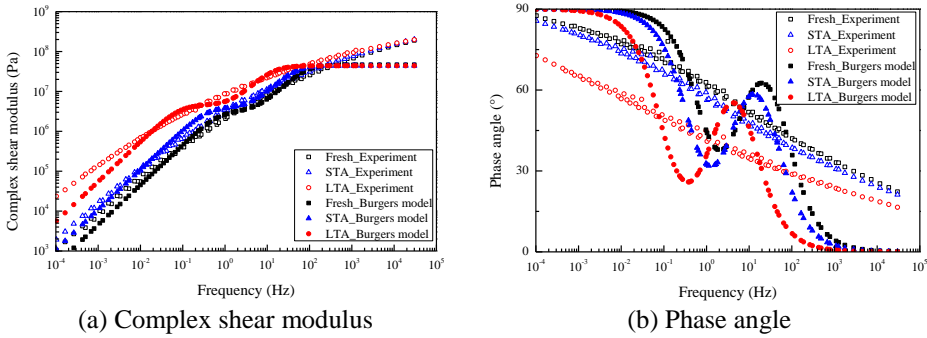


**Figure 7.13 Validation of the Burgers model.**

### 7.3.4 Generalized Maxwell model

The Generalized Maxwell (GM) model [21-23] is one of the most general forms of linear models for viscoelasticity. In this model, several Maxwell elements are assembled in parallel, Figure 7.14.

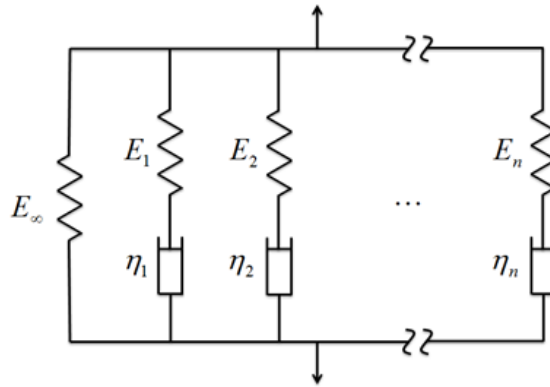


**Figure 7.14 Schematic of the Generalized Maxwell model.**

The constitutive equation of the GM model is defined as

$$\sum_{k=0}^n p_k \frac{d^k \sigma}{dt^k} = \sum_{k=0}^n q_k \frac{d^k \varepsilon}{dt^k} \quad (7.27)$$

where  $p_k$  and  $q_k$  are material parameters. Under sinusoidal loading, the complex modulus can be written as

$$E^*(i\omega) = E_\infty + \sum_{k=1}^n \frac{E_k \omega^2 \eta_k^2 + i E_k^2 \omega \eta_k}{E_k^2 + \omega^2 \eta_k^2} \quad (7.28)$$

Thus, the storage modulus, the loss modulus, the absolute value of the complex modulus and the phase angle can be written as

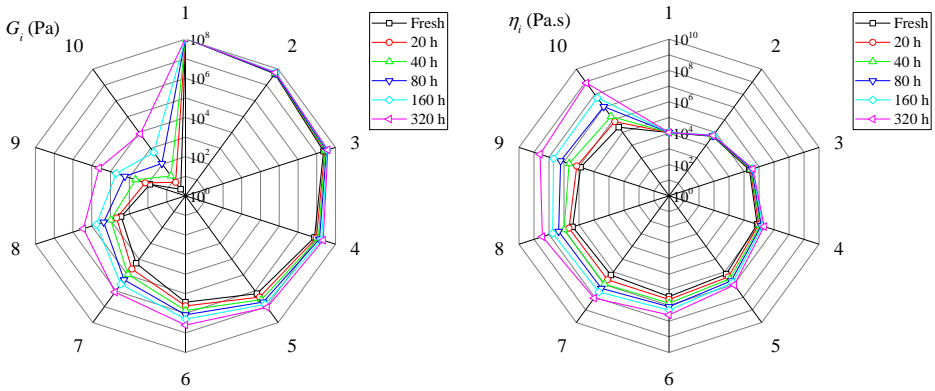
$$E'(i\omega) = E_\infty + \sum_{k=1}^n \frac{E_k \omega^2 \rho_k^2}{1 + \omega^2 \rho_k^2} \quad (7.29)$$

$$E''(i\omega) = \sum_{k=1}^n \frac{E_k \omega \rho_k}{1 + \omega^2 \rho_k^2} \quad (7.30)$$

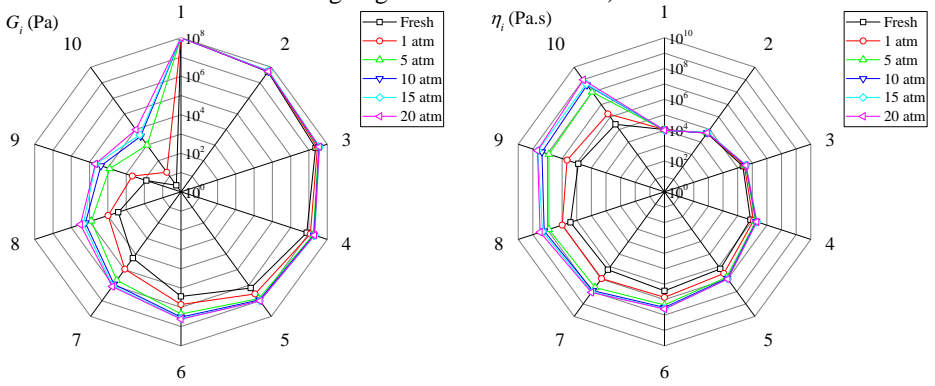
$$|E^*(i\omega)| = \sqrt{(E'(i\omega))^2 + (E''(i\omega))^2} \quad (7.31)$$

$$\delta = \arctan \frac{E''(i\omega)}{E'(i\omega)} \quad (7.32)$$

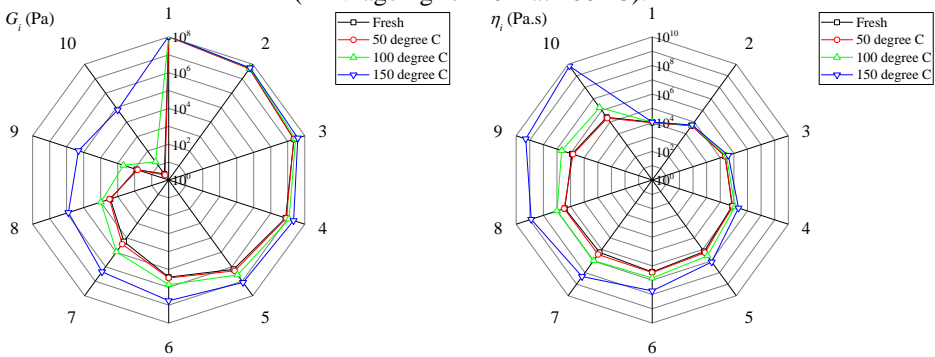
where  $\rho_k = \frac{\eta_k}{E_k}$ ,  $E_k$  and  $\eta_k$  are the elastic modulus and the viscosity of  $k^{\text{th}}$  Maxwell element. In this study, a GM model with 10 parallel Maxwell components was selected to fit the master curve of the complex shear modulus and the phase angle at a reference temperature of 20 °C. The value of  $\rho_k$  was selected to vary from  $10^{-4}$  to  $10^5$ .  $E_\infty = 0$  was chosen. The additional model parameters were obtained by minimizing the mean relative error as shown in Eq. (7.7). The results are presented in Figure 7.15 and the validation of the model for three sets of data is shown in Figure 7.16.



(a) The influence of various ageing times on shear modulus  $G_i$  and viscosity  $\eta_i$  (oven ageing at 100 °C and 1 atm).



(b) The influence of various ageing pressures on shear modulus  $G_i$  and viscosity  $\eta_i$  (PAV ageing for 40 h at 100 °C).



(c) The influence of various ageing temperatures on shear modulus  $G_i$  and viscosity  $\eta_i$  (oven ageing for 40 h at 1 atm).

**Figure 7.15** Shear moduli  $G_i$  and viscosities  $\eta_i$  of each Maxwell element component at different ageing conditions.

Figure 7.15 shows that ageing affects in a greater degree the more viscous Maxwell elements, with longer characteristic relaxation times  $\rho_i$  at unaged conditions. It can be observed that both the complex shear modulus and viscosity increase as bitumen is subjected to longer ageing times as well as higher temperature or pressure. However, it is not unusual to observe larger differences in the values of the complex shear modulus at lower testing frequencies or equivalently higher temperature, at which the viscous component dominates the bitumen behaviour.

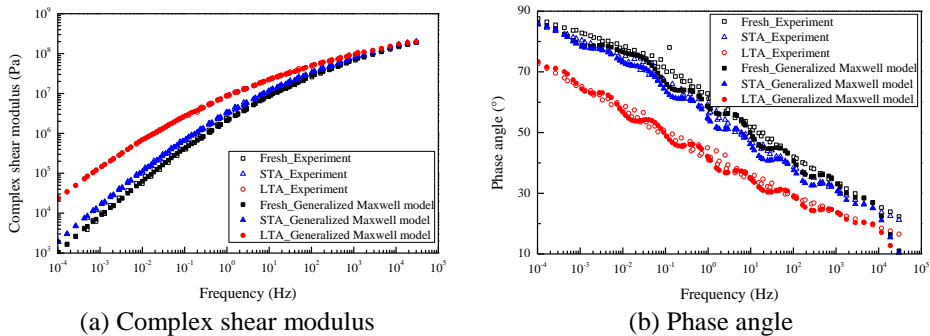


**Figure 7.16 Validation of the Generalized Maxwell model.**

Figure 7.16 shows an overall agreement between the test results and the model results. The more Maxwell components were added into the GM model, the less the deviation between the tests results and the model results. In the meanwhile, this necessitates the use of more model parameters and more difficulty defining the relationship between ageing and model parameters.

### 7.3.5 Huet model

The Huet model [24-27] was initially proposed for modelling asphalt binders and mixture response. It is consisted of a combination of a spring and two parabolic elements in series, Figure 7.17.

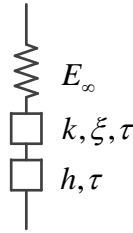


**Figure 7.17 Schematic of the Huet model.**

A parabolic element is a model with a parabolic creep function:

$$J(t) = a \left( \frac{t}{\tau} \right)^h \quad (7.33)$$

where  $a$  is a dimensionless constant,  $h$  is an exponent and  $\tau$  is the characteristic time.

Thus, the creep strain of a parabolic element can be written as

$$\varepsilon = J(t) \sigma_0 = a \left( \frac{t}{\tau} \right)^h \sigma_0 \quad (7.34)$$

Applying Laplace transform

$$\tilde{\varepsilon}(p) = \mathcal{L}(\varepsilon) = \mathcal{L} \left( a \left( \frac{t}{\tau} \right)^h \sigma_0 \right) = a \sigma_0 \mathcal{L} \left( \left( \frac{t}{\tau} \right)^h \right) \quad (7.35)$$

where  $p$  is the Laplace parameter and

$$\mathcal{L} \left( \left( \frac{t}{\tau} \right)^h \right) = \int_0^{\infty} \left( \frac{t}{\tau} \right)^h e^{-pt} dt \quad (7.36)$$

Defining

$$u = pt \quad (7.37)$$

and applying Eq.(7.37) into Eq. (7.36) gives

$$\begin{aligned}
\mathcal{L}\left(\left(\frac{t}{\tau}\right)^h\right) &= \int_0^{\infty} \left(\frac{t}{\tau}\right)^h e^{-pt} dt \\
&= \int_0^{\infty} \left(\frac{u}{p\tau}\right)^h \frac{e^{-u}}{p} du \\
&= \left(\frac{1}{p\tau}\right)^h \frac{\int_0^{\infty} u^h e^{-u} du}{p} \\
&= \left(\frac{1}{p\tau}\right)^h \frac{\Gamma(h+1)}{p}
\end{aligned} \tag{7.38}$$

where  $\Gamma$  is the Gamma function.

Applying Eq.(7.38) into Eq. (7.35).

$$\tilde{\varepsilon}(p) = a\sigma_0 \mathcal{L}\left(\left(\frac{t}{\tau}\right)^h\right) = a\sigma_0 \left(\frac{1}{p\tau}\right)^h \frac{\Gamma(h+1)}{p} \tag{7.39}$$

The Fourier transform of Eq. (7.39) can be easily derived by equating all occurrences of the Laplace parameter  $p$  to  $i\omega$ , which leads to

$$\hat{\varepsilon}(i\omega) = \tilde{\varepsilon}(p)\Big|_{p=i\omega} = a\sigma_0 \left(\frac{1}{i\omega\tau}\right)^h \frac{\Gamma(h+1)}{i\omega} \tag{7.40}$$

Applying Laplace transform into the stress function

$$\tilde{\sigma}(p) = \mathcal{L}(\sigma_0) = \frac{\sigma_0}{p} \tag{7.41}$$

Equivalently the Fourier transform is given by

$$\hat{\sigma}(i\omega) = \tilde{\sigma}(p)\Big|_{p=i\omega} = \frac{\sigma_0}{i\omega} \tag{7.42}$$

Thus, the complex modulus of the parabolic element can be written as

$$E^*(i\omega) = \frac{\hat{\sigma}(i\omega)}{\hat{\varepsilon}(i\omega)} = \frac{\frac{\sigma_0}{i\omega}}{a\sigma_0 \left(\frac{1}{i\omega\tau}\right)^h \frac{\Gamma(h+1)}{i\omega}} = \frac{(i\omega\tau)^h}{a\Gamma(h+1)} \tag{7.43}$$



Because the Huet model is represented by a spring and two parabolic elements connected in series, its creep strain is the summation of the creep strain of the three components.

$$\begin{aligned}\varepsilon &= \frac{\sigma_0}{E_\infty} + J_h(t)\sigma_0 + J_k(t)\sigma_0 \\ &= \frac{\sigma_0}{E_\infty} + a_h \left(\frac{t}{\tau}\right)^h \sigma_0 + a_k \left(\frac{t}{\tau}\right)^k \sigma_0\end{aligned}\quad (7.44)$$

Applying the Fourier transform to Eq. (7.44) results to

$$\hat{\varepsilon}(i\omega) = \frac{\sigma_0}{E_\infty i\omega} + a_h \sigma_0 \left(\frac{1}{i\omega\tau}\right)^h \frac{\Gamma(h+1)}{i\omega} + a_k \sigma_0 \left(\frac{1}{i\omega\tau}\right)^k \frac{\Gamma(k+1)}{i\omega}\quad (7.45)$$

Thus, the complex modulus of the parabolic element can be written as

$$\begin{aligned}E^*(i\omega) &= \frac{\hat{\sigma}(i\omega)}{\hat{\varepsilon}(i\omega)} \\ &= \frac{\frac{\sigma_0}{i\omega}}{\frac{\sigma_0}{E_\infty i\omega} + a_h \sigma_0 \left(\frac{1}{i\omega\tau}\right)^h \frac{\Gamma(h+1)}{i\omega} + a_k \sigma_0 \left(\frac{1}{i\omega\tau}\right)^k \frac{\Gamma(k+1)}{i\omega}} \\ &= \frac{1}{\frac{1}{E_\infty} + a_h \left(\frac{1}{i\omega\tau}\right)^h \Gamma(h+1) + a_k \left(\frac{1}{i\omega\tau}\right)^k \Gamma(k+1)} \\ &= \frac{E_\infty}{1 + a_h E_\infty \Gamma(h+1) (i\omega\tau)^{-h} + a_k E_\infty \Gamma(k+1) (i\omega\tau)^{-k}}\end{aligned}\quad (7.46)$$

By introducing

$$\xi = a_h \Gamma(h+1) E_\infty \quad (7.47)$$

$$1 = a_k \Gamma(k+1) E_\infty \quad (7.48)$$

the complex modulus of the Huet model is given by

$$E^*(i\omega) = \frac{E_\infty}{1 + \xi (i\omega\tau)^{-k} + (i\omega\tau)^{-h}} \quad (7.49)$$

Applying Euler's formula

$$e^{ix} = \cos x + i \sin x \quad (7.50)$$

Eq. (7.49) gives

$$\begin{aligned} E^*(i\omega) &= \frac{E_\infty}{1 + \xi(i\omega\tau)^{-k} + (i\omega\tau)^{-h}} \\ &= \frac{E_\infty}{1 + \xi \left( e^{\frac{\pi_i}{2} i} \omega\tau \right)^{-k} + \left( e^{\frac{\pi_i}{2} i} \omega\tau \right)^{-h}} \\ &= \frac{E_\infty}{1 + \xi(\omega\tau)^{-k} e^{-\frac{\pi}{2}ki} + (\omega\tau)^{-h} e^{-\frac{\pi}{2}hi}} \\ &= \frac{E_\infty}{1 + \xi(\omega\tau)^{-k} \left( \cos\left(\frac{k\pi}{2}\right) - i \sin\left(\frac{k\pi}{2}\right) \right) + (\omega\tau)^{-h} \left( \cos\left(\frac{h\pi}{2}\right) - i \sin\left(\frac{h\pi}{2}\right) \right)} \\ &= \frac{E_\infty}{1 + \xi(\omega\tau)^{-k} \cos\left(\frac{k\pi}{2}\right) + (\omega\tau)^{-h} \cos\left(\frac{h\pi}{2}\right) - i \left( \xi(\omega\tau)^{-k} \sin\left(\frac{k\pi}{2}\right) + (\omega\tau)^{-h} \sin\left(\frac{h\pi}{2}\right) \right)} \end{aligned} \quad (7.51)$$

Introducing the parameters  $\alpha$  and  $\beta$  Eq. (7.51) can be simplified to

$$E^*(i\omega) = \frac{E_\infty}{\alpha - i\beta} \quad (7.52)$$

$$\alpha = 1 + \xi(\omega\tau)^{-k} \cos\left(\frac{k\pi}{2}\right) + (\omega\tau)^{-h} \cos\left(\frac{h\pi}{2}\right) \quad (7.53)$$

$$\beta = \xi(\omega\tau)^{-k} \sin\left(\frac{k\pi}{2}\right) + (\omega\tau)^{-h} \sin\left(\frac{h\pi}{2}\right) \quad (7.54)$$

Thus, the storage modulus, the loss modulus, the absolute value of the complex modulus and the phase angle can be written as

$$E'(i\omega) = \frac{\alpha}{\alpha^2 + \beta^2} E_\infty \quad (7.55)$$

$$E''(i\omega) = \frac{\beta}{\alpha^2 + \beta^2} E_\infty \quad (7.56)$$

$$|E^*(i\omega)| = \sqrt{(E'(i\omega))^2 + (E''(i\omega))^2} \quad (7.57)$$

$$\delta = \arctan \frac{E''(i\omega)}{E'(i\omega)} \quad (7.58)$$

By minimizing the mean relative error, Eq. (7.7), the model parameters were obtained and presented in Table 7.4. It shows that the values of  $\xi$  and  $\tau$  obviously increase with ageing, while the values of  $G_\infty$ ,  $k$  and  $h$  slightly change with ageing.

**Table 7.4** Huét model fitting parameters

Ageing condition				Huét model parameters						CAI
No.	t (h)	T (°C)	P (atm)	$G_\infty$ (MPa)	$\xi$	$k$	$h$	$\tau$	<i>MRE</i>	
1	Fresh			358.80	9.00	0.440	0.890	0.006	9.89	0.010
2	STA			353.13	10.46	0.429	0.890	0.013	7.71	0.014
3	LTA			352.15	17.46	0.410	0.859	0.143	11.08	0.032
4	20	100	1	354.83	10.39	0.430	0.890	0.012	7.55	0.014
5	40	100	1	353.80	11.32	0.424	0.881	0.021	6.85	0.018
6	80	100	1	353.26	13.13	0.419	0.875	0.045	7.53	0.023
7	160	100	1	352.63	14.85	0.417	0.874	0.107	9.27	0.027
8	320	100	1	351.43	22.50	0.407	0.866	0.627	12.75	0.038
9	40	50	1	356.71	10.32	0.425	0.892	0.008	7.10	0.013
10	40	150	1	350.97	22.72	0.393	0.865	0.837	8.92	0.039
11	40	100	5	351.62	16.13	0.409	0.875	0.134	11.20	0.035
12	40	100	10	351.54	25.72	0.402	0.873	0.543	10.85	0.038
13	40	100	15	350.84	27.01	0.395	0.864	0.858	11.98	0.041
14	40	100	20	350.44	30.52	0.387	0.866	0.995	12.47	0.042

The model was validated using three sets of data, Figure 7.18. The results show that the Huét model can describe the response of the materials across the frequency spectrum well, which can also be reflected by the *MRE* values in Table 7.4.

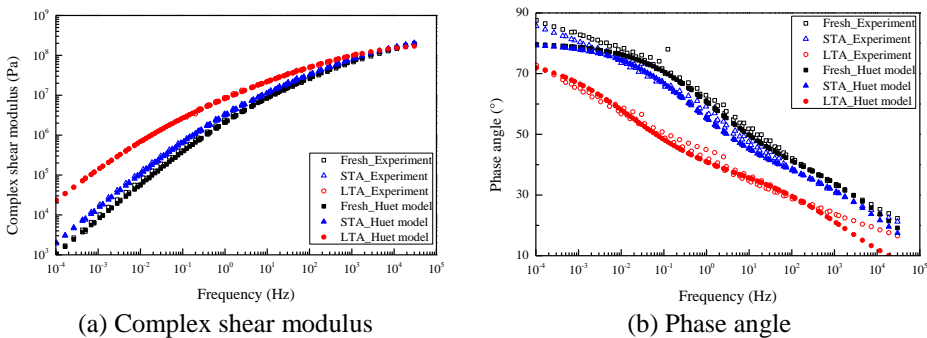


**Figure 7.18** Validation of the Huét model.

### 7.3.6 Comparison and discussion

Based on the study on the ageing effect on five different constitutive models, the values of the mean relative error (MRE) of each aged sample (ageing condition No.*i*) for different constitutive models are presented in Figure 7.19. Smaller MRE value means that the model can better describe the response of the materials across the frequency spectrum.

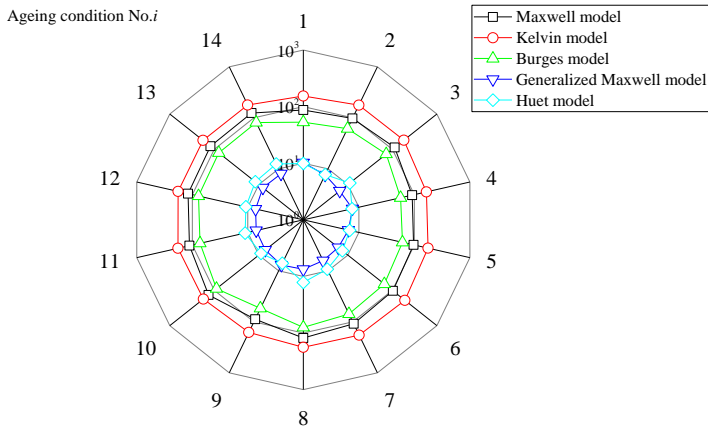


**Figure 7.19** The value of mean relative error (MRE) of each aged sample (ageing condition No.*i*) for the different constitutive models.

The result shows that the MRE values of the Maxwell model, the Kelvin model and the Burgers model are in the order of 100, while the MRE values of the Generalized Maxwell model and the Huet model are in the order of 10. This indicates that, by comparing with other models shown above, the Generalized Maxwell model and the Huet model can describe the master curve of the complex shear modulus and phase more accurately. The accuracy of each model can also be observed in the validation figures of each model, Figure 7.9, Figure 7.11, Figure 7.13, Figure 7.16 and Figure 7.18, respectively.

The MRE values of the Huet model are slightly higher than those of the Generalized Maxwell model. It means that the Generalized Maxwell model can better capture the response of the materials across the frequency spectrum. However, the amount of model parameters in the

Huet model is only five, which is half of that in the chosen Generalized Maxwell model. Moreover, only two of the five model parameters in the Huet model are significantly changed with ageing, Table 7.4. Therefore, the Huet model is selected to develop the chemo-mechanics of ageing model in this study.

## 7.4 Chemo-mechanics of ageing: Constitutive modelling

### 7.4.1 Model development

On the basis of the results in Table 7.4, the ratio of the Huet model parameters at aged state and at fresh state is illustrated in Figure 7.20

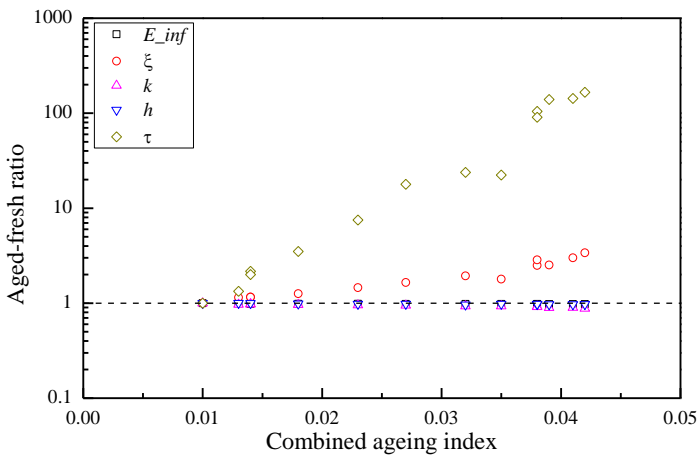


**Figure 7.20** The change of the Huet model parameters due to ageing

Figure 7.20 shows that the values of  $G_{\infty}$ ,  $k$  and  $h$  do not change significantly with ageing. Therefore the values of  $G_{\infty}$ ,  $k$  and  $h$  at any ageing conditions were set the same as the values at the fresh state. Specifically,  $G_{\infty}$  is 358.80 MPa,  $k$  is 0.44 and  $h$  is 0.89. The rest of the model parameters were obtained by minimizing the mean relative error, Eq. (7.7), and are presented in Table 7.5. The validation of the chemo-mechanical Huet model (CM-Huet model in short) for three groups of data is shown in Figure 7.21.

**Table 7.5 CM-Huet model fitting parameters**

Ageing condition				CM-Huet model parameters			CAI
No.	t (h)	T (°C)	P (atm)	$\xi$	$\tau$	MRE	
1	Fresh			9.00	0.006	9.89	0.010
2	STA			10.46	0.013	8.04	0.014
3	LTA			21.00	0.213	10.91	0.032
4	20	100	1	10.39	0.012	7.89	0.014
5	40	100	1	12.20	0.025	7.89	0.018
6	80	100	1	14.44	0.055	9.71	0.023
7	160	100	1	16.81	0.0134	12.23	0.027
8	320	100	1	27.62	1.009	14.06	0.038
9	40	50	1	10.13	0.008	8.28	0.013
10	40	150	1	34.68	3.184	10.9	0.039
11	40	100	5	19.91	0.195	15.69	0.035
12	40	100	10	25.37	0.543	10.86	0.038
13	40	100	15	27.16	0.858	13.49	0.041
14	40	100	20	30.87	1.258	16.57	0.042

where,  $G_\infty$  is 358.80 MPa,  $k$  is 0.44 and  $h$  is 0.89.

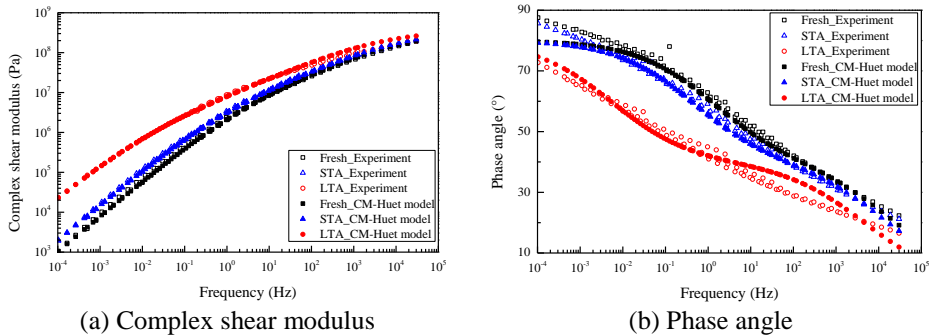
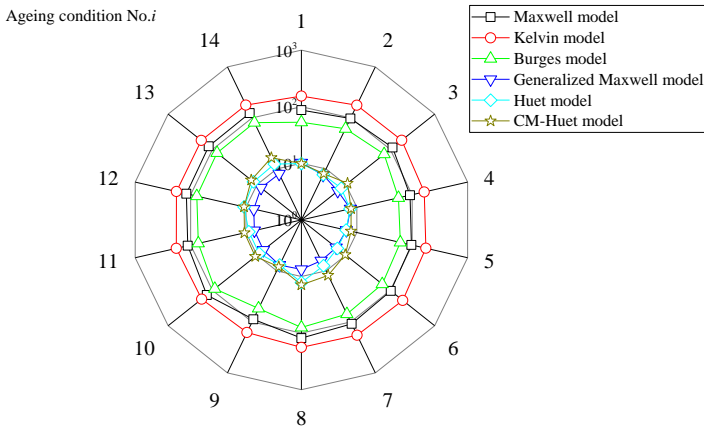
**Figure 7.21 Validation of the CM-Huet model.**

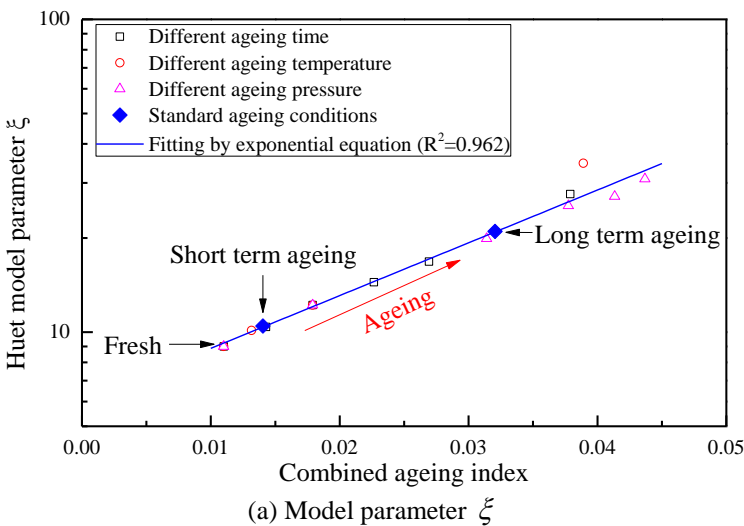
Figure 7.21 shows an overall agreement between the test results and the model predictions, especially for the master curve of the complex shear modulus. The comparison between the MRE value of the CM-Huet model and the other five constitutive models is illustrated in Figure 7.22. It shows that the MRE values of the CM-Huet model are much smaller than that of the Maxwell model, Kelvin model and Burgers model and are slightly higher than those of the Generalized Maxwell model and the

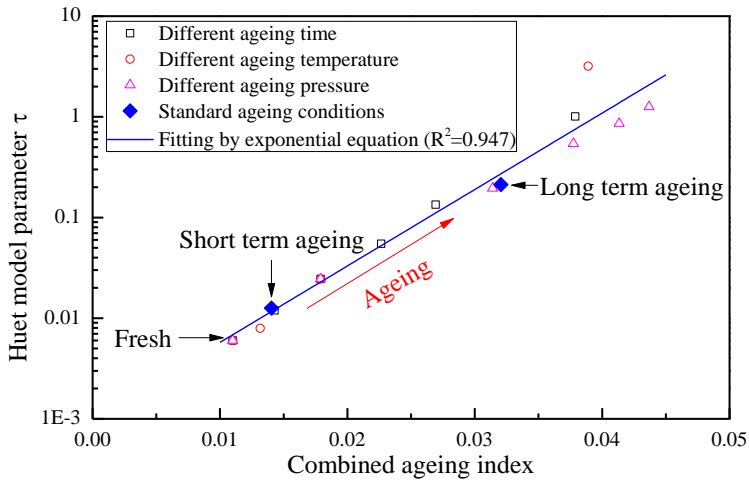
Huet model. In the meanwhile, there are only two model parameters changing with ageing in the CM-Huet model. In other words, these slightly higher MRE values are acceptable.



**Figure 7.22** The value of mean relative error (MRE) of each aged sample (ageing condition No.*i*) for different constitutive models.

In Table 7.5, a significant increase of the values of the model parameters  $\xi$  and  $\tau$  due to ageing can be clearly observed. Combining with the CAI (combined ageing index) values, the relationship between the model parameters and the combined ageing index can be plotted, Figure 7.23.



(b) Model parameter  $\tau$ 

**Figure 7.23 Model parameters vs the combined ageing index at different ageing conditions.**

Figure 7.23 shows that both model parameters  $\xi$  and  $\tau$  are logarithmically related to the combined ageing index. They can be fitted by Eq.(7.59) and Eq.(7.60), respectively.

$$\xi_{CAI} = \xi_a e^{\xi_b CAI} \quad (7.59)$$

$$\tau_{CAI} = \tau_a e^{\tau_b CAI} \quad (7.60)$$

where  $\xi_a$  and  $\xi_b$  are the fitting parameters for the model parameter  $\xi$ , which are 6.01 and 38.86, respectively.  $\tau_a$  and  $\tau_b$  are the fitting parameters for the model parameter  $\tau$ , which are 0.001 and 174.85, respectively.

#### 7.4.2 Model implementation

Because the CM-Huet model is a combination of a spring and two parabolic elements in series, its constitutive equation is the summation of each element contribution and is stated as



$$\varepsilon(t) = \left( \frac{1}{E_\infty} + a_{k\_CAI} \left( \frac{t}{\tau_{CAI}} \right)^k + a_h \left( \frac{t}{\tau_{CAI}} \right)^h \right) \sigma(t) \quad (7.61)$$

where

$$a_{h\_CAI} = \frac{\xi_{CAI}}{E_\infty \Gamma(h+1)} \quad (7.62)$$

$$a_k = \frac{1}{E_\infty \Gamma(k+1)} \quad (7.63)$$

By defining

$$E_{\text{mod}} = \frac{1}{\frac{1}{E_\infty} + a_{k\_CAI} \left( \frac{t}{\tau_{CAI}} \right)^k + a_h \left( \frac{t}{\tau_{CAI}} \right)^h} \quad (7.64)$$

and substituting it into Eq. (7.61), it follows that

$$\sigma(t) = E_{\text{mod}} \varepsilon(t) \quad (7.65)$$

This model behaves clearly like a non-linear elastic material where the modulus is time dependent.

To implement the above described 1D model in 3D, a hyper-elastic isotropic material model was adopted. Its constitutive law is governed by the Neo-Hookean strain energy function [28, 29], which is defined as

$$\Psi(I_1, I_2, I_3) = \frac{\mu}{2} \left[ (I_1 - 3) + \frac{1}{\alpha} (I_3^{-\alpha} - 1) \right], \quad \alpha = \frac{\lambda}{\mu} \quad (7.66)$$

in which  $\mu$  and  $\lambda$  are the Lamé constants defined as

$$\mu = \frac{E_{\text{mod}}}{2(1+\nu)} \quad (7.67)$$

$$\lambda = \frac{2\nu}{1-2\nu} \mu \quad (7.68)$$

where  $E_{\text{mod}}$  is the time-dependent elastic modulus of the 1D model,  $\nu$  is Poisson's ratio and  $I_1$ ,  $I_2$  and  $I_3$  are the three invariants of the right

Cauchy-Green deformation tensor  $C = F^T F$  in which  $F$  is the deformation gradient.

The Cauchy stress  $\sigma$  is now expressed in terms of the deformation gradient and the strain energy function as

$$\sigma = 2JF \frac{\partial \Psi}{\partial C} F^T = 2JF \left( \frac{\partial \Psi}{\partial I_1} \cdot \frac{\partial I_1}{\partial C} + \frac{\partial \Psi}{\partial I_2} \cdot \frac{\partial I_2}{\partial C} + \frac{\partial \Psi}{\partial I_3} \cdot \frac{\partial I_3}{\partial C} \right) F^T \quad (7.69)$$

in which

$$J = \det(F) \quad (7.70)$$

$$\frac{\partial \Psi}{\partial I_1} = \frac{\mu}{2}, \quad \frac{\partial I_1}{\partial C} = I \quad (7.71)$$

$$\frac{\partial \Psi}{\partial I_2} = 0, \quad \frac{\partial I_2}{\partial C} = I_1 I - C \quad (7.72)$$

$$\frac{\partial \Psi}{\partial I_3} = -\frac{\mu}{2} I_3^{-\alpha-1}, \quad \frac{\partial I_3}{\partial C} = I_3 C^{-1} \quad (7.73)$$

Combining Eq. (7.70) to Eq. (7.73) simplifies the definition of the Cauchy stress  $\sigma$  to

$$\begin{aligned} \sigma &= 2JF \frac{\mu}{2} (I - I_3^{-\alpha} C^{-1}) F^T \\ &= J^{-1} \mu (FF^T - I_3^{-\alpha} F C^{-1} F^T) \\ &= \mu J^{-1} (b - I_3^{-\alpha} I) \end{aligned} \quad (7.74)$$

where  $b$  is known as the left Cauchy-Green deformation tensor and  $I$  is the second order identity tensor.

Because of the influence of the parabolic elements, Eq. (7.64), the implemented model demonstrates the nonlinear response due to visco-elastic effect, Figure 7.24.

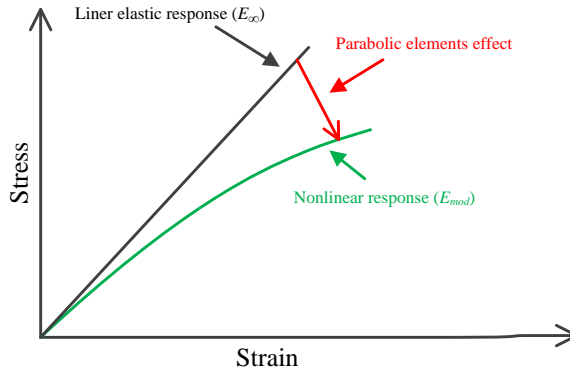


Figure 7.24 Schematic of constitutive response.

### 7.4.3 Model validation

The CM-Huet constitutive model was implemented in the CAPA-3D finite elements system. Simulations of the mechanical response of bitumen at various ageing conditions were performed at various frequencies. The geometry of the bituminous sample was modelled by using a cube  $2 \times 2 \times 2 \text{ mm}^3$ , which represents a material point at the edge of bitumen sample tested in the DSR device, Figure 7.25. This cube was discretized by using 3-D linear eight-node cubic elements and consists of 8 elements in total. During the simulations, a sinusoidal shear stress load, with frequency varying from  $10^{-3} \text{ Hz}$  to  $10^4 \text{ Hz}$  and an amplitude of 5 kPa, was applied on the top surface of the bitumen. The bitumen cube was allowed to freely expand or contract in all directions, but the bottom surface was fixed.

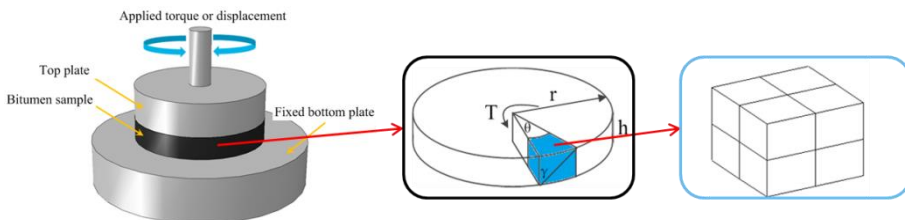
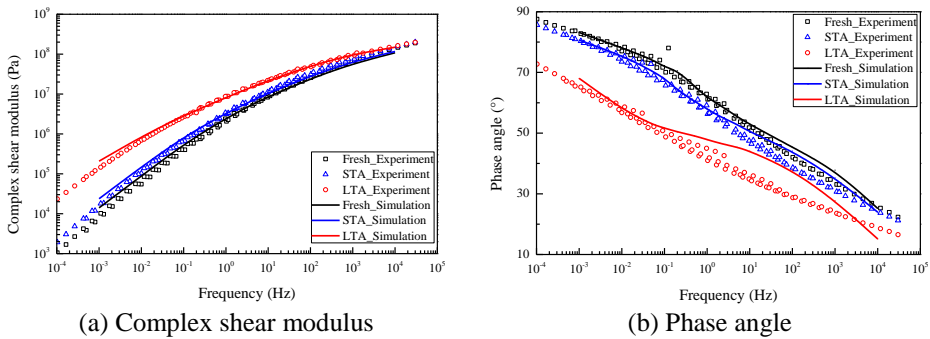


Figure 7.25 Schematic of bitumen cube finite element mesh.

The bituminous material was assumed to be isotropic. In order to simulate the ageing effect on the mechanical response of bitumen, three different cases were considered. The first case involved testing of bitumen at unaged (fresh) state, in the second case the bitumen was assumed to have been STA aged and in the third case the bitumen was assumed to have been LTA aged. The material parameters are shown in Table 7.5. The Poisson's ratio of bitumen was selected as 0.35 [30, 31]. The comparison between the experimental results and the simulation results is shown in Figure 7.26.



**Figure 7.26 Comparison of experimental results and simulation results.**

Figure 7.26 shows an overall agreement between the experimental results and the simulation results, especially for the master curve of the complex shear modulus. Since some parameters (Poisson's ratio, element meshes, time step etc.) in a 3D FEM simulation would have the influence on the results, there is some different between the plots in Figure 7.26 and Figure 7.21, which are the directly fitting results by CM-Huet equation.

In Figure 7.26(a), the simulation results are higher than the experimental results at the low frequency domain. On the contrary the simulation results are lower than the experimental results at the high frequency domain. The main reason is that the same Poisson's ratio was used for all frequency domain simulations. Figure 7.27 illustrates the simulation results with different Poisson's ratios for fresh bitumen.

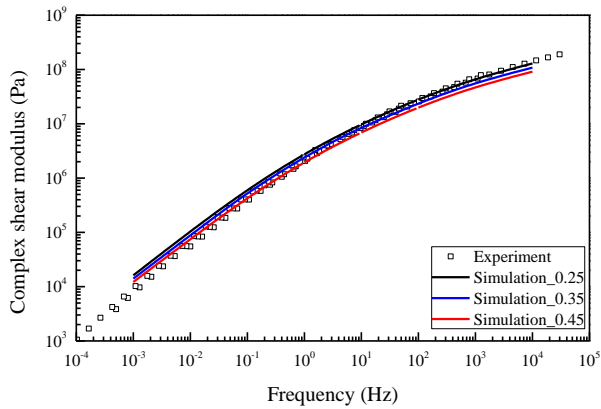


**Figure 7.27 Simulation results with different Poisson's ratios (fresh bitumen).**

In Figure 7.27, it can be observed that the complex shear modulus slightly increases with decreasing Poisson's ratio. It is verified a fact that at low frequency domain, corresponding to high temperature domain, the Poisson's ratio of the bitumen is high as it is in a fluid like state; while at high frequency domain, corresponding to low temperature domain, the Poisson's ratio of the bitumen is low due to its high stiffness and it behaves more like an elastic solid. Therefore, different Poisson's ratio should be used for different frequency ranges in the simulations [32, 33]. Thus the gap between the experimental results and simulations can be further reduced, Figure 7.28.

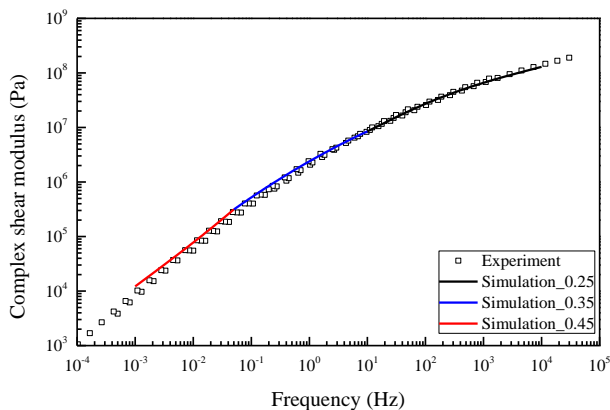


**Figure 7.28 Simulation results with different Poisson's ratios for various frequency ranges (fresh bitumen).**

## 7.5 Summary

Given the strong relationship between the mechanical pavement response and ageing, knowledge of the evolution of the chemical and mechanical properties in bituminous materials is of uppermost importance. For this reason, two empirical models are established and one constitutive model is formulated and implemented on the basis of the experimental results in Chapter 5.

The first empirical model describes the linear relationship between the complex shear modulus (at 10 Hz, 20 °C) and the combined ageing index (carbonyl index + sulfoxide index). Because the first model is limited to consider only the complex shear modulus at specific frequency and temperature, another empirical model was used to correlate the phase change behaviour (bitumen change from viscoelastic fluid to solid) with ageing. The model shows that a linear relationship exists between the combined ageing index and the normalized distance in crossover map. The models were developed on the basis of the results of laboratory aged samples. Nevertheless the models were in good agreement with the results of field aged samples.

Five typical constitutive models were tested for their capability to simulate the effects of ageing on mechanical response. The results indicate that the Generalized Maxwell model and the Huet model can capture the viscoelastic response of the bituminous materials across the frequency spectrum more accurately than the Maxwell, Kelvin and Burgers models. For the Generalized Maxwell model, ageing was observed to influence more the Maxwell elements with longer relaxation time, while for the Huet model, ageing was found to influence more the parabolic elements. Moreover, the Huet model consists of five parameters and two of which are related to ageing. Therefore, the Huet model was modified to include the chemo-mechanics ageing model and implemented using the finite element method. The CM-Huet model was implemented in the CAPA-3D finite element system. Comparison of

experimental and simulation results verified the CM-Huet model. Simulation results with different Poisson's ratios indicate that different Poisson's ratios should be considered for different frequency ranges.

## 7.6 References

1. Kandhal, P.S. and W.C. Koehler, *Significant studies on asphalt durability: Pennsylvania experience*. Transportation Research Record, 1984. **999**: p. 41-50.
2. Rostler, F.S. and R.M. White, *Influence of chemical composition of asphalts on performance, particularly durability*. ASTM STP, 1960. **277**: p. 64-88.
3. Petersen, J.C., *A thin film accelerated aging test for evaluating asphalt oxidative aging*. Transportation Research Board, Washington, DC, 1989. **58**: p. 220-237.
4. Kumar, A. and W. Goetz, *Asphalt hardening as affected by film thickness, voids and permeability in asphaltic mixtures*. in *Association of Asphalt Paving Technologists Proc.* 1977. p. 571-605.
5. Shahin, M., *Design system for minimizing asphalt concrete thermal cracking*. in *Volume I of proceedings of 4th International Conference on Structural Design of Asphalt Pavements*. 1977. p. 920-832.
6. Dauzats, M. and A. Rampal, *Mechanism of surface cracking in wearing courses*. in *International Conference on the Structural Design*. 1987. p. 232-247.
7. Petersen, J.C. and R. Glaser, *Asphalt oxidation mechanisms and the role of oxidation products on age hardening revisited*. Road Materials and Pavement Design, 2011. **12**(4): p. 795-819.
8. Lu, X. and U. Isacson, *Effect of ageing on bitumen chemistry and rheology*. Construction and Building Materials, 2002. **16**(1): p. 15-22.
9. Herrington, P.R., J.E. Patrick, and G.F.A. Ball, *Oxidation of roading asphalts*. Industrial & Engineering Chemistry Research, 1994. **33**(11): p. 2801-2809.
10. Petersen, J.C., *Chemical composition of asphalt as related to asphalt durability: state of the art*. Transportation research record, 1984(999): p. 13-30.
11. Plug, C., A. de Bondt, and H. Roos, *Performance of bitumen 70/100 obtained from different suppliers*. in *EATA*. 2013. p. 1-13.
12. Schlosser, F., et al., *Deformation properties and fatigue of bituminous mixtures*. Advances in Materials Science and Engineering, 2013: p. 1-7.
13. Badami, J.V. and M.L. Greenfield, *Maxwell Model Analysis of Bitumen Rheological Data*. Journal of Materials in Civil Engineering, 2011. **23**(10): p. 1387-1395.
14. Roylance, D., *Engineering viscoelasticity*. Department of Materials Science and Engineering—Massachusetts Institute of Technology, Cambridge MA, 2001. **2139**: p. 1-37.

15. Christensen, R.M., *Chapter I - Viscoelastic stress strain constitutive relations*, in *Theory of Viscoelasticity (Second Edition)*, R.M. Christensen, Editor. 1982, Academic Press. p. 1-34.
16. Komperød, M., *The Kelvin-Voigt model's suitability to explain the viscoelastic properties of anticorrosion bitumen at large shear strain in subsea cables and umbilicals*. in *Proceedings of the 56th Conference on Simulation and Modelling (SIMS 56)*. 2015. Linköping University, Sweden. p. 319-330.
17. Liao, J. and S. Sargand, *Viscoelastic FE modeling and verification of a U.S. 30 perpetual pavement test section*. *Road Materials and Pavement Design*, 2010. **11**(4): p. 993-1008.
18. Rowe, G., et al., *Viscoelastic analysis of hot mix asphalt pavement structures*. *Transportation research record*, 1995. **1482**: p. 44-51.
19. Nilsson, R.N., P.C. Hopman, and U. Isacson, *Influence of different rheological models on predicted pavement responses in flexible pavements*. *Road Materials and Pavement Design*, 2002. **3**(2): p. 117-149.
20. Malkin, A.Y. and A.I. Isayev, *Rheology: concepts, methods, and applications*. 2017: Elsevier.
21. Ren, J. and L. Sun, *Generalized maxwell viscoelastic contact model-based discrete element method for characterizing low-temperature properties of asphalt concrete*. *Journal of Materials in Civil Engineering*, 2016. **28**(2): p. 04015122.
22. Grzegorz, M. and I. Marek, *Modelling of asphalt concrete stiffness in the linear viscoelastic region*. *IOP Conference Series: Materials Science and Engineering*, 2017. **245**(3): p. 032029.
23. Michalczyk, R., *Implementation of generalized viscoelastic material model in Abaqus code*. Vol. 6. 2011. 2883-2890.
24. Xu, Q. and M. Solaimanian, *Modelling linear viscoelastic properties of asphalt concrete by the Huet-Sayegh model*. *International Journal of Pavement Engineering*, 2009. **10**(6): p. 401-422.
25. Olard, F. and H. Di Benedetto, *General "2S2PID" model and relation between the linear viscoelastic behaviours of bituminous binders and mixes*. *Road Materials and Pavement Design*, 2003. **4**(2): p. 185-224.
26. Pronk, A.C., *The Huet-Sayegh model: A simple and excellent rheological model for master curves of asphaltic mixes*, in *Asphalt Concrete: Simulation, Modeling, and Experimental Characterization*. 2006. p. 73-82.
27. Tiouajni, S., et al., *Approximation of linear viscoelastic model in the 3 dimensional case with mechanical analogues of finite size*. *Road Materials and Pavement Design*, 2011. **12**(4): p. 897-930.
28. Blatz, P.J. and W.L. Ko, *Application of finite elastic theory to the deformation of rubbery materials*. *Transactions of the Society of Rheology*, 1962. **6**(1): p. 223-252.
29. Scarpas, A., *A mechanics based computational platform for pavement engineering* (doctoral thesis). Delft University of Technology. 2005.
30. Alanazi, N., et al., *Evaluation of viscoelastic Poisson's ratio of asphalt mixtures*. *International Journal of Pavement Engineering*, 2017: p. 1-8.



31. Nguyen, Q.T., et al., *Nonlinearity of bituminous materials for small amplitude cyclic loadings*. Road Materials and Pavement Design, 2018: p. 1-15.
32. Nguyen, Q.T., H. Di Benedetto, and C. Sauzéat, *Linear and nonlinear viscoelastic behaviour of bituminous mixtures*. Materials and Structures, 2015. **48**(7): p. 2339-2351.
33. Maillard, S., et al., *Bitumen healing investigation using a specific fracture test*. Road Materials and Pavement Design, 2004. **5**(sup 1): p. 45-63.

# 8

## **CONCLUSIONS AND RECOMMENDATIONS**

---

## 8.1 Conclusions

### 8.1.1 Oxygen diffusion and reaction

Ageing of bituminous materials is a coupled oxygen diffusion and reaction process which occurs in the long-term. Both processes are influenced by a number of parameters such as bitumen type and environmental factors. To deepen our understanding of bitumen ageing, it is particularly important to develop a reliable model to simulate the oxygen diffusion-reaction process. In this work, a diffusion-reaction model was developed and implemented by means of three mathematical methods: the numerical integration method, the Laplace transform method and the finite element method. By using the diffusion-reaction model, the changes of the chemical composition of bitumen during ageing can be simulated.

Parametric analysis described the critical roles of reaction order and stoichiometry in the coupled diffusion-reaction model. Reaction order of reactive components in bitumen and oxygen have the same influences on the short term profiles of oxygen within the bituminous layers, but have different influences on the long term profiles of that. Simulations performed by varying the stoichiometry show that it takes less time for the bitumen film to be saturated with higher stoichiometry of reactive components in bitumen. On the contrary, it takes more time for that with higher stoichiometry of oxygen.

So far, there is no standard test method to determine the diffusion coefficient and the reaction constant of oxygen in bituminous materials. In this study, a new methodology has been developed, using FTIR measurements, for the determination of the parameters in the diffusion-reaction model. Based on some necessary and reasonable assumptions on stoichiometry and reaction order, the diffusion coefficient and reaction constant were determined. By using the corresponding model

parameters, the diffusion-reaction model was verified by the results of laboratory measurements.

### 8.1.2 Ageing effect on bitumen chemistry and rheology

Given the strong relationship between the mechanical material response and ageing, which is a chemically-induced process, the knowledge of the evolution of the chemical and mechanical properties in bituminous materials is of uppermost importance. For this reason, a series of experiments were conducted using various laboratory and field ageing.

The analysis of chemical properties showed the high changes in the carbonyl and sulfoxide functional groups with ageing. Furthermore, it confirmed two distinct phases of ageing, with an initial increase of sulfoxides and a second phase in which an increase of the carbonyls occurs. In addition, it has been shown that different ageing protocols can achieve the same ageing effect. It suggests that in the developing of the advanced ageing protocols, extending time and increasing temperature and pressure are the effective way to accelerate bitumen ageing.

The analysis of rheological properties was conducted through DSR testing by looking at the range of the linear viscoelastic (LVE) region, the master curves of complex shear modulus and phase angle, as well as the relaxation and fatigue characteristics. Specifically, ageing definitely has an effect on the linear visco-elastic limits of the materials. In comparison with fresh bitumen, aged bitumen has lower linearity limits for strain, whereas it has higher linearity limits for stress. The fact that bitumen becomes stiffer with ageing was also confirmed by the results of the frequency sweep tests at various temperatures. On the basis of standard fatigue analysis criteria, it appears that ageing seems to have a positive effect on the fatigue life of bitumen. This observation contradicts field observations and raises question about the suitability of such criteria. However, the fatigue tests give false impression with

ageing and that relaxation properties are more relevant. Results from the relaxation tests show that, in comparison with fresh bitumen, the aged samples had higher residual shear stress and longer relaxation time and, were therefore more susceptible to stress accumulation and consequently cracking.

The evolution of the rheological properties and chemical indices of the field aged samples were correlated with the climate data collected from the weather station. The results show that thermal ageing is the main cause of pavement ageing in the Netherlands. The rate of field ageing was about twice higher for porous asphalt than for dense asphalt due to the high air voids. The bitumen recovered from various depths of the PA cores shows the ageing propagation across the depth of the pavement and more severe ageing occurred on the surface of the pavement. The laboratory-aged bitumen following the standard long term ageing protocol, RTFOT+ PAV, is aged equivalently to the surface of a porous asphalt layer that has been in place for 3 years in the Netherlands. Field ageing at the pavement surface is far more severe than standard laboratory ageing protocols and cannot be simulated by RTFOT and PAV ageing.

### 8.1.3 Chemo-mechanics of ageing

The test results have indicated that the ageing mechanism affects the chemical composition of bitumen and it was clear that the rheological properties would be changed as well. If the specific relationship between the chemical properties and mechanical response of bitumen is established, predictions of pavement performance over longer time periods could become possible. In order to achieve this goal, two empirical models were established and one constitutive model was formulated and implemented.

The first empirical model described the linear relationship between the complex shear modulus (10 Hz, 20 °C) and the combined ageing index (carbonyl index + sulfoxide index). Because the first model was limited to consider only the complex shear modulus at specific frequency and temperature, another empirical model attempted to correlate the phase change behaviour (bitumen change from viscoelastic fluid to solid) with ageing. The second model showed that a linear relationship exists between the combined ageing index and the distance in crossover map, in which crossover map was the plot that the crossover modulus against crossover frequency. These two models were developed on the basis of the results of laboratory aged samples. Nevertheless the both models were in good agreement with the results of field aged samples.

In the end, five typical constitutive model were tested for their capability to simulate the effects of ageing on mechanical response of bitumen. The results indicated that the Generalized Maxwell model and the Huet model can capture the viscoelastic response of the bituminous materials across the frequency spectrum more accurately than the Maxwell, Kelvin and Burges models. For the Generalized Maxwell model, ageing was observed to influence more the Maxwell elements with longer relaxation time, while for the Huet model, ageing was found to influence more the parabolic elements. The Huet model was modified to include the chemo-mechanics ageing model and implemented by using the finite element method.

## **8.2 Recommendations**

In this study, a methodology was developed for the determination of the parameters of the diffusion-reaction model. However, the methodology requires a large number of samples to be prepared, aged and tested using the FTIR method. A more simple and efficient parameter determination methodology needs to be developed.

Bitumen is composed of complex hydrocarbons, and contains a number of chemical components such as calcium, iron, sulphur, and oxygen. Therefore, it may be that carbonyls and sulfoxides are not the only oxidation products. More advanced test equipment and methodologies need to be used or developed to obtain a more accurate qualitative and quantitative analysis of the oxidation products, and determine other alternative ageing indicators instead of the aforementioned traditional ones.

The findings of this study show that the current standard short- and long-term ageing protocols (RTFOT and PAV) cannot accurately describe the short- and long-term ageing behaviour (both on chemistry and mechanics) of porous asphalt. It is recommended to validate these findings for different mixture types such as stone mastic asphalt.

As a continuation of this research, the chemo-mechanics relationship and models should be validated for other bitumen types. The same methodology will be used to develop a chemo-mechanics model of ageing for mastics, mortars and mixtures. Meanwhile, finite element simulations will be performed to characterize the influence of ageing on the chemical properties and on the mechanical response of them.

Finally, constitutive modelling is not sufficient to describe the mechanical behaviour of bituminous materials. Other models such as an ageing damage model should be developed and coupling with other environmental factors such as moisture and UV needs to be considered.

# Summary

Research of the ageing mechanisms in the Netherlands is crucial to deal with ageing infrastructure and the growing pressure on and lack of natural resources. The use of porous asphalt incurs the additional costs because of the shorter service life and the more expensive maintenance required. On the other hand, the Dutch road engineering community has made significant efforts in recycling of pavements after the end of their service life. Currently, 90% of the asphalt is demolished and used in new asphalt pavement. Ideally, it would be nice to keep recycling asphalt concrete indefinitely, but this should be done without loss of functionality or environmental risks.

This thesis aims to acquire an advanced understanding of the fundamental thermal ageing processes of bituminous materials, by conducting a series of experiments and developing a set of computational models. A greater understanding of the bitumen ageing mechanisms and how they change physico-chemical properties of bitumen can help to accurately predict the service life of an asphalt pavement and develop high performance bituminous products that are less sensitive to ageing.

Ageing of bituminous materials is a coupled oxygen diffusion and reaction process which occurs in the long-term. In this thesis, a diffusion-reaction model was developed and implemented, which considers a number of parameters such as the bitumen type and environmental factors. With the help of this model, the chemical changes in bitumen and the profile of the oxidation products in bitumen would be understood well. Moreover, a new methodology has been developed for the determination of the parameters in the diffusion-reaction model using Fourier Transform Infrared (FTIR) measurements. By using the corresponding model parameters, the diffusion-reaction model was verified by the results of laboratory measurements.



Ageing of bituminous materials is a chemically-induced process, which is accompanied by major chemical and mechanical processes. In this thesis, Fourier Transform Infrared (FTIR) spectrometer and Dynamic Shear Rheometer (DSR) tests were utilized to investigate the effect of ageing on the chemical and mechanical properties of bituminous materials, which were aged at various conditions in laboratory and field. The FTIR tests results were used to quantify the changes in the chemical functional groups and to calculate ageing indices (carbonyl index and sulfoxide index) of bitumen. In addition, the DSR tests results were analysed to determine the evolution of the rheological, relaxation and fatigue properties of bitumen. Furthermore, the ageing behaviour of asphalt mixtures were investigated as well.

Ageing of bituminous materials is a physico-chemical process. In this thesis, correlations were made between the ageing indices and complex shear modulus, providing thus a chemo-mechanics framework to describe bitumen ageing. The results were validated by using data of field aged samples. Moreover, five typical constitutive model were evaluated for their capability to simulate the effects of ageing on mechanical response of bitumen. Finally, the Huet model was modified to include the chemo-mechanics ageing model and implemented by using the finite element method.

In conclusion, this thesis contributes to understanding the oxygen diffusion and reaction processes, determining the evolution of chemical and mechanical properties of bitumen during ageing, and establishing a relationship of the chemo-mechanics of ageing. The proposed experimental methods and computational models can serve as a tool to develop new materials, improve mixture design and predict the performance of asphalt pavement. Ultimately, this thesis contributes to build a well-functioning, long-lasting and safe highway infrastructure.

# Samenvatting

Onderzoek naar verouderingsmechanismen in Nederland is cruciaal in het licht van de verouderende infrastructuur en de toenemende druk op en het gebrek aan natuurlijke hulpbronnen. De toepassing van Zeer Open Asfalt vergroot de additionele kosten vanwege de kortere levensduur en het duurdere onderhoud. Anderzijds heeft de Nederlandse wegensector belangrijke vorderingen gemaakt met de recycling van verhardingen na het einde van hun levensduur. Thans wordt 90% van het vrijkomend asfalt hergebruikt in nieuwe asfaltverhardingen. Idealiter zou zijn om asfalt eeuwig te recyclen maar dit moet wel gebeuren zonder verlies aan functionaliteit en zonder milieurisico's.

Dit proefschrift beoogt om diepgaand inzicht te verwerven in de fundamentele thermische verouderingsprocessen van bitumineuze materialen door een serie experimenten uit te voeren en een set numerieke modellen te ontwikkelen. Een beter inzicht in de verouderingsmechanismen van bitumen, en hoe die de fysisch-chemische eigenschappen veranderen, kan bijdragen tot een accurate voorspelling van de levensduur van een asfaltverharding en tot de ontwikkeling van hoogwaardige bitumineuze producten die minder onderhevig zijn aan veroudering.

Veroudering van bitumineuze materialen is een combinatie van zuurstofdiffusie en een reactie proces op de lange termijn. In dit proefschrift is een diffusie-reactie model ontwikkeld en geïmplementeerd waarin een aantal parameters is opgenomen zoals het bitumen type en omgevingsfactoren. Dit model biedt een goed inzicht in de chemische veranderingen in bitumen en het profiel van de oxidatieproducten in bitumen. Bovendien is een nieuwe methode ontwikkeld voor de bepaling van de parameters in het diffusie-reactie model op basis van Fourier Transform Infrared (FTIR) metingen. Door de corresponderende modelparameters te gebruiken is het diffusie-reactie model geverifieerd met de resultaten van laboratoriummetingen.

Veroudering van bitumineuze materialen is een chemisch geïnitieerd proces dat gepaard gaat met belangrijke chemische en mechanische processen. In dit proefschrift zijn FTIR en Dynamic Shear Rheometer (DSR) metingen uitgevoerd om het effect van veroudering op de chemische en mechanische eigenschappen van bitumineuze materialen te onderzoeken die onder verschillende condities in het laboratorium en in de buitenlucht zijn verouderd. De FTIR meetresultaten zijn gebruikt om de veranderingen in de chemische functionele groepen te kwantificeren en om verouderingsindices (koolstofindex en zwavelindex) van bitumen te berekenen. De DSR meetresultaten zijn geanalyseerd om de ontwikkeling van de rheologische, relaxatie en vermoeiings eigenschappen van bitumen te bepalen. Verder is ook het verouderingsgedrag van asfaltmengsels onderzocht.

Veroudering van bitumineuze materialen is een fysisch-chemisch proces. In dit proefschrift zijn verbanden gelegd tussen de verouderingsindices en de complexe schuifmodulus. Op deze wijze is een chemisch-mechanisch kader voor de beschrijving van de veroudering van bitumen verkregen. De resultaten zijn gevalideerd met data van in de buitenlucht verouderde proefstukken. Bovendien is voor vijf typische constitutieve modellen nagegaan in hoeverre zij de effecten van veroudering op de mechanische respons van bitumen kunnen simuleren. Tenslotte is het chemisch-mechanisch verouderingsmodel ingebouwd in het Huet model en geïmplementeerd in de eindige elementen methode.

Concluderend wordt gesteld dat dit proefschrift er aan bijdraagt om de zuurstof diffusie en reactieprocessen te begrijpen, om de ontwikkeling van de chemische en mechanische eigenschappen van bitumen tijdens veroudering te bepalen, en om een relatie tussen de chemisch-mechanische processen bij veroudering vast te stellen. De voorgestelde experimentele methoden en numerieke modellen kunnen dienen als hulpmiddel bij de ontwikkeling van nieuwe materialen, kunnen het mengselontwerp verbeteren en het gedrag van asfaltverhardingen beter voorspellen. Uiteindelijk draagt dit onderzoek bij aan een goed functionerende, duurzame en veilige weginfrastructuur.

# Curriculum vitae

Ruxin Jing

荆儒鑫

05 May 1990	Born in Inner Mongolian, China
Sep. 2008-Sep.2012	B.S in Road, Bridge and River Crossing Engineering Honors School Harbin Institute of Technology, China
Sep. 2012-Sep.2014	M.S in Highway and Railway Engineering School of Transportation Science and Engineering Harbin Institute of Technology, China
Sep. 2014-Feb.2019	PhD candidate Section of Pavement Engineering Faculty of Civil Engineering and Geosciences Delft University of Technology

# List of publications

## Publications

R. Jing, A. Varveri, X. Liu, A. Scarpas, S. Erkens, *Laboratory and Field Ageing Effect on Bitumen Chemistry and Rheology in Porous Asphalt Mixture*. 98th Annual Meeting of the Transportation Research Board, Washington D.C., United States, 13/01/2019.

R. Jing, X. Liu, A. Varveri, A. Scarpas, S. Erkens, *The Effect of Ageing on Chemical and Mechanical Properties of Asphalt Mortar*. Applied Sciences (Switzerland), 2018. 8(11): p. 2231.

R. Jing, A. Varveri, X. Liu, A. Scarpas, S. Erkens, *Ageing Effect on Chemo-mechanics of Bitumen*. RILEM Bookseries, vol. 20, Springer Netherlands, pp. 71-76, RILEM 252-CMB-Symposium on Chemo Mechanical Characterization of Bituminous Materials , Braunschweig, Germany, 17/09/2018.

R. Jing, A. Varveri, X. Liu, A. Scarpas, S. Erkens, *Ageing Effect on the Relaxation Properties of Bitumen*. International Conference on Advances in Materials and Pavement Performance Prediction, Doha, Qatar, 16/04/2018.

R. Jing, A. Varveri, X. Liu, A. Scarpas, S. Erkens, *Chemo-Mechanics of Ageing on Bituminous Materials*. 97th Annual Meeting of the Transportation Research Board, Washington D.C., United States, 07/01/2018.

R. Jing, D. van Lent, C. kasbergen, A. Scarpas, X. Liu, S. Erkens, *Experimental and Computational Investigation of Gas Diffusion in Bitumen*. 96th Annual Meeting of the Transportation Research Board, Washington D. C., United States, 8/01/2017.

## Presentations

The 5th Chinese European Workshop on Functional Pavement Design, Changsha, China, 27/10/2018

The 6th International Transportation Doctoral Student Symposium, Urbana-Champaign, the Unite States, 20/10/2017.

The 4th TU Delft Workshop on Chemo-mechanics of Bituminous Materials, Delft, the Netherlands, 17/03/2017.

Chinese-Netherlands PhD & Master Student Symposium on Pavement Engineering, Chonqing & Chengdu, China, 29/07/2016.

The 4th International Transportation Doctoral Student Symposium, Harbin, China, 31/05/2015.